Cardiovascular Imaging of Myocardial Viability after Acute Myocardial Infarction

Nur Hayati Jasmin Bsc. MRes.

December 2020

For the degree of Doctor of Philosophy

University College London, UK

Centre for Advanced Biomedical Imaging (CABI)

Paul O'Gorman Building

72 Huntley Street

London, WC1E 6DD

Declaration

I, Nur Hayati Jasmin, confirm that the worked presented in this thesis is my own. Where information has, from other sources, I confirm that this has been indicated in the thesis. The work is based on research that was conducted by me during the period from September 2016 to September 2020 at the Centre for Advanced Biomedical Imaging (CABI) within University College London.

Nur Hayati Jasmin

09 December 2020

Abstract

Myocardial infarction is a major cause of death and disability worldwide. In patients with myocardial infarction, the extent and severity of ischemic injury are important prognostic factors for mortality and morbidity. After myocardial infarction, there is a window of opportunity in which intervention can salvage the affected, but still reversible damage caused to the cardiomyocytes. Non-invasive imaging has become a front-line method in the assessment of myocardial viability. A major challenge for present cardiovascular imaging is to identify better ways to assess viable (but threatened) myocardium to stratify patients into optimal treatment pathways. Manganese (Mn^{2+}) is an intracellular contrast agent and can enter myocytes through L-type calcium channel, making it an interesting imaging probe for Ca^{2+} fluxes. Manganese-enhanced magnetic resonance imaging (MEMRI) could provide an assessment on cardiac structure and function as well as in vivo monitoring of intracellular calcium ion (Ca^{2+}) changes. As a central regulator of cardiac contractility, intracellular Ca^{2+} changes could be used to assess viable myocardium after acute ischemic injury. Thus, the aim of my research was to investigate the accuracy of manganese as a marker of cell viability and develop cardiovascular imaging for assessment of myocardial viability in a mouse model of acute myocardial infarction. To accomplish this, this project is divided into three parts, ultimately leading towards the development of cardiovascular imaging for assessment of myocardial viability after acute myocardial infarction; (1) Characterisation of manganese to optimise dose and ensure safety, (2) Investigation of manganese as an early imaging indicator of cell viability using T1 mapping, and (3) Using manganese-enhanced MRI for functional assessment of the myocardium for early infarct size quantification in acute myocardial infarction: validation against the gold standard, late gadolinium enhancement (LGE-MRI).

Keywords: Cardiovascular imaging, Manganese-enhanced MRI (MEMRI), Myocardial viability, Acute myocardial infarction

Impact statement

The research presented in this thesis build upon the contributions of other researchers in the cardiovascular imaging and basic sciences communities. The completion of the works in this thesis would not be possible without their contributions. In return, I hope that my work will benefit researchers working inside and outside of academia in the following ways:

1. Manganese is a potent paramagnetic contrast agent that could give essential information on cellular viability. However, concern over manganese cardiotoxicity has limited its usage in the heart. Work presented in Chapter 2 provides a way to overcome cardiac toxicity as demonstrated with real-time high-resolution ultrasound imaging and MRI in vivo, supported by an in vitro MRI study. The findings from this work can benefit researchers with a greater insight into the cardiotoxicity effect of manganese and help to optimise the required dosage needed for different formulations (intravenous route, intraperitoneal route, and calcium supplement).
2. The work should encourage researchers and practitioners to think more broadly about applying this technique to other cardiovascular diseases, or other diseases that involve changes in calcium levels. The results presented in Chapter 3 should serve as an example of one approach to tracking changes in intracellular calcium levels at the early stage and the involvement of the nervous system in acute myocardial infarction model.
3. The work presented in Chapter 4 aims to validate the efficacy of manganese-enhanced MRI (MEMRI) against the current gold standard, late gadolinium enhancement (LGE-MRI) in acute myocardial infarction. This work proposes new ways for functional imaging of the myocardium at an early stage. These should give more confidence for clinical translation and inspire clinical practitioners to apply MEMRI for imaging myocardial viability. This approach would help in the assessment of viable myocardium that is salvageable at an acute stage intending to stratify patients into optimal treatment pathways.
4. Looking from a broader context, the technique used in work presented in this thesis could also be used to study the efficacy of new drug that targets acute myocardial infarction and cardiac regenerative therapy. Therapeutic agents aimed at reducing infarct size after acute myocardial infarction are under intensive investigation and have shown promise in pre-clinical and clinical models. In vivo imaging of response of therapy will guide optimisation of therapeutic dose, timing, and route of delivery, delivering a novel therapy for myocardial infarction.

Acknowledgement

Alhamdulillah, first and foremost, I would like to express my sincerest gratitude to my supervisors, Dr Daniel Stuckey and Professor Sean Davidson, who has guided and supported me throughout the course of my PhD study. More specifically, I would like to thank my primary supervisor Dr Daniel Stuckey for giving me the opportunity to work with him, for his endless encouragement, advice, and critique of my work, for giving me the chance to learn multiple skills. I would like to thank my secondary supervisor Prof Sean Davidson for his advice and for keeping me focused throughout my research. I would like to also thank Dr Jack Wells for his kind support with MRI physics since my first year.

I would like to thank the whole of CABI for their support during my time with them, without the incredible range of knowledge possessed by these people I would surely be worse off. Professor Mark Lythgoe has somehow cultured an atmosphere in the lab of academic excellence but made sure it never feels like I'm coming to work. Specifically, I would like to thank Cardiac group in CABI, Chris, Stephen, Annalisa, Xiao Xiao, Heather, and Shahrani for their kind support and advice. I would like to thank CABI alumni, Tom, Laurence and John for showing me what an MRI scanner and MATLAB are. CABI is full of people I cannot thank enough for their time, knowledge and camaraderie I am eternally grateful to.

I would like to extend my gratitude to friends, Nurul Ain, Dr Atiqah, Dr Rahimah, , Lyana, Afifah, Kak Rose, Nek Jah, Dr Zainab and family and all my friends, I am sure you know who you are, for their ongoing support and encouragement throughout the PhD journey. I would like to thank the King Scholarship of Malaysia (BYDPA) and University Sultan Zainal Abidin (UniSZA) for funding me during my time at UCL whose sponsorship I am incredibly grateful for. I want to also thank my late Uncle Yunus and Malaysages for being a limitless source of encouragement and inspiration.

Finally, and most importantly, I want to thank my parents Hj Jasmin Jasmin and Hjh Aminah Sinring and my family who have always supported me since forever and motivated me throughout my PhD journey.

Publications and awards arising from this PhD

Peer-reviewed journals articles – under review

2020

Jasmin, N.H. et al., 2020. Myocardial viability imaging using manganese enhanced MRI. *Science Advances*.

George, M.J., Jasmin, N.H. et al., 2020. Selective interleukin-6 trans-signalling blockade is more efficacious than pan-antagonism in re-perfused myocardial infarction. *JACC Basic to Translational Science*.

Published abstracts

2016

Wage, R., Gatehouse, P., Jasmin, N.H. et al., 2016. Myocardial T1 and ECV mapping: how we optimise technical aspects of acquisition. *Journal of Cardiovascular Magnetic Resonance*, 18(S1), pp.1–2.

2017

Jasmin, N.H. et al., 2017. Quantifying manganese-calcium interaction for optimal cardiac manganese-enhanced MRI. *British Chapter ISMRM-Postgraduate meeting (2017)*.

Jasmin, N.H. et al., 2017. 158 Quantifying manganese-calcium interaction for optimal cardiac manganese enhanced MRI. *Heart*, 103(Suppl 5), pp.A113.

2018

Jasmin, N.H. et al., 2018. T1-mapping cardiac-manganese enhanced MRI: assessment of calcium homeostasis and ischemic injury in mice. In *Journal of Cardiovascular Magnetic Resonance (2018)*. p. 4765.

Jasmin, N.H. et al., 2018. 112 In Vivo investigation of intracellular calcium levels in acute myocardial infarction using cardiac T1 mapping-manganese-enhanced MRI. In *Heart*. pp. A86

2019

Jasmin, N.H. et al., 2019. 4 Manganese-enhanced T1 mapping of calcium homeostasis in acute myocardial infarction. In *European Molecular Imaging Meeting (2019)*. pp. A3.

Jasmin, N.H. et al., 2019. 5 Manganese-enhanced MRI can quantify myocardial infarct size earlier than gadolinium-enhanced MRI. In *European Molecular Imaging Meeting (2019)*. pp. A4.

Jasmin, N.H. et al., 2019. MEMRI can quantify myocardial infarct size earlier than LGE-MRI. In *Journal of Cardiovascular Magnetic Resonance (2019)*. p. 824.

Awards

September 2019: **Mansfield Research Innovation Award, BCISMRM 25th Anniversary Meeting 2019**

(Manganese-enhanced MRI can quantify myocardial infarct size earlier than gadolinium-enhanced MRI).

May 2019: **Magna cum laude award, ISMRM annual meeting 2019**

(Manganese-enhanced MRI can quantify myocardial infarct size earlier than gadolinium-enhanced MRI).

March 2019: **Best Poster Award for Cardiovascular, European Molecular Imaging Meeting 2019**

(Manganese-enhanced MRI can quantify myocardial infarct size earlier than gadolinium-enhanced MRI).

May 2018: **2nd Best Oral Presentation, UCL Annual Cardiovascular Symposium 2018**

(In vivo investigation of intracellular calcium levels in acute myocardial infarction using cardiac T1 mapping-manganese-enhanced MRI)

March 2017: **3rd Best Poster Presentation, BCISMRM Postgraduate meeting 2017**

(Quantifying manganese-calcium interaction for optimal cardiac manganese-enhanced MRI)

Table of contents

List of figures

List of tables

Abbreviations

^{201}Tl	^{201}Thalium
AAR	Area at Risk
AMI	Acute myocardial infarction
ATP	Adenosine triphosphate
BP	Blood pressure
Ca	Calcium
Ca^{2+}	Calcium ion
CABI	Centre for advanced biomedical imaging
CHD	Coronary heart disease
CICR	Calcium-induced calcium release
CMR	Cardiac magnetic resonance imaging
CO	Cardiac output
CVD	Cardiovascular disease
ECG	Electrocardiogram
ECV	Extracellular volume
EDD	End diastolic diameter
EDV	End diastolic volume
EF	Ejection fraction
EM	Extracellular matrix
ESV	End systolic volume
ET	Echo time
eTR	Effective time to relax (TR)
FA	Flip angle
FDG	Fluorodeoxyglucose
FS	Fractional shortening
FSE	Fast spin echo
GBD	Global burden disease
Gd	Gadolinium
Gd-DTPA	Gadolinium diethylenetriaminepentaacetic acid (chelated Gd)
GE	Gradient echo
GEMS	Gradient echo multi-slice
HR	Heart rate
LAD	Left anterior descending coronary artery
LCA	Left main coronary artery

LGE	Late gadolinium enhancement
LGE-MRI	Late gadolinium-enhanced MRI
LL	Lock-Locker
LVDP	Left ventricular developed pressure
LVEF	Left ventricular ejection fraction
LVM	Left ventricular mass
MEMRI	Manganese-enhanced MRI
MI	Myocardial Infarction
Mn^{2+}	Manganese ion
$MnCl_2$	Manganese (II) chloride
MnDPDP	Mn-dipyridoxyl-diphosphate
MRI	Magnetic resonance imaging
NCX	$3Na^{+}$- Ca^{2+} exchanger
NSTEMI	Non-ST-elevation myocardial infarction
PCI	Percutaneous coronary intervention
PE	Phase encode gradient
PET	Positron emission tomography
PLAX	Parasternal long-axis view
PPCI	primary percutaneous coronary intervention
PSAX	Parasternal short-axis view
ROI	Region of Interest
ROS	Reactive oxygen species
RR	Radiofrequency readout
SA	Sinoatrial
SERCA	Sarco/endoplasmic reticulum Ca^{2+}-ATPase
SNR	Signal to noise ratio
SPECT	Single photon emission computed tomography
SR	Sarcoplasmic reticulum
STEMI	ST-elevation myocardial infarction
SV	Stroke volume
SVR	Systemic vascular resistance
TTC	Triphenyl tetrazolium chloride

Chapter 1 : Introduction

This chapter introduces the research aims and structure of the thesis. I then discuss cardiac physiology, cardiovascular diseases (CVDs) and the process and consequences of myocardial infarction. Imaging is playing an increasingly prevalent role in the diagnosis, management, treatment and understanding of CVDs and is the primary focus of this thesis. Therefore, I introduce the range of imaging techniques that can be used to evaluate cardiac function with a particular focus on the technique most extensively utilised within my work – magnetic resonance imaging (MRI). Finally, I present an overview and discuss the limitations of current cardiovascular imaging methods for acute myocardial infarction and speculate that manganese-enhanced MRI may be able to address some of these requirements and improve diagnostic and prognostic accuracy.

1.1 Introduction

1.1.1 Clinical need and research aims

Cardiovascular disease (CVD) remains the most common cause of death worldwide causing 17.3 million deaths globally according to the 2013 Global Burden Disease (GBD) study, and accounting for 31.5% of all global deaths [1]. Acute myocardial infarction is the most severe manifestation of coronary heart disease (CHD) and was the most common causes of CVD deaths accounting for 1.8 million deaths in Europe [1]. In patients with acute myocardial infarction, the extent and severity of ischemic injury are an important prognostic factor for mortality and morbidity. After myocardial infarction, there is an opportunity in which intervention can salvage cardiomyocytes with reversible damage, clinically referred to as viable myocardium. Non-invasive imaging has become a front-line method for assessment of salvageable myocardium. A major challenge for present cardiovascular imaging is to identify better ways to assess viable myocardium that is salvageable at an acute stage with the aim to stratify patients into optimal treatment pathways.

Manganese (Mn^{2+}) is an intracellular contrast agent that can enter myocytes through the L-type calcium channels, making it an interesting imaging probe for Ca^{2+} fluxes. Manganese-enhanced magnetic resonance imaging (MEMRI) could provide an assessment on cardiac structure and function as well as in vivo monitoring of intracellular calcium ion (Ca^{2+}) changes. As a central regulator of cardiac contractility, intracellular Ca^{2+} changes could be used to assess viable and salvageable myocardium after acute ischemic injury.

The primary aim of this project was to develop a cardiovascular imaging technique for the assessment of myocardial viability in a mouse model of acute myocardial infarction using manganese. This thesis consists of three main objectives:

- Objective 1: Optimise manganese dose to ensure safety and sufficient myocardial enhancement.
    - Q1: How do different Mn^{2+} dosages and formulations affect cardiac contractility?
    - Q2: How do different Mn^{2+} dosages and formulations affect image enhancement in MRI?
    - Q3: How much Mn^{2+} accumulates in organs after administration.
- Objective 2: Investigating manganese as an early imaging contrast agent for cell viability using T1 mapping.
    - Q1: How long is manganese retained in the myocardium?
    - Q2: Can T1 mapping identify subtle changes of Mn^{2+} reflecting changes in Ca^{2+} during the first hours after an acute ischemic injury?
- Objective 3: Functional assessment of the myocardium for early infarct size quantification in acute myocardial infarction: MEMRI versus late-gadolinium enhancement (LGE-MRI)
    - Q1: What is the washout rate of the dosage used for MEMRI and LGE-MRI?
    - Q2: Can MEMRI quantify infarct earlier than LGE-MRI?

Completion of these objectives ultimately leads towards the development of a cardiac imaging method for assessment of myocardial viability after acute myocardial infarction, which could be used to test the efficacy of new drugs therapy that targets acute MI.and regenerative therapy.

1.1.2 Structure of the thesis

This thesis is structured into five chapters. Each chapter has a specific role within the body of work and fits into the common theme of developing MEMRI for evaluation of cardiac viability. Figure 1.1 summarises the thesis framework.

Chapter 1 consists of three parts. The first part introduces research aims and structure of the thesis. The second part provides broad background information on acute myocardial infarction, including the physiological context underpinning the work presented in this thesis. The third part describes the theory behind the imaging techniques used for cardiac imaging in general practice and those that are specific to this work. Magnetic resonance imaging (MRI) and manganese-enhanced MRI (MEMRI) are discussed in detail, as this forms a significant part of this thesis.

Chapter 2 describes the characterisation of manganese and quantifying the effects of manganese on cardiac function for optimal manganese-enhanced MRI. Although manganese was the first contrast agent used for MRI, Manganese has not been widely used in clinical cardiac imaging due to its cardiac toxicity. In this section, I directly investigated the effects of manganese on cardiac toxicity using real-time ultrasound imaging and correlate it with image enhancement using MRI to develop optimal Manganese-enhanced MRI techniques.

Chapter 3 shows the assessment of manganese as an imaging agent for calcium changes relating to acute myocardial infarction. This work focuses on the development of imaging techniques for the assessment of acute myocardial infarction using manganese. Manganese could provide essential information on calcium homeostasis and further assist our understanding of the pathophysiology of MI in an acute setting. This technique is presented in the context of acute myocardial infarction, but the technique developed applies to the wider field or cardiac disease.

In Chapter 4 manganese is validated against the current gold standard late gadolinium enhancement (LGE). As a functional contrast agent, manganese could detect cell death early compared to LGE. The methodologies applied here give a direct insight into myocardial viability which is useful for cardiac regeneration therapy and drug studies that target acute MI.

Finally, Chapter 5 provides a summary of the work presented as well as the findings of this thesis, offering a discussion of future developments that would be beneficial to the work. This is followed by a discussion of the future directions of the projects for myocardial regeneration therapy and the role imaging has within its translation to clinical practice.

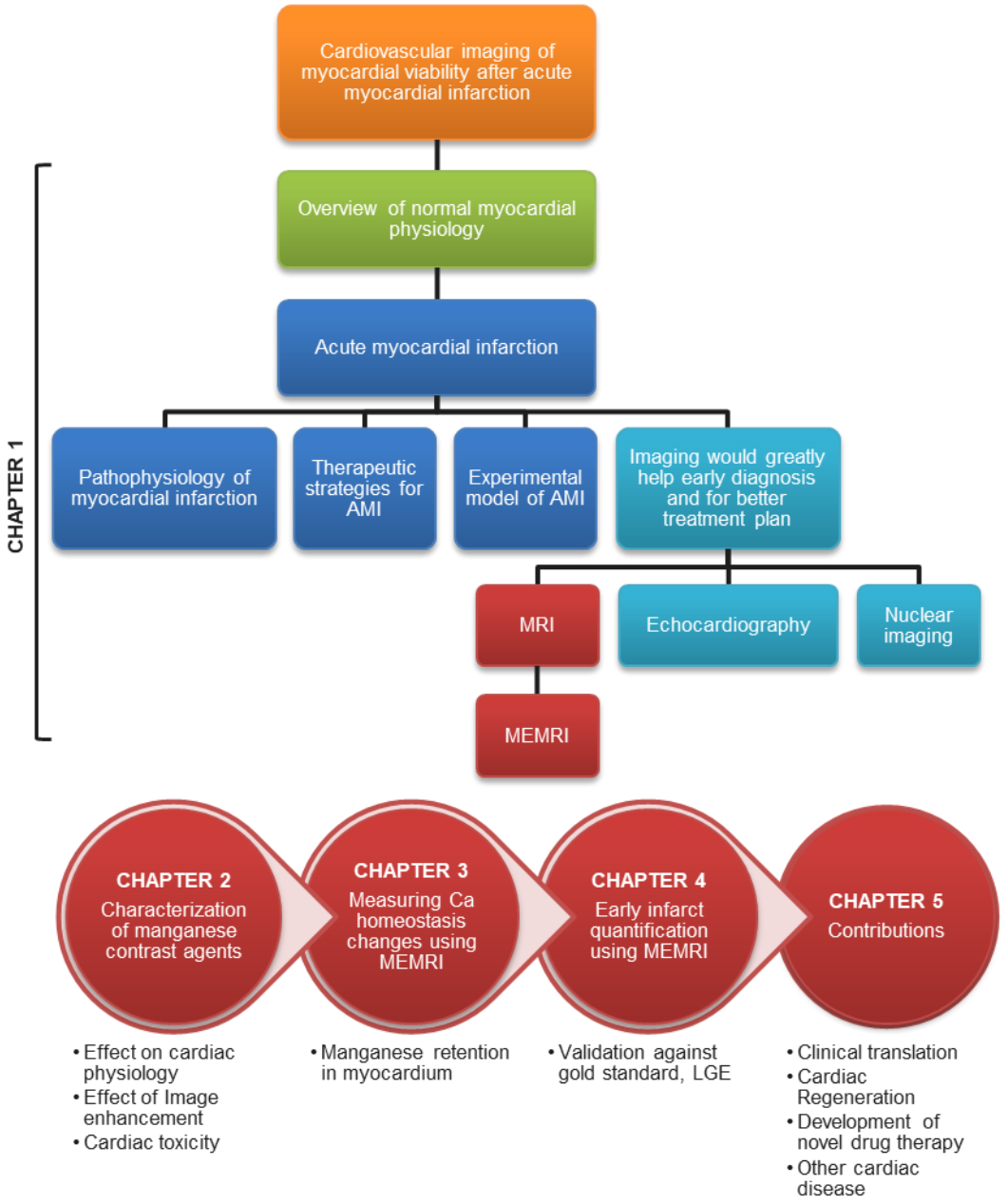

Figure 1.1: Thesis framework

Chapter 1 provides an overview of normal myocardial physiology and acute myocardial infarction (pathophysiology, treatment and imaging for AMI). The current challenges in the field are also discussed. Three projects were discussed in Chapter 2, 3, and 4 that ultimately leading to the development of a new method for cardiovascular imaging of myocardial viability after AMI. AMI = Acute myocardial infarction; MEMRI = Manganese-enhanced MRI; LGE = Late gadolinium enhancement.

1.2 Introduction to acute myocardial infarction

1.2.1 Overview of normal myocardial physiology

In order to understand the pathophysiology of acute myocardial infarction, it is necessary to appreciate the normal physiology of cardiomyocytes and their cumulative roles in normal cardiac function.

1.2.1.1 Anatomy and physiology of the heart

The heart is separated by the septum into the left and right part that creates the division of the circulatory system into two separate systems. Each left and right part of the heart is further divided into upper and lower parts - the atrium and the ventricle. The contractile units of the myocardium are the cardiomyocytes. Cardiomyocytes constitute 75% of the heart mass and are designed to perform two fundamental functions: initiation and conduction of electrical impulses and contraction. Most myocardial cells can perform these functions, with the vast majority being predominantly contractile cells (myocytes) and a small number being designed specifically as electrical cells (sinoatrial node, atrioventricular node, atreioventricular bundle), collectively known as the conducting system of the heart (Figure 1.2). Sinoatrial (SA) node can generate electrical impulses automatically by spontaneous depolarisation and initiates action potential, which is then conducted to the myocytes, leading to contraction of the heart in a rhythmic and coordinated fashion.

The main function of the heart is to supply the body with oxygen and nutrients by pumping blood through the blood vessels. Deoxygenated blood from the body returns to the right atrium via inferior and anterior vena cava during diastole. Blood is then transported to the right ventricle during arterial contraction initiated by the P wave. During the arterial contraction in the left atrium, blood is pumped into the left ventricle and then ejected via the aorta into the systemic circulation during ventricular contraction in the left ventricle. During ventricular contraction (QRS and T wave), the ventricle pumps blood to the lungs where blood is oxygenated in pulmonary capillaries. Simultaneously, the oxygenated blood from the lungs is collected by the four pulmonary veins and flows into the left atrium. In short, during the alternating cycles of systole and diastole, blood is continuously pumped from the pulmonary circulation through the right heart, the lungs, the left heart, and finally into the systemic circulation.

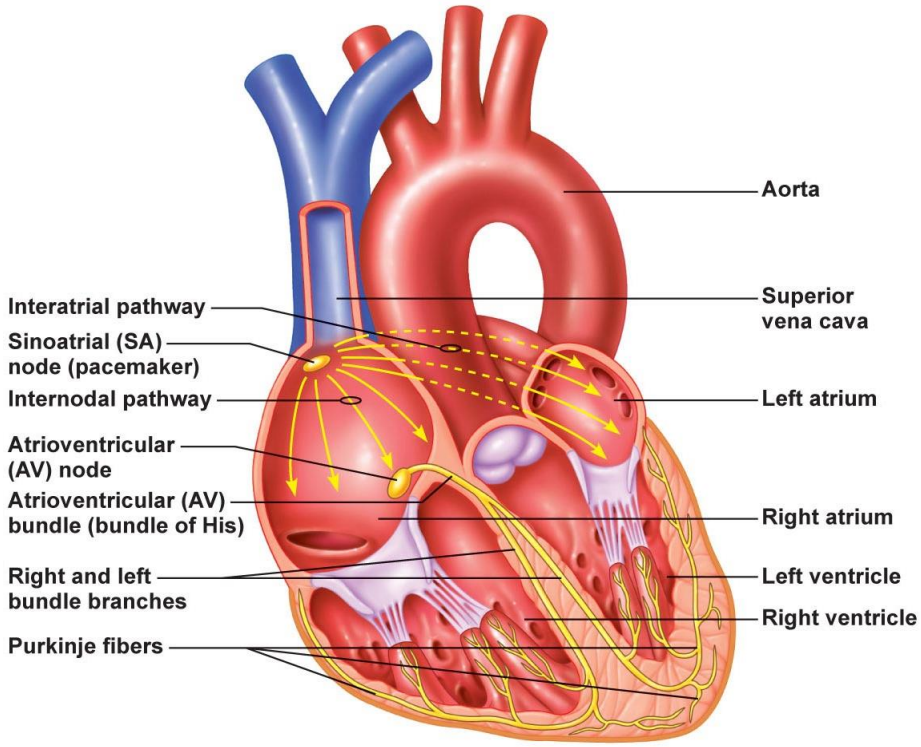

Figure 1.2: The anatomical structure and the conduction system of the heart.

Sinoartrial (SA) node or also known as pacemaker generates electrical impulses leading to the contraction of the heart in a rhythmic and coordinated fashion. From there, the signal travels to the AV node, through the bundle of His, down the bundle branches, and through the Purkinje fibers, causing the ventricles to contract. Deoxygenated blood from the body returns to the heart via inferior and anterior vena cava during diastole. Oxygenated blood from the lungs is collected by the pulmonary veins and pumped out to the whole body via the aorta during systole. Adapted from Pearson Education (2011).

1.2.1.2 Excitation-contraction coupling in cardiac muscle

The strength of contraction of the cardiac muscle is regulated by varying the intracellular calcium concentration during activation of the cells. The initial influx of Ca^{2+} into myocytes through L-type Ca^{2+} channels during the ventricular action potential (Figure 1.3) is insufficient to trigger the contraction of myofibrils. This signal is amplified by the calcium-induced calcium release (CICR) mechanism (Figure 1.4), which triggers a much greater release of Ca^{2+} from the sarcoplasmic reticulum (SR). The cell membrane of cardiomyocytes, called sarcolemma, contains invaginations (T-tubules) that bring L-type Ca^{2+} channels into close contact with ryanodine receptors, specialised Ca^{2+} release receptors in the SR. When Ca^{2+} enters the cells through L-type channels, ryanodine receptors change conformation and induce a larger release of Ca^{2+} from abundant SR stores. Large levels of intracellular Ca^{2+} act on tropomyosin complexes to induce myocyte contraction.

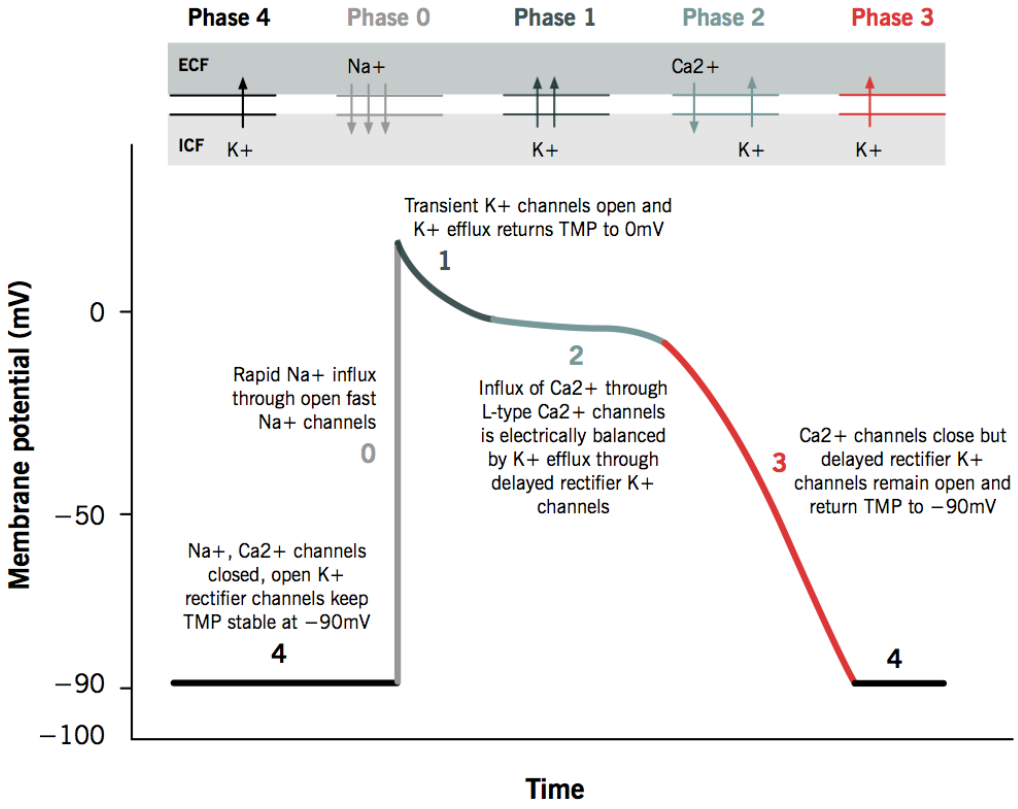

Figure 1.3: Action potential of ventricular cardiac muscle.

The cardiac ventricular action potential in typical cardiomyocytes is composed of 5 phases (0-Resting, 1-Depolarisation, 2-Early repolarization, 3-Plateau, 4-Repolarization), beginning and ending with phase 4. Adapted from Ikonnikov et al. (2018).

When the intracellular calcium ion concentration rises, calcium ions binds to troponin C, leading to a conformational change in tropomyosin that exposes the active site between actin and myosin. Myosin heads interact with active sites on actin filaments and “flex,” like oars on a boat, to “row” myosin along actin induces cross-bridge formation between myosin head and active site on actin. Interaction between myosin head and actin trigger “firing” of myosin head, causing it to pull itself along the actin filament producing a small contraction. The cycle can then repeat itself, allowing myosin to travel further along the actin molecules and progressively shorten the muscle fibres. The force of cardiac contraction is proportional to the number of cross-bridges formed, a parameter which in turns depends on the Ca^{2+} inside myocytes. Each cycle of cross-bridge formation involves the hydrolysis of an adenosine triphosphate (ATP) molecule. Cardiac muscle cells are continually contracting and require a substantial amount of energy from oxidative phosphorylation and the myocytes thus contain large numbers of mitochondria.

During relaxation, some Ca^{2+} is transported back out of the cell and some replaced into the SR. Ca^{2+} is predominantly expelled from the myocytes via a $3Na^{+}$-Ca^{2+} exchanger which uses the inward 'down-hill' movement of the $3Na^{+}$ to move Ca^{2+} out of the cell (Figure 1.4). A portion of the Ca^{2+} is actively expelled from the cell across the plasma membrane by Ca ATPases. ATP is also used to pump Ca^{2+} back into the SR stores. Ca^{2+} homeostasis plays a critical role in regulating cardiac contractility. Physiological stimulation, via sympathetic nervous system activation which increased intracellular $Ca^{2+,}$ can generate a more forceful cardiac muscle contraction compared with that which occurs at resting levels. Disordered Ca^{2+} homeostasis will also be observed during ischemia and in other diseases.

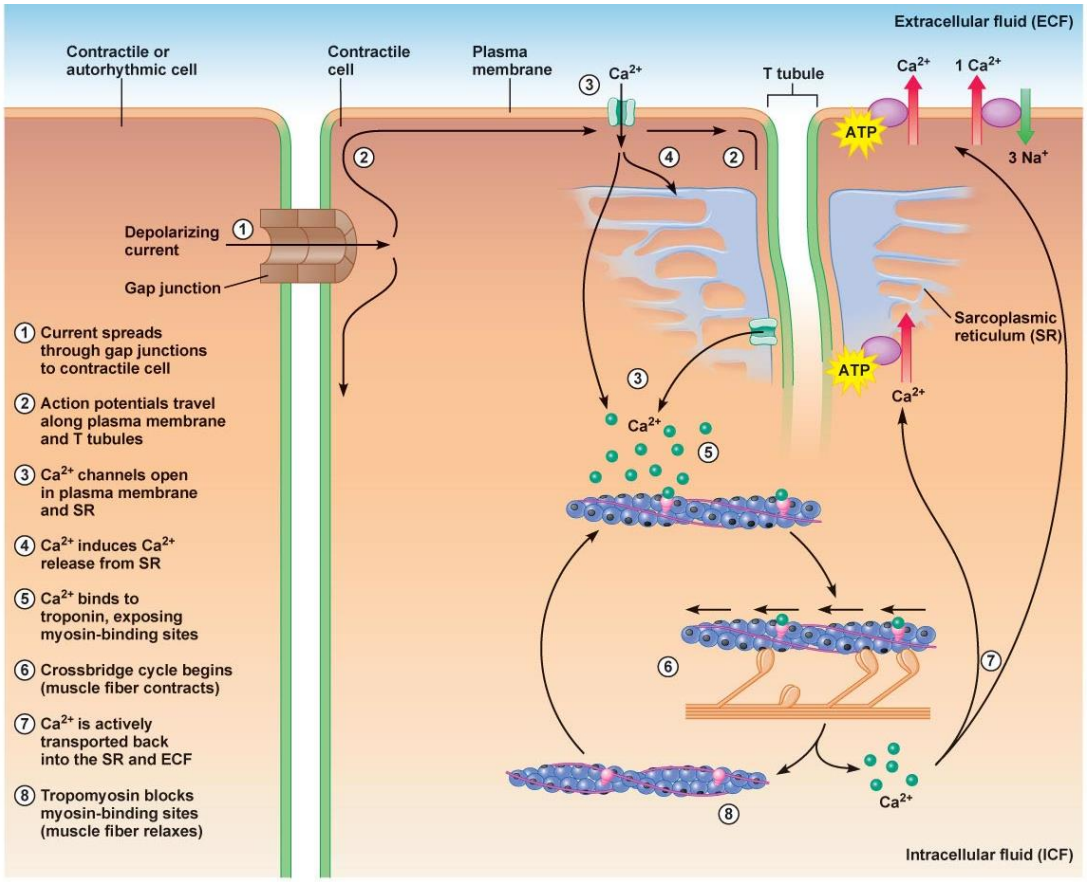

Figure 1.4: Schematic diagram of CICR mechanism.

The influx of Ca^{2+} via L-type calcium channels triggers the release of Ca^{2+} from the SR, a mechanism known as calcium-induced calcium release (CICR). Ca^{2+} then binds to troponin and induces myocyte contraction. $Ca^{2+}$is transported out of cell and back into the SR during relaxation. ATP = adenosine triphosphate; SR = sarcoplasmic reticulum; ECF = extracellular fluid. Adopted from Pearson Education (2011).

1.2.2 Pathophysiology of acute myocardial infarction

Myocardial infarction (MI) is a life-threatening disease defined as sudden and prolonged ischemic death of myocardial tissue. It is frequently caused by atherosclerosis, a pathological process characterised by the formation of fatty, atherosclerotic plaques (or thrombi) that restrict and potentially block the flow of blood in the coronary arteries [3]. Disruptions in the cellular and molecular process are observed within a few minutes of the onset of ischemia [4]. In this section, I focus on the key myocardial cellular and molecular changes and response following ischemic injury that is important from an imaging point of view (Figure 1.5). Acute myocardial infarction can be diagnosed by clinical features, including electrographic findings, elevated values of biochemical markers (such as cardiac troponin [5], brain natriuretic peptide [6] and creatine kinase MB isoform [7]) and by imaging methods which can identify evidence of regional and new loss of viable myocardium [8].

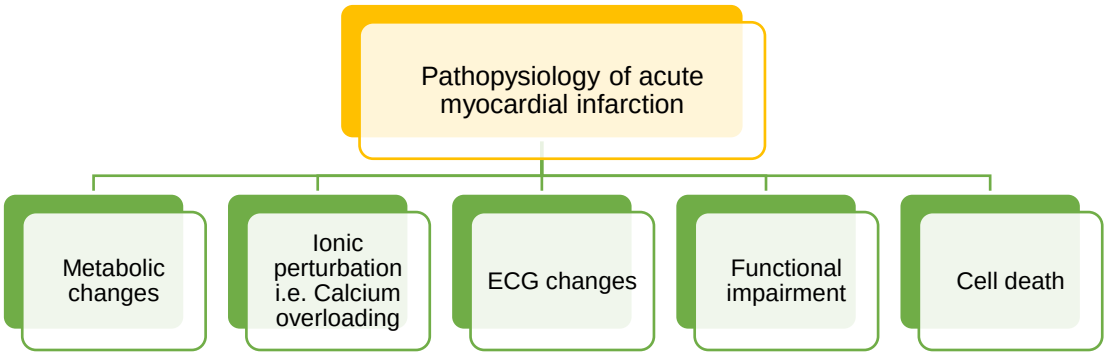

Figure 1.5: The pathophysiology of acute myocardial infarction.
The myocardial ischemic injury involves changes in the metabolic process, calcium overloading and other cellular and molecular changes. Myocardial response after ischemic injury includes ECG changes, functional impairment and followed by cell death.

1.2.2.1 Metabolic Changes

Ischemia causes a sudden cessation of oxidative phosphorylation resulting in a shift to an alternative pathway for the generation of ATP in ischemic cardiomyocytes, anaerobic glycolysis. This occurs as soon as 30 seconds of the onset of coronary artery occlusion [9]. The ATP now is mainly generated from the anaerobic glycolysis and results in rapid accumulation of lactate in the ischemic myocardium [10]. The absence of perfusion means glucose cannot be supplied to the cardiomyocytes. Thus, the main substrate for glycolysis is from the limited intracellular glycogen stores. As a result, anaerobic glycogen cannot meet the high demand for

ATP, and the rate of anaerobic glycolysis is further deprived as intracellular acidosis occurs due to the accumulation of lactate which inhibits many enzymes necessary for the glycolytic pathway. ATP is consumed at a much faster rate than it is produced. Insufficient ATP production causes disruption in normal cellular homeostasis and cardiac function and in turns causes a series of cytosolic changes including rise in concentration of ADP and Pi [11]. Failure to maintain cellular homeostasis is associated with the development of irreversible cardiomyocytes death.

1.2.2.2 Ionic Perturbation - Calcium Overloading

It is postulated that the altered metabolic system can also induce alteration in the cell membrane function leading to an altered electrolyte homeostasis, including increased in free cytosolic calcium. Calcium accumulation in the cytoplasm is a well-established feature in the pathogenesis of myocardial ischemic injury [12]. The potential mechanism for an early increase in cytosolic Ca^{2+} includes changes in transport systems in the sarcolemma, sarcoplasmic reticulum and mitochondria which attempt to maintain ionic homeostasis. Intracellular calcium overloading accelerates interactions between contractile proteins which increases energy utilisation thus exacerbates energy depletion of the ischaemic cardiomyocytes [11]. Prolonged calcium overloading leads to progressive membrane and electrolyte alterations. Perturbation of ionic balance have profound effects on cardiac electrophysiology and will be discussed in the next section. The potential recovery from calcium overloading is influenced by the mechanism of calcium overloading and the magnitude and duration of calcium overloading [12].

1.2.2.3 Electrocardiogram changes

The electrocardiogram (ECG) represents the sum of total electrical activity of the heart, where each segment of the integrated ECG trace is mostly influenced by action potentials occurring in a specific region of the heart. Myocardial ischemia resulting from acute coronary occlusion causes marked changes in the ventricular potential in the perfusion defect, which can be visualised in the integrated ECG trace. Acute myocardial infarction commonly occurs in the left ventricle, which specifically affects the ST-segment [13]. The changes seen in the ST-segment in the ECG trace is a result of differences in resting potential between perfused and ischemic cardiomyocytes which disturb the tight coupling of myocardial activity [11]. Changes in the plateau phase of ventricular action potential and ST-segment is associated with slow electrical conduction and calcium overloading in the ischemic cardiomyocytes [13], [14].

1.2.2.4 Functional impairment

Cardiac contractile function is rapidly reduced upon myocardial ischaemia, as evidenced by relative akinesis of the left ventricular free wall following left anterior descending (LAD) artery occlusion. In experimental models, the onset of systolic dysfunction is much more rapid, as a consequence of ceased contractility approximately after 60 seconds of ischemia [15]. The immediate functional impairment is associated with two main mechanisms. First, the generation of inorganic phosphate that inhibits the function of contractile proteins [16]. Secondly, intracellular acidosis that, in turn, decreases calcium binding to contractile proteins inhibiting contractility [17]. Rapid cessation of function may prolong survival of ischemic cardiomyocytes, as the limited stores of high energy phosphates are used slowly and allow cardiomyocytes to survive longer despite the absence of perfusion.

1.2.2.5 Cell death

Early loss of function in myocytes in the ischemic heart is fully reversible upon restoration of blood flow within 5 minutes of occlusion, whereas prolonged ischemia associated with prolonged myocyte dysfunction (myocardial stunning) (Figure 1.6). If left unresolved, myocardial ischemia will eventually result in irreversible myocardial injury (necrosis). Experimentally, necrosis progresses from the subendocardium to the subepicardium over several hours. The evolution of cell death after myocardial ischemia is discussed in detail in Section 4.1.1. The time course of cell death is dependent on the duration of ischemia, the presence of collaterals vessels, time to reperfusion and other related factors [18]. The most effective strategy for reducing cardiomyocytes death and thus infarct size is rapid and effective restoration of coronary blood flow.

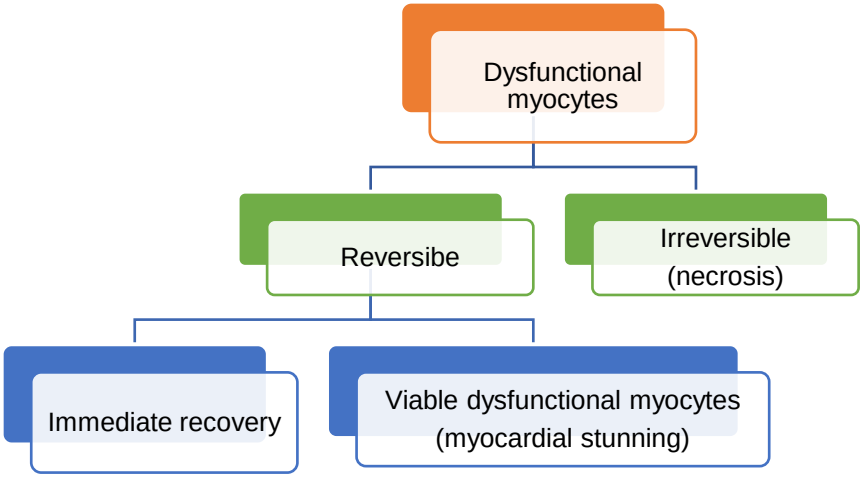

Figure 1.6: Schematic of cardiomyocytes death post-ischemia.

1.2.3 Therapeutic strategies in acute myocardial infarction

The term “acute myocardial infarction” should be used when there is evidence of myocardial injury with necrosis and consistent with symptoms of myocardial ischemia. Myocardial infarction (MI) can be classified into several categories with the most common classification being the ST-elevation myocardial infarction (STEMI) and non-STEMI (NSTEMI). The usual practice for making initial diagnosis of STEMI is when there is evidence of persistence chest discomfort or presentation of symptoms suggestive of ischemia and ST-elevation in at least 2 leads in the ECG. STEMI typically results from the partial blockage of a coronary vessel; hence rapid pre-hospital ECGs can reduce the time to diagnosis and improve treatment by facilitating the triage of STEMI patients to hospitals with percutaneous coronary intervention (PCI) capabilities. The absence of persistence ST-elevation accompanied by an elevation in cardiac biomarkers (i.e. cardiac troponin) is suggestive of NSTEMI. ST depression, transient ST-elevation and/or prominent T-wave elevation may also be present. NSTEMI typically have full blockage of a coronary vessel and may have more severe dysfunction and thrombolysis therapy is reserved only when medical therapy is not effective [19], [20]. In addition to these classic categories, MI is also classified based on pathological, clinical, and prognostic differences [8], where different categories of AMI may have different treatment strategies [21]. Here I attempted to highlight the general and most common therapeutic strategies in STEMI. The therapeutic strategy for NSTEMI is referred to the 2014 American Heart Association (AHA) and American College of Cardiology (ACC) Guideline [19].

The next step and what would be the most challenging step is the determination of the state of the myocardial injury to help risk stratification, whether the patient will benefit from reperfusion therapy (restoration of blood flow to area-at-risk (AAR-MI)). Coronary angiography will be performed to determine the severity and location of occlusion and finding the best approach to re-open the occluded coronary artery. To date, reperfusion therapy accompanied by medical therapy remains the most effective intervention for STEMI patients to limit myocardial infarction and improve ventricular function if implemented early [22]. In patients with a clinical suspicion of myocardial ischaemia and ST-segment elevation, reperfusion therapy needs to be initiated as soon as possible. Reperfusion therapy can be done through two methods: primary percutaneous coronary intervention (PPCI) or fibrinolysis. Figure 1.7 shows an example of therapeutic strategies in STEMI patients.

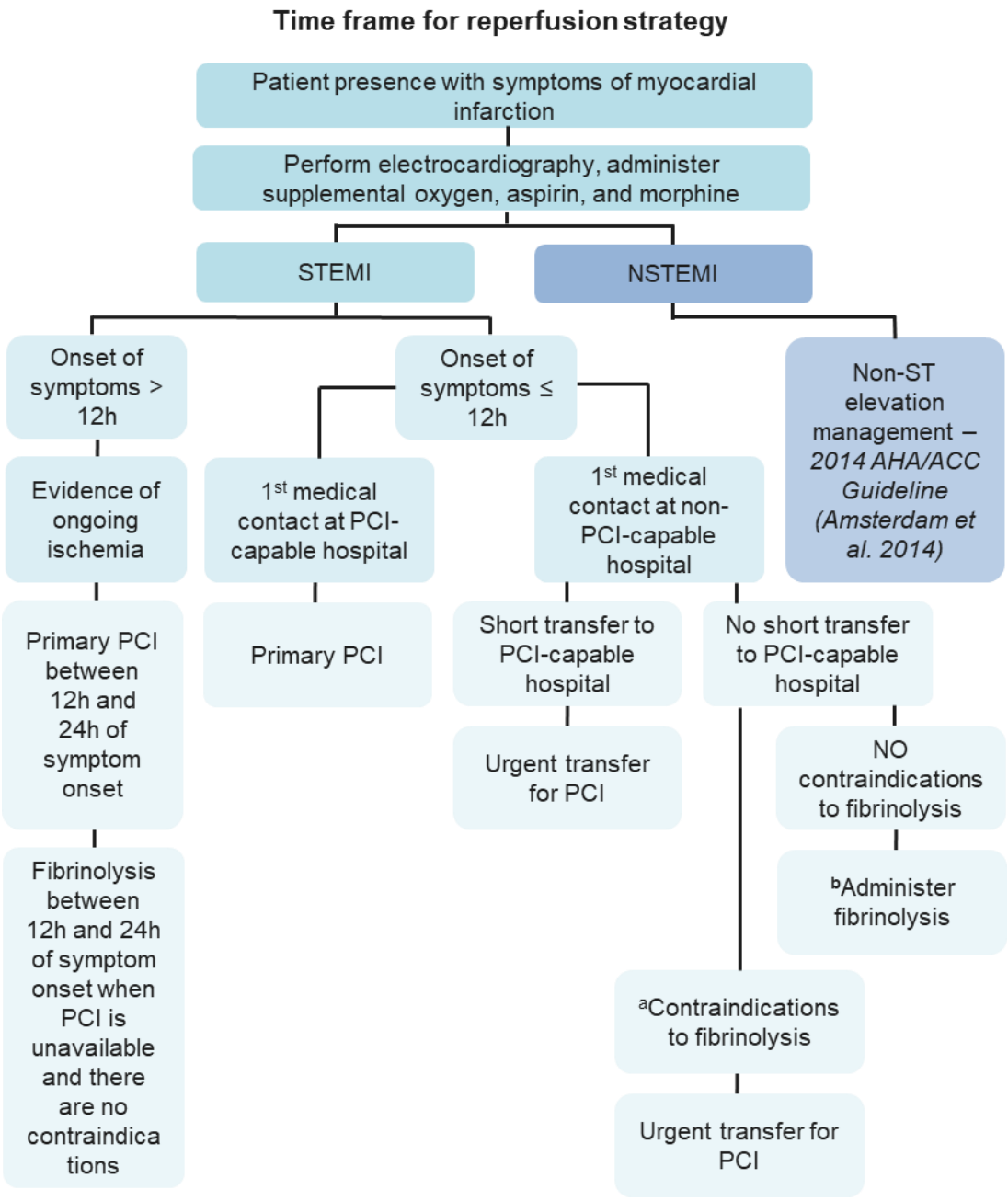

Figure 1.7: Time frame for reperfusion strategy.

STEMI diagnosis is the time 0 for the strategy clock. Target times from STEMI diagnosis represent the maximum time to do specific interventions. [a]If fibrinolysis is contraindicated, direct for primary PCI strategy regardless of time to PCI. [b]10 min is the maximum target delay time from STEMI diagnosis to fibrinolytic bolus administration, however, it should be given as soon as possible after STEMI diagnosis (after ruling out contra-indications). ECG= electro-cardiogram; PCI = Percutaneous Coronary Intervention; STEMI = ST-segment elevation myocardial infarction. Adopted from [19], [20].

PPCI is the preferred strategy in patients with STEMI within 2 hours of symptoms onset. However, the process of restoring coronary flow to the ischemic tissue can, itself, induce myocardial injury and cardiomyocyte death, a phenomenon known as 'myocardial-reperfusion injury' [23]. Cardioprotection studies to target myocardial reperfusion injury in reperfused STEMI patients have been investigated over the last few years. This includes (1) ischemic conditioning, (2) pharmacological activation [24] and (3) regenerative therapy [25]. Figure 1.8 shows various time-windows for applying therapeutic studies for reducing myocardial infarct size in STEMI patients undergoing PPCI.

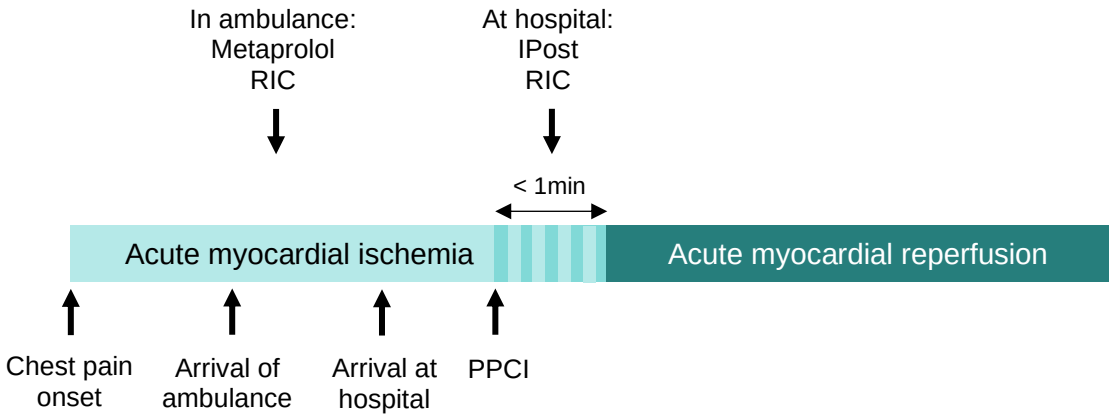

Figure 1.8: Therapeutic strategies in STEMI patients.

Various time-windows for applying therapeutic strategies for reducing myocardial infarct size in STEMI patients undergoing PPCI. RIC: Remote ischemic conditioning, IPost: Ischemic post-conditioning. Adapted from D. J. Hausenloy et al. (2017).

The difficulty in preventing myocardial reperfusion injury in patients with ST-segment elevation myocardial infarction is mainly due to an incomplete understanding of mechanisms underlying myocardial reperfusion injury, including variable reperfusion times, and multiple pathophysiology factors; calcium overload, and inflammatory reactions, and mitochondrial dysfunction making it complex to target effectively [24]. Non-invasive imaging could dramatically enhance our ability to assess pathological changes after ischemic and reperfusion injury. The current cardiovascular imaging after acute myocardial infarction will be explained further in the next section (Section 1.3.1).

The development of new strategies directly targeting myocardial injury, repair and remodelling in the infarcted heart has been less impressive. Thus, the current practice is still using the traditional drug therapy approaches which include beta blocker, ACE inhibitors, and statins have remained the most effective and most used drugs therapy for patients with myocardial infarction [4]. Early administration of beta-blockers in patients with myocardial infarction reduces myocardial oxygen consumption by decreasing heart rate and blood pressure and by exerting negative inotropic effects. Both clinical and pre-clinical evidence suggests that beta-blockers help reduces adverse postinfarction remodelling. ACE inhibitors, on the other hand, shown to decrease the mortality rate and prevent the development of heart failure. This is also the similar effects of statins in patients with acute coronary syndromes [26]. Therapeutic drugs aimed at reducing infarct size after acute myocardial infarction and regenerative therapies using stem cells and tissue engineering are also under intensive investigation and have shown promise in pre-clinical and clinical models [24], [27], [28].

1.2.4 Experimental models of myocardial infarction

The use of an animal model of myocardial infarction plays a significant role in the understanding of mechanisms and any kind of therapeutic approach. Animal models are the preliminary tools in drug development, which also provide an in-depth understanding of disease pathophysiology [29]. In order to better understand the pathophysiology and evolution of ischemia into myocardial infarction, animal models of myocardial infarction have gained much interest and provide insights that cannot be gained through clinical studies. Pre-clinical myocardial infarction studies help in hypothesising new strategies in the diagnosis, prevention and treatment, and translation into clinical settings. Small animals such as mice, rats, and rabbits are frequently used in experimental cardiovascular research due to their small size, ease of handling and maintenance, and relatively low cost. However, due to the small heart size in small animal models, proper training and extensive practice are required to produce a reproducible model and high survival rates. Large animals, including pig, dog, and sheep more closely resemble humans, but are relatively expensive and require more significant maintenance.

Experimental coronary occlusion was attempted even before cardiac infarcts had been recognised at autopsy. The first attempts were made in the 1690s, Chirac [30], [31] found that the heart stopped beating almost immediately after the coronary artery of a dog was ligated. Similar studies were carried out in the early 1800s by Erichsen [32]. However, in this experiment, the animal survived only for a few minutes. They noted the heart muscle that first becomes pale associated with the area supplied by the occluded blood vessels. In the late 1800s, Kolster [33] conducted a study in 12 dogs where he tied only a small branch of the coronary artery and successfully kept some of the animals alive. The survival periods range from a few days to a year following the surgery. The infarcts that he produced were however not a complete infarct, probably because only a small-sized vessel was occluded. Then in 1899, Baumgarten [34] published an excellent experimental coronary occlusion study where he ligated various branches of the right and left coronary arteries in dogs and cats. From the study, he discovered and established the distribution of the coronary arteries by the infarction method. He was able to map out which areas of the myocardium received blood from each branch of the coronary artery.

In 1954, Johns and Olson et al. [35] were the first to performed experimental coronary occlusion in small animals such as mice and rats. They ligated different regions of the coronary artery. In comparison to the dogs, these species showed increased in survival rate and consistency of infarct size. Since that, the technique has been widely used with left main coronary artery (LCA) ligation as the most preferred site for ligation [36]–[39]. To produce an acute myocardial infarction model, with further modification of the conventional techniques, ligation was performed in the left anterior descending artery (LAD) which has shown to have a higher long-term survival rate and a better control of the size and site of infarction in both rats [40], [41] and mice [42]–[44]. This is desirable, especially in understanding the evolution of infarction as well as investigating prognosis and novel therapies of acute myocardial infarction. In order to get better achievement, an accurate method for assessing the heart function and outcomes of new treatments is needed. Non-invasive imaging could be used for evaluating heart function and further aid the understanding of the disease process and development of treatment which is discussed in the next section.

1.3 Imaging acute myocardial infarction

1.3.1 Current clinical cardiovascular imaging in acute myocardial infarction

Cardiovascular imaging plays many roles in patients with known or suspected MI. However, this section concerns only its role in the diagnosis and characterisation of the disease progression of disease in the setting of acute myocardial infarction (AMI). Regional myocardial hypoperfusion and ischemia lead to a cascade of events including myocardial dysfunction, cell death, and healing by fibrosis. Non-invasive imaging can be used to assess these pathological characteristics and is useful in making diagnosis and characterisation of myocardial injury and necrosis in acute myocardial infarction. Important imaging parameters include myocardial perfusion, myocyte viability, myocardial thickness, thickening and motion, and the change in the kinetics of contrast agents which reflects fibrosis or scar following myocyte loss. Currently used imaging techniques in acute myocardial imaging and prior to MI are echocardiography, radionuclide imaging using positron emission tomography (PET) or single-photon emission computed tomography (SPECT), and cardiac magnetic resonance imaging (CMR). There is some overlap in their capacities, and each of the techniques can access myocardial viability, perfusion, and function to a certain extent. To date, only the radionuclide techniques provide a direct assessment of myocyte viability because of the inherent properties of the tracers used. Other techniques are based on indirect assessments of myocardial viability, such as contractile response in echocardiography during a stress test, or increased extracellular space following myocyte loss in CMR. Here, the roles of each of the techniques will be highlighted.

Echocardiography provides an assessment of both cardiac structure and function in real-time; myocardial thickness; thickening/thinning; and motion. Echocardiography has been shown to be able to detect abnormal regional wall motion induced by ischemia almost immediately after the onset or when more than 20% transmural myocardial thickness is affected [45], [46]. These abnormalities are also useful in case of new or unknown aetiology to support the diagnosis of MI when cardiac biomarkers, i.e. cardiac troponin level, are abnormal. Recent advancement in echocardiography such as the use of intravenous contrast agents can enhance visualisation of the endocardial border. It can be used for the assessment of myocardial perfusion and microvascular obstruction. Besides, targeted echocardiographic contrast agents that target specific molecular processes have been developed but have not been used in the clinical setting of MI [47]. Apart from

that, tissue doppler and strain imaging now permit quantitative global and regional function [48], [49].

In nuclear imaging, several radionuclide tracers can be used to image viable myocytes. The most commonly used PET tracers includes ^{18}F-FDG for metabolic study and Rubidium-82 (^{82}Rb) for perfusion study. ^{18}F-FDG is based on the assessment of myocardial metabolism by measuring the accumulation of the radioactive glucose analogue 18F fluorodeoxyglucose (FDG) within metabolically active cells. ^{18}F-FDG-PET has been considered the reference standard for viability imaging given the extensive clinical experience, and it is relatively high accuracy for predicting functional recovery following reperfusion therapy [50]. Myocardial PET imaging provides a direct evaluation of viability and is capable of assessing different stages of myocardial injury; (1) Stunned myocardium defined as abnormal contractile function despite relatively normal perfusion, caused by a recent ischemic event [51], [52] (2) Hibernating myocardium defined as alive, viable myocardium that is chronically hypo-perfused at both rest and stress and has diminished contractile function and (3) Myocardial infarction defined as necrotic, scarred (dead) myocardial tissue. For the assessment of myocardial viability, ^{18}F-FDG tracers are performed following perfusion imaging with ^{82}Rb. Stunned myocardium has positive uptake during perfusion but reduced FDG uptake (mismatch pattern). A negative uptake in rest perfusion and reduced perfusion in ^{82}Rb stress perfusion study but preserved FDG uptake (mismatch pattern) indicates hibernating myocardium. Whereas a negative uptake on both rest and stress perfusion ^{82}Rb and FDG uptake (match pattern) reflecting areas of the infarct.

SPECT can also be acquired in acute MI to identify viable myocardium. The uptake of the radionuclide perfusion tracer is dependent on the myocardial perfusion and the integrity of the cell membrane. Myocardial segments with preserved rest radiotracer uptake are viable. Regions with reduced radiotracer uptake may or may not be viable, which can be resolved by imaging myocardial substrate metabolism or contractile reserve. One of the earliest SPECT tracers used for this purpose is ^{201}Thalium (^{201}TI). ^{201}TI is a potassium analogue that is actively taken up by myocytes and is able to redistribute over time into cells that are viable within perfusion defects. Another tracer that commonly used is ^{99m}Tc Sestamibi, an alternative to ^{201}TI. However, there are concerns that ^{99m}Tc Sestamibi undergoes less redistribution and may underestimate viability compared to ^{201}TI.

Nuclear imaging has high sensitivity, but it involves ionising radiation and low resolution and is logistically challenging. It requires cyclotrons and an additional method for generating tracers.

Cardiac magnetic resonance imaging (CMR) has emerged as the most robust imaging modality for the assessment of acute myocardial infarction due to its high tissue contrast and resolution. In the setting of acute MI, CMR can be used to assess the presence and extent of myocardial oedema, myocardial viability, microvascular obstruction, intramyocardial haemorrhage [53], and infarct size. These are all markers of myocardial injury that have prognostic value [54]. The most commonly routine imaging is late gadolinium enhancement (LGE-MRI); which can be used for assessment of myocardial viability through quantification of an increase in the extracellular space that is associated with infarction. Locca et al. 2010 [55] show that LGE-MRI can detect even small areas of infarct as little as 1g. CMR also can assess the extent of myocardial oedema/inflammation, allowing the distinction between acute and chronic myocardial injury [8]. Another potential new CMR method is manganese-enhanced MRI (MEMRI) that shown promise as a direct imaging marker of viable myocardium but has not been used in routine clinical practice.

Applying imaging in acute myocardial infarction is particularly crucial for diagnosis and better treatment management. Although few imaging methods as discussed above have been developed over the years and decades, a significant challenge for present cardiovascular imaging remains; that is to identify a better direct marker of myocardial viability with the aim to stratify patients into optimal treatment pathways. Myocardial ischaemia progresses with the duration of coronary occlusion and the delay in time to reperfusion determines the extent of irreversible necrosis. After myocardial infarction, there is a golden time in which intervention can salvage the affected, but reversible damage before it progresses to irreversible necrosis. Thus, the ultimate aim of this thesis is to develop new cardiovascular imaging for myocardial viability after acute myocardial infarction using cardiac magnetic resonance imaging.

1.3.2 Cardiac magnetic resonance imaging

Cardiac magnetic resonance imaging in acute myocardial infarction is the main focus of the work presented in this thesis; therefore, an understanding of the physical principles underlying cardiac magnetic resonance imaging is required and is discussed in this section. The physics of cardiac magnetic resonance imaging is highly complex [56] and will not be discussed in great detail as the main focus of this work is the application of CMR. Hence, the present chapter will only give a brief overview of the fundamental MRI Physics with a specific focus on cardiovascular MR sequences used in this thesis. This chapter will start by describing the fundamental MRI Physics from nuclear spin until the generation image in MRI. Next local MRI hardware used in CABI will be covered followed by cardiac imaging planes. Finally, imaging sequences used in Cardiac MR; 1) Cine MRI, 2) Cardiac T1 Mapping, and 3) Inversion recovery method for contrast-enhanced MRI will be described.

1.3.2.1 Basic MRI physics

Nuclear magnetic resonance (NMR)

Magnetic resonance imaging (MRI) primarily uses the signal from the nuclei of hydrogen atoms for image generation. Hydrogen nuclei (single protons) are found abundantly throughout the body in water and fat. All subatomic particles; electrons, protons and neutrons can be visualised as spinning on an axis, and the hydrogen nucleus is thus a continuously rotating positive charge. Basic electromagnetism describes that a moving charge has an associated magnetic field. Hence, the hydrogen nuclei (proton) generates its field like a tiny magnet with north and south poles and is therefore also called the magnetic dipole moment. The spin of hydrogen proton possess an intrinsic form of angular momentum. In Quantum theory, the angular momentum of atomic nuclei is constrained to 2I + 1 possible spin orientations. A single proton has spin = ½, therefore the hydrogen nucleus has two possible spin orientations (2(½) + 1). In the presence of a magnetic field, the spin orientation of the protons will either align or anti-align with the magnetic field (Figure 1.9). The two spin orientations have different energy levels; aligned (low energy state) and anti-aligned (high energy states) separated by an energy difference $\Delta E = \hbar\omega$ (Figure 1.8c). The population of these spin orientations is governed by the Boltzmann distribution:

$$\frac{N_u}{N_d} = e^{-\frac{\Delta E}{kT}} \qquad \text{[Equation 1.1]}$$

where Nu and Nd represent the number of nuclei in the upper and lower spin states, respectively, ΔE is the energy difference between the two spin states, k is Boltzmann's constant and T is temperature. As it is energetically favourable for the nuclei to occupy the lower energy state, more nuclei align with the magnetic field. This imbalance in populations results in a small net magnetisation vector, M_0, in the direction of B_0 (Figure 1.9b).

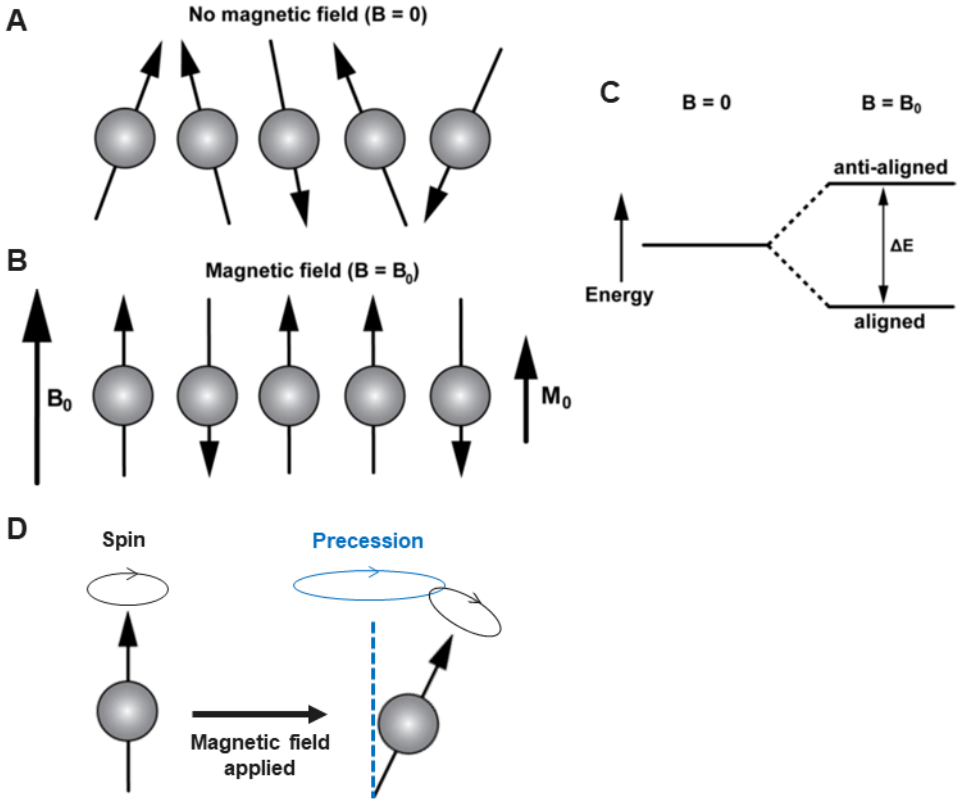

Figure 1.9: Spin orientation of protons in the presence of a magnetic field.

Nuclei in the absence of a magnetic field (A) are randomly orientated, and there is no net magnetisation. In the presence of a magnetic field (B), the nuclei occupy one of two possible spin states (C). The nuclei are either aligned or anti-aligned with the magnetic field. Overall, there are more nuclei align with the magnetic field as it is energetically favourable. (D) The magnetic field also causes the nuclei to precess around the direction of the magnetic field. [57].

The magnetic field also causes the nuclei to precess around the direction of the magnetic field (Figure 1.9d). This phenomenon was first described by Sir Joseph Larmor in 1909 [58]. He stated that nuclei with non-zero spin placed within a magnetic field will possess a magnetic moment and therefore experience a torque. The precessional frequency (ω) of the nuclei is determined by the nuclear gyromagnetic ratio (γ) and the strength of the magnetic field (β_0), as described by the Larmor equation:

$$\omega = \gamma\, \beta_0 \qquad \text{[Equation 1.2]}$$

The gyromagnetic ratio is a constant specific to various nuclei (Table 1.1). The precessional frequency of any particle at a certain magnetic field strength can be calculated using the Larmor equation and the table. For example, in a typical clinical 1.5T MRI scanner the precessional frequency, ω, of hydrogen protons is therefore approximately 64 MHz. In a 9.4T pre-clinical scanner this increases to 400 MHz.

Table 1-1: The gyromagnetic ratio of different nucleus

Nucleus	Gyromagnetic ratio (γ) in MHz/Tesla
^{1}H	42.58
^{13}C	10.71
^{19}F	40.05
^{23}Na	11.26
^{31}P	17.24

In 1946, Bloch and Purcell discovered the nuclear magnetic resonance (NMR) phenomenon, a process of absorption and emission of RF energy at the resonance (Larmor) frequency of nuclei when place within a magnetic field when there is a transition between spin orientations. Bloch and Purcell measure the nuclei properties in condensed matter; water and paraffin, respectively [59], [60]. These discoveries serve as the fundamental for the development of magnetic resonance imaging, allowing us to see a detailed image of the inside of the body.

As mentioned previously, at equilibrium, there is a net magnetisation vector, M_0, in the direction of B_0. At this state, the individual protons rotate out of phase with one another and thus there is no phase coherence. The application of an RF pulse at the Larmor frequency causes two important phenomena to occur: (1) phase coherence is induced between the nuclei causing them to rotate in synchrony, and (2), the nuclei are excited to a higher energy state (flipped away from the direction of B_0. This process is shown in the schematic diagram (Figure 1.10) using a coordinate system which rotates at the Larmor frequency.

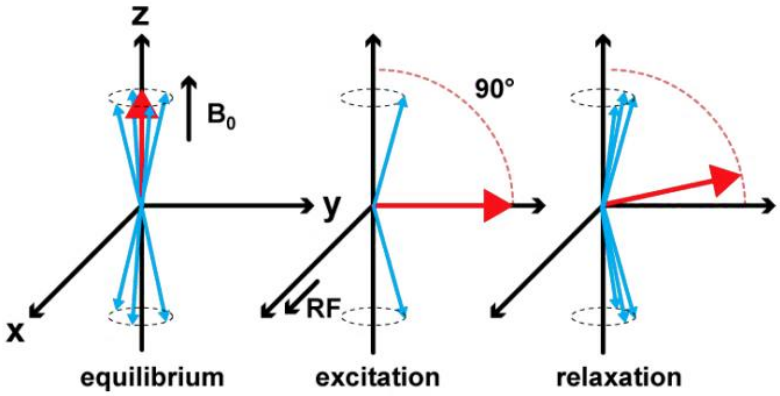

Figure 1.10: The excitation and relaxation of magnetisation in a reference frame rotating at the Larmor frequency.

At equilibrium the spins (blue) are aligned or anti-aligned with the magnetic field. A 90° RF pulse excites the spins, causing them to gain phase coherence and the net magnetisation vector (red) to point in the transverse plane. During relaxation, the spins dephase and the net magnetisation vector recovers to the align with the magnetic field [57].

The RF pulse excites the nuclei of hydrogen atoms and rotates the net magnetisation (M_0/M_z) into the xy-plane and is now called transverse magnetisation or M_{xy}. Following the RF pulse, the magnetisation will return to its equilibrium state (M_z), a process called relaxation, where the nuclei simultaneously lose phase coherence (T2 relaxation) and transition between energy levels (T1 relaxation), returning to their original spin states and re-emitting RF pulses in the process. During this period, the rotating magnetisation vector rotating in the x-y plane is detected by Faraday induction in the RF receiver coil of the MRI scanner.

Mechanism of T1 and T2 relaxation

The NMR phenomenon involves two forms of energetic relaxation following excitation of nuclei in a magnetic field; T1 (spin-lattice) and T2 relaxation (spin-spin), which represent time constants. Spin-lattice and spin-spin relaxation mechanisms are due to dipole-dipole interactions, and relaxations times depend on molecular motions within tissues. Different types of media or tissue have their own T1 and T2 time. Relaxation times can be measured using a special pulse sequence such as T1 mapping sequences and is altered in the presence of contrast agents or pathological tissues.

T1, or spin-lattice relaxation, refers to the time taken for energised nuclei to return to their equilibrium state. T1 is also known as the longitudinal relaxation time because diagrammatically it represents the time taken for the net magnetisation vector, M_0, to return to the B_0 direction following excitation. The mechanism underlying T1 relaxation is the thermal transferral of energy from the spins to their surrounding lattice. Nuclei residing within a sample are held in a lattice. The nuclei in the lattice are subject to vibrational and rotational motion, which creates a separate, complex, magnetic field. This magnetic field can share frequency and phase equal to the Larmor frequency of the nuclei, causing the nuclei to lose energy and return to the lower spin state. This is a thermal process because every transferral of energy causes a very small temperature rise in the sample.

T2, or spin-spin relaxation, is a much more rapid process which refers to the time taken for coherent nuclei to lose coherence (dephase). T2 is also known as transverse relaxation because diagrammatically it represents the time for the transverse magnetisation vector Mxy to reduce to zero. The mechanism underlying T2 relaxation is the interaction of magnetic fields between neighbouring nuclei. For example, a proton aligned with B_0 exerts a slightly higher magnetic field on its neighbour ($B_0 + \Delta B$) than an anti-aligned proton which exerts a magnetic field on its neighbour slightly weaker ($B_0 - \Delta B$) than the B_0 field. As a result of the Larmor equation (equation 2.2), nuclei residing closest to the aligned proton will have a faster precessional frequency. Similarly, nuclei in the vicinity of the anti-aligned proton will have a slower precessional frequency. Thus, the sample is no longer perfectly coherent, and on a macroscopic scale, the sample dephases. The rapidity of T2 relaxation is further increased by inhomogeneities which are present in all magnetic fields. Fluctuations in the magnetic field at different locations cause nuclei within a sample to precess at different frequencies, causing increased dephasing. This is also

known as T2* relaxation, to distinguish it from T2 relaxation, which is caused purely by spin-spin interactions.

Image contrast

Different tissues in the body have their T1 and T2 time. These relaxation times describe the time duration required for the tissue to get back to the equilibrium after an RF pulse. Different relaxation times produce different signal intensities or brightness. The differences are described as the image contrast in MR images. A wide range of image contrasts can be produced in MRI by using different imaging techniques, known as pulse sequences by controlling the imaging parameters of the sequences, i.e. the repetition time (TR), echo time (TE) and flip angle. These allow us to see the boundaries between tissues, such as the white matter and grey matter in the brain. The pulse sequence is stored in the scanner computer, and imaging parameters can be controlled from this computer. There are many different types of sequences; each has different TR and TE values which can be modified to get the required image contrast. There are three main types of image contrast in MRI: T1-weighted, T2-weighted, and proton density-weighted (PD-weighted).

In T1-weighted images, the bright pixels are associated with short TR, which requires a short TR and short TE during acquisition to enhance the image contrast. While for T2-weighted images, the bright pixels are associated with long T2 relaxation time which requires long TR and long TE during acquisition. PD-weighted images are a bit different and the signal intensities, hence brightness is depending on the number of proton densities, i.e. water content in the tissue or region. To produce PD-weighted images, a long TR and short TE are required during acquisition. Fluids such as cerebrospinal fluid, oedema have long T1 (e.g. in clinical, 1500-2000ms), water-based tissues such as muscle are usually mid-range (e.g. in clinical, 400-1200ms), and fat-based tissues such as fat, bone marrow have the shortest T1 (e.g. in clinical, 100-150ms). T2 always have shorter time than T1 for a given tissue. Fluids have the longest T2 (e.g. in clinical, 700-1200ms), water-based tissues tend to have longer T2 than fat-based tissues (e.g. in clinical, 40-200ms and 10-100ms respectively).

Pathological tissues usually have either oedema or altered blood supply, or fibrous bands; thus, their appearance can be a mixture of water-based tissues and fluids. These ultimately lead to a change in the tissue T1 and T2 times. Imaging parameters in the pulse sequence can be modified to get image contrast that enhances the pathological region. T1 and T2 relaxation time can also be measured quantitatively by using advance image sequences such as T1/T2 mapping which

provide a more sensitive approach to detect early pathological changes and pathological processes. Besides, image contrast can be enhanced further using MRI contrast agents such as gadolinium and manganese. The main pulse sequence used in this thesis; CINE, T1 mapping and inversion recovery are described in Section 1.3.2.3 to 1.3.2.4.

Contrast agents in MRI

Contrast agents can improve image contrast by enhancing signal intensity within the regions in which they accumulate. MR imaging is highly sensitive to detecting pathological conditions at an early stage, but not very specific. Several different pathologies have similar appearances, and the native contrast is sometimes not profoundly different from that of healthy tissue. Contrast agents can help improve the specificity by producing an extra set of images with higher image contrast. Contrast agents can also increase the signal to noise ratio (SNR), which improves image quality and allows higher resolution. There are two main types of contrast agents in MRI; positive contrast agents (paramagnetic) and negative contrast agents (superparamagnetic).

Bulk water in its free state has long T1 relaxation as it consists of small molecules and has a fast tumbling rate. When the water molecules bound to other molecules, its tumbling rate may be slowed, and therefore has much shorter T1 value than that of free water. One example is when water molecules are in close proximity with MR contrast agents such as gadolinium or other metal ions. Gadolinium has seven unpaired electrons in its *4f,* making it a strong paramagnetic that decreases T2 and T1 relaxation times of protons in the immediate vicinity of the molecule [61]. This results from dipolar interactions between water nuclei (in tissue) and electron spins at the metallic centre. As mentioned previously, protons, electrons, and NMR-active nuclei can be thought of as tiny magnets with north and south poles ("dipoles") whose electromagnetic fields interact through space. This dipole-dipole interaction is responsible for the mechanism of T1 and T2 relaxation in biological tissues.

Paramagnetic ion complexes can be viewed as having a separate coordination sphere, the inner sphere that consists of ligand directly bonded to the metal ion, and the outer sphere where water freely diffuses. Theories describing how gadolinium complexes (or other paramagnetic ion complexes) produce these effects are beyond the scope of this thesis and readers could find a detail explanation in the paper included in the references [61], [62]. In brief, there are two ways in which this paramagnetic ion complexes agents induce effects in bulk water; 1) inner sphere

relaxation and 2) outer sphere relaxation. Inner sphere relaxation describes direct and intimate interactions between water molecules and gadolinium ion within a mean distance up to ~0.4 nm. At a distance of above 0.4 nm, an indirect interaction between gadolinium ion and another group of water molecule on the surface of the ligand occur and referred to as outer sphere relaxation. The outer sphere interactions could interact with bulk water at much further away up to within 1 nm. These two types of interactions between gadolinium complexes and water results in the shortening the relaxation of water protons.

At low concentrations such as those used in clinical and pre-clinical studies, the significant effect is the T1 shortening and tissues which take up the agent have an enhanced signal intensity on post-contrast T1-weighted images. For example, in myocardial infarction patients, gadolinium chelates will accumulate the infarcted region, where there is increased extracellular space. As a result, the infarct region will appear bright in the post-contrast T1-weighted images. Gadolinium is toxic, so is bound within chelators to prevent its interaction with biological properties. When gadolinium is injected into the body, it is initially in the blood vessels but rapidly redistributes into the extracellular fluid spaces (11 minutes half-life), and is then gradually excreted via kidneys with a 90-min half-life in patients with normal kidney function. It is completely washed out after 24 hours. Manganese is another positive contrast agent which shortens T1 through similar processes to gadolinium.

Negative contrast agents such as a super-paramagnetic iron oxide (SPIO) have more profound effects on T2. SPIO agents create a large inhomogeneity which in turn increase the dephasing rate of protons, reducing T2* and well as T2 relaxation time. SPIO agents reduce the T2 in tissues where they accumulate, causing lower signal intensities, hence darker regions on the postcontrast T2-weighted images. These are commonly used in liver and spleen imaging. The healthy tissue takes up the contrast agent, thus reducing the signal intensity in the healthy tissue, leaving the pathological tissues relatively bright only in T2-weighted images.

Local hardware

Imaging was performed using a 9.4T MRI system (Agilent Technologies, Santa Clara, USA) equipped with 1000mT/m gradient inserts and a 39mm volume resonator RF coil (RAPID Biomedical, Rimpar, Germany). These gradient configurations were used for mouse imaging. The basic components of the magnet setup are described in Figure 1.11. Optimal signal detection was achieved by tuning and matching of the electrical resonance of the RF coils every time before the start of each experimental session. Tuned and matched was done at the NMR frequency of water using an external Probe Tuning Device 505NV+ (Morris Instruments Inc, Ottawa, Canada). The imaging system was controlled using the Varian VNMRJ software v 3.1 (Agilent, Santa Clara, CA, USA). This program serves as a platform to perform imaging, shimming and calibration protocols.

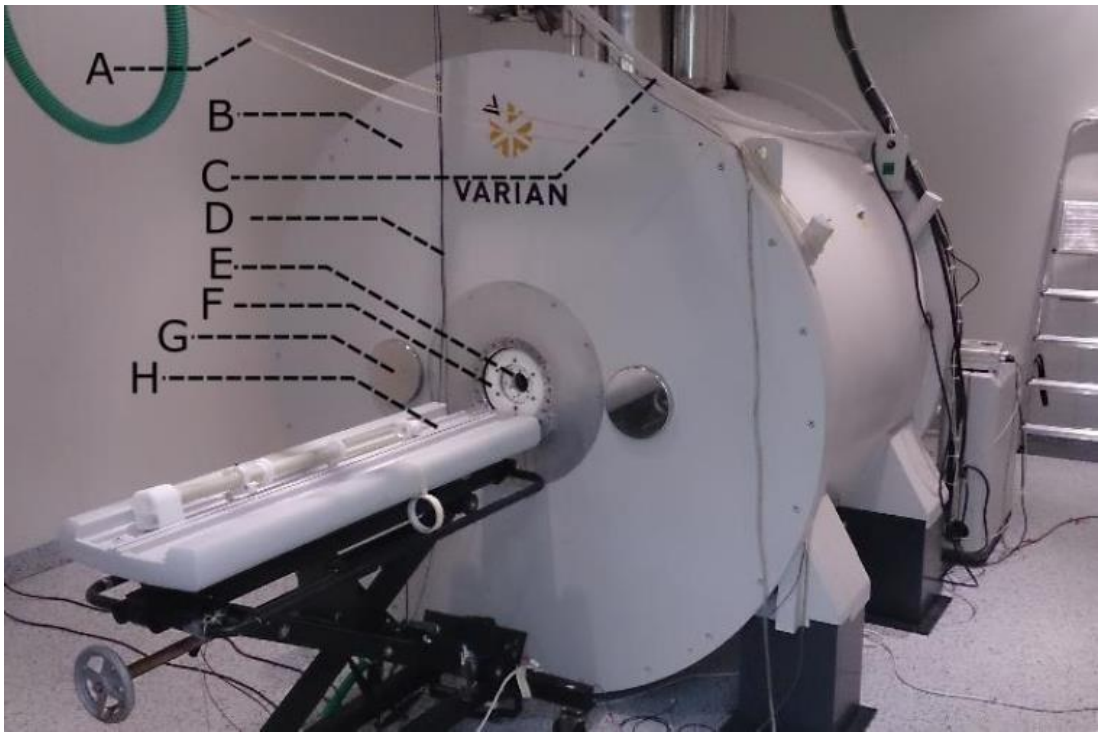

Figure 1.11: Varian system used for all MRI experiments.

(A) heated water lines; (B) main magnet and cryogen storage; (C) anaesthetic delivery and scavenger; (D) fibre optic cables for physiological monitoring; (E) small gradient inserts; (F) larger gradients; (G) shim coils; (H) scanner bed.

Image acquisition gating

The heart continually moves during contraction and relaxation of the atria and ventricles as well as blood flow. At the same time, the heart is largely displaced during inspiration and expiration. These two sources; cardiac motion and respiratory motion, caused significant motion artefacts in the images. Artefacts due to cardiac and respiratory motion are most effectively controlled by synchronising imaging to the animal's physiology; heart rate and respiration rate of the animal and gated or triggered the MRI pulse sequences according to the physiological traces. A gated acquisition means a specific component of the pulse sequence, such as an RF pulse or gradient waveform, are synchronised to occur at the particular physiological event in the ECG trace and respiratory phase, so that image is acquired with a motion-free heart.

In pre-clinical imaging, ECG is measured using three electrodes inserted subcutaneously under both armpits and in the peritoneal region, which then translate the electrical impulses of the heart into a continuous voltage waveform. Simultaneously, respiration motion is measured using a neonatal apnoea pad taped to the abdomen of the mouse. At the same time, the temperature of the animal is also being monitored throughout the experiment as the temperature will also affect the heart, which in turns affect the image acquisition gating. Therefore, the temperature should be maintained between 36.5 to 37ºC. Similarly, the amount of anaesthesia given during the imaging should also be monitored as it has an effect on the respiratory rate; therefore, a constant dosage should be maintained within a narrow range as possible during the entire experiment. The detailed set-up of physiological monitoring is described in Section 2.3.2.3.

Cardiac imaging planes

When a patient or animal is placed in an MRI scanner, the heart lies obliquely in the chest relative to the imaging gradients. Therefore, MR images are acquired in the cardiac imaging planes by reoriented the anatomical planes of the body, as shown overlaid in an illustrated human heart in Figure 1.12A. Typically, three orthogonal planes (e.g. Figure 1.12.A.A-C-E) are used for orientation. The reorientation process to obtain the slice planes reliably takes some practice. The 2-chamber long-axis view was acquired starting from the pilot scans. A 4-chamber-long-axis view was then acquired perpendicular to the 2-chamber plane. Finally, from the 4-chamber view, with the 2-chamber view as a second reference, a short or a series of short-axis images were acquired perpendicular to the LV-long-axes of the 2- and 4-chamber

images. Representative images of the wild type mouse heart in these planes are shown in Figure 1.12B to illustrate their appearance in MRI. The most used axis for describing the heart is the short-axis view, and this will be used as a convention for presenting results in this thesis.

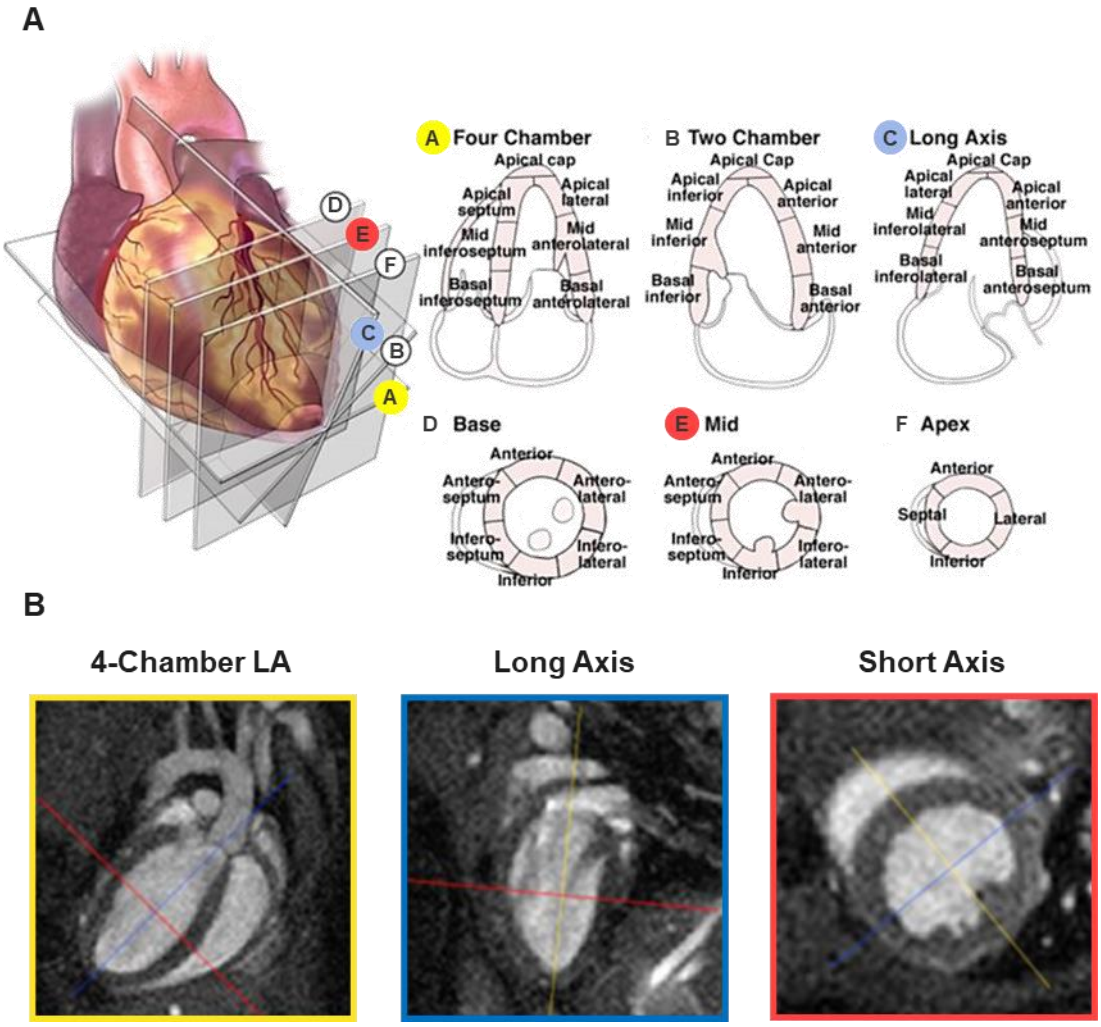

Figure 1.12: Cardiac imaging planes.

(A) Illustration describing the cardiac imaging planes. Long axis images (1,2,3) are typically used for orientation of the short axis planes (4,5,6) although are also useful in providing the complete single slice views of the heart. Cardiac MRI for structural and functional assessment typically uses a stack of cardiac short-axis images covering the whole LV. (B) Representative images showing the appearance of the cardiac axes in bright- blood MR images. LA- long axis; SA- short axis; ED- end-diastole. Adapted from [63], [64]

1.3.2.2 CINE MRI sequence

CINE sequence, shorthand for cinematic, acquires a time series of static images of the heart that when displayed sequentially show the beating heart. Cine imaging relies on accurate gating for physiological motion. A gated gradient echo sequence was used to acquire cine cardiac images. The basic principles of the cine acquisition scheme and the GRE pulse sequence are described in Figure 1.13.

The raw data acquired in cine sequence fills a stack of 2D k-space arrays. In a single heartbeat, one line of k-space is acquired for each frame; therefore, matrix 128 x 128, 128 heartbeats are required to complete k-space for a single slice CINE. Each 2D k-space array represents a single frame in the cardiac cycle. Imaging parameters for mice were as follows; echo time (TE) = 1.18ms, repetition time (TR) = 5ms, flip angle = 15°, slice thickness = 1 mm, field of view (FOV) = 25.6 × 25.6mm, matrix size = 128 × 128, number of signal averages = 2. In a single slice of CINE, the number of frames (NF) is depending on the heart rate. Given the temporal resolution of 5ms (TR), for a mouse heart that has 500 beats per minutes (120ms R-R interval), will have a maximum of approximately 25 frames in every cardiac cycle. The phase encoding (PE) was incremented linearly following each cycle. Typically, 9 to 10 short-axis slices were acquired for full heart coverage, taking approximately 5 minutes. Scan time is calculated as follows (equation 1.3):

$$\text{Scan time} = \text{TR} \times \text{Matrix size} \times \text{NF} \times \text{No. of slices} \times \text{Average}$$

[Equation 1.3]

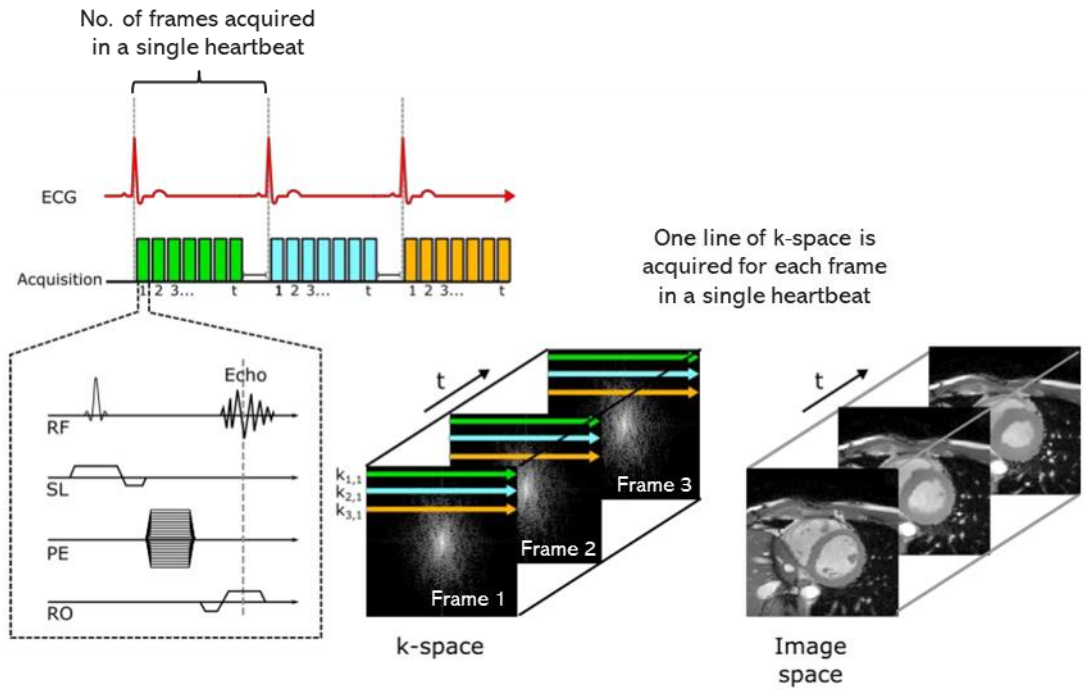

Figure 1.13: CINE MRI acquisition sequence.

GRE readout acquires one line of k-space per time frame sequentially for each ECG trigger. This repeats until each 2D k-space matrix is filled. An FFT applied to the data translates the frequency and phase information in k-space to image space [64].

1.3.2.3 Cardiac T1 mapping sequence

Imaging was performed using the standard look-locker (LL) inversion recovery sequence, which first developed by Look and Locker [65] as shown in Figure 15 below. After the first instance of respiration and ECG gate, a complete global 180º inversion RF pulse to flip every spin within the imaging volume by 180º. Following inversion, the longitudinal T1 magnetisation begins to recover to equilibrium following the T1 recovery curve (Figure 1.14). A sampling at positions along this relaxation curve allows for fitting of the T1 relaxation time. Each sampling on the T1 relaxation curve requires an excitation and gradient readout that removes energy from the system and perturbs relaxation. Hence, the more frequently the recovery curve is sampled, the greater the saturation of the recovery as more samples are acquired. The flip angle during sampling also influences the saturation, the greater the flip angle, the greater the saturation. However, this saturated recovery can be accounted for when fitting the T1 recovery curve by applying the look-locker correction factor as derived by Deichmann et al. (2004) [66].

Figure 1.14 above shows an example of 13 inversion times (TI – the time since the inversion pulse) with the acquisition triggered at each ECG signal. The Look-Locker acquisition scheme acquires a single line of k-space per RR interval. Since data is acquired in the frequency domain, the data is filled into a mathematical k-space matrix. Simply put, k-space stored the frequency information where it could be transformed using a mathematical process called Fourier transform into spatial information known as the image space. Each point in k-space represents a specific spatial frequency within the acquired FOV. High spatial frequencies carry image resolution and edges, while low spatial frequencies carry the image contrast. Each pixel in the acquired k-space matrix contains complex signals measured by the surfaces coils. Performing a 2D fast Fourier transform on this data produces another complex image in image space from which magnitude and phase images can be calculated.

In cardiac MRI, the TI must always be an integer multiple of the RR interval so that data is acquired at exactly the same phase of the cardiac cycle (end-diastole). Following each sequence of samples, sufficient inversion recovery delay time must be given to allow full magnetisation recovery before the next inversion. The sequence shown is repeated for every phase encoding line until the whole FOV has been sampled and produce a sequence of images from which the recovery of the T1 signal can be calculated. Since the MRI scanner measures all signals as positive, the recovery curve is constrained to lie above the x-axis resulting in an image sequence that starts from bright, goes dark and then recovers to bright again.

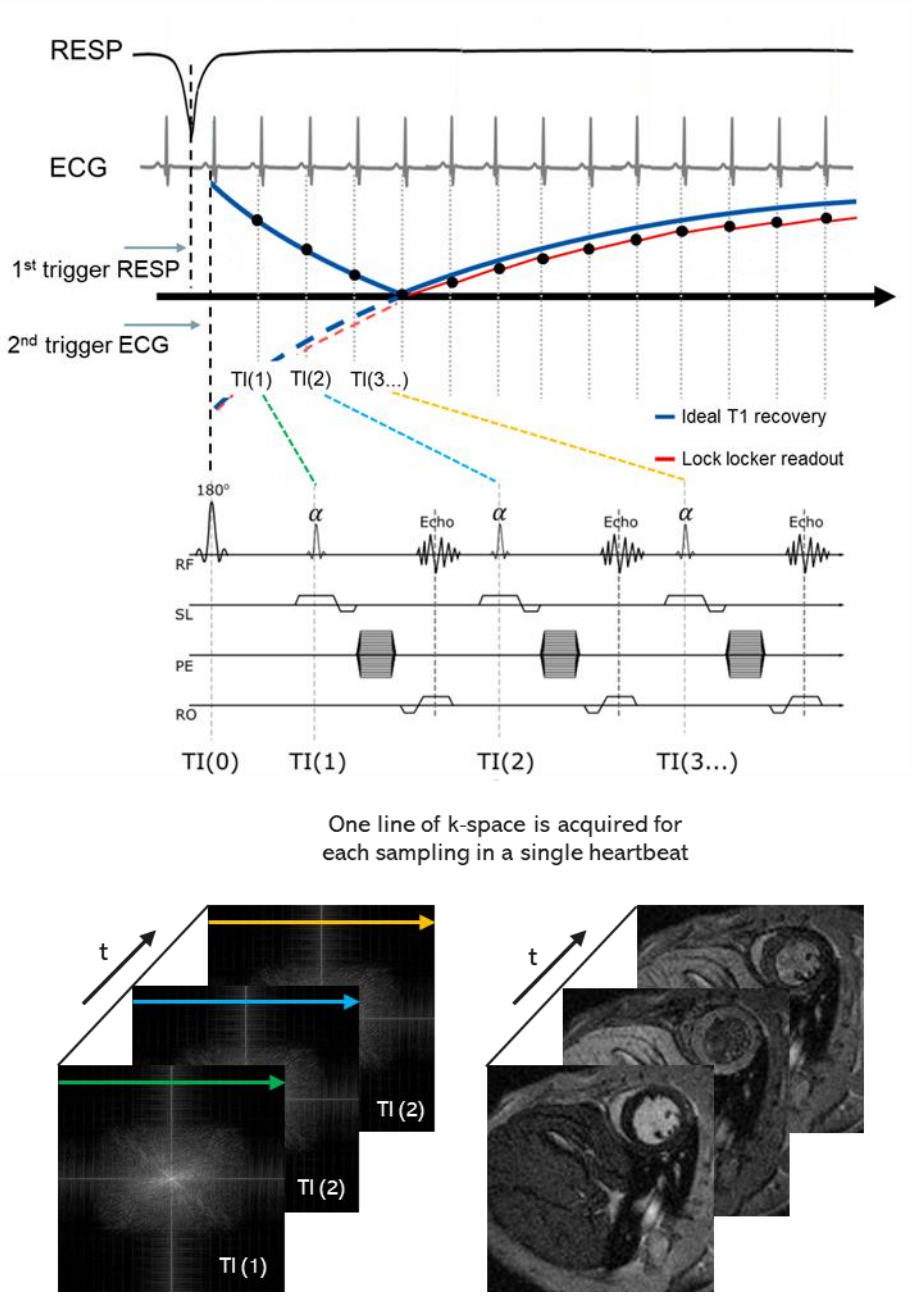

Figure 1.14: Basic cardiac inversion recovery imaging sequence.

Following the detection of respiration and ECG trigger, the sequence applies a 180° inversion pulse and then samples the T1 recovery curve using a small flip angle (α) GRE readout at each subsequent ECG trigger to the specified number of inversion times. The sequence repeats for each phase encoding step. The saturation effect of the look-locker readout on the T1 recovery curve is shown in red. RESP = Respiration, ECG = Electrocardiogram.

Longitudinal relaxation (T1) fitting

T1 mapping resulted in an image sequence where signal intensity could be modelled by a 3-component model, as shown in equation 1.4.

$$S(TI) = S_0(1 - Be^{-TI/T1^*}) + [C] \quad \text{[Equation 1.4]}$$

Where TI is the time following the radiofrequency lock-locker inversion pulse, B is fitted parameter to account for imperfect inversion and $T1^*$ is the apparent T1 under the influence of Look-Locker saturation. This saturated recovery can be accounted for when fitting the T1 recovery curve by applying the look-locker correction factor as derived by Deichmann et al. (1992) [67]. This is corrected by the correction factor (equation 1.5)

$$T1 = (B - 1)\, T1^* \quad \text{[Equation 1.5]}$$

T1 maps were generated by performing pixel-wise curve fitting as described above using in house Matlab optimisation code written by Dr Laurence Jackson (2016b, The Mathworks, Inc., Natick, USA) based on the Nelder-Mead Simplex Method [68].

1.3.2.4 Inversion recovery sequence

For many MRI studies, it can be advantageous to null the signal from specific regions of the image. Inversion recovery (IR) pulse sequences enable the suppression of signal from tissues of a specific T1, thus making the tissue appear hypointense in the final image. This can reveal and facilitate the delineation of specific tissues or structures that would otherwise be masked in conventional T1- or T2-weighted images. IR pulse sequences typically involve applying a 180° RF pulse before waiting a period of time – known as the inversion time, TI – when a 90° RF pulse is applied, and the magnetisation is measured. If the duration of TI is chosen appropriately, it is possible to suppress the signal from a specific tissue. Usually, the choice of TI requires some a priori knowledge of the tissue relaxation times within the sample. In cardiac MRI, the TI must always be integer multiple of the RR interval.

Imaging was acquired using a multi-slice IR-GRE (IRmSL) sequence with a single inversion time (TI) point and flip angle of 90° [69]. The optimum TI was selected from the multiple frames of the LL inversion recovery sequence performed prior to the IRmSL sequence. TI was selected to null the healthy myocardium for MEMRI, while for Late-Gadolinium Enhancement MRI (LGE-MRI), TI was selected to null the infarcted myocardium (Figure 1.15). This provides the best contrast between healthy and infarcted myocardium.

Figure 1.15A shows a relaxation curve during an IR pulse sequence. The 180° RF pulse causing every spin within the imaging volume to flip by 180º. Following this, the sample recovers according to T1 relaxation curve. For MEMRI, TI is chosen so that the 90° readout pulse is acquired at a point where the infarcted myocardium has zero magnetisation and thus appears hypo-intense, which then enhance healthy myocardium and vice versa for LGE-MRI (Figure 1.15B-C).

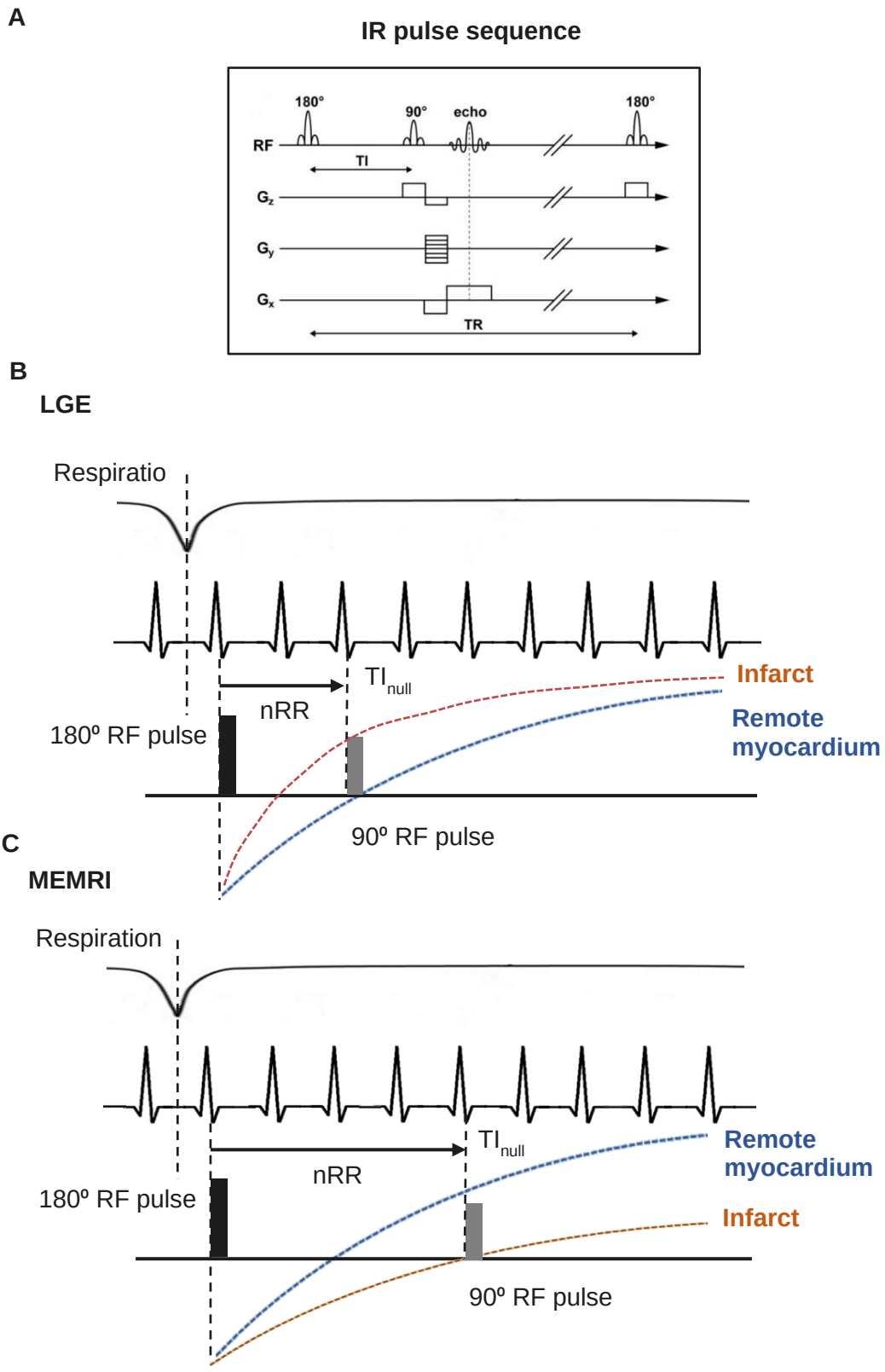

Figure 1.15: Inversion recovery sequence.

The sample magnetisation which subsequently recovers according to T1 relaxation, passing through a null point corresponding to zero magnetisation at time, TI. TI was selected to null the healthy myocardium for LGE-MRI, while for MEMRI TI was selected to null the infarcted myocardium.

1.3.2.5 Current challenges of myocardial viability imaging in CMR

Viable myocardium is defined by the presence of living myocytes, irrespective of contractile function. Studies have demonstrated that hypo-contractile myocytes in the setting of acute myocardial ischemia or chronic myocardial hypoperfusion may remain viable and are potentially salvageable. A significant challenge for contemporary cardiovascular imaging is to adequately assess viable myocardium with the aim to optimise patient selection for coronary revascularisation. The question remains in how much myocardium has been salvaged and how much left still potentially salvageable? To answer this question, one must have the tools to assess myocardial viability and infarct size accurately. Several parameters that can be used to determine the presence and extent of infarction are summarised and ranked from least to most accurate in Figure 1.16. For example, wall motion abnormality does not directly imply infarcted myocardium, as there may be viable tissue but have contractile dysfunction as seen in stunning and hibernating myocardium. ECG findings alone have lack sensitivity to small and early infarct, whereas cardiac biomarkers such as cardiac troponin often very helpful in the acute setting of myocardial infarction but does not carry information regarding the location and size of the infarct.

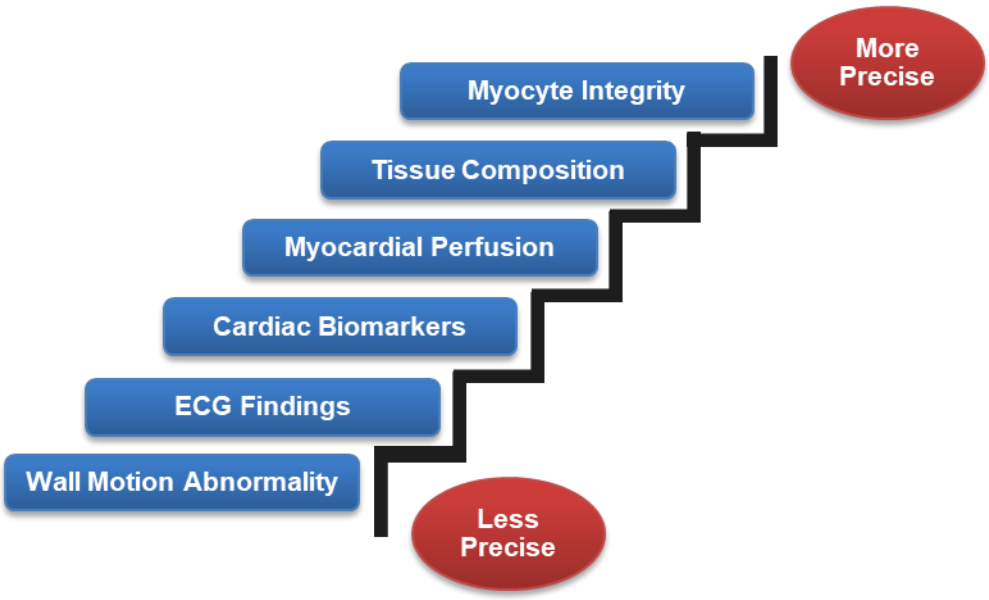

Figure 1.16: Clinical and physiological markers of myocardial infarct size.
Adopted from Kaul 1998; Jamiel et al. (2017).

Cardiac imaging has revolutionised our ability to diagnose heart disease and quantify mechanisms of pathology and therapy [72]. Current techniques can interrogate structure, contractility, metabolism and fibrosis [73]–[75] but struggle to directly quantify one of the most important determinants of patient morbidity, myocardial viability [76], [77]. Late Gadolinium-enhanced MRI (LGE-MRI) is routinely used clinically to assess myocardial damage in infarcted regions [78]. Despite LGE-MRI being one of the most important diagnostic and prognostic measures of infarct size [72], [73], [79], it has several limitations: 1) Chelated Gd^{3+} accumulates non-specifically in the infarct owing to a mixture of cell membrane rupture, increased extracellular space, oedema and perfusion deficits in damaged tissue, meaning changes in image contrast relate to several different tissue properties [80]; 2) Infarct-related increases of extracellular space and oedema develop at variable rates and over several hours after damage, compromising the accuracy of LGE-MRI early in acute myocardial infarction (AMI) [81]: 3) concerns over the safety of Gd-based contrast agents have been raised [82].

Alternatively, T2-based MRI, MRI myocardial perfusion imaging, arterial spin labelling (ASL), and blood oxygenated level dependency (BOLD), have been used to assess myocardial viability - each has its challenges, limitations and does not directly looking at viable myocardium. T2-based MRI is one of the most common and established methods for assessment or area-at-risk after myocardial infarction. Ischemia results in an increase in myocardial water content manifesting as myocardial oedema, causing local changes in T1 and T2 relaxation times. Quantifying AAR, coupled with assessment infarct size using the gold standard, LGE MRI would give us more information on the viability of the myocardium. However, from a mechanistic viewpoint, the assumption that T2- CMR depicts the AAR-MI because of myocardial oedema is questionable. The bulk of experimental evidence points to substantial oedema occurring in the infarcted region, with minimal oedema occurring in the AAR-MI portion [83].

MRI also can be used to study myocardial perfusion. MRI perfusion imaging is performed by monitoring the first-pass of bolus contrast injection, i.e. Gd-DTPA. The unenhanced region during the first pass reflect areas associated with perfusion defects. This method is also used for stress and rest perfusion study using vasodilators to assess perfusion reserves [84]. Improved myocardial perfusion with stress is considered viable and hibernating, which serves as a strong predictor of functional recovery following revascularization and long-term prognosis [85], [86]. A new advance method in cardiac imaging, ASL, provides a quantitative mapping of regional blood flow that is compatible with the conventional MRI perfusion imaging but does not require any contrast agents [87]. ASL may also be used as an alternative method for quantifying AAR after AMI [88]. Another approach for identifying ischemic myocardium and thus assessing the viability of the myocardium is by using BOLD. The application of BOLD in cardiovascular imaging is based on the alterations in the blood oxygenation and myocardial blood volume in ischemic myocardium. Rest and stress BOLD CMR at 3Tesla proved feasible in clinical imaging and able to discriminate between ischemic, non-ischemic, and normal myocardial segments [89], [90]. Although all the techniques discussed above are promising, the implementation in clinical imaging is still relatively challenging owing to the hardware requirements, the presence of artefact and complex MR pulse-sequence.

One property that is highly sensitive to altered myocardial viability and changes rapidly after the damage is calcium handling. Calcium is integral to cardiomyocyte contraction, and alterations to calcium uptake and handling are present in many cardiomyopathies [91]. Hence, a method to quantify calcium uptake within live cells, animals and patients would give valuable information on cardiac viability and insights into pathological and therapeutic mechanisms [76], [92], [93]. Manganese(II) is a calcium analogue which enters contractile cardiomyocytes through voltage-gated calcium-channels [94]–[96]. Mn^{2+} is also an MRI contrast agent. Hence, Mn^{2+} contrast can be quantified *in vivo* using MRI to give surrogate measurements of calcium uptake and thus myocardial viability. Several pre-clinical [97]–[101] and clinical studies [102]–[104] have investigated MEMRI for measuring myocardial viability.

1.3.3 Manganese-enhanced MRI (MEMRI)

The following section will further discuss the properties of manganese ion (a positive MR contrast agents and an analogue of calcium ions), the effects of manganese ion on cardiovascular systems and the application of MEMRI. Figure 1.17 summarises the four aspects of MEMRI.

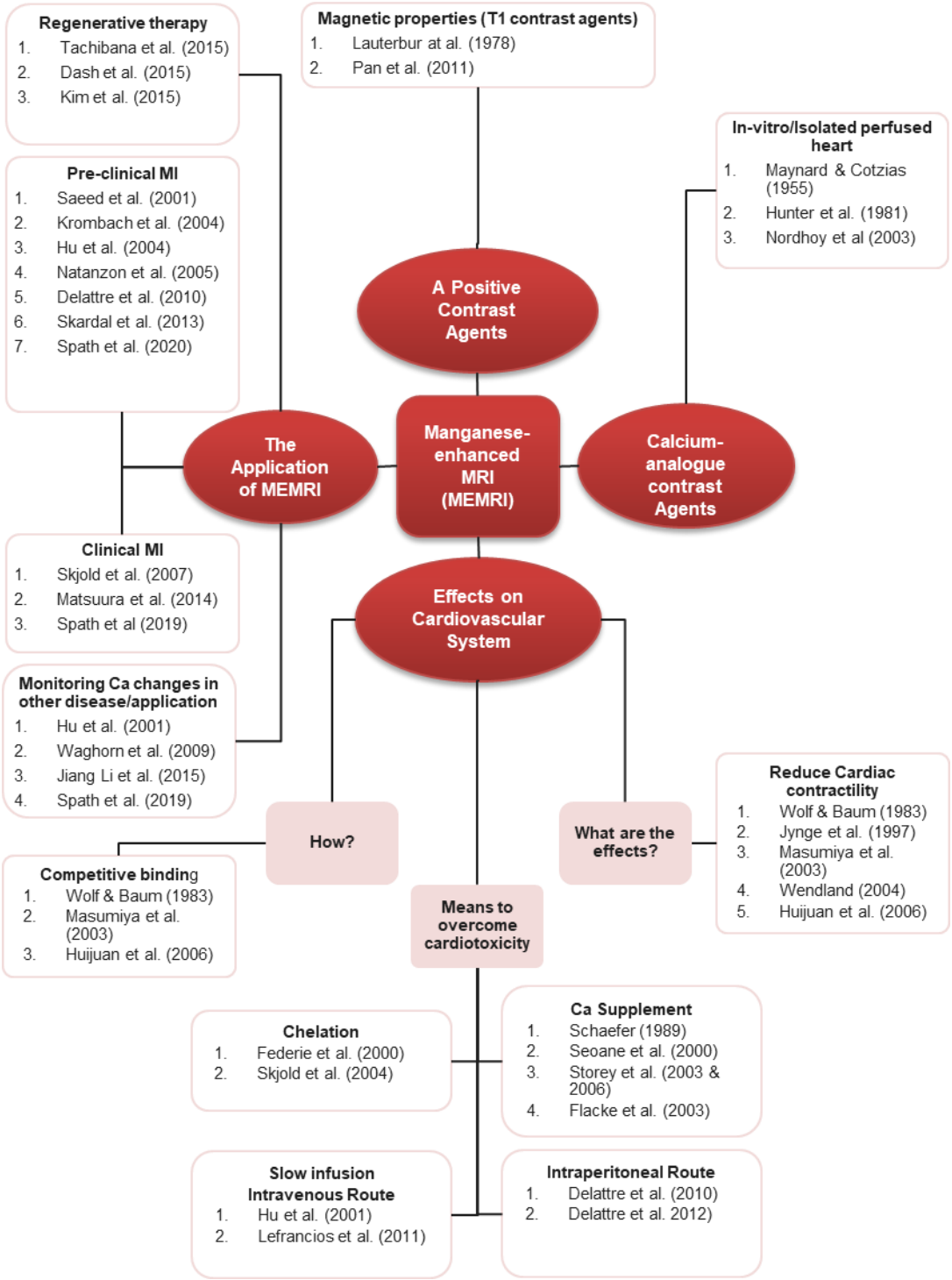

Figure 1.17: Manganese-enhanced MRI framework.

1.3.3.1 Manganese – A positive MRI contrast agents

Manganese is a paramagnetic transition metal and an essential trace nutrient with a stable nutrient abundance in the body. Manganese is an essential dietary element that primarily functions as a coenzyme in many biological processes. This includes macronutrient metabolism, bone formation, free radical defence system and in the brain, acting in ammonia clearance and neurotransmitter synthesis [105]. Concentrated levels of Mn are found in mitochondria abundant tissues such as liver, pancreas and heart. Dietary requirement for Mn is 1.8 and 2.3 mg per day for healthy adult women and men [105], [106]. Mn can be found in food such as nuts, whole grain and brewed tea. Dietary manganese is absorbed in the small intestine in a highly regulated manner, and blood Mn^{2+} is transported to the liver where it is rapidly excreted through the bile. As it is the case of many essential trace elements, excessive levels of manganese are toxic. Doses of 93 mg/kg for rats and 38 mg/kg for mice show significant adverse effects and mortality rates [107].

Mn^{2+} possess a magnetic moment due to its five unpaired electrons [108]. The relatively large magnetic moment, and the large number of unpaired electrons and long electron relaxation time primarily make Mn^{2+} an effective enhancer of nearby proton relaxation. Manganese ion (Mn^{2+}), when used as a contrast agent, works similarly as other paramagnetic ions, like gadolinium (Gd^{3+}), which can shorten the T1 of water protons, thus increasing the signal intensity of T1-weighted MR Images. Manganese ion (Mn^{2+}) is an intracellular positive contrast agent. It is a functional contrast agent that could be useful for measuring myocardial viability. Mn^{2+} enters viable cardiomyocytes via Ca^{2+} channels and enhances intracellular T1 relaxation allowing for assessment of myocardial physiology and function. However, due to competitive binding with Ca^{2+}, Mn^{2+} at high dose could cause negative cardiac inotropy [109]–[112]. Mn-induced negative inotropy, however, could be avoided by confining the extracellular Mn^{2+} concentration to a low level [111], thereby reducing the competitive binding with Calcium.

1.3.3.2 Manganese – A Calcium-analogue contrast agents

The underlying physiological principle behind MEMRI is the uptake and retention of manganese ion (Mn^{2+}) in myocytes [96], [113]. Mn^{2+} enters myocytes through L-type Ca^{2+} channels [95]. Outside cells, Mn^{2+} concentrations compete effectively with Ca^{2+} concentrations due to high affinity to Ca^{2+} channel binding sites. It is the activity of Ca^{2+} channels that forms the basis for myocardial Mn^{2+} uptake and the potential efficacy of MEMRI for assessment of myocardial function and viability. Slow channel activity is under autonomic control and can be influenced by positive and negative inotropic drugs. Previous studies using physiological modulators [114], [115] and animal model with altered Ca^{2+} channel activity [116] have been done to study the role of Ca^{2+} channel as entering point for Mn^{2+}. Importantly, in pathologic conditions, particularly during ischemia, L-type Ca^{2+} channel activity and Mn^{2+} uptake are retarded in parallel with decaying energy metabolism but are resumed in viable cells on reperfusion [95].

1.3.3.3 Manganese – Effects on Cardiovascular System

Although manganese-enhanced MRI (MEMRI) can be used to non-invasively image myocardial viability, concerns over Mn^{2+} cardiotoxicity [77], [112] have limited the number of MEMRI studies conducted in the heart. However, Mn^{2+} is also an essential trace element for maintaining cell viability and could potentially be used as a therapeutic intervention by blocking calcium channels. Moreover, with the increase in stability and sensitivity of MRI scanners, it should be possible to use much lower doses of Mn^{2+} [77]. Manganese contrast agents are now used in clinical trials [117] using calcium gluconate as a supplement to further reduce the toxicity effects. Moreover, acute effects of Mn^{2+} like the depression of contractility and heart rate is rapidly reversible; and rat hearts accumulate and buffer large amounts of Mn^{2+} without affecting cardiac function or energy metabolism in the acute stage [118].

1.3.3.4 The application of manganese-enhanced MRI in cardiac imaging

$MnCl_2$ was the first substance suggested as an MRI contrast agent by Lauterbur et al. (1978) [108], who observed elevation of R1 in liver, heart, and kidneys [119]. Free ionic manganese ($MnCl_2$) is commonly used for MEMRI. Three main applications for cardiac MEMRI have emerged: myocardial viability, perfusion, and function.

Myocardial viability is a major interest in the clinical setting. The differentiation of infarcted from healthy tissue in the complex pathophysiology of the myocardium following prolonged ischemic episode is possible in MEMRI where Mn^{2+} lightens up viable cells [93], [101], [115], [120]–[126]. Viability assessment has been conducted in animals with myocardial stunning, and in a differentiated manner in patients with myocardial infarction [102]. Myocardial function utilises Mn^{2+} as a probe for Ca^{2+} channel activity at the myocyte level. Inotropy can be changed pharmacologically (positive with dobutamine [114], [115], or negatively with diltiazem [115]) and monitored by MEMRI. In a transgenic animal models [127]–[129], MEMRI provides means to assess the change in Ca^{2+} channel activity. Myocardial perfusion is indirectly assessed in MEMRI. Several hypo-perfused areas have myocytes with reduced Ca^{2+} channel activity, such as in the hibernating condition, and will thus take up less Mn^{2+} than normally perfused and contracting myocytes [122], [130]–[132].

In patients with myocardial infarction, the extent and severity of ischemic injury are important prognostic factors for mortality and morbidity. Consequently, methods for non-invasive and accurate measurement discrimination between viable myocardium, peri-infarct area, and infarct size have been desired as a valuable tool in patient management. Manganese, a calcium-analogue intracellular contrast agent, can provide additional information on the cellular integrity after myocardial infarction. MEMRI has demonstrated its efficiency in identifying viable myocardium evident as a hyperintense region, suggesting uptake of Mn^{2+}. Whereas area of reduced Mn^{2+} accumulation have been observed in area-at-risk [122], [133], stunned cardiomyocytes [93], the peri-infarct area adjacent to the infarct zone [99], and infarct zone [120], [123] depending on the stage of myocardial injury.

Conversely, gadolinium (Gd) chelates are typically extracellular contrast agent that distributes passively throughout the blood and extracellular space [134]. In an infarcted region of the myocardium, gadolinium contrast agent exhibits delayed accumulation and longer retention [135] due to decreased tissue perfusion and increased extracellular volume compared to healthy myocardium. Late gadolinium enhancement MRI (LGE-MRI) is an established method for infarct quantification [136], [137]. The information on extracellular changes from LGE-MRI and cell viability from MEMRI will allow for quantification of viable myocardium, peri-infarct, and infarct regions. LGE-MRI will enhance infarcted myocardium and while MEMRI will enhance viable myocardium.

In addition, MEMRI also could be used to assess the successful of regenerative therapy. Recent studies have documented the potential of stem cell therapy as a stand-alone therapy for those patients who have exhausted all conventional therapies and where revascularisation is no longer an option due to lack of suitable conduit vessels [25], [138]. This approach might prevent or even reverse this process of remodelling and consequent ventricular failure. The development is currently hindered as currently no reliable methods for monitoring of the mechanism and extent to which anti-cell death strategy induce tissue repair in need of methods for serial monitoring of the mechanism and extent to which anti-cell death strategy induce tissue repair. As a positive intracellular contrast agent, Mn^{2+} has positioned itself as an excellent marker of cell viability. The assessment of regeneration of tissue in the myocardium following stem cell therapy could be done using manganese-enhanced MRI. To date, there were two studies found where MEMRI is used as a confirmation of tissue restoration following stem cell therapy in a porcine ischemia-reperfusion model [98], [139]. Also, MEMRI could be used as an imaging biomarker to assess the effectiveness of pre- and post-conditioning therapy but is yet to be explored.

To take full advantages of MEMRI in future application of effectiveness of treatments (mechanical, pharmacological, and regenerative) and hence improvement in patient management, the technique requires further optimisation and validation so that MEMRI can be effectively used to assessment myocardial viability.

Chapter 2 : Quantifying the effects of manganese on cardiac function for optimal manganese-enhanced MRI

Manganese ions (Mn^{2+}) are positive MRI contrast agent that accumulate intracellularly and could be useful for measuring myocardial viability. However, because Mn^{2+} is a calcium analogue, there has always been a concern over Mn^{2+} cardiotoxicity, and this has limited the number of MEMRI studies conducted in the heart. The main objectives of this chapter are to investigate the effects of Mn^{2+} on cardiac function (cardiac contractility) using real-time ultrasound imaging and to characterise the effects of different Mn^{2+} formulations to achieve optimal image contrast. Working towards this aim, I tested different Mn^{2+}-based contrast agents using different approaches.

Abstract

Quantifying manganese-calcium interaction for optimal cardiac manganese-enhanced MRI

Introduction: Manganese ions (Mn^{2+}) are positive MRI contrast agent that can accumulate intracellularly. Mn^{2+} enters viable cardiomyocytes via Ca^{2+} channels and enhances intracellular T1 relaxation [96], allowing for assessment of cardiac physiology and function. As intracellular Ca^{2+} is a central regulator of cardiac contractility, high Mn^{2+} concentration can be cardiotoxic, causing negative cardiac inotropy [96], [112]. Mn-induced negative inotropy, however, could be avoided by confining the extracellular Mn^{2+} concentration to a low level [111]. Here, three different approaches that should overcome inotropy while still providing enhancement of viable myocardium have been tested: 1) calcium supplementation, 2) reduced manganese concentration, and 3) altered route of injection. The study aimed to investigate the effects of Mn^{2+} on cardiac function (cardiac contractility) and the effects of different Mn^{2+} administration methods to achieve optimal image contrast.

Methods and Materials: Seven groups with different contrast injections were tested; $MnCl_2$ high dose [0.1mM $MnCl_2$] and low dose [0.02mM $MnCl_2$], Calcium gluconate [0.1mM CaG], $MnCl_2$ supplemented with CaG [MnCaG 1:1], Mn^{2+} :Ca^{2+} 1:1 and [MnCaG 2:1] Mn^{2+} :Ca^{2+} 2:1 and Phosphate-Buffered Saline (PBS) were administered via intravenous injection. The same high dose $MnCl_2$ [0.1mM $MnCl_2$ (*i.p.*)] was also administered via intraperitoneally. Imaging was performed using VisualSonics Vevo 2100 in an adult male C57Bl/6 mice at baseline and up to 5 minutes post-contrast injection. MEMRI was then acquired at baseline, 10min, 30min, 60min and 24h post-injection in four groups [0.02mM $MnCl_2$], [MnCaG1:1], [MnCaG2:1], and [0.1mM $MnCl_2$ (*i.p.*)] using a 9.4T Agilent MRI and scanned using multi-inversion time Look-Locker sequence in the short-axis orientation as described [69], [74]. Next, to give a rough estimate of the actual Mn^{2+} concentration within the myocardium in vivo, data were compared with R1 values form $MnCl_2$ phantoms.

Results: Ultrasound showed an immediate and transient reduction of myocardial contractility after 0.02 and 0.1mM $MnCl_2$ *i.v.*, with contractility severely impaired at the higher dose (Figure 2.14, Figure 2.15 and Table 2.2). This depression was reduced when 0.1mM $MnCl_2$ was supplemented with 0.05mM CaG and reversed with 0.1mM CaG. Administration of CaG *i.v.* showed a transient increase in contractility, whilst PBS *i.v.* and 0.1mM $MnCl_2$ *i.p*. had no effect on contractility. Heart rate was immediately and transiently reduced after 0.1mM $MnCl_2$ i.v. but not significantly altered by any of the other treatments (Figure 2.16, Figure 2.17 and Table 2.3). Myocardial R1 calculated from T1 mapping MEMRI was significantly increased as soon as 10 min after administration. In animals that received *i.v.* injections, myocardial R1 was greatest at 10 min and reduced from 10 to 60 min, returning to baseline by 24h (Figure 2.22 and Table 2.4). In animals that received *i.p.* injection, maximal myocardial R1 was delayed to 60 min after injection and remained stable for 3h owing to the slow, sustained absorption of Mn^{2+} from the peritoneal cavity into the blood. An estimation of the concentration of Mn^{2+} within the myocardium was made from the in vivo images via a standard curve of $MnCl_2$ diluted in serum.

Discussion: The data presented here demonstrate that Mn^{2+} is a potent contrast agent that competes with Ca^{2+} to enter cardiomyocytes. Negative cardiac inotropy immediately after injection of high dose manganese is due to competitive binding of Mn^{2+} to Ca^{2+} channels in the extracellular space. At a later times, cardiac inotropy improves and returns to normal as blood washes out and dilutes the concentration of Mn. Importantly, Ca^{2+} supplements Mn^{2+} to overcome cardiac inotropy while still providing excellent enhancement of the viable myocardium.

Conclusion: This is the first study to quantify the real-time effect of Mn at various doses and formulation on cardiac function. Using both ultrasound imaging and MRI, we showed that Mn can safely be used and is a potent intracellular positive MRI contrast agent for the assessment of myocardial viability and is directly translatable to clinical practice.

2.1 Introduction

Manganese ions (Mn^{2+}) are positive MRI contrast agents that can actively accumulate intracellularly within viable myocytes and can thus act as functional contrast agents for measuring myocardial viability. Although manganese-enhanced MRI (MEMRI) has been used to image myocardial viability non-invasively, concerns over Mn^{2+} cardiotoxicity have limited the number of MEMRI studies conducted in the heart. Mn^{2+} enters viable cardiomyocytes via Ca^{2+} channels and enhances intracellular T1 relaxation. As Ca^{2+} is a central regulator of cardiac contractility, high Mn^{2+} concentration can be cardiotoxic. However, these effects can be counteracted by optimising Mn dose, calcium supplements and imaging technique. Understanding of the underlying manganese-calcium interaction is essential to produce optimal cardiac manganese-enhanced MRI. Hence, this chapter aimed to investigate the effects of Mn^{2+} on cardiac function (cardiac contractility) using real-time ultrasound imaging and to characterise the effects of different Mn2+ administration methods to achieve optimal image contrast.

To best interpret the experiments in this chapter, an understanding of Calcium handling in heart muscle and their cumulative roles in normal cardiac function is helpful and is discussed in Section, 2.1.1. An overview of Mn uptake by myocardial cells is discussed in section 2.1.2. Then Section 2.2 outlines the aims and objectives of the experiments in this chapter, followed by Section 2.3, which discusses experiments carried out to study the manganese-calcium interaction for optimal manganese-enhanced MRI. Finally, the results are presented in Section 2.4 and discussed in Section 2.5.

2.1.1 Calcium handling in heart muscle

Calcium ions enter cardiomyocytes via L-type calcium channels located in the myocardial cell surface membrane. L-type calcium channels are also rich in the t-tubules, close to the intracellular calcium store, the sarcoplasmic reticulum (SR) [140]. L-type Ca^{2+} channels are activated when the membrane potential reaches a threshold about -40 mV to -30 mV during the action potential [141]. L-type calcium channel activity is under autonomic control and can be influenced by positive and negative inotropic drugs [110], [115].

The opening of L-type calcium channels cause inward Ca^{2+} flow but is insufficient to trigger the contraction of myofibrils. The influx of Ca^{2+} increases cytosolic Ca^{2+} concentration which stimulates Ca^{2+} release from the SR through activation of the SR calcium release channel (Ryanodine receptors) (Figure 2.1). This mechanism is called calcium-induced calcium release (CICR), which triggers a much greater release of Ca^{2+} from the sarcoplasmic reticulum (SR). Large levels of intracellular Ca^{2+} interacts with Troponin C, leading to a conformational change in tropomyosin, exposing the active-binding sites on actin for the myosin head to interact and induces cross-bridge formation, producing a small contraction. The force of cardiac contraction is proportional to the number of cross-bridges formed, which depends on the Ca^{2+} inside myocytes. Each cycle of cross-bridge formation involves the hydrolysis of an ATP molecule. Cardiac muscle cells are continually contracting and require a substantial amount of energy from oxidative phosphorylation, and the myocytes thus contain large numbers of mitochondria. After contraction, Ca^{2+} must be rapidly cleared to allow relaxation of the muscle.

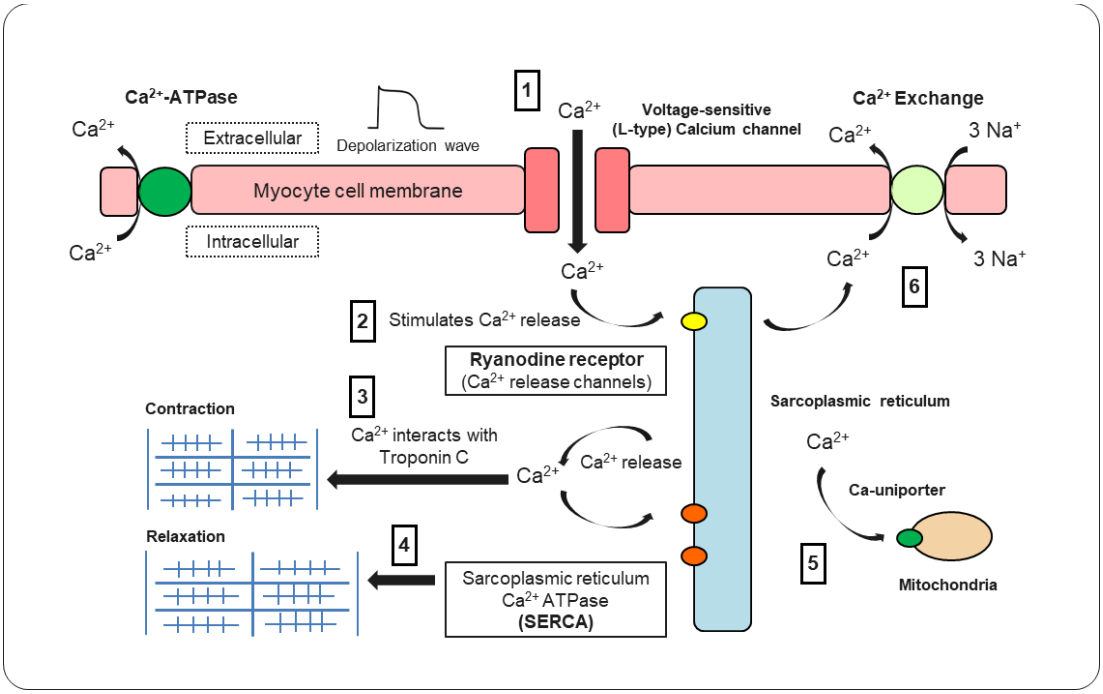

Figure 2.1: Calcium handling in heart muscle.

(1) L-type Ca^{2+} channels open during ventricular depolarisation phase in the plasma membrane. (2) Ca^{2+} induces Ca^{2+} release from SR. (3) Ca^{2+} binds to Troponin C, exposing myosin-binding sites. (4) Ca^{2+} actively transported back into the SR. (5) Ca^{2+} is actively transported to mitochondria via ca-uniporter before it is then released more slowly back into the cytosol to be dealt with by SERCA and plasma-membrane Ca^{2+}-ATPase. 6, Ca^{2+} is actively transported back to extracellular space.

During relaxation, some Ca^{2+} are transported back out of the cell and some replaced into the SR. Ca^{2+} is predominantly expelled from the myocytes via a $3Na^{+}$-Ca^{2+} exchanger (NCX) (Figure 2.1). A portion of the Ca^{2+} is actively expelled from the cell across the plasma membrane by Ca^{2+}-ATPases. ATP is also used to pump Ca^{2+} back into the SR stores. Other lower-level Ca^{2+} handling activities in the heart which account for low-level background current across the cell membrane include the mitochondrial Ca uniporter [142] before it is then released more slowly back into the cytosol to be dealt by SERCA and plasma-membrane Ca^{2+}-ATPase.

Ca^{2+} homeostasis plays a critical role in regulating cardiac contractility. In rats and mice, 90% of the increase in cytosolic Ca^{2+} during each cycle is derived from internal stores and less than 10% from the uptake of extracellular Ca^{2+} [143], [144]. Each of the Ca^{2+} handling activities in the heart is highly regulated to enable heart function at a wide range of demands. Each Ca^{2+} handling activities is a potential interaction site for Mn^{2+} and a potential route for influx and efflux of Mn^{2+} in the cell.

2.1.2 Manganese uptake by myocardial cells

Extracellular free Mn^{2+} is taken up by cardiac cells predominantly via the L-type Ca^{2+} channels. At the cell surface, Mn^{2+} competes effectively with Ca^{2+} due to high affinity to Ca^{2+} channel binding sites (Figure 2.2). Ochi et.al [145] showed that Mn^{2+} is a potent competitive inhibitor of Ca^{2+} and entered myocytes via L-type calcium channels [95], [96]. Addition of positive and negative inotropic drugs that are known to influence Ca^{2+} uptake by myocytes caused a similar alteration in Mn^{2+} uptake [96], [115]. Hunter et al. [96] showed that heart rate elevation, adrenergic stimulation, and decreased Ca^{2+} perfusate concentration caused an increase in Mn^{2+} uptake in perfused rat heart. In contrast, decreased Mn^{2+} uptake is driven by an increase in perfusate Ca^{2+} concentration and calcium channels blocker.

Unlike Ca^{2+} which rapidly redistributes intracellularly and extracellularly as previously described, Mn^{2+} is retained in the cardiomyocytes for several hours. There are three possible fates for Mn^{2+} once inside a cardiomyocyte, though it is not currently known which mechanism predominates. First, Mn^{2+} might accumulate intracellularly in the cytoplasm during each heartbeat in an additive fashion [115], [146] Secondly, Mn^{2+} could interact with Ca^{2+} binding sites and accumulate in protein-rich organelles such as sarcoplasmic reticulum through the Ca^{2+}-ATPase [113]. Thirdly, Mn^{2+} could be taken up by the mitochondria via Ca-uniporter [147] before it releases back into the cytoplasm and transported out with time from the cell via Na-Ca exchanger [99].

In addition, Mn^{2+} might also bind to the sodium-calcium exchanger (NCX) and thereby influence both influx and efflux of Ca^{2+} and Mn^{2+} as Ca^{2+} flux across the sarcolemma is bidirectional in a beat wise manner. A previous study showed stable Mn^{2+} accumulation in human myocardium after a single Mn-dipyridoxyl-diphosphate (MnDPDP) infusion up to 4 hours [103]. Atkins et al. (1979) also found only subtle changes in Mn content in the heart from 30 minutes up to 4 hours post-injection in rodents with approximately 30% remaining in the heart after 24 hours. Notably, the prolonged Mn^{2+} retention is most likely derived from the tight intracellular protein binding and not solely from low Mn^{2+} efflux. Importantly, the kinetics and accumulation of Mn^{2+} differ with different dosage post-injection, and types of contrast agent used. These theories are summarised in the schematic diagram in Figure 2.2.

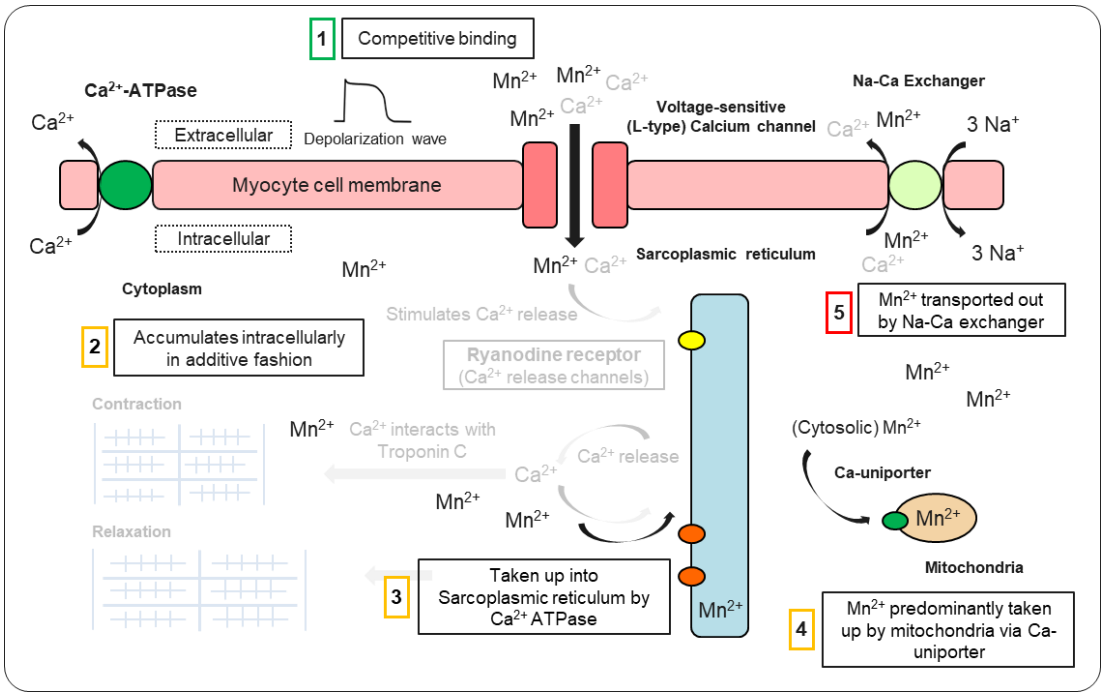

Figure 2.2: Manganese uptake by myocardial cells.

(1) Mn^{2+} enter cardiomyocytes via L-type calcium channels and is a competitive inhibitor of Ca^{2+}. (2) Mn^{2+} accumulates intracellularly in an additive fashion. (3) Mn^{2+} is taken up into SR by Ca^{2+} ATPase. (4) Mn^{2+} taken up by mitochondria via Ca-uniporter before it released back into the cytoplasm and transported out of the cell. (5) Mn^{2+} transported out by NCX and plasma-membrane Ca^{2+}-ATPase.

2.2 Chapter outline and aims

The main objective of the work in this chapter was to quantify the effects of manganese on the cardiac function for optimal manganese-enhanced MRI (MEMRI). Three studies were carried out to achieve the ultimate aim of this chapter.

Study One: Effects of Manganese and Manganese-Calcium contrast agents on cardiac physiology.

Investigate the effect of high dose manganese on cardiac function and implement three different approaches to overcome any toxicity observed, namely; calcium supplementation; reduced $MnCl_2$ concentration; and altered route of injection.

- In the first approach, calcium supplement was used to reduce the competitive binding to calcium channels on the cell membrane of the cardiomyocytes while maintaining the same manganese ion proportion in the formulation.
- The second approach used a lower concentration of $MnCl_2$ administered intravenously, thus reducing the concentration of Mn in the extracellular space of the myocardium.
- In the third approach, intraperitoneal manganese injection was used to induce the slow release of manganese ion in the extracellular space of the myocardium while maintaining the same Mn^{2+} concentration administered.

Study Two: Effects of different manganese administration approaches on MRI contrast

Test the effects of the four different manganese administration methods on the image contrast in MRI using quantitative longitudinal relaxation imaging (T1 mapping) over several hours after administration.

Study Three: Estimating manganese content in the heart

Perform in vitro measurements on phantoms of known manganese concentration to get an estimate of manganese content in the heart in vivo.

2.2.1 Study 1 – Effect of manganese contrast agents on cardiac physiology

Different strategies have been used to formulate the manganese-based contrast agents. The first attempt is to use a manganese chelate (MnDPDP) that allows the slow release of Mn^{2+}. MnDPDP and has been safely used in humans for MRI of the liver [148], pancreas and heart [103]. $MnCl_2$ releases Mn^{2+} much more rapidly than MnDPDP, allowing for more rapid uptake of the free manganese ions by myocytes, but it may cause more harmful effects on heart function due to direct competition with Ca^{2+}. However, this could be overcome through my first approach which is by using a calcium supplement that acts as "cardioprotective" to the Mn^{2+} salt such as the recently developed clinical grade contrast agent EVP 1001-1 [149], [150]. Finally, the cardiotoxicity effect of Mn could also be overcome by controlled intravenous infusion of $MnCl_2$ to avoid cardiac depression which is widely explored in animal studies [115], [151]. In some cases, an intraperitoneal injection is used instead to allow slow release of Mn into the heart [123], [126].

The concentration of $MnCl_2$ solution, the rate of infusion, the route of administration and the manganese formulations seem to play an important role in determining the maximum effective dose that can be safely administered without significant side effects. To date studies regarding the cardiotoxicity effects of manganese were based on looking at the changes in heart rate (HR) or left ventricular developed pressure (LVDP) observed in Langendorff perfused heart [152]–[154]. However, the direct effects on cardiac contractility have not been well explored in vivo. Therefore, the aim of this study is to investigate the direct effect of the three approaches of delivering manganese; calcium supplementation, reduced $MnCl_2$ concentration and altered route of injection on cardiac physiology using high-resolution real-time ultrasound.

2.2.2 Study 2 – Effects of manganese and manganese-calcium contrast agents on image contrast in MEMRI

Different manganese formulations could affect the influx and accumulation of Mn in the myocardium and hence affect the T1 relaxation. Improved safety may also, in theory, be at the expense of efficacy. Thus, the elevation of extracellular calcium (Ca) when using Ca supplement may impair the influx of Mn into cardiac cells, thus, reducing enhancement of the myocardium in MRI images. Quantitative magnetic resonance relaxometry can be used to determine the relaxation time constants. Quantitative tissue maps in vivo can be generated to also help distinguish the healthy tissue from pathology [155]. Tissue maps also serve a critical role in the characterisation of MRI contrast agents that shorten T1 relaxation time. Assuming all manganese is in a similar molecular environment, the amount of shortening in T1, and hence image contrast of nearby tissue, is proportional to the concentration of the contrast agent. Therefore, the aim of this study is to assess the effects of the different manganese administration methods on the image contrast in MRI using a quantitative T1 mapping over several hours after administration.

2.2.3 Study 3 – Estimating manganese content in the heart

To give a rough estimate of the actual Mn concentration within the myocardium in vivo, I compared in vivo R1 values with those of Mn phantoms made up across a range of Mn concentrations in saline. Some phantoms were made up in serum, to make the measurements more biologically relevant, whilst some were made in CaG, to identify any effects on R1 from the addition of the calcium supplement. Thus, the aim of this study is to perform in vitro measurements on phantoms of known manganese concentration to get an estimate of Mn^{2+} content in the heart in vivo.

2.3 Methods

2.3.1 Study 1 – Effect of Manganese contrast agents on cardiac physiology

2.3.1.1 Preparation of contrast agents and injection protocol

Six different solutions were prepared; manganese (II) chloride at high and low concentration, calcium gluconate, manganese with calcium supplement (calcium gluconate) in 1 to 1 and 2 to 1 ratio and PBS (Figure 2.3).

Manganese (II) chloride, 1.00 ± 0.01 M solution ($MnCl_2$) (Sigma Chemical Co., St. Louis, Mo.) was diluted in NaCl 0.9% solution to obtain a stock solution of 50mM. Two $MnCl_2$ dosages were used: 25mM $MnCl_2$ solution was produced from the stock solution for high dose intravenous injection [0.1mM $MnCl_2$] and intraperitoneal intravenous [0.1mM $MnCl_2$ (i.p.)], and 5mM $MnCl_2$ solution was produced from the stock solution for low dose intravenous injection [0.02mM $MnCl_2$] group.

Calcium-gluconate powder was dissolved in NaCl 0.9% solution to obtain a stock solution 50mM and diluted to 25mM depending on the experiments. 25mM calcium-gluconate solution used for the [0.1mM CaG] group. Calcium supplement was then mixed with $MnCl_2$ maintaining the same manganese ion (Mn^+) proportion in the solution. Two ratios of manganese-calcium contrast agents were used: 50 mM $MnCl_2$ was supplemented with 50 mM calcium-gluconate to produce 1:1 ratio [MnCaG1:1] and 50mM $MnCl_2$ supplemented with 25mM calcium-gluconate to produce 2:1 ratio [MnCaG2:1]. Phosphate buffered saline (PBS) were used as the control group. All solutions were administered with a volume of injection of 2 µL/gram body weight via intravenous injections and intraperitoneal injection.

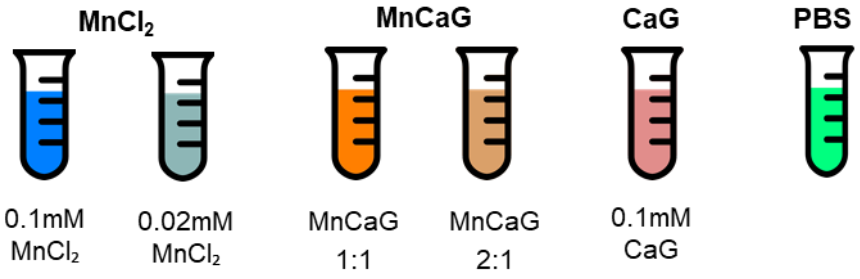

Figure 2.3: Preparation of contrast agents.

$MnCl_2$ (0.1mM and 0.02mM) and manganese supplemented with calcium-gluconate (MnCaG1:1 and MnCaG2:1), contrast agents. Calcium-gluconate and PBS with the same dosage (2 µL/gram body weight) were used as control.

2.3.1.2 Animal Preparation

Ultrasound imaging in this study was carried out on a VisualSonics Vevo 2100 (CA, USA) system (Figure 2.4) using a VisualSonics 550D 30 MHz transducer. Mice were anaesthetised with 1.5-2.0% isoflurane in 2 l/min O_2 and positioned supine (Figure 2.5) on a physiological monitoring platform which simultaneously regulated body temperature and measured respiratory and ECG traces. A small amount of coupling gel is placed on the copper leads on the platform and paws taped to them; this provides the ECG and respiratory physiology. A rectal probe is inserted to monitor the temperature of the animal during the imaging session. Any changes in cardiac physiology were recorded throughout the experiments. The mouse tail vein was cannulated for administration of Mn-based contrast agents. Prior to imaging, hair removal cream (Veet, UK) was applied to the chest to reduce attenuation of the ultrasound signal.

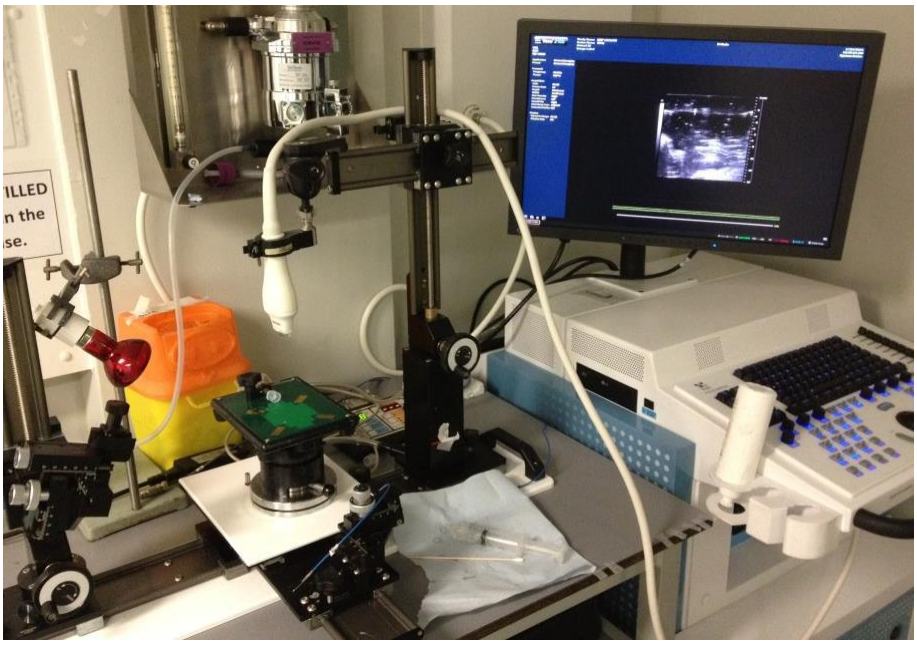

Figure 2.4: Ultrasound imaging system.

The VisualSonics Vevo 2100 ultrasound scanner in CABI showing the animal platform (green), ultrasound probe and hardware to control the system.

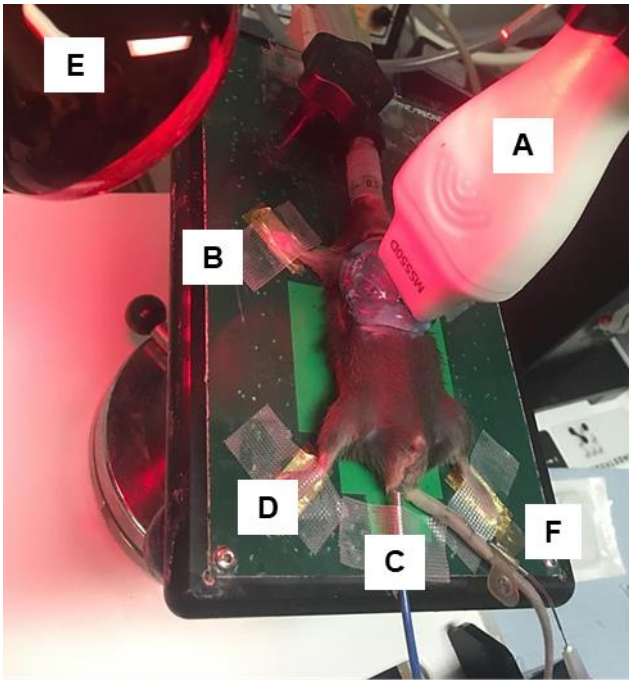

Figure 2.5: Animal preparation for ultrasound imaging.

Image showing the positioning of the 550D 30 MHz transducer on a mouse for ultrasound imaging. A: Ultrasound probe, B: Gel (on ECG pad), C: Temperature probe, D: ECG pad, E: Heat lamp and F: IV cannulation

2.3.1.3 Ultrasound Image Acquisition

The transducer was placed in a vertical fashion, with notch pointing towards the animals head. Then, the transducer was rotated approximately 35º counter-clockwise to get the parasternal long-axis view (PLAX) of the heart. From the PLAX view, parasternal short-axis view (PSAX) was obtained by rotating the probe 90º clockwise. Refer to Figure 2.6. Adult male C57BL/6 mice were used and real-time ultrasound images were acquired at baseline and immediately post-injection of several Mn-based contrast agents (Figure 2.7). To maintain the same anatomical positioning and to be able to acquire images at every 10 seconds, ultrasound images were acquired in PLAX view only at baseline and throughout the imaging up to 5 minutes post-injection. At the end of each experiment, three short-axis images were acquired at three different levels; basal, mid and apical and a PLAX view for Simpson measurement.

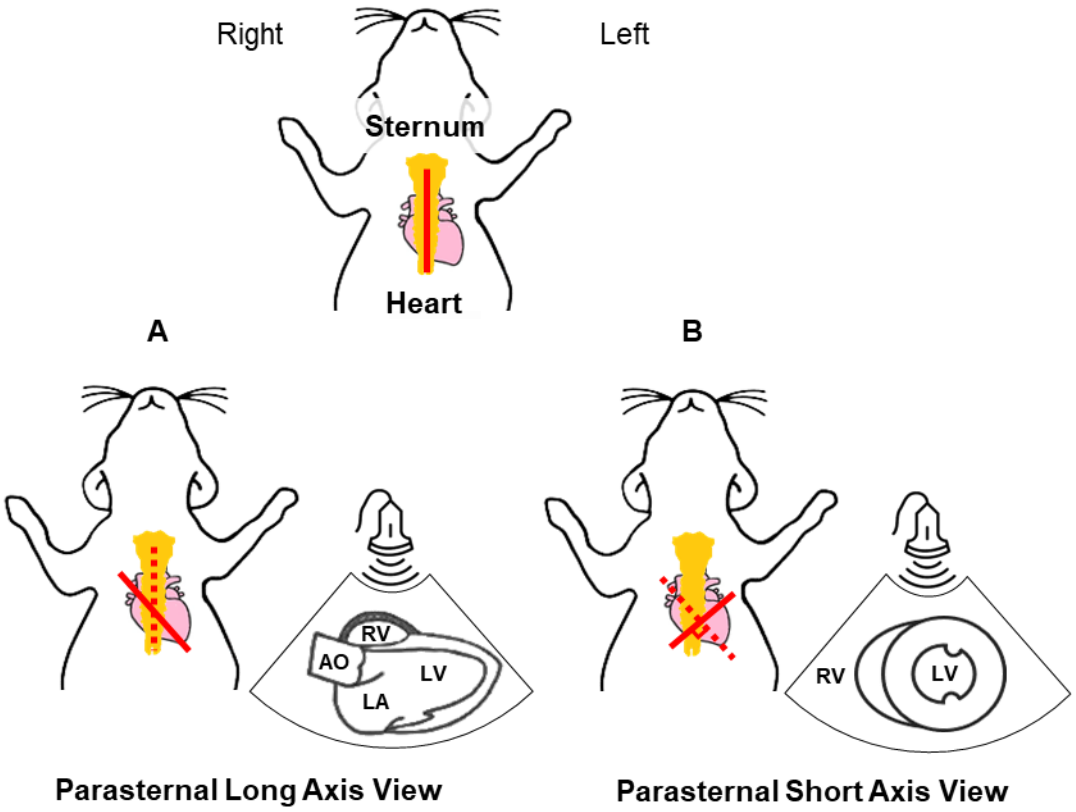

Figure 2.6: Diagrams showing two echo planes of the heart.

(A) Echo plane cut the heart in the parasternal long-axis view (PLAX) and (B) the parasternal short-axis view (PSAX) with the corresponding diagram of the heart at the right side. AO: Aorta, LA: Left atrium, LV: Left ventricle, RV: Right ventricle.

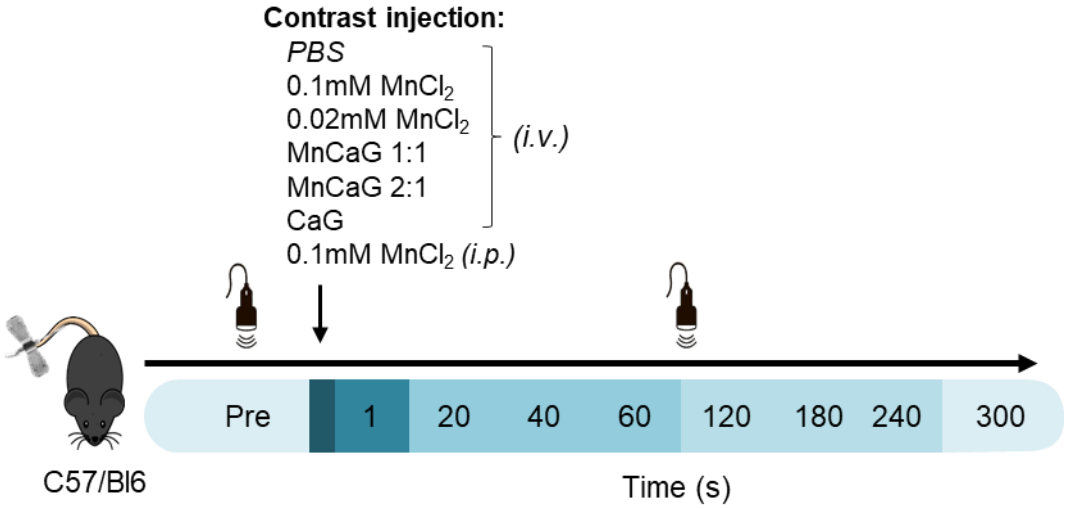

Figure 2.7: Schematic of ultrasound scanning.

Ultrasound imaging was initially performed at baseline, during the first minutes at every 20 seconds, then every 1min up to 5min post-injection of Mn-based contrast agents via a cannulated tail vein or intraperitoneal injection.

2.3.1.4 Ultrasound Image Analysis

Two analysis were performed: LV Fractional shortening from B-Mode and Simpson measurements to measure the ejection fraction (EF), diastolic volume, systolic volume and stroke volume (SV). Fractional shortening was used as a parameter that I observed throughout the 5 minutes infusion on Mn-based contrast agents while Simpson measurements were used to assess the overall cardiac function at baseline and post-injection of Mn-based contrast agents.

Fractional shortening was calculated as the percentage change in LV cavity dimensions during diastole and systole. I measured the end-diastolic diameter and end-systolic diameter to get the percentage change in the LV cavity (Figure 2.8). The baseline FS, when measured from direct 2-D measurement in B-Mode, is ~42 ± 6% [156].

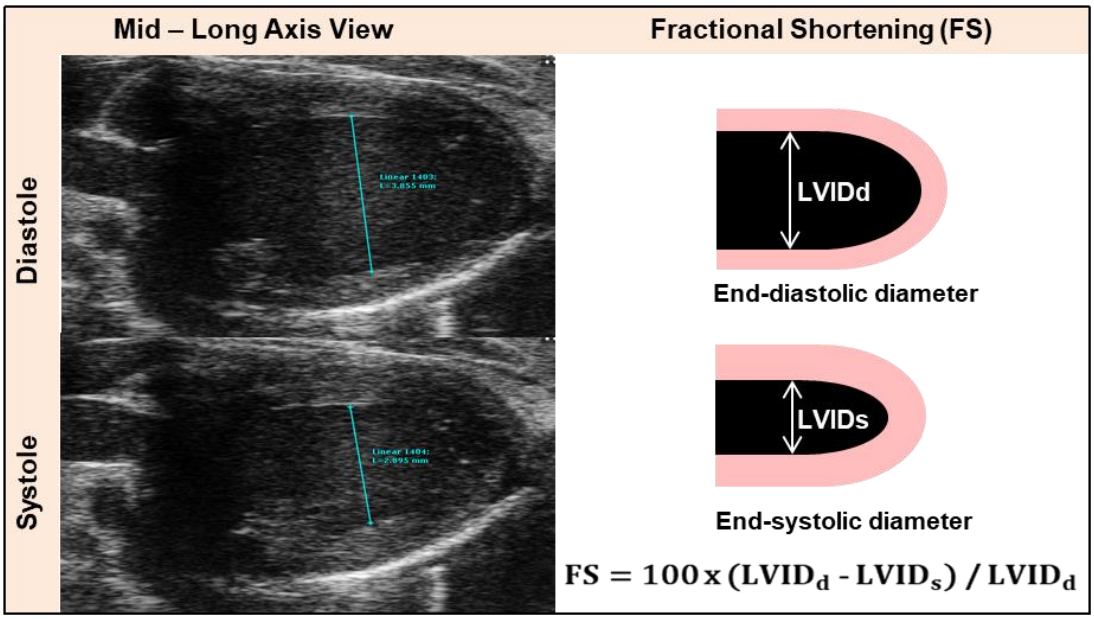

Figure 2.8: Ultrasound image analysis for fractional shortening (FS).

Fractional shortening is calculated by measuring the percentage change in left ventricular diameter during systole, for estimating systolic function In this study, FS was measured in parasternal long-axis view in B-mode, FS (%) = 100 X ($LVID_d$ - $LVID_s$)/$LVID_d$.

Simpson's method measures the LV at multiple planes at diastole and systole and yields calculations of LV diastolic and systolic and stroke volume (Figure 2.9 and Table 2.1). Three short-axis images were acquired at three different levels; basal, mid and apical. The endocardial border in diastole and systole were traced for each plane (Figure 2.10). A parasternal long-axis view was also acquired and measured the length from the aortic annulus to the endocardial border at the apex level in diastole and systole. Once the measurements were made, the available calculations are displayed in the calculation menu. Simpson's method is more accurate than 1D fractional shortening measurement but takes significantly longer to acquire because multiple planes need to be acquired.

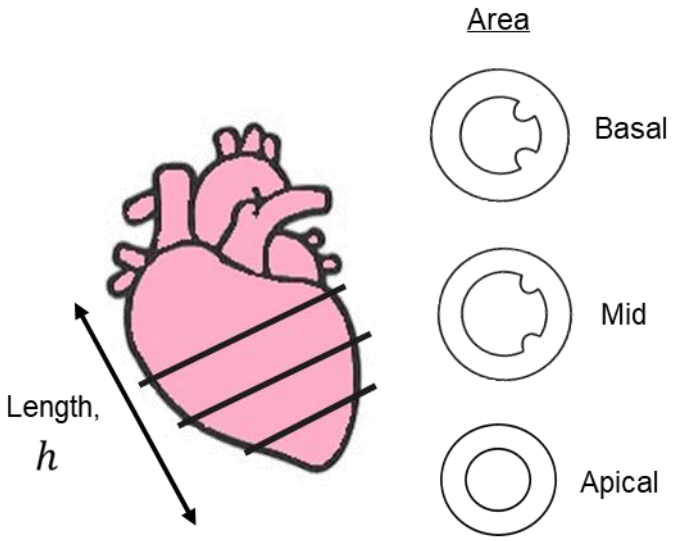

$$\mathrm{V} = \left(\frac{A_{basal} + A_{mid}}{2}\right)\frac{h}{3} + \left(\frac{A_{mid} + A_{apical}}{2}\right)\frac{h}{3} + \frac{1}{3}A_3 \cdot \frac{h}{3}$$

$$EF = \left(\frac{V_{diastole} + V_{systole}}{V_{diastole}}\right)$$

Figure 2.9: Simpson's measurement.

Simpson's method measures the LV at three planes during diastole and systole. Short axis views were acquired at basal, mid and apical plane during diastole and systole. A long axis view was also acquired at diastole and systole.

Table 2-1: Simpson's Calculation

Name	Descriptions	Units	Formula
Simp Volume; d	Simpson's volume calculation in diastole	µl	$V = \left(\frac{A_{basal} + A_{mid}}{2}\right)\frac{h}{3} + \left(\frac{A_{mid} + A_{apical}}{2}\right)\frac{h}{3} + \frac{1}{3}A_3 \cdot \frac{h}{3}$ Where: h = Simpson Length in diastole
Simp Volume; s	Simpson's volume calculation in systole	µl	$V = \left(\frac{A_{basal} + A_{mid}}{2}\right)\frac{h}{3} + \left(\frac{A_{mid} + A_{apical}}{2}\right)\frac{h}{3} + \frac{1}{3}A_3 \cdot \frac{h}{3}$ Where: h = Simpson Length in systole
Simp SV	Stroke Volume	µl	Simp Volume; d – Simp Volume; s
Simp %EF	Ejection Fraction	%	100 * Simp SV / Simp Volume; d 100 * Simp Volume; d - Simp Volume; s / Simp Volume; d
Simp CO	Cardiac Output	ml/min	Simp SV * Heart Rate

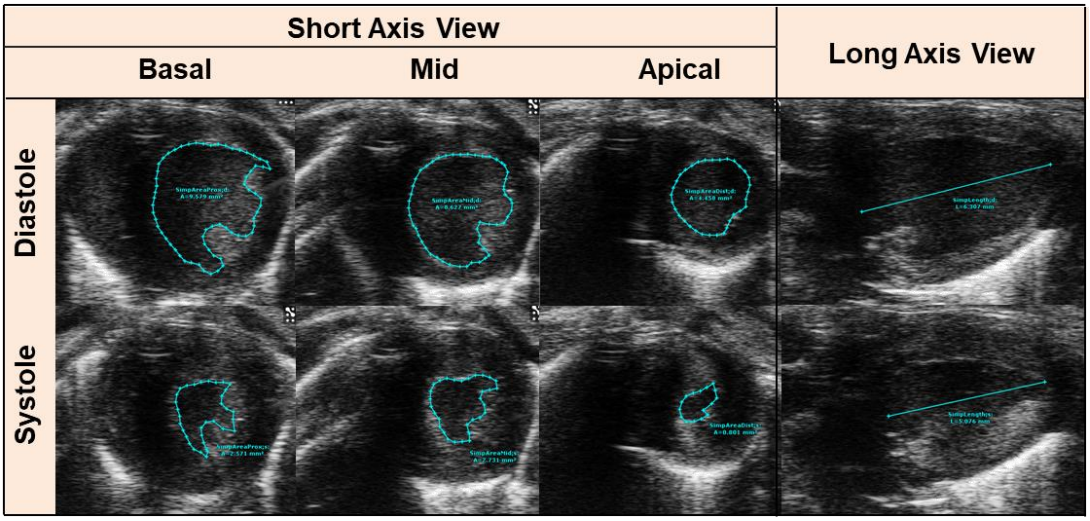

Figure 2.10: Views required to perform Simpson's measurement.

2.3.2 Study 2 – Effect of manganese and manganese-calcium contrast agents on image contrast in MEMRI

Study 2 consisted of two parts; parameter optimisation and myocardial enhancement in manganese-enhanced MRI (MEMRI). In the first part, T1 mapping was performed in Mn phantoms made up across a range of Mn concentration in saline. In the second part, the optimised parameters were used to acquire T1 mapping following injections of 4 manganese-based contrast agents; MnCaG1:1, MnCaG2:1, 0.02mM $MnCl_2$, and 0.1mM $MnCl_2$ (*i.p.*) in in vivo healthy mice.

2.3.2.1 Parameter optimisation (T1 mapping) – Phantom studies

Mn phantoms consisted of $MnCl_2$ in saline at various concentrations ranging from 50 to 1000µM and were used to optimise the acquisition parameters in T1 mapping further. T1 mapping was performed using a 9.4T MRI system (Agilent Technologies, Santa Clara, USA) equipped with 1000mT/m gradient inserts and a 39mm volume resonator RF coil (RAPID Biomedical, Rimpar, Germany). T1 mapping was acquired using the standard Look-Locker (LL) inversion recovery sequence developed by Look and Locker [65] and previously used in this lab [74], [157], [158] and described in Section 1.3.2.3.

The T1 mapping sequence and parameters has been well studied and establised in my labolatory. However, the ultimate aim of my thesis is to developed an imaging methods for early phase of ischemic injury, a higher image resolution and shorter scan time is needed while still maintaining the accuracy of T1 measurements. Sampling flip angle (FA) and time to repeat inversion (effective TR) are the two important parameters that has significant effects on the image resolution and scan time respectively. Thus, to further optimise the T1 mapping acquisition for MEMRI, a number of different sampling FA and effective TR were tested.

A higher image resolution could be achieved with a higher sampling FA but may compromised the accuracy of T1 measurements. To evaluate the effect of changing FA on T1 measurements, T1 mapping was performed using sampling FA 15º and 20º and were compared to the sampling FA = 10º (the established parameters used in the lab), the reference standard for this study. A shorter scanning time could be achieved by reducing the eTR. However, a shorter eTR would caused saturated signal and hence inaccurate T1 values. In small animal cardiac imaging, eTR is dependent on the number of inversion times collected and inversion recovery delay (the time from the last sampling to the next global inversion). Here I tested two different eTR, ~7s (long) and ~4s (short) which can be achieved by varying the number of inversions (40 and 18 respectively) or using 18 inversions with increasing inversion recovery (IR) delay to get eTR ~7s. The eTR was chosen to allow acquisition at least five times of T1 (~7s for baseline and ~4s for post-contrast imaging). Other acquisition parameters were as follows: TE = 0.99ms, FOV = 25.6 x 25.6 mm, matrix size = 128 x 128, and slice thickness = 1.5 mm. TI was set in the interval of 100ms (the average RR time in mouse heart). 40 inversions have TI range between 100-4000ms, and 18 inversions have TI between 100-1800ms, which results in an eTR of ~7s and ~4s respectively. Typical values for these parameters result in total acquisition time around ~15 minutes and ~8 minutes respectively for a single slice.

2.3.2.2 Longitudinal relaxation (T1) fitting

T1 mapping resulted in an image sequence where signal intensity could be modelled by a 3-component model, as shown in equation 2.1.

$$S(TI) = S_0(1 - Be^{-TI/T1^*}) + [C] \quad \text{[Equation 2.1]}$$

Where TI is the time following the radiofrequency lock-locker inversion pulse, B is fitted parameter to account for imperfect inversion and $T1^*$ is the apparent T1 under the influence of lock-locker saturation. This saturated recovery can be accounted for when fitting the T1 recovery curve by applying the look-locker correction factor as derived by Deichmann et al. (1992). This is corrected by the correction factor (equation 2.2)

$$T1 = (B - 1)\, T1^* \quad \text{[Equation 2.2]}$$

T1 maps were generated by performing pixel-wise curve fitting as described above using in house Matlab optimisation code written by Dr Laurence Jackson (2016b, The Mathworks, Inc., Natick, USA) based on the Nelder-Mead Simplex Method [68].

2.3.2.3 MRI animal preparation

Manganese-enhanced MRI experiments were performed in adult male C57BL/6 mice (14 weeks old, mean ± SD weight 28 ± 3.3 g) following the guidelines of the UK Home Office and local animal care and welfare committees. Mice were placed supine in a cradle, which could be positioned in the centre of the MRI scanner bore (Figure 2.11). For artefact-free cardiac images, animal physiology must be monitored, and MRI pulse sequences must be 'gated' or 'triggered' according to the recorded physiological traces. A gated acquisition is one in which specific components of a pulse sequence, such as an RF pulse or gradient waveform, are synchronised to occur in time with a physiological event, such as the QRS complex of an ECG trace. A small animal physiological monitoring system (SA Instruments, Stony Brook, NY) was used to maintain the depth of anaesthesia and animal physiology throughout the MRI session.

In pre-clinical imaging, the ECG trace was recorded using 3-lead subcutaneous electrodes, respiration rate was measured using a neonatal apnoea pad taped to the abdomen of the mouse, and internal temperature was measured using a rectal probe. The temperature was regulated using a hot water system which pumped the water through tubes placed on top of the animal. Body temperature and anaesthesia dose should also be monitored to keep the animal physiologically stable throughout the duration of the imaging session. Moreover, body temperature affects heart rate and parameters of cardiac function, and in turn gating, therefore it should be maintained at between 36.5-37°C for a consistent heart rate. Similarly, anaesthetic has a large impact on respiratory rate. Therefore, a constant dosage should be maintained as far as possible. In this study, animals were anaesthetised under a mixture of 1–2% isoflurane in oxygen.

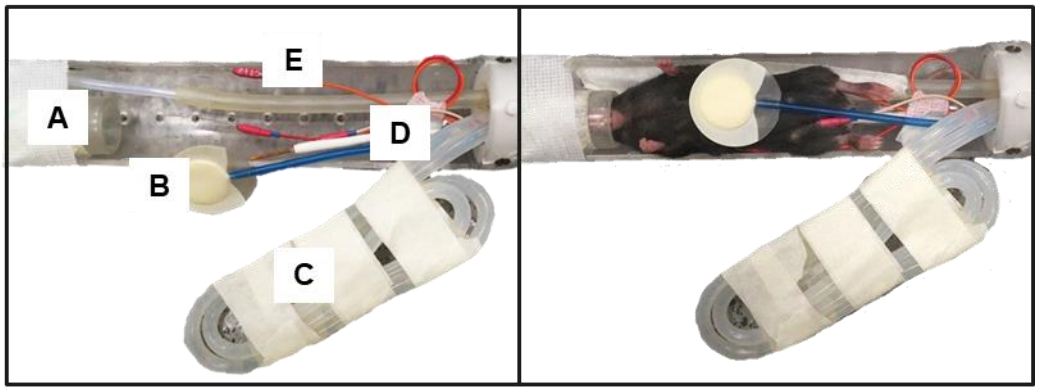

Figure 2.11: Animal cradles used for imaging mice in the MRI scanner.
A: anaesthetic nose cone, B: heated water tubes, C: rectal temperature probe, D: respiration pad, E: three-lead subcutaneous ECG elect.

2.3.2.4 T1 mapping MEMRI - image acquisition and analysis

When the animal is placed in an MRI scanner, the heart lies obliquely in the chest relative to the imaging gradients. Therefore, cardiac imaging initially requires the acquisition of pilot scans to determine cardiac axes accurately. Initially, axial and longitudinal scout images were acquired to plan the 2-chamber long-axis view. A 4-chamber long-axis view was then acquired perpendicular to the 2-chamber orientation, after which a series of short-axis images were obtained perpendicular to the LV long-axis from the 2- and 4- chamber images. In this study, I acquired images at baseline, at 10min up to 60min and 24h post-injection (Figure 2.12).

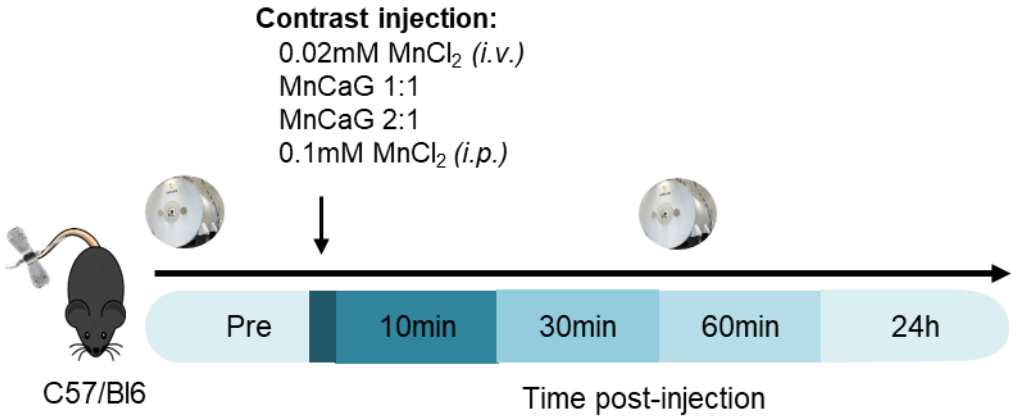

Figure 2.12: Schematic of MRI image acquisition protocol.
MRI scanning was performed at baseline, 10min, 30min, 60min, and 24h post-injection of Mn-based contrast agents via intravenous or intraperitoneal injection.

Cardiac T1 mapping using Look-Locker (LL) Inversion Recovery sequence for quantitative assessment of T1 relaxation described in the previous section. In this study, I acquired 18 short-axis gradient-echo images with the following parameters: TE = 0.99ms, TR_{ir} = ~4s, TI = ~100-1800ms (depending on the heart rate), FOV = 25.6 x 25.6 mm, matrix size = 128 x 128, flip angle = 20º, and slice thickness = 1.5 mm. Typical values for these parameters result in an acquisition time around ~8 minutes for single slice depending on the heart rate. Imaging parameters used in this study was as previously optimised.

T1 mapping of the myocardium is a parametric reconstructed image, where each pixel intensity directly corresponds to the T1 relaxation time of the corresponding myocardial voxel. Due to the long sampling time for T1 decay the acquisition was acquired over respirations, images corrupted with respiration motion were automatically excluded from fitting using the phase-encoded noise-based image rejection scheme [159]. T1 maps were generated by performing pixel-wise curve fitting as described above using in house Matlab optimisation code written by Dr Laurence Jackson (2016b, The Mathworks, Inc., Natick, USA) based on the Nelder-Mead Simplex Method [68]. The myocardium, blood pool regions, liver and muscles T1 were segmented from T1 maps to calculate the mean T1 value (Figure 2.13). The relaxation rate, the R1 value is calculated as $R1 = 1/T1$.

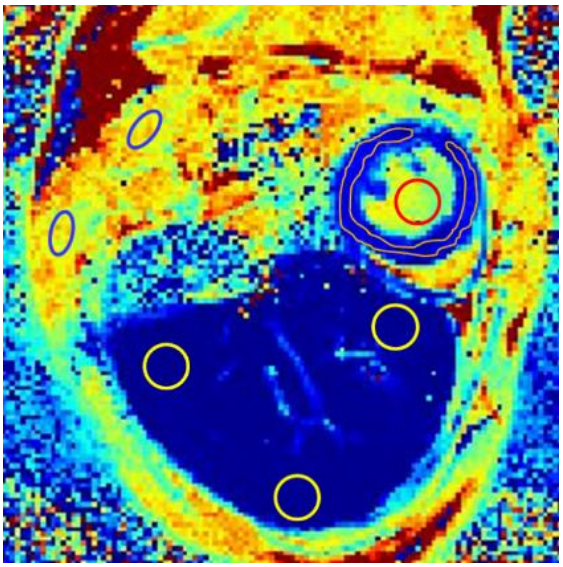

Figure 2.13: Representative ROIs segmented from T1 maps.
Red, Blood pool region; Orange, Myocardium; Blue, Muscle; and Yellow, Liver. Liver regions were drawn to minimise the contribution from major blood vessels.

2.3.3 Study 3 – Estimating manganese content in the heart

2.3.3.1 Manganese phantom study

$MnCl_2$ solutions with concentrations of 0, 50, 100, 150, 200, 250, 300, 350, 400, 500, 550 and 1000 µM were made up in 0.9% NaCl in Eppendorf tubes. Some phantoms were made up in serum, to make the measurements more biologically relevant, whilst some were made in a ratio of 1:1 and 2:1 with calcium gluconate. This is to identify any effects on R1 from the addition of the Ca supplement. All phantoms were scanned using quantitative T1 mapping in which the imaging parameters were chosen to match the imaging parameter used in the in-vivo study in Study 2 to enable a direct comparison of the results to give an idea on Mn content in the heart. The analysis was done as described in the previous sections (Section 2.3.2.4).

2.3.3.2 Relaxivity

Relaxivity (r) is another parameter that describes the effectiveness of the contrast agent to reduce T_1 and T_2 as a function of the concentration [160]–[162]. The relaxation times in the presence of contrast agents can be approximated by:

$$R_i = \left(\frac{1}{T_{i\,,obs}}\right) = \left(\frac{1}{T_i}\right) + \left(\frac{1}{T_{i,p}}\right).C$$

Where $\left(\frac{1}{T_{i\,,obs}}\right)$ is the observed relaxation rate constant (R_i) in the presence of a paramagnetic species, and $\left(\frac{1}{T_i}\right)$ is the relaxation rate constant in the absence of a paramagnetic species. $\left(\frac{1}{T_{i,p}}\right)$ represents the additional paramagnetic contribution (saline in this study).

In the absence of solute-solute interactions, the solvent relaxation rate constants are linearly dependent on the concentration of the paramagnetic contrast agent (C).

$$R_{i,obs} = R_i + r_i\,.[C]$$

r_i is the relaxivity defined as the slope of the dependence in units of $(s\ mM)^{-1}$ for in vitro experiments [95], [163], [164].

2.3.4 Statistical tests

All results are presented as mean value ± standard error mean (SEM). Data were analysed using two-way ANOVA, one-way ANOVA and linear regression analysis. In all cases, a p-value of less than 0.05 was considered significant. All statistical analysis was performed using Graphpad Prism software version 8.0. One-way ANOVA was used to measure one independent variable in more than two groups (first part in Study 1 and Study 2 and Study 3) with Tukey's multiple comparisons test to compare each group to every other group. At the same time, two-way ANOVA was used to measure the effects of two independent variables (the second part of Study 1 and Study 2) with Dunnet's multiple comparisons test to compare each group to a control group (baseline). Repeated measures analysis was performed for data measured at a different time point in the same group (Study 1 and Study 2).

- Study 1: Fractional shortening and heart rate were compared between group ($MnCl_2$ 0.1mM, $MnCl_2$ 0.02mM, MnCaG1:1, MnCaG2:1, CaG 0.1mM, PBS and $MnCl_2$ 0.1mM *i.p.*) at each time point (baseline, 1s, 20s, 40s, 1min, 2min, 3min, 4min and 5min) by one-way ANOVA Tukey's multiple comparison test and in each group, data were compared to baseline by repeated measure two-way ANOVA with Dunnett's multiple comparisons.
- Study 2: Data were analysed between group ($MnCl_2$ 0.02mM, MnCaG1:1, MnCaG2:1, and $MnCl_2$ 0.1mM *i.p.*) in each region (myocardium, blood, muscle and liver) by one-way ANOVA Tukey's multiple comparison test and data were compared to baseline in each group in each region by repeated measures two-way ANOVA with Dunnett's multiple comparisons.
- Study 3: Linear regression analysis was performed to find the correlation between R1 (s^{-1}) with a concentration of $MnCl_2$. The difference in the estimated manganese concentrations in each region (liver, myocardium, blood and muscle) at 10min, 30min, 60min and 24h post-manganese-based contrast agents injections (0.02mM $MnCl_2$, MnCaG1:1, MnCaG2:1, and $MnCl_2$ 0.1mM *i.p.)* were analysed by one-way ANOVA with Tukey's multiple comparison test.

2.4 Results

2.4.1 Study 1 – Effects of manganese contrast agents on cardiac physiology

2.4.1.1 Cardiac contractility

Fractional shortening (FS) was used as the parameter to measure changes in cardiac contractility following injections of different manganese-based contrast agents as it permitted rapid data acquisition and analysis. FS measurements were made at baseline and every 10s up to 1min and then every minute up to 5min post-injection of seven different solutions – 0.1mM $MnCl_2$, 0.1mM CaG, MnCaG1:1, MnCaG2:1, 0.02mM $MnCl_2$, 0.1mM $MnCl_2$ (*i.p.*), and PBS. Figure 2.14 shows the mean ± SEM of all seven groups, while Figure 2.15 shows the FS in each group with (*) marked the significant difference of FS post-injection as compared to baseline.

Figure 2.14 shows a drastic and significant FS reduction with high dose Mn (0.1mM $MnCl_2$) (0.1 mmol/kg) during the first 1 minutes with a maximal FS depression is 1.29 ± 0.5% ($p<0.001$) at 20s post-injection as compared to baseline (38.21 ± 2.5%). FS then gradually returned to the baseline. In contrast, in the CaG group, the graph shows a sharp increase in FS with maximal elevation reached 56.65 ± 3.7% ($p<0.001$) immediately post-injection as compared to baseline (40.75 ± 2.7%). Fractional shortening remained slightly elevated for up to 1min post-injection as compared to baseline (Figure 2.15 and Table 2.2). These data show that as expected, manganese induced a transient negative cardiac inotropy while administration of calcium-gluconate induced positive cardiac inotropy.

In the $MnCaG_{1:1}$ group, where the same amount of Mn^{2+} was administered but with Ca^{2+} supplement, the graph shows a steady increased in FS for 1 minute and gradually returned to baseline. Maximal FS elevation of 53.94 ± 2.8% ($p<0.05$) at 40s post-injection as compared to baseline (38.55 ± 2.3%). Conversely, in the MnCaG2:1 group, slightly decreased FS was seen with maximal depression of 23.59 ± 7.5% at 10s post-injection, followed by a delayed increase in FS at 50s up to 5min post-injection with a maximal elevation of 51.04 ± 3.6% ($p<0.05$) at 1min post-injection as compared to baseline (38.70 ± 2.3%). It can be inferred that the correct titration of calcium supplement could overcome the negative inotropic effect of manganese.

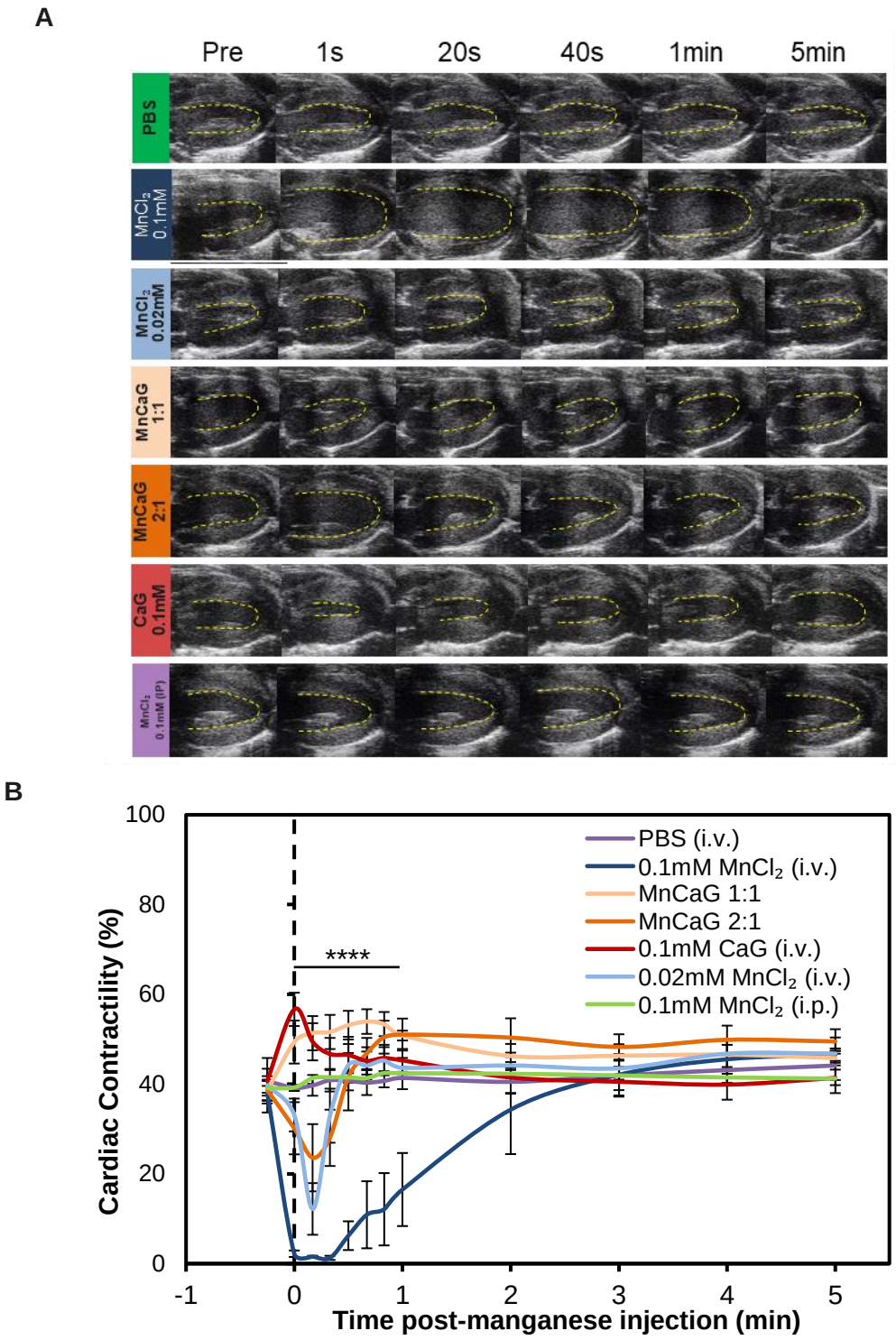

Figure 2.14: Effect of manganese on cardiac function.

*(A) Representative systolic ultrasound images acquired before and after injection of the compounds indicated. (B) Time course of myocardial contractility quantified as fractional shortening showed immediate reduction in myocardial contractility after i.v. infusion of 0.1mM $MnCl_2$ (n=6) which can be reversed when Mn is supplemented with CaG (MnCaG) at either 1:1 and 2:1 ratio (n=6). Mean value ± standard error mean (SEM). Data were compared between group at each time point by one-way ANOVA (****p<0.0001) and compared to baseline for each group by repeated measure one-way ANOVA (Figure 2.15). Each point represents the mean ± SEM value. Raw data is presented in Table 2-2.*

In the 0.02mM $MnCl_2$ group (0.02 mmol/kg), Mn concentration was five times lower than in the 0.1mM MnCl2 group. FS depression was seen during the first 20 seconds only before it immediately returned to baseline. The maximal FS depression of approximately 2.19 ± 5.8% ($p<0.001$) at 10-seconds post-injection as compared to baseline (39.75 ± 6.1%). These data show that reducing Mn concentration could reduce cardiotoxicity effects. However, reducing Mn concentration in turn, also reducing the contrast enhancement in MR image. This effect is described in Study 2.

No change in FS was seen in 0.1mM $MnCl_2$ (*i.p.*) throughout the 5 minutes duration. It is known that intraperitoneal injection induced more slow released in the body. Similarly, no change in FS is seen in the PBS group. This shows that intraperitoneal injection the volume injected intravenously had no effect in cardiac contractility.

Normalisation of FS was complete in all group except for the manganese-calcium groups, MnCaG1:1 and MnCaG2:1 during the 5 minutes duration. Measurements for each group are shown in Figure 2.15 and tabulated in Table 2.2.

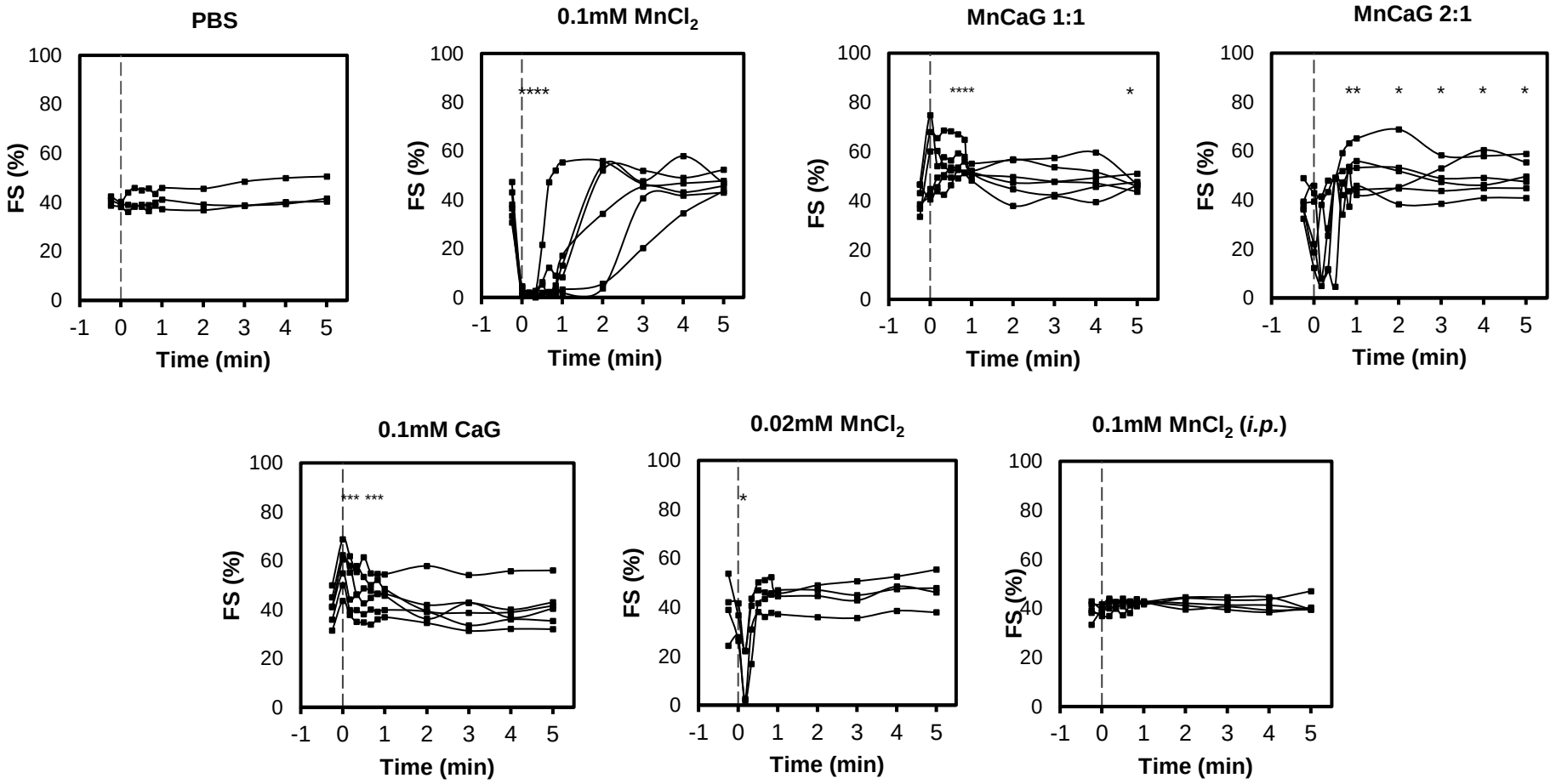

Figure 2.15: The effect of manganese-based contrast agents on cardiac contractility.

Cardiac contractility was measured as percentage of fractional shortening at baseline, 1s, 20s, 40s, 1min, 2min, 3min, 4min, and 5min post-injection. Note that (*) shows significant differences at the time points post manganese injection as compared to baseline in each group (Table 2-2 for p value). in each group, data were analysed by two-way ANOVA with Dunnet's multiple comparison test.

Table 2-2: Fractional shortening manganese contrast agents at different formulation.

Time (s)	PBS (n=3)	0.1mM $MnCl_2$ (n=6)	MnCaG 1:1 (n=6)	MnCaG 2:1 (n=6)	0.1mM CaG (n=6)	0.02mM $MnCl_2$ (n=4)	0.1mM $MnCl_2$ (*i.p.*) (n=5)
Pre	(n=3)	38.21 ± 2.5	38.55 ± 2.3	38.70 ± 2.3	40.75 ± 2.7	39.75 ± 6.1	39.08 ± 1.7
0	40.69 ± 1.1	2.21 ± 0.7‡	49.37 ± 4.8	30.17 ± 5.8	56.65 ± 3.7‡	33.13 ± 3.7	39.27 ± 0.8
10	39.19 ± 0.6	1.57 ± 0.2‡	51.35 ± 3.8	23.59 ± 7.5	49.43 ± 4.1*	12.19 ± 5.8*	41.35 ± 1.3
20	39.72 ± 2.3	1.29 ± 0.5‡	51.62 ± 3.8	28.03 ± 6.3	46.71 ± 3.6*	32.96 ± 6.0	41.51 ± 0.5
30	40.86 ± 2.5	6.23 ± 3.2†	53.14 ± 3.2*	41.54 ± 7.4	46.48 ± 4.1	44.22 ± 2.7	41.49 ± 1.2
40	40.71 ± 2.1	10.89 ± 7.5	53.94 ± 2.8*	46.81 ± 3.5	45.18 ± 3.0†	44.13 ± 3.1	41.34 ± 0.8
50	40.33 ± 2.8	12.12 ± 8.1	53.37 ± 2.7†	50.46 ± 3.7*	45.82 ± 2.9†	45.27 ± 3.0	42.47 ± 0.5
60	40.71 ± 1.4	16.51 ± 8.1	50.81 ± 1.1†	51.04 ± 3.6*	45.29 ± 2.5‡	43.62 ± 2.2	42.41 ± 0.2
120	41.38 ± 2.5	34.30 ± 9.9	46.26 ± 2.7	50.35 ± 4.3*	41.48 ± 3.4	44.15 ± 2.9	42.31 ± 0.9
180	40.51 ± 2.6	42.08 ± 4.6	46.33 ± 2.5	48.28 ± 2.8†	40.54 ± 3.3	43.52 ± 3.1	41.93 ± 0.9
240	41.94 ± 3.3	45.54 ± 3.2	46.57 ± 3.2	49.88 ± 3.2*	39.89 ± 3.4	46.76 ± 3.0	41.49 ± 1.2
300	43.13 ± 3.4	46.56 ± 1.4	45.80 ± 1.6*	49.50 ± 2.7†	41.38 ± 3.4	46.81 ± 3.6	41.23 ± 1.5

Values represent mean ± SEM. $MnCl_2$, manganese(II) chloride; MnCaG1:1, manganese to calcium-gluconate ratio (1:1); MnCaG2:1, manganese to calcium-gluconate ratio (2:1); CaG, calcium-gluconate; PBS, Phosphate-buffered saline; i.p., intraperitoneal injection. Data were analysed using paired one-way ANOVA. Boxes marked red and green indicates cardiac contractility below and above the normal level, respectively. *P<0.05, †P<0.01, ‡P<0.001 as compared to baseline (pre).

2.4.1.2 Heart rate

Using the physiological monitoring system on the ultrasound, heart rate (HR) measurements were made throughout the above imaging study at baseline and every 10s up to 1min and then every minute up to 5min post-injection of seven different solutions – 0.1mM $MnCl_2$, CaG, MnCaG1:1, MnCaG2:1, 0.02mM $MnCl_2$, 0.1mM $MnCl_2$ (*i.p.*), and PBS. Changes in HR were only seen in the high dose Mn group (0.1mM $MnCl_2$). Figure 2.16 shows a slight decreased in HR during the first 1 minutes and returned to baseline. No changes in HR were observed in the other 6 groups. This shows that calcium supplement and low Mn concentration had no effect on HR. Measurements for each group are shown in Figure 2.17 and tabulated in Table 2.3.

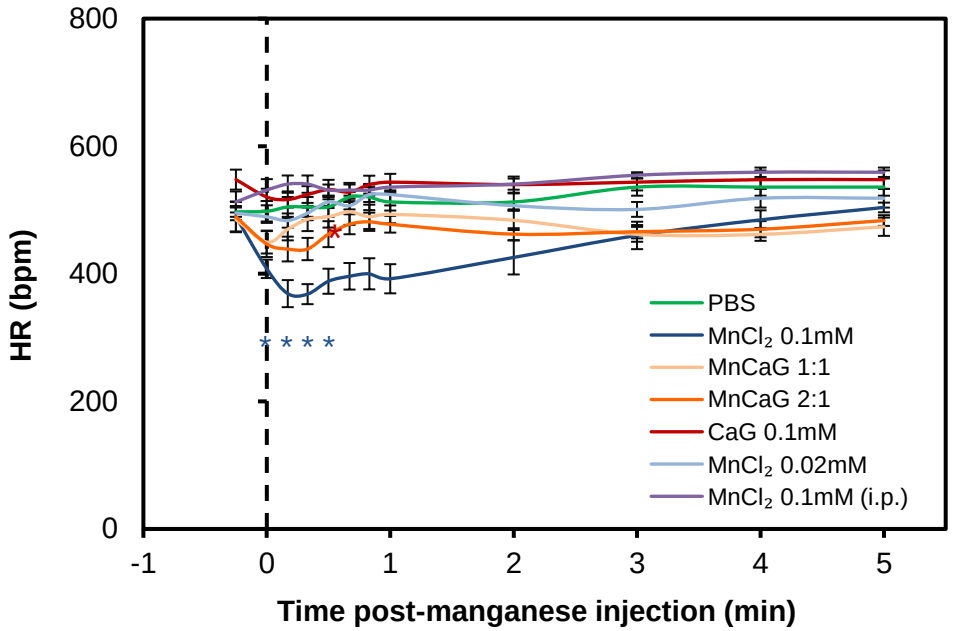

Figure 2.16: The effects of manganese on mouse heart rate.

*Heart rate taken from physiological data recorded during ultrasound showed significant reduction after i.v. infusion of 0.1mM MnCl2 (n=6) during the first 30 seconds, which could be reversed by supplemented with CaG (n=6). Mean value ± standard error mean (SEM). Data were compared to baseline by repeated measure one-way ANOVA (*p<0.05) (Figure 2.17 for p-value). Data were also analysed by unpaired t-test Raw data is presented in Table 2-3.*

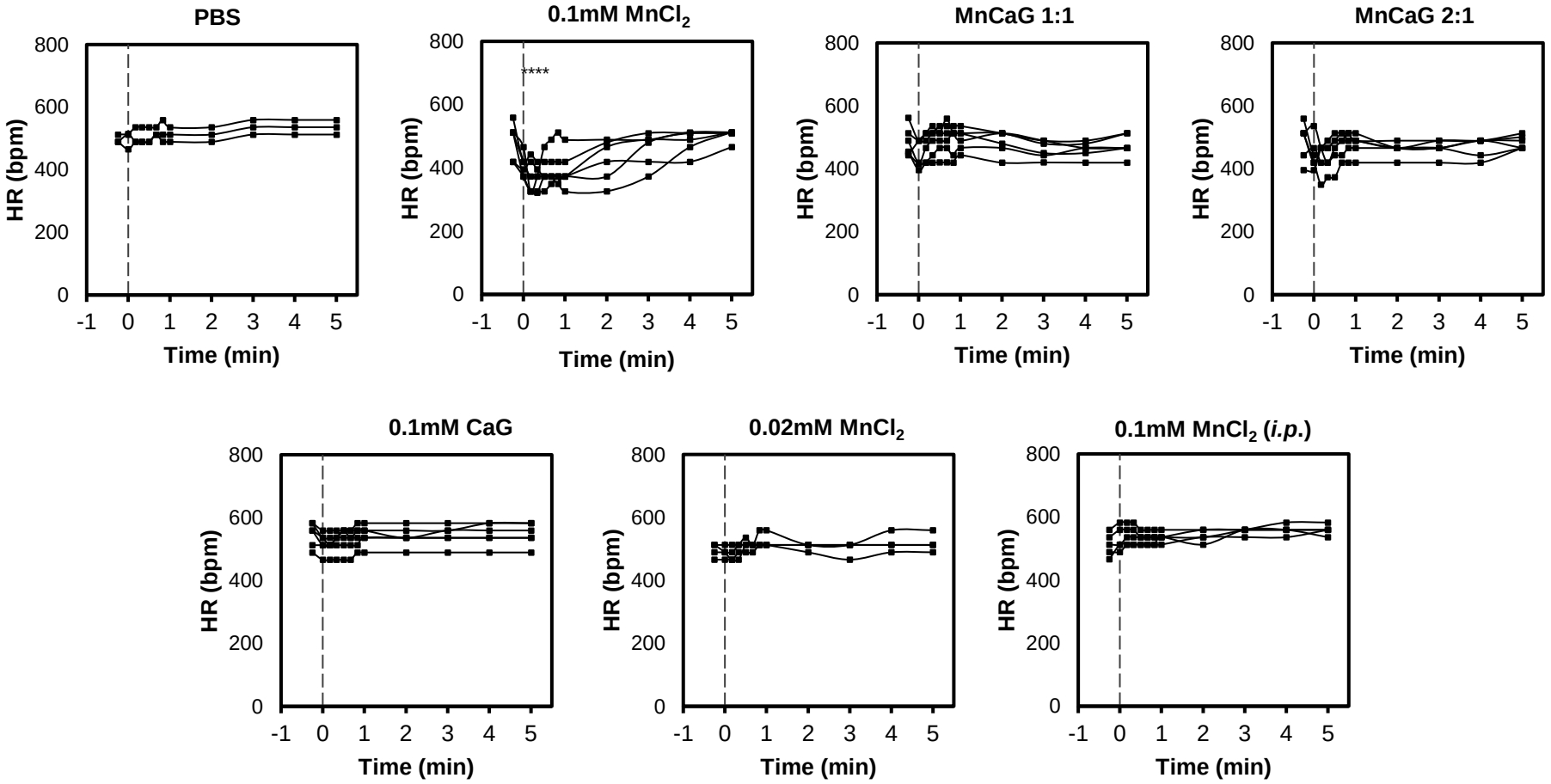

Figure 2.17: The effect of manganese-based contrast agents heart rate.

Heart rate (HR) at baseline, every 10s to 1min and every minute up to 5min post-injection. Note that (*) shows significant differences at the time points post manganese injection as compared to baseline in each group (Table 2-3 for p value). In each group, data were analysed by two-way ANOVA with Dunnet's multiple comparison test.

Table 2-3: The effect of manganese on heart rate.

Time (s)	0.1mM $MnCl_2$ (n=6)	0.02mM $MnCl_2$ (n=4)	MnCaG 1:1 (n=6)	MnCaG 2:1 (n=6)	0.1mM CaG (n=6)	PBS (n=3)	0.1mM $MnCl_2$ (*i.p.*) (n=5)
Pre	489 ± 23	495 ± 11	485 ± 19	489 ± 24	548 ± 16	497 ± 8	513 ± 16
0	407 ± 14*	489 ± 10	450 ± 18	447 ± 20	521 ± 13	498 ± 16	531 ± 17
10	369 ± 21*	483 ± 11	470 ± 17	439 ± 19	517 ± 13	505 ± 16	541 ± 14
20	368 ± 16*	495 ± 11	485 ± 18	439 ± 17	524 ± 13	505 ± 16	541 ± 14
30	388 ± 20*	512 ± 10	489 ± 17	462 ± 20	532 ± 15	505 ± 16	531 ± 9
40	396 ± 21	507 ± 6	497 ± 20	478 ± 16	528 ± 14	520 ± 8	531 ± 9
50	400 ± 24	524 ± 12	489 ± 19	482 ± 14	549 ± 14	520 ± 21	531 ± 9
60	392 ± 23	524 ± 12	493 ± 14	478 ± 13	544 ± 13	513 ± 13	536 ± 7
120	426 ± 27	507 ± 6	484 ± 15	462 ± 9	549 ± 13	513 ± 13	541 ± 9
180	460 ± 22	501 ± 12	462 ± 12	466 ± 10	544 ± 13	536 ± 13	555 ± 5
240	485 ± 15	518 ± 15	462 ± 10	470 ± 13	548 ± 15	536 ± 13	559 ± 7
300	504 ± 8	518 ± 15	474 ± 14	483 ± 8	548 ± 15	536 ± 13	559 ± 7

*Values represent mean ± SEM. $MnCl_2$, manganese(II) chloride; MnCaG1:1, manganese to calcium-gluconate ratio (1:1); MnCaG2:1, manganese to calcium-gluconate ratio (2:1); CaG, calcium-gluconate; PBS, Phosphate-buffered saline; i.p., intraperitoneal injection. Data were analysed using paired one-way ANOVA. Boxes marked red indicates heart rate below the normal level. *P<0.05 compared to baseline (pre).*

2.4.1.3 Animal recovery

All mice recovered quickly after anaesthesia was halted, and even in the mananese high dose group, all mice showed normal behaviour, and there was no mortality over the following four weeks.

2.4.2 Study 2 – Effect of manganese and manganese-calcium contrast agents on image contrast in MEMRI

2.4.2.1 Parameter optimisation (T1 Mapping)

Higher flip angles in the Look-Locker sequence produce more MR signal but could lead to an overestimation of the T1 value. The lower the flip angle, the more accurate the T1 value but at the expense of increasing image noise. Figure 2.18 shows that FA 20º had the highest signal to noise ratio (SNR). All three different FA exhibited similar T1 values, as shown in Figure 2.19 A-C shows. These data suggested that increasing flip angle to 20º resulted in better image quality while still maintaining the accuracy of T1 estimation.

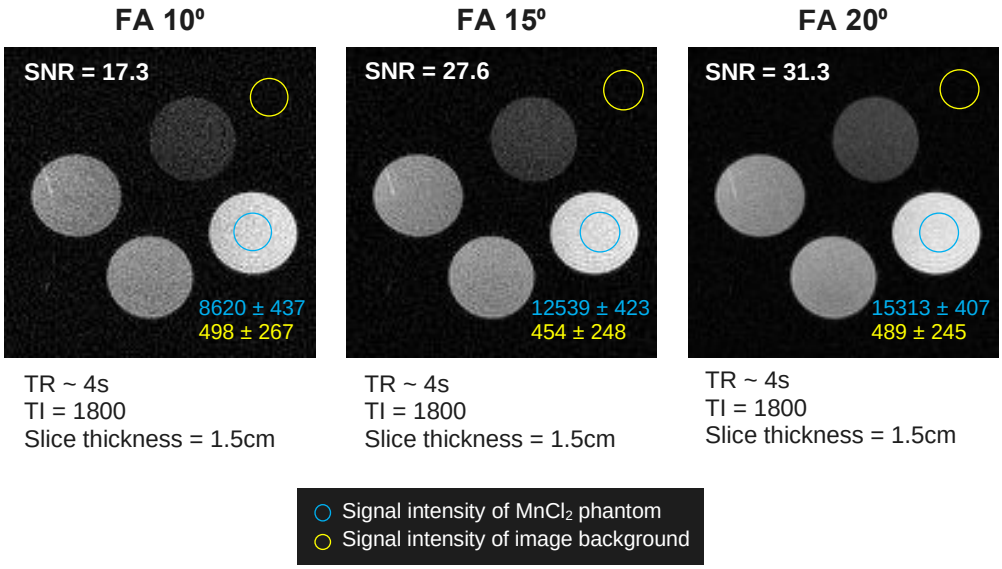

Figure 2.18: Representative T1-weighted image acquired at different FA.
Signal intensity values represent mean ± SD.

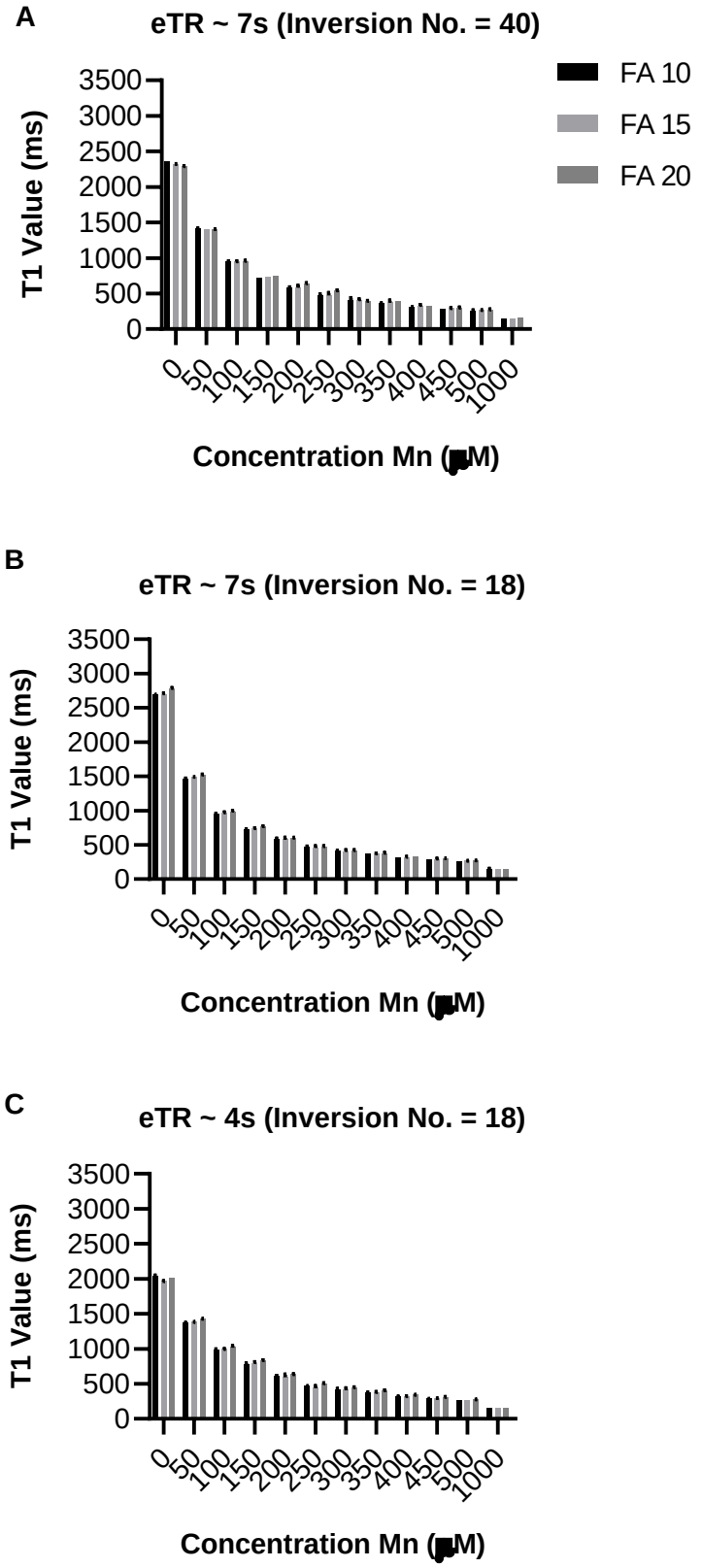

Figure 2.19: Effects of flip angle and effective TR on T1 value.

Bar graphs show the mean ± SD (n=3) of $MnCl_2$ phantoms with concentrations ranging from 50 to 1000 μM. T1 mapping was performed using three different FA (10º, 15º, and 20º) and two different TR (~7s and ~4s).

Longer eTR is required to make sure the longitudinal relaxation to fully relaxed before the next inversion pulse. However, longer eTR will increase scan time. Figure 2.20 shows that different eTR exhibited different T1 value when the T1 is 1.5s and longer. However, no variation in T1 value below was seen when the T1 is 1.5s. in can be inferred from these data that I could use shorter eTR for post-contrast imaging to reduce the scan time.

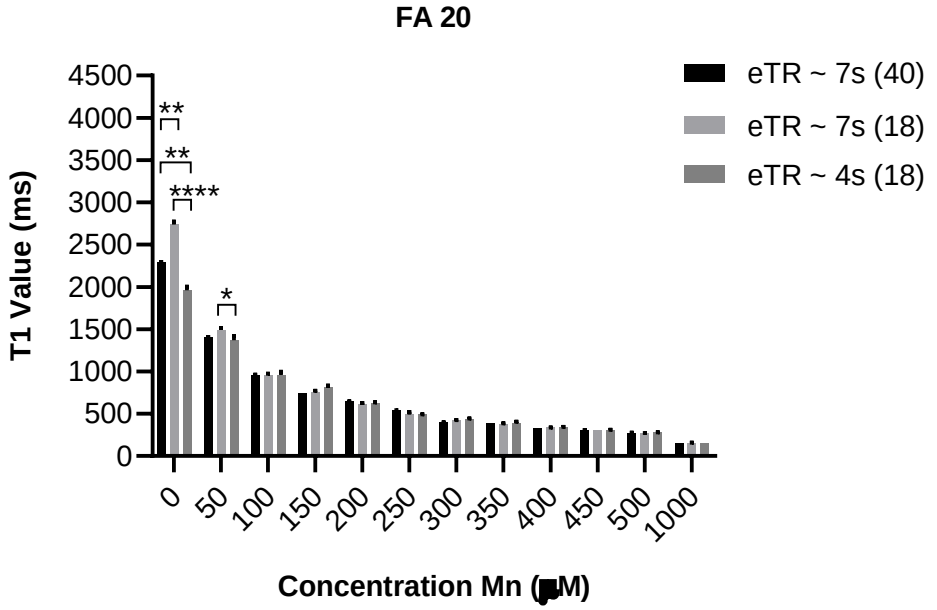

Figure 2.20: Effects of flip angle (FA 20º) on T1 value.

*Bar graph represents mean ± SD T1 relaxation times of Mn phantoms with concentrations ranging from 50 to 1000 μM. *P<0.05, **P<0.01, and ****P<0.0001.*

2.4.2.2 Myocardial Enhancement in MEMRI

Figure 2.21 shows the representative T1 maps in the four groups tested for in vivo studies; MnCaG1:1, MnCaG2:1, 0.02mM $MnCl_2$, and 0.1mM $MnCl_2$ (*i.p.*) at baseline, 10min, 60min and 24h post-injection. When compared with the T1 maps at baseline, T1 reduction was observed in all four groups and recovers after 24 hours. Correspondingly, R1 (1/T1) in myocardium, blood, muscle and liver increased from baseline in all four groups, as shown in Figure 2.22, Figure 2.23 and Figure 2.24. All R1 data were tabulated in Table 2.4. Increased in R1 value indicates an increase in Mn^{2+} uptake. *I.v.* injection of 0.1 mmol/kg $MnCl_2$ was not tested as the data presented in Study 1 indicated it has a significant effect on heart function.

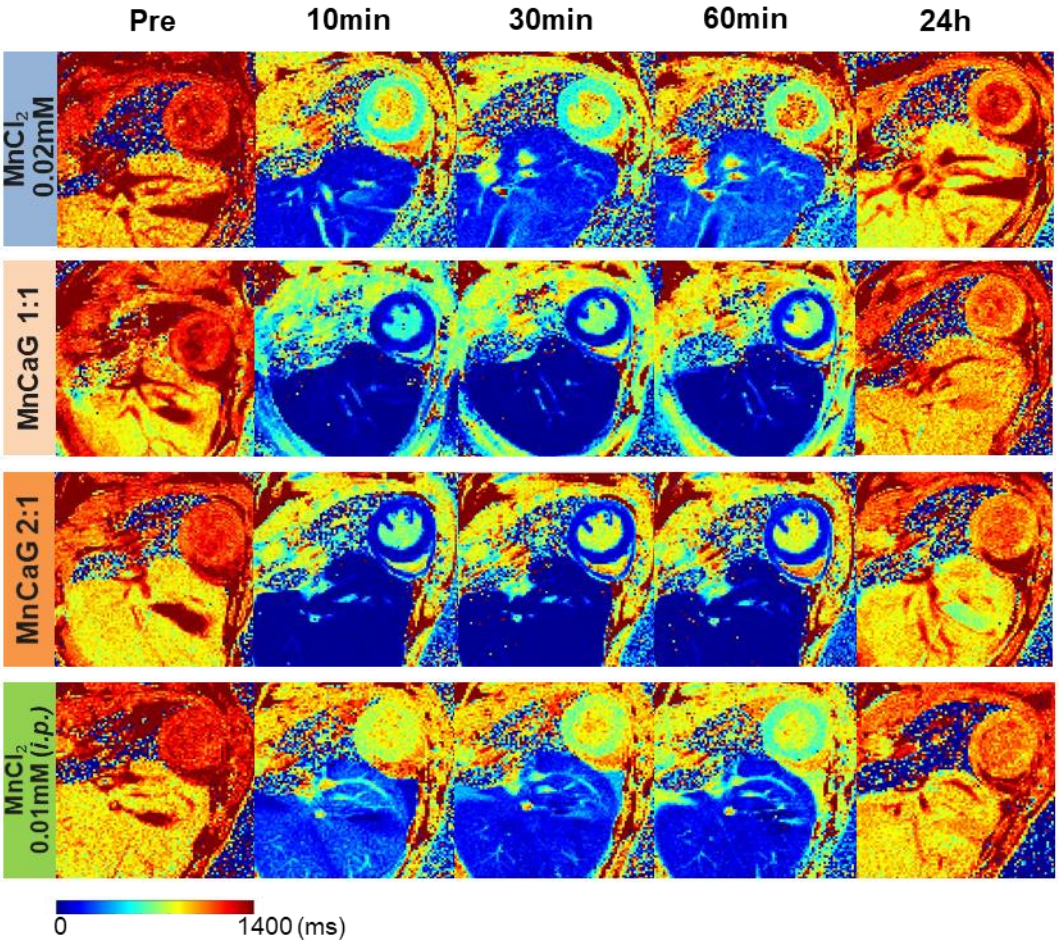

Figure 2.21: Representative T1 maps in the four manganese-based contrast agents. *MnCaG1:1, MnCaG1:1, 0.02mM $MnCl_2$, and* 0.1mM $MnCl_2$ (*i.p.*) *at baseline, 10min, 60 min and 24h post-injection.*

In the MnCaG1:1 group, myocardial R1 were significantly increased at 10min, 30min and 60min post-injection with maximum Mn-induced R1 increases observed 10 minutes post-injection (7.08 ± 1.37 s^{-1}) which is significantly higher as compared to baseline (0.92 ± 0.03 s^{-1}) ($p<0.05$) (Figure 2.22A and Table 2.4). Similarly, myocardial R1 in the MnCaG2:1 were significantly increased at 10min, 30min and 60min post-injection with maximum Mn-induced R1 increases was observed 10 minutes post-injection (10.38 ± 0.68 s^{-1}) and was significantly higher compared to baseline (0.91 ± 0.02 s^{-1}) ($p<0.001$). Both MnCaG1:1 and MnCaG2:1 greatly enhanced image contrast in MRI, as shown in Figure 2.22B. These data show that calcium supplement could overcome cardiotoxicity of manganese while still maintaining excellent image contrast in MRI.

Myocardial R1 in the 0.02mM $MnCl_2$ were significantly increased at 10min, 30min and 60min post-injection with maximum Mn-induced R1 increase observed at 10min post-injection (1.65 ± 0.08 s^{-1}) and was significantly higher compared to baseline (0.91 ± 0.03 s^{-1}) ($p<0.001$). Administration of manganese via intraperitoneal injection also caused a significant increase in myocardial R1 in the 0.1mM $MnCl_2$ (*i.p.*) at 10min, 30min and 60min post-injection. However, the maximum Mn-induced R1 increases were observed at a later time point, 60 minutes post-injection (2.28 ± 0.23 s^{-1}) and was significantly higher when compared to baseline (0.91 ± 0.02 s^{-1}) ($p<0.01$). A lower concentration on Mn^{2+} amount results in low image contrast as shown in Figure 2.22B.

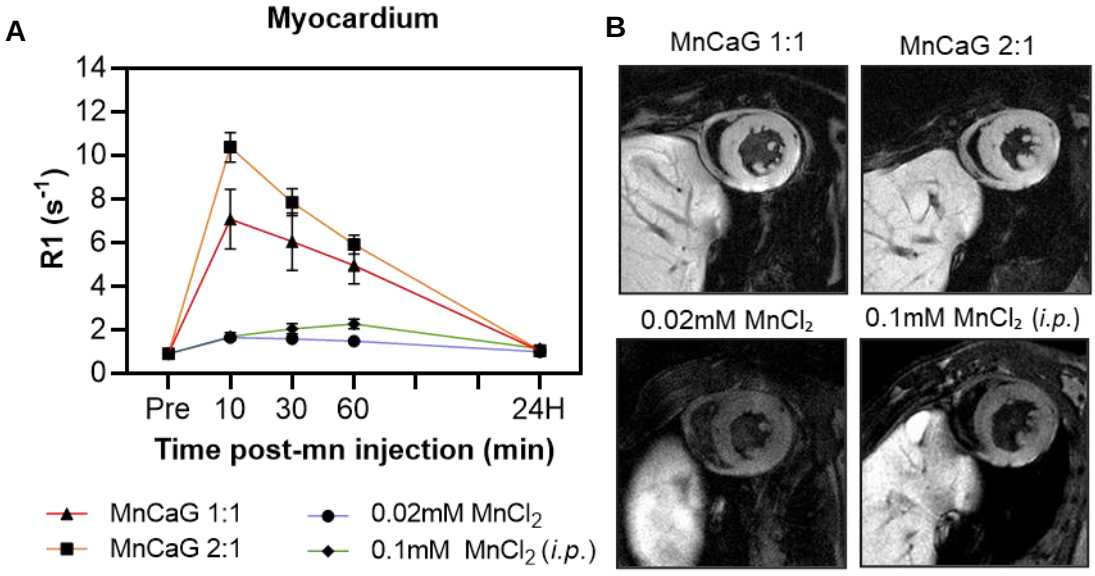

Figure 2.22: Time course of manganese uptake in the myocardium in control mice.

(A) R1 values in myocardium at baseline, 10min, 30min and 60min and 24h post-Mn injection. Each point represents the mean ± SEM value (n=5). (B) representative images for each group at 60 minutes post-Mn injection is shown in the right-hand side.

Figure 2.23A-C shows that Mn uptake in the MnCaG2:1 group was higher than the MnCaG1:1 group at 10 minutes post-injection ($p < 0.05$). There was no significant difference in Mn uptake between MnCaG1:1 and MnCaG2:1 at 30min and 60min post-injection. These data show that a higher Mn proportion resulted in a higher Mn uptake in the myocardium. It can be inferred from these data that Ca supplement has an effect on reducing the rate of Mn uptake into the myocardium.

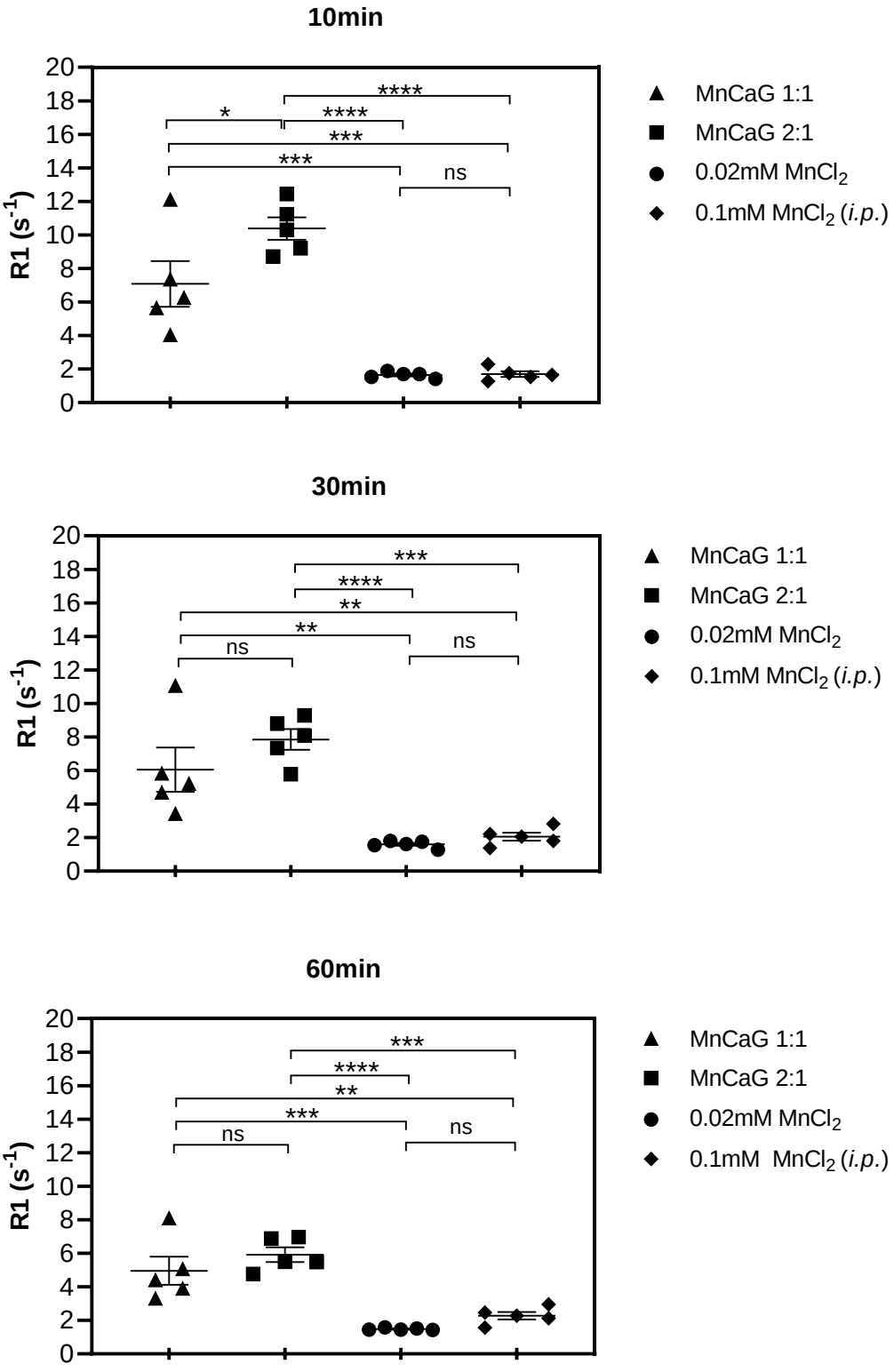

Figure 2.23: Manganese uptake in the myocardium.

*Graph represent R1 value (mean ± SEM) in myocardium at 10min, 30min, and 60min post-manganese injection. Data were analysed by one-way ANOVA with Tukey's multiple comparison test. *P<0.05, **P<0.01, ***P<0.001 and ****P<0.0001 (n=5).*

Table 2-4: R1 in the myocardium, blood, muscle and liver at baseline and post four different manganese formulations.

(MnCaG1:1 and MnCaG2:1), route of injections (0.1mM $MnCl_2$ i.p.*) and low concentration (0.02mM $MnCl_2$).*

Time	MnCaG 1:1 (n=5)	MnCaG 2:1 (n=5)	0.02mM $MnCl_2$ (n=5)	0.1mM $MnCl_2$ (*i.p.*) (n=5)
Myocardium				
Pre	0.92 ± 0.03	0.91 ± 0.02	0.91 ± 0.03	0.91 ± 0.02
10	7.08 ± 1.37*	10.38 ± 0.68†	1.65 ± 0.08†	1.70 ± 0.17*
30	6.06 ± 1.31*	7.86 ± 0.61**	1.60 ± 0.09**	2.05 ± 0.24*
60	4.95 ± 0.84*	5.92 ± 0.43**	1.48 ± 0.03‡	2.28 ± 0.23**
24H	1.04 ± 0.02	1.06 ± 0.02*	1.01 ± 0.03*	1.15 ± 0.04**
Blood				
Pre	0.88 ± 0.01	0.83 ± 0.01	0.85 ± 0.03	0.87 ± 0.03
10	1.47 ± 0.08**	1.40 ± 0.01‡	1.08 ± 0.03**	1.31 ± 0.06**
30	1.29 ± 0.03†	1.31 ± 0.02‡	1.05 ± 0.05*	1.22 ± 0.04†
60	1.25 ± 0.01‡	1.25 ± 0.03†	0.99 ± 0.02*	1.25 ± 0.05**
24H	0.90 ± 0.02	0.91 ± 0.02*	0.85 ± 0.04	0.96 ± 0.01
Muscle				
Pre	0.93 ± 0.05	0.90 ± 0.03	0.91 ± 0.05	0.92 ± 0.01
10	1.36 ± 0.02**	1.19 ± 0.02**	1.14 ± 0.06	1.15 ± 0.01‡
30	1.22 ± 0.02**	1.20 ± 0.03**	1.12 ± 0.06	1.17 ± 0.03**
60	1.14 ± 0.02*	1.15 ± 0.03†	1.05 ± 0.02	1.18 ± 0.03**
24H	0.95 ± 0.03	0.95 ± 0.02	0.93 ± 0.03	1.01 ± 0.03*
Liver				
Pre	1.15 ± 0.05	1.09 ± 0.03	1.14 ± 0.05	1.20 ± 0.03
10	75.55 ± 3.61†	77.02 ± 8.50**	6.51 ± 0.67**	18.69 ± 7.84
30	79.02 ± 6.89†	85.27 ± 3.54‡	4.71 ± 0.60*	32.61 ± 11.61*
60	61.13 ± 9.21**	67.24 ± 7.41**	3.65 ± 0.42*	32.53 ± 11.23*
24H	1.13 ± 0.03	1.21 ± 0.03	1.12 ± 0.02	1.27 ± 0.05

*Values represent mean R1 (s^{-1}) ± SEM. MnCaG 1:1, manganese ratio calcium-gluconate 1:1; MnCaG 2:1, manganese ratio calcium-gluconate 2:1; Mn Low, manganese low dose; and IP, intraperitoneal injection. *P<0.05 as compared to baseline (pre); **P<0.01 as compared to baseline (pre), †P<0.001 as compared to baseline (pre); ‡P<0.0001 as compared to baseline (pre). The analysis was performed using repeated measures two-way ANOVA with Dunnett's multiple comparisons test. Boxes marked green indicates the maximum R1 in each group and regions.*

R1 (1/T1) in blood, muscle and liver were significantly increased at 10min, 30min, and 60min post-injection as compared to baseline in all four groups, as shown in Figure 2.24 and Table 2.4. The peak R1 in blood and muscle were seen at 10 minutes post-injection in all four groups; MnCaG1:1, MnCaG2:1, 0.02mM $MnCl_2$, and 0.1mM $MnCl_2$ (*i.p.*). The peak R1 in the liver was at 30min post-injection in MnCaG1:1, MnCaG2:1, and 0.1mM $MnCl_2$ (*i.p.*) groups and 10min post-injection in 0.02mM $MnCl_2$ group.

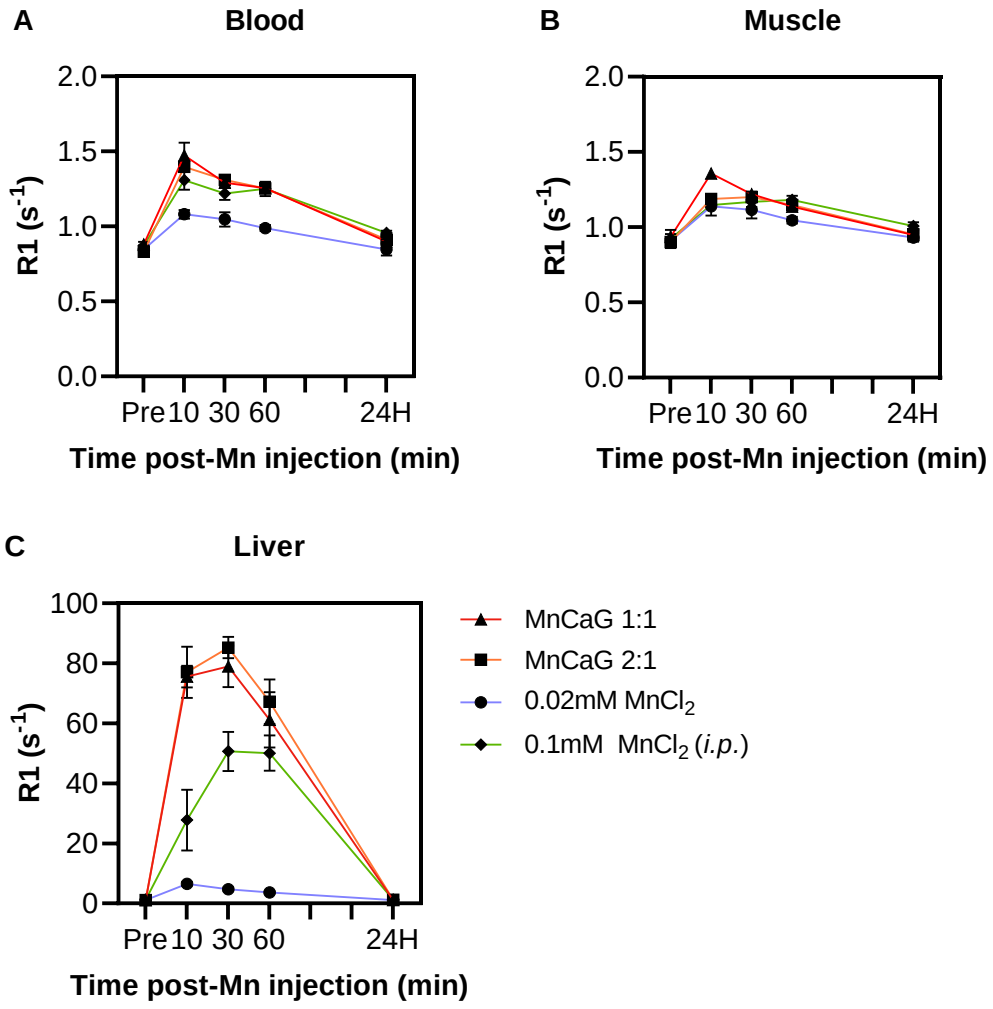

Figure 2.24: Manganese uptake in the blood pool, muscle and liver.
R1 (mean ± SEM) changes baseline, 10min, 30min, 60min and 24h post-manganese injection. (A) Blood, (B) Liver, and (C) Muscle regions. Each point represents the mean and SEM value (n=5).

2.4.3 Study 3 – Estimating manganese content in the heart

2.4.3.1 Influence of calcium supplement on relaxivity of manganese

The differences in manganese (Mn) administrations were further studied in a Mn phantom study. Relaxivity (r_1) for Mn in saline, Mn with CaG in 1:1 ratio (MnCaG1:1) and 2:1 ratio (MnCaG2:1) were 6.4 $(s\ mM)^{-1}$, 6.1 $(s\ mM)^{-1}$ and , 6.4 $(s\ mM)^{-1}$ respectively. This values are close to reported values [163], [165], [166] where r_1 is 6.9 $(s\ mM)^{-1}$ ($r^2 = 0.99$). As seen in Figure 2.25, there was, as would be expected, no significant differences between manganese and manganese supplemented with calcium. A slightly lower relaxivity was noted in Mn phantom made of serum, 5.8 s (mM^{-1}) compared to saline, 6.4 $(s\ mM^{-1})$. There was a close correlation manganese concentration (mM) and the relaxation rate constant (R1) in all four different phantoms (Figure 2.25).

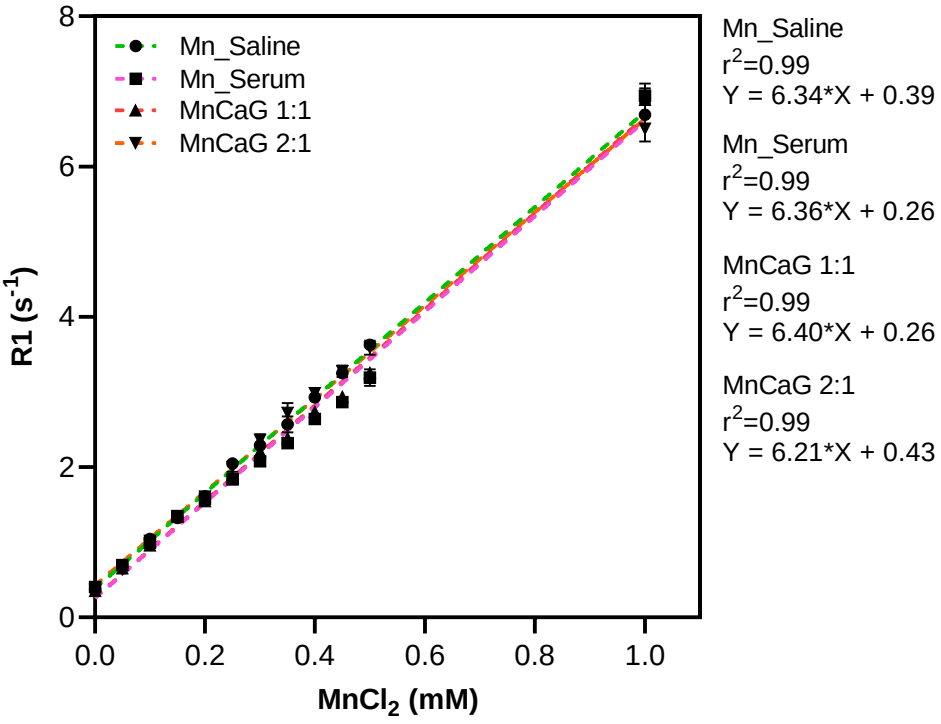

Figure 2.25: The influence of calcium supplement on the relaxivity of manganese.
Longitudinal relaxation rate constant (R1) versus Mn^{2+} concentration (mM). The apparent value (round) and intrinsic value (dotted line) are shown. The correlation coefficient (r^2) is noted ($P < 0.0001$). With a linear curve fit approximation, the relaxivities expressed in $(s\ mM)^{-1}$ were 6.4 $(s\ mM)^{-1}$, 5.8 $(s\ mM)^{-1}$, 6.1 $(s\ mM)^{-1}$and 6.4 $(s\ mM)^{-1}$ in Mn saline, Mn serum, MnCaG1:1, and MnCaG2:1 respectively.

2.4.3.2 Manganese distributions

The distributions of manganese accumulation in the heart, blood, muscle and liver were estimated from the in vivo images via a standard curve of $MnCl_2$. R1 values calculated from the T1 mapping MEMRI in vivo in Section 2.4.2.2 was used to estimate the Mn^{2+} content in the heart, blood, muscle and liver in the four manganese contrast agents formulations (MnCaG1:1, MnCaG2:1, 0.02mM $MnCl_2$ and 0.1mM $MnCl_2$ (*i.p.*).

Figure 2.26A shows the manganese concentration (mM) in the heart at 10min, 30min, 60min and 24h post injections.The highest Mn^{2+} content was seen in MnCaG2:1 group followed by MnCaG1:1, 0.02mM $MnCl_2$ and 0.1mM $MnCl_2$ (*i.p.*). The peak manganese uptake was seen at 10min post-injection in MnCaG1:1, MnCaG2:1, and 0.02mM $MnCl_2$ group (0.96 ± 0.21 mM, 1.53 ± 0.11 mM and 0.12 ± 0.01 mM respectively). In animals that received *i.p.* injection, maximal myocardial R1 was delayed to 60 min after injection (0.22 ± 0.03 mM), reflecting the slow absorption of Mn^{2+} from the peritoneal cavity into the blood. There are significant differences in Mn concentration of MnCaG1:1 compared to MnCaG2:1 (10min, $P<0.05$), 0.02mM $MnCl_2$ (10min, $P<0.001$; 30min, $P<0.01$; and 60 min, $P<0.001$), and 0.1mM $MnCl_2$ (*i.p.*) (10min, $P<0.001$; 30min, $P<0.01$; and 60 min, $P<0.01$). Mn concentration in MnCaG2:1 were also significantly different from 0.02mM $MnCl_2$ (10min, $P<0.001$; 30min, $P<0.01$; and 60 min, $P<0.001$), and 0.1mM $MnCl_2$ (*i.p.*) (10min, $P<0.001$; 30min, $P<0.01$; and 60 min, $P<0.01$). No significant differences were seen between 0.02mM $MnCl_2$ and 0.1mM $MnCl_2$ (*i.p.*) at all time points.

Figure 2.26B shows the estimate of manganese content in the heart in g/L. The highest manganese content was seen in MnCaG2:1 group followed by MnCaG1:1, 0.1mM $MnCl_2$ (*i.p.*) and 0.02mM $MnCl_2$ at all time points (10-, 30-, 60 minutes and 24 hours). Maximum Mn uptake was seen at 10min post-injection in MnCaG1:1, MnCaG2:1, and 0.02mM $MnCl_2$ group (0.12 ± 0.03 g/L, 0.19 ± 0.01 g/L and 0.015 ± 0.001 g/L respectively). In 0.1mM $MnCl_2$ (*i.p.*) group, maximum Mn uptake was seen at a later time point, 60 minutes post-injection (0.027 ± 0.004 g/L). The manganese content in the heart was normalised to the baseline (pre-contrast injection).

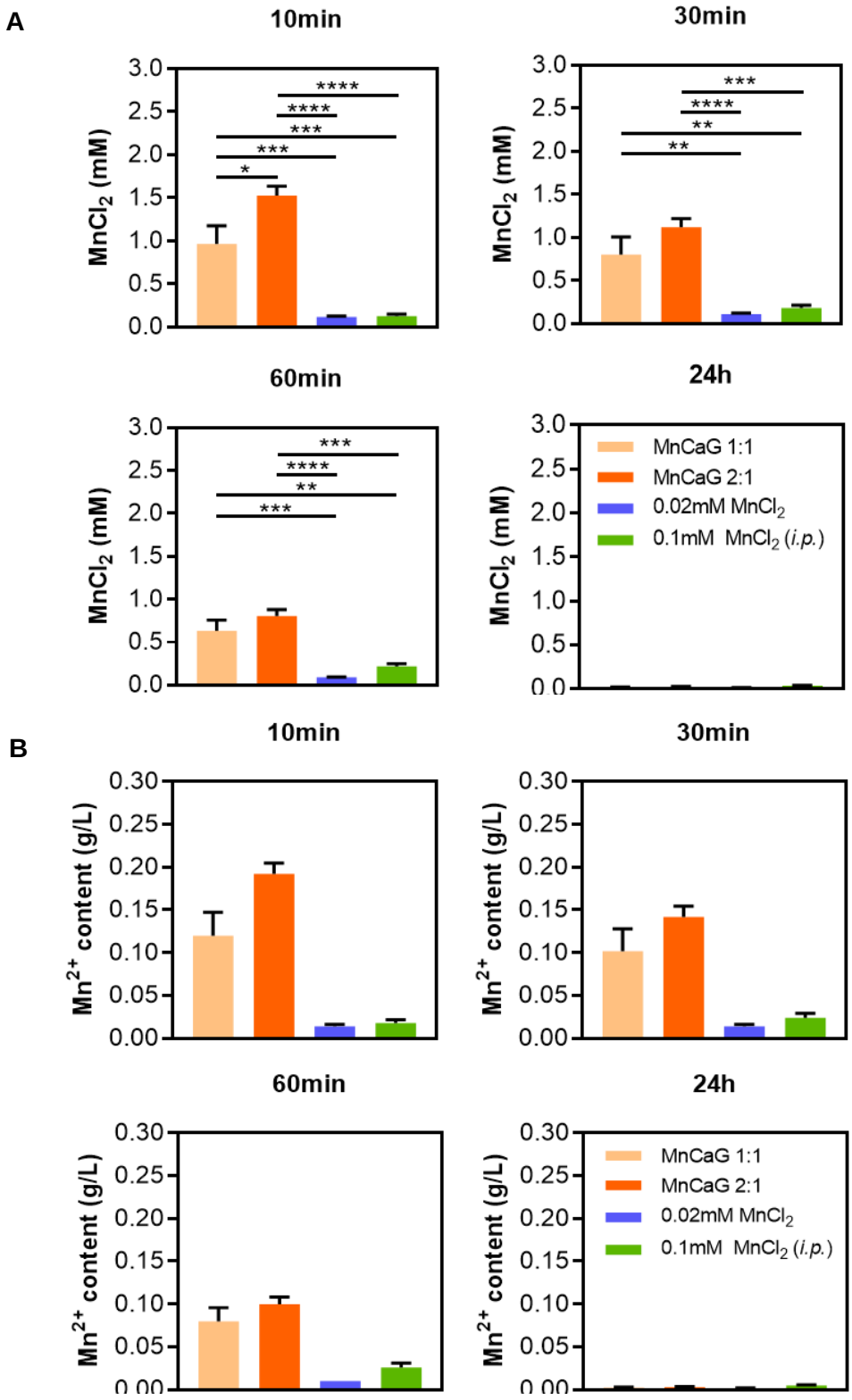

Figure 2.26: Accumulation of manganese in the myocardium following injection of four different formulations of manganese-based contrast agents.

*(A) Manganese concentration (mM) and (B) Mn^{2+} content (g/L) in the myocardium at 10min, 30min, 60min and 24h post-Mn-based contrast agents injections. Bar represent different manganese administration methods; 0.02mM $MnCl_2$ i.v. (n=5); 2) MnCaG1:1 (0.1mM $MnCl_2$ + 0.1mM CaG i.v.) (n=5); 3) MnCaG2:1 (0.1mM $MnCl_2$ + 0.05mM CaG i.v.) (n=5); and 4) 0.1mM $MnCl_2$ i.p. (n=5). Bars represents mean ± SEM normalised to the baseline. Data were analysed using one-way ANOVA (*P<0.05, **P<0.01, ***P<0.001 and ****P<0.0001).*

Next, manganese concentration in the heart following injection of manganese-based contrast agents (MnCaG1:1, MnCaG2:1, 0.02mM $MnCl_2$ and 0.1mM $MnCl_2$ (*i.p.*) were compared to baseline. Figure 2.27 shows that manganese concentration was significantly elevated post-contrast administrations. The accumulation of manganese at 10min post-injection MnCaG1:1 and MnCaG2:1 were approximately 5 and 8 times higher than 0.02mM $MnCl_2$ and 0.1mM $MnCl_2$ (*i.p.*).

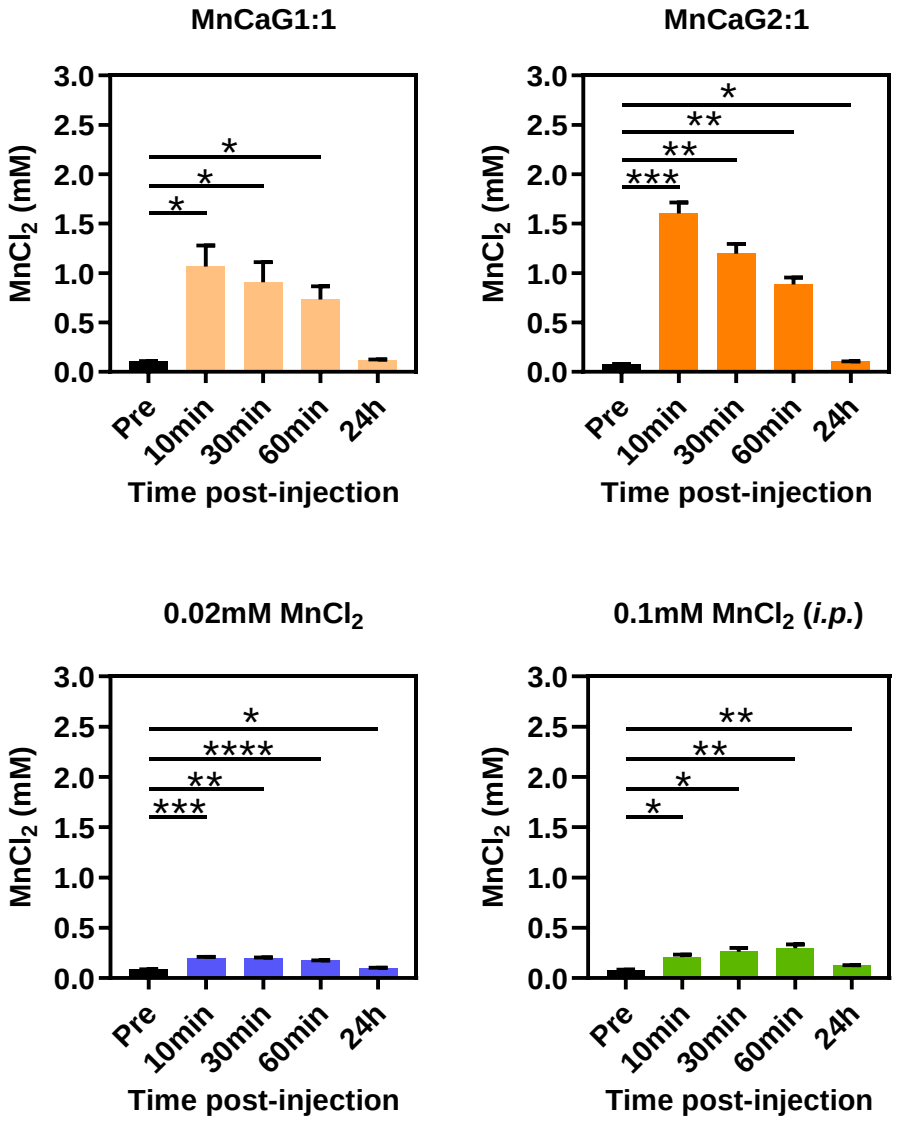

Figure 2.27: Manganese distributions in the heart post-injection of different manganese contrast agents.

*Four different formulations of manganese were used: 0.02mM $MnCl_2$ i.v.; 2) MnCaG1:1 i.v.; 3) MnCaG2:1 i.v.); and 4) 0.1mM $MnCl_2$ i.p.. Data are presented as mean ± SEM (n=5). Bar represent time points; baseline, 10min, 30min, 60min and 24h post-injections. Data are presented as mean ± SEM. Data were analysed using two-way ANOVA, and Dunnets for multiple comparisons test comparing each time points post-injection (*P<0.05, **P<0.01, ***P<0.001 and ****P<0.0001).*

Figure 2.28 shows the time course manganese concentration in the liver, myocardium, muscle and blood in each group; MnCaG1:1, MnCaG2:1, 0.02mM $MnCl_2$, and 0.1mM $MnCl_2$ (*i.p.*). The highest Mn concentration was seen in the liver, followed by myocardium, blood and muscle. There are significant differences between administration methods; calcium supplement (MnCaG1:1 and MnCaG2:1), reduced $MnCl_2$ concentration (0.02mM $MnCl_2$) and route of delivery ($MnCl_2$ *i.p.*) at 10min ($P<0.001$, $P<0.0001$), 30min ($P<0.001$, $P<0.0001$), 60min ($P<0.01$, $P<0.0001$) post-injection in the liver and myocardium respectively. At 24h post-injection, a significant difference was only seen in the myocardium, reflecting the long retention of manganese in the myocardium. No change was seen between manganese administration methods in the blood pool and muscle regions suggesting a rapid clearance on manganese, except for during the early time point (10min post-injection, $P<0.05$).

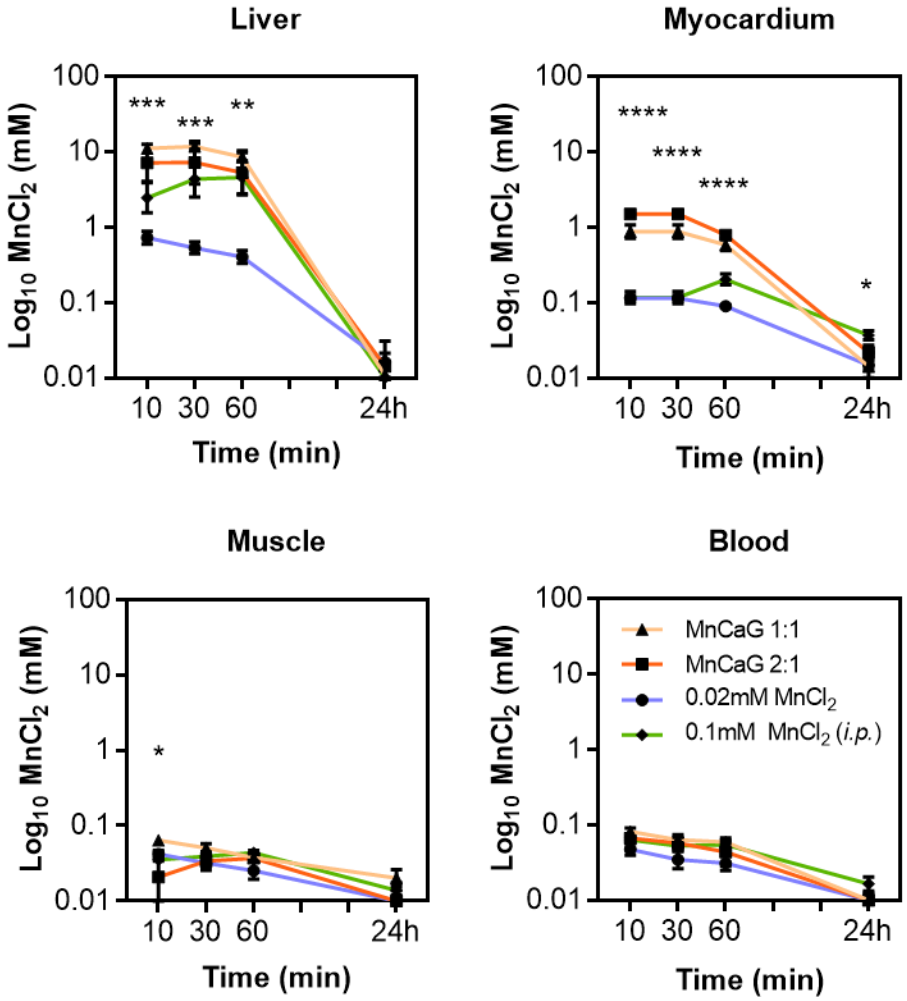

Figure 2.28: Time course manganese concentration in the liver, myocardium, muscle, and blood.

*Manganese concentration presented as mean ± SEM. Data were analysed by one-way ANOVA (*P<0.05, **P<0.01, ***P<0.001, and ***P<0.0001).*

Figure 2.30 shows the distribution of Mn across four regions; myocardium, blood, muscle, and liver at 10min and 60min post-injection in each group; MnCaG1:1, MnCaG2:1, 0.02mM $MnCl_2$, and 0.1mM MnCl2 (*i.p.*). The liver has the highest Mn^{2+} content followed by myocardium, blood and muscle in all groups at each time points post-injection. No change was seen between 10min and post 60min except for the MnCaG2:1 (myocardium, 13% to 8%). A small difference was also seen post-injection of 0.02mM $MnCl_2$ and 0.1mM $MnCl_2$ (*i.p.*) likely due to the differences in injection infusion.

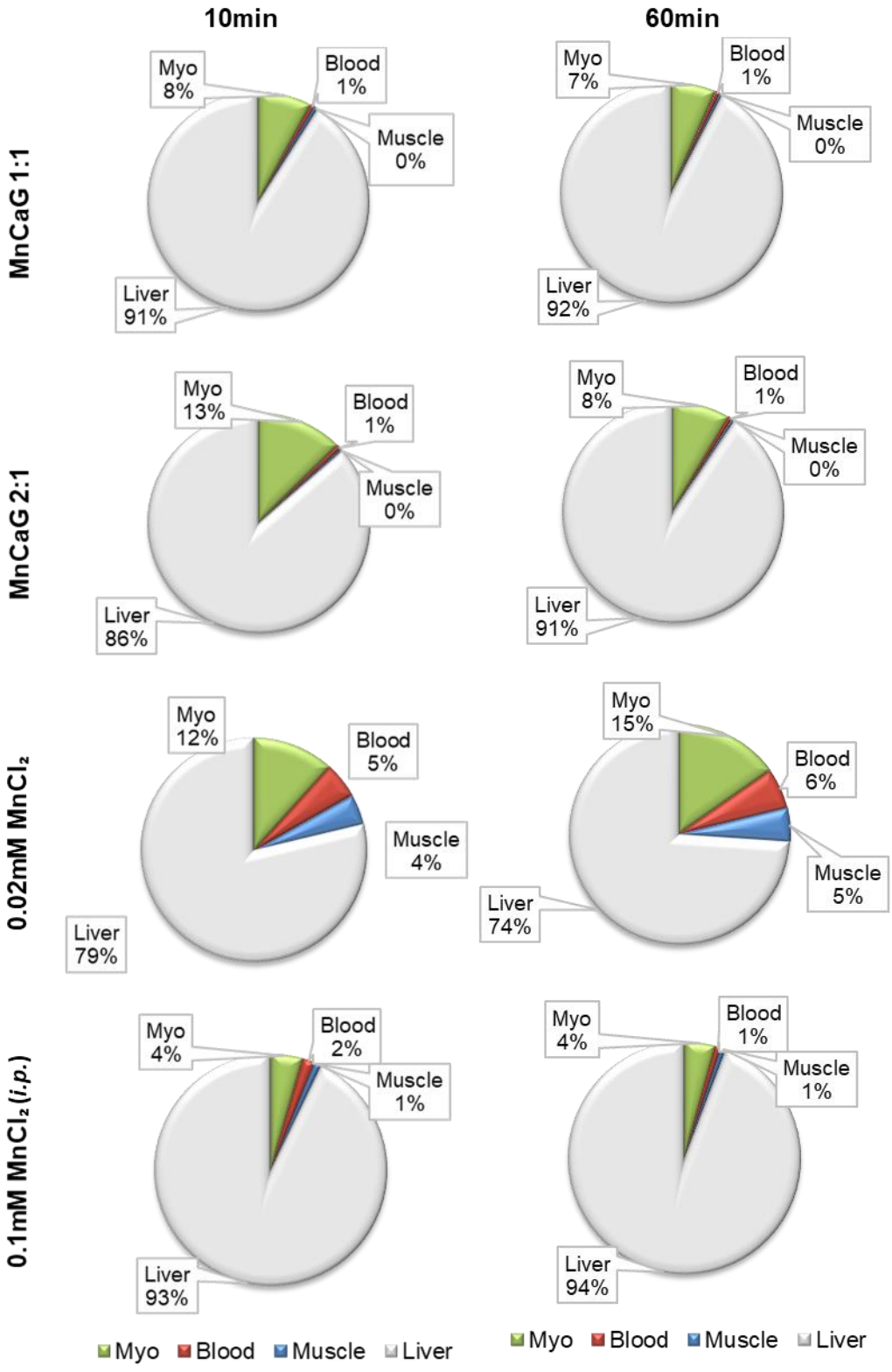

Figure 2.29: Distributions of manganese in myocardium, blood, muscle and liver.

Manganese concentration across four regions (myocardium, blood, muscle, and liver) at 10min and 60min post-injection post different manganese formulations (MnCaG1:1, MnCaG2:1, 0.02mM $MnCl_2$ and 0.1mM $MnCl_2$ (i.p.).

2.5 Discussion

There are several major findings from the studies in this chapter, discussed from three aspects; 1) the effects of manganese contrast agents on cardiac physiology, 2) the effects of manganese contrast agents on image enhancement in MEMRI, and 3) the manganese content in the heart and other regions post-contrast injection.

2.5.1 Effect of manganese contrast agents on cardiac physiology

Intracellular Ca^{2+} is a central regulator of cardiac contractility. Thus, manganese, when administered at high dose, can be cardiotoxic. The primary aim of this study was to investigate the effects of manganese (Mn) contrast agents on cardiac function and the means to overcome the cardiotoxicity of manganese. To our knowledge, this is the first study to investigate the effects of different Mn^{2+} formulations on real-time cardiac contractility. As expected, myocardial contractility was rapidly and transiently depressed by high $MnCl_2$ (0.1 mM) bolus intravenous injection (*i.v.*). The cardiac contractility is reduced by 97% during the first few seconds and returned to baseline within 5 minutes post-Mn injection. In contrast, myocardial contractility was increased transiently by about approximately 40% when injected with 0.1 mM CaG before it returned to baseline. A similar trend was seen in the previous study where there also find a contractile failure and contractile overshoot post-injection of high Mn and Ca respectively in an isolated perfused rat's heart [167].

The reduction in cardiac contractility is likely due to competitive binding for cell entry via slow Ca^{2+} channels [95], [96], [115], [118], [168], [169]. The cardio depressant effect is transient and reversible as blood washes out, clearing the pool of Mn^{2+} in the extracellular space causing blockage for the Ca^{2+} influx – only Mn^{2+} influx occurs when there is high Mn^{2+} concentration in the extracellular space. Ca^{2+} is an integral part of binding intracellular and initiate cardiac contraction. Thus, a reduction in Ca^{2+} influx due to competitive binding with high Mn^{2+} concentration caused a reduction in cardiac contractility [145]. Whereas increased levels of the Ca^{2+} ion in the blood, promote an increase in Ca influx and increased cardiac contractility as seen following Ca injection. A similar pattern is seen when positive and negative inotropic drugs that are known to influence Ca^{2+} uptake by myocytes caused a significant alteration in Ca^{2+} influx which resulted in an increased and decreased cardiac contractility [96], [115].

The present study shows that 2 of the 3 strategies improved the safety of manganese. The cardio depressant effect from high Mn infusion was negated when administered with a calcium supplement. The improvement in cardiac inotropy was potentially achieved from balancing the competition of manganese with calcium during cell entry by administering calcium ion together with the Mn^{2+} in the extracellular space. Administering calcium supplement to manganese in 1:1 ratio causes a small increase in cardiac contractility, whereas a 2:1 Mn^{2+} to Ca^{2+} ratio helped reduced cardiac depression more than 50% when compared to when no calcium supplement was used. These ratios were nearly similar to earlier work by Schaefer et al. 1989 [132]. They were the first to use Ca supplement to improve the safety of manganese were they used 20% more Mn compared to Ca (Mn^{2+} to Ca^{2+}). They also reported no changes in LV pressure and heart rate with only minimal reduction in mean arterial pressure. The latest invention of manganese contrast agent, SeeMore™ (EVP1001), used a similar approach, containing non-chelated Mn^{2+} (12%) and calcium gluconate (10%) that has now been tested in clinical trials [170].

In contrast, Bruvold et al. 2005 [152] reported that the use of Ca supplements to Mn was counterproductive as it induces a potent positive inotropic response. In the study, however, they only tested a single ratio, 1:10 (Mn^{2+} to Ca^{2+}), which was also rather extreme. A similar ratio was suggested from the early EVP1001 patent in 1999 [171]. They reported that the preferable ratios of Mn^{2+} to Ca^{2+} were 1:8 to 1:10. The basic principles behind EVP1001 were presented, but its formulation was not revealed, and only changes in blood pressure were presented. Variability and lack of essential information make it difficult to apply the present findings to those particular papers which used different animal model and approaches. The study presented here was the first to quantify changes in cardiac contractility in-vivo directly following injection of manganese and the effect of Ca supplements. A suitable amount of calcium and manganese to calcium ratio are essential when using Calcium supplement to Mn to prevent an excessive positive inotropic.

The cardio depressant effect also was nullified through the slow release of manganese achieved by administering contrast via intraperitoneal *(i.p.)* injection. Intraperitoneally delivered substances were first absorbed into mesenteric vessels that drain into the portal vein. Substances pass through the liver before they reach the systemic circulation and go into the heart [172]. In contrast, in the intravenous route of delivery, the substances are administered directly into the blood system. The intravenous route allows rapid delivery of substances, which also means they could

lead to detrimental effect when administered in large volume or high concentration. Intraperitoneal injection is often used for small animals in which intravenous access is challenging. A more detailed discussion about the different administration can be found in the review paper [173].

The results from this chapter showed that manganese cardiotoxicity was slightly improved by reducing manganese concentration to one fifth, thus reducing Mn dose. However, the contrast-induced enhancement was fairly low and was not sustained over a long period. Other MRI studies have investigated different strategies to overcome manganese's cardiotoxicity. For example, Mn^{2+} chelators such as Mn-dipyridoxyl-diphosphate (MnDPDP) [112], [174] allows slow release of the Mn^{2+} ions, and this approach has been found nontoxic [175], [176]. However, chelation reduced Mn uptake into myocytes, meaning changes in relaxivity were small and hence reduced image enhancement.

The clinical use of manganese-enhanced MRI has been limited as it is well documented that high doses of *i.v.* Mn^{2+} can reduce myocardial contractility [177] with doses >5 mg/kg (0.04mM) $MnCl_2$ causing decreased heart rate and blood pressure in dogs [178] and an LD50 of 0.3 mM in rats [179]. However, low dose MEMRI has been safely tested in healthy human volunteers via a 3 min infusion of $MnCl_2$ to a total of 5µM [104]. In addition to that, as what has been shown from the finding in this chapter, adding Ca supplement can efficiently overcome the transient effect of Mn toxicity. It is, therefore, feasible to use Mn-Ca contrast agents to safely estimate calcium changes in real-time. There is only minimal changes to heart rate were also observed, suggested that high Mn^{2+} and Ca^{2+} levels directly affect Ca^{2+} mediated myocyte contractility rather than heart rate (HR), and the mice survived for at least four weeks after the ultrasound experiments. This result is in line with the previous study that also found no changes in HR [152].

The study presented here has been limited only to investigate the effect of Mn on cardiac contractility but not the effect of manganese directly on calcium transient and action potential. The next stage would be to incorporate in vitro study to see the effect of Mn at the cellular level, and the effects on the organelles – long term. Another limitation of the present study is that no measurement was performed to investigate the effects of blood pressure (BP) and systemic vascular resistance (SVR) due to unavailability of instruments required in our laboratory. Stroke volume was only measured at the end of each experiment once cardiac contractility has returned to baseline but not during the early phase of manganese (first 0-3 minutes) infusion during which it induces reduced cardiac contractility. At high manganese dose,

cardiac contractility is reduced, which in turns impaired the pumping of blood in and out of the heart, hence reducing the stroke volume and decreased in BP. Previous studies reported that the administration of high dose manganese caused a decrease in systolic blood pressure which can be negated when calcium is supplement is used in their newly invented manganese contrast agents, EVP1001 [171]. It would also be useful to test the EVP1001 using the method presented in this paper and compare to the present findings to get a more insight on the safety and efficacy of the proposed ratios and amount of calcium supplement used in this project.

2.5.2 Effect of manganese and manganese-calcium contrast agents on image contrast in MEMRI

Mn^{2+} is paramagnetic and has been used to enhance MRI signal by the shortening of water T1. Mn was the first agent suggested being used as an MRI contrast agent by Lauterbuer et al. [108]. In the present study, T1 mapping sequence was used and optimised to be used as a mean to detect the changes in T1 relaxations following injections of the four Mn-based contrast agents approaches. This shows that T1 value was affected by the effective time to repeat (eTR) at baseline but not affected when contrast agents were used as it shorten the T1 relaxation time. No noticeable effect was seen when using the flip angle between 10, 15, and 20 degrees. Optimum eTR of ~7 seconds is recommended for pre-contrast imaging and ~4 seconds is recommended for post-contrast imaging to keep the scan time short while still maintaining the accuracy in quantifying t1 value. Fast scan time is needed to be able to track changes in T1 value in the early phase of myocardial infarction. The eTR and flip angle were kept constant and was also used for all experiments in chapter 3. The parameters used for T1 mapping sequence in this study were similar to what had been used previously [74], [157], [180].

The four formulations (MnCaG2:1, MnCaG1:1, 0.02mM $MnCl_2$, and 0.1mM $MnCl_2$ (*i.p.*)) that showing promise to overcome cardiac toxicity of manganese were taken forward for further study to investigate the effects on image enhancement in MRI. The result from the T1 mapping demonstrated that all Mn^{2+} doses tested produced significant increases in R1 within 10 mins of administration and would produce sufficient image contrast to be used for myocardial viability imaging. Chelation can dramatically reduce toxicity with MnDPDP having an LD50 of 1.89 mM in mice [179], and has been tested in humans at 15μM infused over 30 mins [102], [103]. However, myocardial uptake and T1 shortening are also reduced several folds as the chelated form does not pass through calcium channels [97], [179], meaning a

higher dose is needed to gain enhancement. It has been shown that CaG based EVP-1001-1 provides similar T1 shortening to $MnCl_2$ [97], thus offering a potent agent for imaging myocardial viability.

The high doses of Mn^{2+} (0.1 mM/kg) that could be safely delivered *i.v.* with Ca^{2+} supplement yielding the most significant changes in R1 and generating high image contrast. At 10min post-injection, MnCaG2:1 had a significantly higher R1 as compared to MnCaG1:1. At 30min and 60min post-injection, R1 value, hence Mn concentration, were similar in MnCaG2:1 and MnCaG1:1 group. Higher Mn^{2+} concentration in the solution means more Mn^{2+} ion is delivered into the extracellular space, and thus more Mn^{2+} ion influx occurred as reflected in an increase in R1. Similarly, when the Mn^{2+} concentration used was reduced (0.02 mM/kg), the increase in R1 was also minimal. These results indicated that Mn^{2+} influx and hence, changes in R1 is dose-dependent. *I.p.* administration of 0.1 mM $MnCl_2$ also produced good image contrast at 60 mins, which remained at stable levels over several hours. Intraperitoneal delivery of contrast offers a more practical method of substrate administration to small animals, especially for serial injection at multiple time-points in models of cardiovascular disease. Hence *i.p.* delivery was taken forward for experiments in mice subjected to myocardial infarction in the rest of the thesis.

In this study, the R1 changes in other regions in the body – blood, liver, and muscle, were also measured. The liver showed the highest manganese uptake among the four regions. Similar findings were reported in studies that measure distribution of manganese up to 24 hours in mice [181] and rats [182]. Different formulations slightly alter the liver to heart ratio. This could be due to the higher first pass when injected intravenously compared to the intraperitoneal injection. The intravenous injection delivers substances directly into the blood vessels, bypasses the need for solute absorption. In contrast, substances administered intraperitoneally are absorbed into the mesenteric vessels which drain into the portal vein and pass through the liver [173]. Blood and muscle showed minimum changs in R1 and hence less Mn uptake in these regions. This resulted in higher myocardium to blood ratio that is favourable for imaging the heart, leading to high image contrast. The low R1 seen in blood was probably due to the short half-life of manganese in the blood as previously approximated as 3 min [181], [183]. Whereas in muscle, R1 is low indicating no or less manganese uptake in the muscle as contrast agents were injected once mice are under anaesthesia, which means no muscle contraction during the entire imaging. Mn clearance was achieved at 24 hours post-injection with a recover of all mice, and no effect was seen in the month following the experiment.

In the current study, the relaxivity of Mn with calcium supplements was not compared with the relaxivity of high dose *i.v.* Mn. This is due to the cardiac depression effect of high dose manganese seen in the in-vivo ultrasound study. Thus, only low Mn was used in the in-vivo MRI experiments. However, and estimation of the relaxivities could be calculated from the in vitro phantom study, which will be discussed in the next sections. The earliest time point of imaging in the present study was 10 minutes post-injection. A future study could perform imaging at an earlier time point and higher temporal resolutions potentially by further optimising the T1 mapping sequence. This might give additional information, especially during early time points.

2.5.3 The manganese content in the heart

The concept of quantifying the concentration of contrast agents from the relaxation properties in MRI images was first introduced to calculate the concentration and distribution volume of Gd-DTPA from a sample of cells suspended in media containing Gd-DTPA [184], [185]. This concept could be used to give an estimation of manganese concentration and distributions by calculating the relaxivity of manganese and MRI images of the heart and other regions of interest. Previous studies correlate in vitro with ex vivo manganese concentration and found Mn^{2+} relaxivities in ex vivo hearts [60 $(s\ mM)^{-1}$] is almost one order magnitude higher than $MnCl_2$ in water in vitro [6.9 $(s\ mM)^{-1}$] [95], [163]. Potential mechanisms that lead to these differences including the bindings of Mn^{2+} to other macromolecules in the cells [163]. Intracellular protein bindings enhance relaxation enhancement [165]. The manganese phantom used in the present study does not provide a direct measurement of manganese concentrations and distributions. However, it is a good approximation to study the relative change of manganese content following injection of different manganese formulations. A lower Mn concentration is expected in vivo due to higher relaxivity.

A more direct to assess the accumulation of Mn^{2+} quantitatively is by using radioactive manganese. One of the earliest studies, for example, used radioactive manganese to locate the distributions of Mn^{2+} in organs like liver, pancreas and kidney and also to locate the accumulation of manganese in intracellular organelles in rats [113], [181]. Another application of radioactive manganese, ^{54}Mn is used to look at the uptake of manganese in a healthy and ischemic myocardium in rats, suggesting its potential to be used in myocardial imaging [186]. Radioactive manganese has also been used as a calcium ion probe to study the L-type calcium channels in an isolated perfused rat heart [96]. These show higher sensitivity of radioactive manganese to quantify Mn^{2+} intracellularly, but it is limited as it logistically challenging and involves ionising radiation.

Manganese based contrast agents are intracellular and accumulate inside cardiomyocytes allowing for a wider imaging window. Manganese is an excellent paramagnetic contrast agent, with a higher relaxivity compared to gadolinium [132], [187]. The effect of calcium supplement used in this study on relaxivity was investigated. Following from that, it is also essential to quantify the manganese content in the heart and the distributions in other parts of the body following injection in order to assess further the safety profile of the dosage and formulations of Mn-based contrast agents. In these experiments, a wide range of Mn concentrations has been tested in vivo, with high dose infused *i.v.* known to cause cardiotoxicity, whist slow infusions have good safety profiles in pre-clinical and clinical studies. The similar relaxivity between groups in the phantom study indicated that the addition of CaG did not alter the molecular environment in a way that altered manganese's ability to shorten T1. The values were much similar to those reported [163], [165], [166] where r_1 is 6.9 $(s\ mM)^{-1}$. The present suggested that calcium supplement does not change the relaxivity of Mn.

An estimation of the concentration of Mn^{2+} within the myocardium suggests maximum loading concentrations of 0.22 ± 0.03mM for 0.1mM $MnCl_2$ i.p. is approximately twenty times the natural abundance of manganese in the body (~0.02mM) [177]. In healthy human volunteers, $MnCl_2$ at 5μM infused over 3 mins [104], and chelated MnDPDP at 15μM infused over 30 mins has been safely tested. Although these experiments were not designed to inform on the safe clinical use of Mn^{2+} directly, however, they provide valuable information on the mechanism through which manganese affects cardiac function and suggest Mn^{2+} based MRI contrast can be effectively utilised in pre-clinical studies.

The present data shows that Mn content is high in mitochondrial-rich organs; liver and heart, in line with previous studies [113], [181], [182]. The liver is the known clearance route for Mn so it is understandable that such high concentrations are found there. Skeletal muscle showed little Mn content as these muscles are not contracting as the animal was under anaesthesia when the imaging was performed. In the blood, Mn content was also low as the half-life of Mn in the blood is short as previously mentioned. The rapid clearance of Mn in the blood and high manganese uptake in the myocardium suggests that this would make a good tracer to study myocardial perfusion.

2.6 Summary

In summary, real-time ultrasound imaging shows that high dose manganese causes rapid and transient cardiac depression, which can be negated using Ca supplement. Mn infusion leads to significant signal enhancement with Mn supplemented with Ca showing the best contrast enhancement. Mn when administered intraperitoneally also shows a promising image quality and added with its simplicity to be used as a method for further study. Although these experiments were not designed to inform Mn^{2+} clinical safety, they provide valuable information on the mechanism by which Manganese affects cardiac function and suggests that Mn^{2+} based MRI contrast can be used effectively in pre-clinical and clinical studies. Furthermore, the technique using real-time ultrasound may be applicable for measuring calcium homeostasis during the early stage of myocardial infarction. Finally, our ability to do these studies in the in vivo mouse should make MEMRI useful for studying a variety of mouse models and disease with altered calcium influx.

Chapter 3 : Manganese-enhanced T1 mapping as an early imaging indicator of intracellular Ca^{2+} homeostasis in acute myocardial infarction model

The efficiency of manganese as an MRI contrast agent that induced changes in T1 relaxation of nearby tissue have been well studied [163], [165]. As Mn^{2+} is a Ca^{2+} analogue, it has great potential as an MRI indicator of Ca^{2+} influx into the cardiomyocytes in vivo. Intracellular calcium is the central regulator of cardiac contractility. It is becoming increasingly important to be able to quantitatively assess intracellular calcium in the heart to help in understanding the pathophysiology of an early phase of heart disease and to investigate a new intervention strategy. Thus, the aim of this chapter is to assess the efficacy of manganese-enhanced T1-mapping in monitoring dynamic changes of intracellular Ca^{2+} response to ischemic injury in a mouse model of acute myocardial infarction. This technique is presented in the context of acute myocardial infarction but could be applied in a wide range of cardiac diseases.

Abstract

Manganese-enhanced T1 mapping as an early imaging indicator of intracellular Ca^{2+} homeostasis in acute myocardial infarction model

Introduction: Intracellular MRI contrast agents can provide essential information on cell viability. Mn^{2+} enters viable cardiomyocytes via L-type calcium channels and enhances intracellular T1 relaxation. As an analogue of calcium, Mn^{2+}-induced changes in T1 can be used as an indicator of Ca^{2+} influx rate into cardiomyocytes in vivo. They could provide additional information to that routinely acquired using late gadolinium-enhanced MRI. The hypothesised is that Mn^{2+} mediated changes in T1 could reflect Ca^{2+} influx in the myocardium during ischemic injury. By pre-loaded the myocardium with Mn prior to coronary occlusion, the present study aimed to assess the efficacy of MEMRI T1-mapping in monitoring dynamic features of intracellular Ca^{2+} response to ischemic injury in a mouse model of myocardial infarction (MI). The present study is the first quantitative in vivo MRI assessment of calcium homeostasis in the early phase of myocardial injury.

Methods: All procedures complied with the UK Home Office and local animal care and welfare committees. In the MI group, adult male C57B1/6 mice received intraperitoneal injections of $MnCl_2$ (0.1mmol/kg) 40 minutes before a permanent left anterior descending (LAD) coronary artery ligation so that the level of Mn^{2+} within the myocardium would be reasonably stable during the imaging time-points 1h to 3h post-MI (See the pilot study in Section 3.4.1). T1-mapping was used to monitor dynamic alterations of calcium homeostasis at 1h, 2h and 3h after LAD occlusion and at 2d, with $MnCl_2$ injected 100 minutes prior to MRI (Mn loading time similar to the 1h post-MI group). R1 values (1/T1=the relaxivity of the tissue) were analysed from the area-at-risk of infarction segments (AAR-MI, n=12) and viable segments (Remote-MI, n=12) of infarcted hearts, and naïve control heart (Viable-Naïve, n=12). Imaging was performed using a 9.4T Agilent MRI system and a multi-inversion time Look-Locker sequence in the short-axis orientation (TE/TR = 3.04/1.11ms, 18 inversion times at consecutive R waves, 20º excitation pulse, slice thickness = 1.0mm, FOV = 25.6 x 25.6 mm, matrix size = 128 x 128) as described [74].

Results: As soon as 1 hour after LAD occlusion, R1 values were significantly higher in the Remote-MI tissue compared with AAR-MI tissue ($5.06 \pm 0.6s^{-1}$ and $2.90 \pm 02s^{-1}$ respectively) ($p=0.0025$), allowing early delineation of the infarct region (Figure 3.8 and Table 3-1). When compared to naïve control animals, R1 values in the Remote-MI were significantly higher at 1h, 2h and 3h post-MI ($p=0.0008$, $p=0.002$, and $p=0.002$ respectively). In contrast, the AAR-MI tissue was not significantly different as compared to Viable-Naïve. Interestingly, R1 in the Remote-MI tissue continued to rise at 2h and 3h post-MI ($p=0.051$ and $p=0.048$ respectively and $R^2 = 0.94$) (Figure 3.9 and Figure 3.10), but remained constant in the AAR-MI and Healthy-Naive. The R1 values of the LV blood pool in MI and Naïve groups were similar and did not change over the 3 hours (Figure 3.10 and Table 3-1). By two days post-MI, R1 levels in the surviving myocardium were normalised and now have similar Mn^{2+} uptake with the healthy myocardium in the naïve control group but were still higher in the AAR-MI tissue. A small increase in R1 values at, 2h and 3h post-ischemic injury in the AAR-MI tissue which remains constant over the 3 hours but lower than controls at two days post-MI

Discussion: Acutely after ischemic injury a large increase in R1 (reflecting increased Mn^{2+} uptake) occurred in Remote-MI myocytes, likely due to elevated catecholamine levels acutely post-MI; increased cardiac work and thus increased Ca^{2+}/Mn^{2+} uptake. By 2 days the catecholamine storm has passed, and R1 levels in the surviving myocardium normalise, while Mn uptake in the dead infarct region was reduced due to lack of functional myocytes. A striking rise in cytosolic Ca^{2+} during acute ischemia has been well documented previously [188]–[191].

Conclusions: T1-Mapping manganese-enhanced-MRI offers a valuable in vivo tool for optimisation of the many emerging pharmacological and biological interventions which aim to modulate Ca^{2+} homeostasis acuity after MI.

3.1 Introduction

Myocardial ischemia is a consequence of an imbalance between oxygen supply and demand. In the clinical context, myocardial ischemia is usually due to thrombotic occlusion of the coronary artery caused by rupture of a vulnerable plaque. Coronary artery occlusion causes ischemia (hypo-perfusion of blood) in the perfusion bed. Myocardial ischemia causes an immediate loss of contractility in the affected myocardium; a condition termed hypokinesis, which induces systolic dysfunction. Changes in intracellular Ca^{2+} concentration regulate cardiac contractility. The ability to quantitatively measure changes in intracellular Ca^{2+} at an early phase during ischemia will help improve disease management and prognostic outcome in patients with acute myocardial infarction. The experiment conducted in this chapter aims to assess the efficacy of MEMRI T1-mapping in quantifying dynamic changes of intracellular Ca^{2+} response to ischemic injury in a mouse model of acute myocardial infarction.

To best interpret the experiments in this chapter, an understanding of intracellular calcium regulation and cardiac contractility in cardiac muscle in healthy heart, and myocardial ischemia would be helpful, which is discussed in sections, 3.1.1 and 3.1.2 respectively. An overview of methods for measuring intracellular calcium during ischemia is discussed in section 3.1.3. Section 3.2 discusses the aims of the experiments in this chapter, followed by section 3.3, which discusses the methodological approach for the study. Finally, the results are presented in section 3.4 and discussed in section 3.5.

3.1.1 Regulation of intracellular Ca^{2+} and cardiac contractility

Myocardial contractility represents the ability of the heart muscle to contract and relax in a well-coordinated manner. It is well known that Ca^{2+} homeostasis plays a critical role in regulating cardiac contractility on a beat-to-beat basis. The primary factor that regulates cardiac contractility is the level of intracellular Ca^{2+} [192]. Calcium ions bind to troponin C and initiate cardiac muscle contraction. The force of cardiac muscle contraction is determined by two factors. First, it depends on the amount of Ca^{2+} bound to troponin, which relies on both the amplitude and the duration of the rise of cytosolic Ca^{2+}. Second, it depends on the strength of calcium-binding, which is controlled by several factors such as phosphorylation. In rats and mice, the Ca^{2+} that triggers the contraction of cardiac muscle comes from two sources: the Ca^{2+} taken up from the extracellular fluid via L-type calcium channels (about 10% of the total) and also the Ca^{2+} that is released from the sarcoplasmic reticulum by the process of calcium-induced calcium release (about 90% of the total) [143], [144].

For normal heart function, cytoplasmic calcium must be sufficiently high during systole and low during diastole. It is also important to note that normal cardiac function requires intracellular Ca^{2+} to recover quickly to basal levels to allow myocardial relaxation and refilling of blood into the ventricles. Therefore, both systolic and diastolic intracellular Ca^{2+} need to be tightly regulated. For relaxation of the heart during diastole to occur, Ca^{2+} is pumped out of the cell via Na^{+}-Ca^{2+} exchanger (NCX) and into the sarcoplasmic reticulum (SR) via sacro/endoplasmic reticulum Ca^{2+}-ATPase (SERCA). Ca^{2+} influx into the cell during each beat must be equal to the efflux of Ca^{2+} in order to maintain homeostasis. Equally, the amount of Ca^{2+} released from SR must be equal to the amount that is taken back up [192]. For a full description of the role of calcium and other associated factors such as the sarcoplasmic reticulum release complex and calcium current in modulating contraction and flux balance, readers are directed to review article by Bers et al. (2000) [126] and Eisner et al. (2017) [178].

Intracellular Ca^{2+} changes also occur in association with the increase in cardiac contractility when there is β-adrenergic stimulation. One example where β-adrenergic stimulation occurs is during the fight-or-flight response. The fight-or-flight response is a physiological response to stress, fear, or exercise, and leads to the release of catecholamines and activation of β-adrenoreceptors [193]. Activation of β-adrenoreceptors leads to a rise in intracellular cyclic AMP. This second messenger activates protein kinase A (PKA) which through phosphorylation activates L-type

Ca^{2+}, accelerates SERCA, increases SR Ca^{2+} release via ryanodine receptors and decreases myofilament Ca^{2+} affinity. The net result is an increase and acceleration of force generation and relaxation, also known as positive inotropic and lusitropic effects [192], [194], [195]. The increasing amount of Ca^{2+} stored in the SR leads to increased cardiac contractility. The rate of relaxation of cardiac muscle is also increased as Ca^{2+} is taken up into the SR more quickly.

Calcium fluxes in the heart are also altered following administration of pharmacological drugs. Pharmacological agents that increase contractility are also known as positive inotropes. An example of a positive inotrope drug is isoproterenol, which has a sympathomimetic action resembling endogenous noradrenaline and adrenaline, inducing an increase in cytosolic Ca^{2+} leading to an increase in cardiac contractility [190], [196]. In some clinical conditions such as hypertension or angina (an early clinical sign of myocardial infarction), it may be appropriate to decrease the force of cardiac contraction of the heart muscle. In this case, negative inotropes drugs might be used. An example of negative inotropic drugs is the β-adrenoreceptor blockers, which suppress the effects of activating the sympathetic nerves to the heart, and calcium channel blocking drugs which act on the L-type calcium channels. Verapamil and diltiazem, for example, reduce the flux of calcium ions into cardiac muscle.

3.1.2 Calcium homeostasis imbalance during myocardial ischemic injury

Calcium homeostasis imbalance is a well-recognised feature of myocardial ischemic injury. Several studies proposed an increase in the level of intracellular Ca^{2+} as one of the early pathological changes during the early phase of acute myocardial infarction [189]–[191]. Myocardial ischemia occurs when there is an imbalance between oxygen supply and demand. The supply of oxygen to the myocardium depends on two main factors; oxygen content of the blood and the rate of coronary blood flow (Figure 3.1). The main determinants of blood oxygen content are: (1) the haemoglobin concentration, and (2) the degree of systemic oxygenation. Coronary blood flow *(Q)* is determined by coronary perfusion pressure (*P*) and vascular resistance (*R*).

$$Q = \frac{P}{R}$$

[Equation 3.1]

The greatest blood flow occurs during diastole, when the myocardium is relaxing. During systole, coronary perfusion is impaired by the compression of the small coronary branches as they course through the contracting myocardium. Conditions that decrease perfusion pressure (common cardiac conditions in heart failure and coronary artery disease) decrease coronary artery pressure and may lessen myocardial blood supply [197]. Patients with these conditions are more prone to myocardial ischemia. On the other hand, coronary artery resistance is regulated by (1) forces that externally compress the coronary arteries and (2) factors that alter the intrinsic coronary tone (regulated by the accumulation of local metabolites, endothelium-derived substances, and neural innervation). For myocardial oxygen demand, the major determinants of are: (1) ventricular wall stress, (2) heart rate, and (3) contractility (which will be the main discussion in this section) (Figure 3.1). In the setting of coronary atherosclerosis, the fall in perfusion pressure distal to the arterial stenosis, along with the dysfunction of endothelium in the vascular bed with reduced perfusion, causes a mismatch between the available blood supply and myocardial oxygen demand.

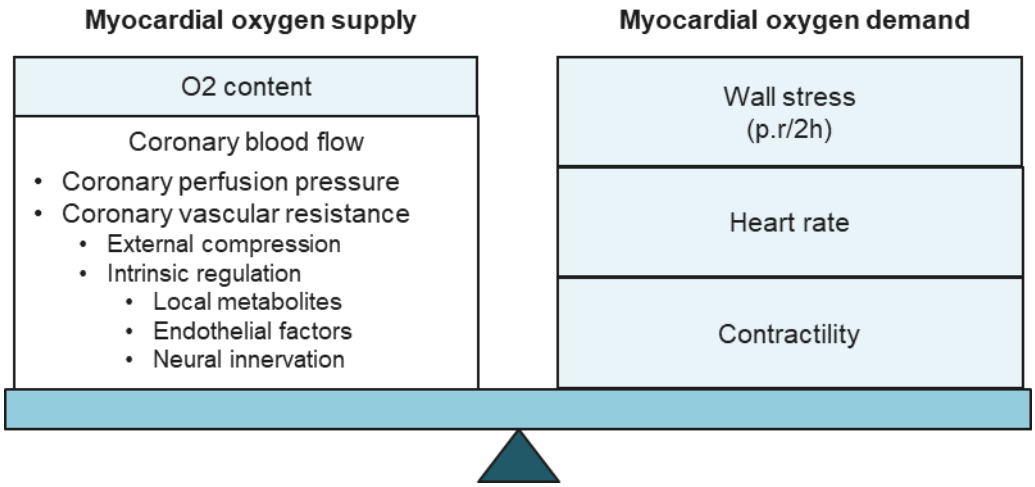

Figure 3.1: Major determinants of myocardial oxygen supply and demands.
P, ventricular pressure; r, ventricular radius; h, ventricular wall thickness. Adapted from Leonard 2001.

Lack of blood flow and the consequent decrease in pO_2 inhibits mitochondrial oxidative phosphorylation, causing a major loss of ATP production for energy metabolism. During ischemia, myocytes switch from aerobic to anaerobic metabolic pathways for ATP production. This, however, leads to the accumulation of hydrogen ions (H^+) and lactate, resulting in intracellular acidosis and inhibition of glycolysis. It is postulated that the altered metabolism can induce alterations in the cell membrane function while still preserving the cell membrane integrity, leading to ionic perturbation, including an increase in intracellular Ca^{2+}. The early increase in intracellular Ca^{2+} develops due to multifactorial changes in the activity of the transport system in the sarcolemma (i.e. Na^+, K^+-ATPase and NCX) and sarcoplasmic reticulum (i.e. SERCA). The possible mechanisms involve; (1) Increase in K^+ efflux (due to accumulation of metabolites and phosphate) hence, increased accumulation of K^+ in the extracellular space, leading to reduction of the action potential amplitude, rate of rise, and duration; (2) Increase in free Mg^{2+} (due to release of Mg^{2+} from hydrolysed ATP and deficiency of removal of Mg^{2+}); (3) Influx of Cl^- and water leads to cell swelling; (4) Na^+, K^+-ATPase is inhibited (due to the decline in ATP) resulting in a further decline in K^+ and increase Na^+; (5) In response to an increases level of Na^+, the NCX operates in a reverse mode, transporting Na^+ out of the cell and more Ca^{2+} into the cytosol; (6) Reduced activity of the SERCA pump following due to lack of ATP, resulting in reduce Ca^{2+} in SR and further causing an increase in cytosolic Ca^{2+}.

This initial increase in cytosolic Ca^{2+} causes the activation of proteases which decrease the sensitivity of myofilaments to Ca^{2+}, leading to reduced cardiac

contractility in the ischemic zone despite the elevated cytosolic Ca^{2+}. [12], [189], [198]. Prolonged, altered metabolic activity with a sustained increase in cytosolic Ca^{2+} activates phospholipase, which releases lysophospholipids and free fatty acids which leads to phospholipid degradation. These mechanisms contribute to ATP depletion and marked calcium overload, mediating the progressive impairment of membrane integrity and cell death. Previous studies have reported an increase in intracellular Ca^{2+} during the first 20 minutes of ischemia [199], [200]. However, they only investigate up to 20 minutes post occlusion, meaning the extent of intracellular Ca^{2+} elevation over longer periods is unknown. Intracellular Ca^{2+} increases before cardiomyocytes died and ruptured [191], thus, monitoring intracellular Ca^{2+} changes can serve as an early indicator of cell injury after myocardial ischemia. Figure 3.2 summarises mechanisms of altered calcium homeostasis and other ionic perturbations during myocardial ischemia. For a full description of the mechanisms, the reader is referred to review articles [201], [202].

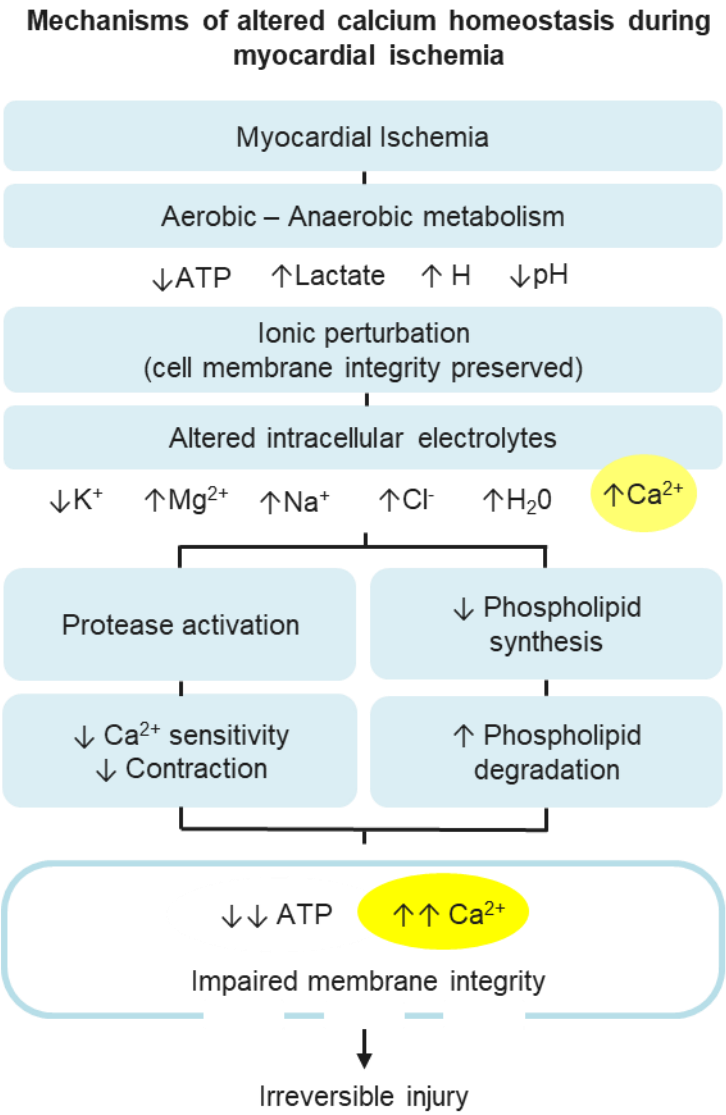

Figure 3.2: Mechanisms of calcium homeostasis during myocardial ischemia.

Oxygen deficiency induces metabolic changes, including decreased adenosine triphosphate (ATP), decreased pH, and lactate accumulation, in ischemic myocytes. The altered metabolism leads to impaired membrane transport with resultant derangements in intracellular electrolytes. Adapted from [202].

During myocardial ischemia, increased sympathetic stimulation is also observed [203] (Figure 3.3). This may be due to the normal compensatory mechanism due to reduced cardiac output, and can also be due to the release of catecholamines during ischemia. High levels of catecholamines have been seen in patients with acute myocardial infarction [204]–[206]. The release of catecholamines during ischemia occurs through three mechanisms: (1) exocytotic release, (2) increase cardiac efferent sympathetic nerve activity, and (3) local metabolic release [207]. Sympathetic activation during acute myocardial infarction is a critical response to an increase in intracellular Ca^{2+}, which increases cardiac contractility to maintain the cardiac output. Excessive catecholamines release, however, is associated with the occurrence of arrhythmias at the early phase of myocardial infarction. Thus, measuring the level of sympathetic activation during ischemia would be beneficial to help in the management of the consequences of diseases, i.e. arrhythmias.

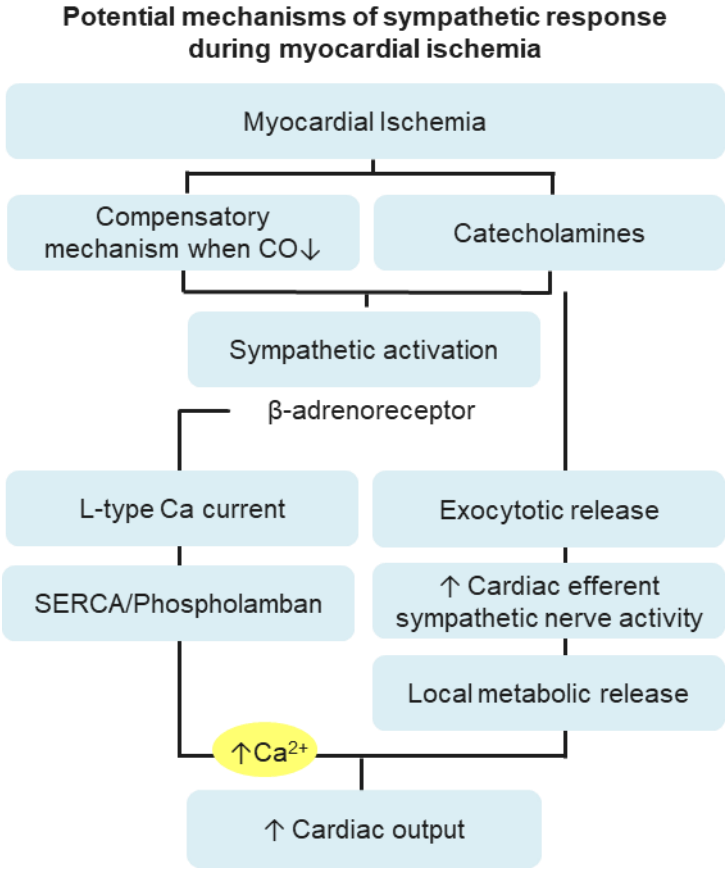

Figure 3.3: Postulated mechanisms of sympathetic response during myocardial ischemia.

Adapted from [192], [203], [207]–[209].

3.1.3 Methods for measuring Intracellular Ca^{2+} in a whole heart

As an indicator of early cell injury, quantification of intracellular Ca^{2+} in a contracting heart and investigation of the potential role of altered intracellular calcium in the pathogenesis of myocardial ischemic injury and cell death would contribute to the understanding of cardiac physiology and mechanisms of cardiac disease. As a central regulator of cardiac contractility and viability, the measurement of intracellular calcium in the whole heart is essential. Direct measurement of Ca^{2+} in myoplasm is exceptionally difficult for two reasons : (1) the amount of Ca^{2+} in the cell is extremely small compared to the amount of extracellular Ca^{2+}, and (2) the Ca^{2+} that enters the cell does not remain long due to the rapid cellular activity of calcium. Various approaches have been developed to try to accurately measure intracellular calcium in the whole heart including: (1) NMR spectroscopy, (2) Bioluminescence imaging, (3) Fluorescence imaging, (4) Optical imaging, and (5) Manganese-enhanced MRI.

One strategy that has been used to estimate the intracellular Ca^{2+} in the perfused heart is NMR spectroscopy. ^{19}F NMR detectable Ca^{2+} indicators are made by fluorination of a Ca^{2+} chelator (5F-BAPTA). The NMR spectrum changes when the 5F-BAPTA combined with Ca^{2+}. Intracellular Ca^{2+} change is then assessed by measuring the ^{19}F NMR spectra in a perfused heart loaded with 5F-BAPTA. This successfully detected an increase in intracellular Ca^{2+} after 10 to 20 minutes of ischemia [191], [199]. However, data acquisition is challenging, requiring an average of several cardiac cycles, making it less sensitive to detect changes in intracellular Ca^{2+}.

Another strategy is to use bioluminescent imaging and fluorescent imaging. A variety of light-emitting compounds have been used to image intracellular Ca^{2+} within myocardial tissue. One of the earliest compound used to study Ca^{2+} was aequorin. Aequorin was isolated from the jellyfish *Aequorea victoria and* emits blue bioluminescence when bound to Ca^{2+}. Aequorin emits light from an intramolecular reaction and does not require optical excitation. One of the limitations of bioluminescence imaging (BLI) is that it requires microinjection of the compound as it does not pass freely across the sarcolemma [210]. Kihara et al. 1989 performed the first study that used BLI to look at intracellular Ca^{2+} in an isolated perfused heart. They measured intracellular Ca^{2+} changes during 3 minutes of global ischemia and reported an increase in Ca^{2+} as LV systolic and diastolic pressure decreased [188].

In addition to the aequorin method, calcium fluorescence probes have been used to study changes in intracellular Ca^{2+}. The general structure of a fluorescence probe consists of a fluorophore, a chelator for binding to Ca^{2+}, and an optional conjugation to allow the probe to cross the cell membrane. Quin 2, a highly selective Ca^{2+} indicator derived from fluorescent quinolone, was the first calcium indicator used for continuous measurement of the effects of pharmacological agents on intracellular Ca^{2+} [196]. They reported an increased in cardiac inotropy when there was a release of catecholamines. Several other Ca^{2+} fluorescence probes used in whole-heart studies looking at changes in Ca^{2+} during ischemia include indo-1 [189], [190], fura-2 [211], fluorescein (fluo 1, fluo 2, and fluo 3), chromophores rhodamine (Rhod-2) [200], [212]. The most recent development in Ca^{2+} fluorescence probes is the genetically encoded Ca^{2+} indicator, the GCaMP series. Rhod-2 and GCaMP are among the most commonly used Ca^{2+} fluorescence probes in optical imaging.

Optical imaging is currently the preferred method to measure spatial and temporal Ca^{2+} changes. Optical mapping requires a light source to illuminate the heart with a fluorescent reporter and a detector to sense the changes in fluorescence [213], [214]. An advantage of optical mapping is that it can measure both intracellular calcium changes and the action potential simultaneously using a Ca^{2+} fluorescent probe and potentiometric probe, respectively. The potentiometric probe works in a way it will provide a fluorescent signal when there are changes in transmembrane potential reflecting changes in the action potential. The development of Ca^{2+} fluorescence probes is driven by the aim of producing a higher quantum yield, better emission and excitation spectrums. Despite the promising advancement in of Ca^{2+} fluorescence probes and optical imaging technologies, there remains a challenge to measure intracellular Ca^{2+} in vivo that is clinically translatable. One possible approach is by using a paramagnetic contrast agent that has similar physical properties to Ca^{2+}, such as manganese ion (Mn^{2+}).

Manganese ion is known to enter cardiac myocytes via L-type calcium channels and act as an excellent T1 contrast agent. The ability of Mn^{2+} to enter a cell and enhances nearby T1 relaxations time makes it a potent intracellular MR contrast agent to measure in intracellular Ca^{2+} in the heart. It is well documented that pharmacological agents cause an increase and decrease in intracellular Ca^{2+} in the heart [190], [196]. A study by Hunter et al. (1981) using radioactive manganese (^{54}Mn) shows increased and decreased in Mn^{2+} uptake following administration of isoproterenol and verapamil, respectively. A similar finding was reported by Hu et al. (2001) using T1-weighted MRI following injection of $MnCl_2$ [115]. These findings show

the potential of Mn as a surrogate marker of changes in intracellular Ca. Since that, manganese-enhanced MRI has been used to quantify myocardial infarction in pre-clinical in-vivo studies.

Quantitative measurement of Mn^{2+} uptake and hence Ca^{2+} uptake in a myocardial infarct model showed a different T1 relaxation time, reflecting a different manganese uptake in the remote and infarcted myocardium [97], [99], [101], [121]. However, these studies are limited to the assessment of myocardial infarction at later phases. Studies performed during and at early time post-ischemia, but have poor image resolution, and assessment relies on the enhancement pattern, which is prone to over and underestimation and lack sensitivity in detecting early cell injury. There remains the need for a quantitative in-vivo assessment for measuring subtle changes during the early ischemic injury [122], [133].

3.2 Chapter outline and aim

Mn^{2+} is a Ca^{2+} analogue and can enter cardiomyocytes through the L-type Calcium channel, giving a direct insight into the pathogenesis of ischemic injury. It can be used as a surrogate marker of changes in Ca^{2+} flux. Imaging at the early phase of myocardial injury will allow assessment of calcium homeostasis and progress of cell death in the early phase of myocardial injury. Manganese coupled with T1 Mapping sequence offers a more sensitive imaging biomarker assessment of myocardial viability, allowing early detection of ischemic injury. In this chapter, we will implement and optimise T1 mapping to see the subtle changes of Mn^{2+} during early acute ischemic injury ability.

The aim of this chapter is to assess the efficacy of MEMRI T1-mapping in monitoring dynamic features of intracellular Ca^{2+} response to ischemic injury in a mouse model of myocardial infarction (MI). By pre-loading the myocardium with Mn prior to coronary occlusion, I hypothesised that Mn^{2+} mediated changes in T1 could reflect Ca^{2+} influx in the myocardium during ischemic injury.

3.3 Methods

This chapter consisted of two parts. In the first part, a pilot study was conducted to determine the manganese retention in the myocardium using T1 mapping. In the second part, T1 mapping-Manganese-enhanced MRI was used to assess Calcium homeostasis after coronary occlusion in an acute myocardial infarction model.

3.3.1 Pilot Study: Manganese retention in myocardium

T_1 weighting and T_1 mapping are the two primary methods used to characterise Mn^{2+} uptake in MEMRI [99], [115], [215]. Signal to noise in T_1 weighted images provides a high temporal resolution method for detecting the relative change in the signal after Mn^{2+} injection. However, it does not provide direct quantification of Mn^{2+} uptake in cells. In contrast, T1 mapping offers quantitative measurement of the Mn^{2+} accumulation because of the linear relationship between the relaxation rate (R1 = 1/T1) and Mn^{2+} concentration within the specific range [95], [99].

In this study, I used T1 mapping to measure the kinetics of Mn^{2+} in the mouse heart. My previous study in Section 2.4.1 showed that administration of 0.10mmol/kg $MnCl_2$ via intravenous injection (*i.v*) (when supplemented with CaG in 1:1 and 2:1 ratio) and via intraperitoneal injection (*i.p.*) has no significant effect on the cardiac contractility and is within the safe dose limit. The following studies comprised of experiments conducted in a mouse model of myocardial infarction during the first hour after surgery and hence the time for animal preparation in MRI scanner. Considering the challenging MRI set-up and the time constraint in between surgery and image acquisition, I used intraperitoneal injection which offers a more convenient approach in administering contrast agents in MRI for the rest of experiments in this thesis.

So that imaging could be performed during the steady-state of enhancement, a pilot study was performed to assess the accumulation and retention of Mn^{2+} in the myocardium after $MnCl_2$ injection The aim of the pilot study is to investigate the kinetics of manganese in myocardium and blood by measuring the T1 values at baseline and every 10 minutes up to 4 hours (n=5) post $MnCl_2$ injections. Images were acquired using a LL inversion recovery sequence as described in Section 2.3.2.3. Previous studies have shown that Mn^{2+} stays in the myocardium for up to 4 hours [103]. However, that also depends on the concentration and dose given. Thus, it is important to study the retention time with the selected dose in this study. This will allow us to determine the rate of change in Mn^{2+} uptake in normal cardiac physiology

of the heart. Cine MRI was performed simultaneously to monitor the global cardiac function over the course of the experiment.

3.3.2 Myocardial infarction model

Animal models of myocardial infarction play an important role in the prevention, diagnosis and development of therapeutics for human myocardial infarction [42]. In this project, I used a permanent occlusion model of myocardial infarction, where the left anterior descending (LAD) coronary artery was occluded. Surgeries were conducted by Ms. Valerie Taylor in a controlled, sterile surgical suite with aseptic operating practices. Anaesthesia was induced and maintained in the mice using isoflurane anaesthetic at 4% and 1.5%, respectively, in 1.5l/min. Analgesia was provided using a 0.1mg/kg intramuscular injection of buprenorphine at the beginning of surgery, and both 6- and 24-hours post-surgery. Mice were positioned supine on a heated operating table to maintain physiological body temperature, which was monitored using a rectal thermometer. Artificial respiration was provided by a ventilator (MiniVent Type 845, Hugo Sachs Electronik, Germany) via oral intubation. Open-chest surgery was performed to gain access to the heart. The LAD was identified, and a suture was placed under the vessel approximately 2 mm below the tip of the left atrium (Figure 3.4) was used to occlude the LAD. The ligature was left in place, all surgical openings were closed, and the animal was recovered. All procedures complied with the UK Home Office and local animal care and welfare committees.

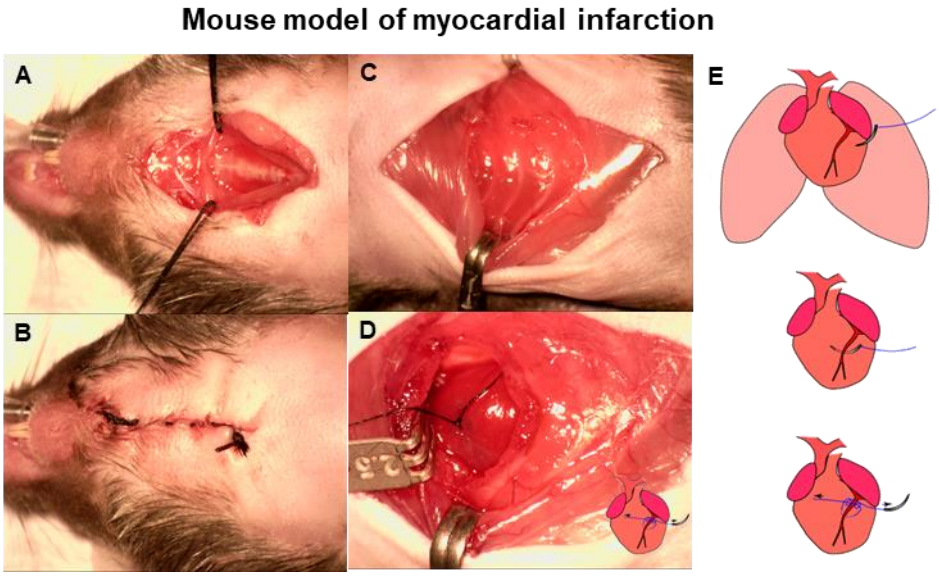

Figure 3.4: In vivo myocardial infarction model after LAD ligation.

A, Mice were placed in the supine position and the next extended. Direct observation of the trachea was used to aid intubation by creating a small skin incision to the neck. The trachea was exposed and the ventilation cannula was passed through the mouth into the trachea. B, The incision was sutured once successful intubation was confirmed once is visualised inside the trachea and by observing regular chest movement upon ventilation. C, For access to the LAD, a skin incision was made laterally across the chest at the approximate position of the 4th intercostal space. D & E, The LAD was identified by its brighter red colour and often by its pulsatile appearance. The LAD was sutured using 7-0 Sofsilk Black (VS809, Coviden, US). Successful ischaemia upon occlusion of the snare system was confirmed primarily by appreciable myocardial pallor distal to the suture.

3.3.3 Experimental design: T1 mapping-manganese-enhanced MRI was used to assess calcium homeostasis

For MI group, adult male C57B1/6 mice (n=8) received intraperitoneal injections of 2 µL per gram body weight of 50mM (0.10mmol/kg) $MnCl_2$ 40 minutes before left anterior descending (LAD) coronary artery occlusion. From the pilot study data in Section 3.3.1, 40 minutes suffice to allow the uptake manganese in the myocardium. By pre-loading the mouse heart and hence label the entire myocardium with manganese, the study aims to see the changes in manganese uptake in the perfusion defect following acutely post-LAD ligation. I hypothesized that manganese uptake in the perfusion defect will be decreased as myocytes loss its functionality.

T1-mapping was used to monitor dynamic alterations of manganese uptake which reflects the calcium fluxes at 1, 2 and 3 hours after LAD occlusion and at 2 days, with the second dose of Mn^{2+} injected 100min prior to MRI (Mn^{2+} loading time similar to the 1-hour post-MI group) (Figure 3.5). Mid-papillary short-axis view was acquired using a Look-Locker inversion recovery sequence as described in section

2.3.2.4. Cardiac function was measured using CINE MRI sequence as described in 1.3.2.2. Whereas in the naïve control group adult male C57B1/6 mice (n=5), imaging was performed at the same time post-Mn injection as the MI group. All mice were sacrificed at the end of the MRI scan.

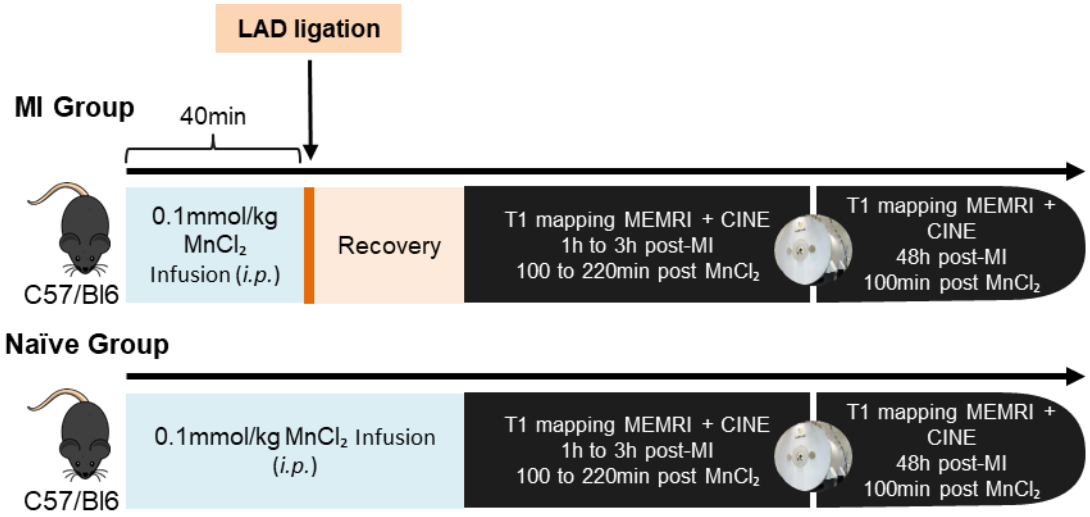

Figure 3.5: Schematic of MRI image acquisition protocol.
Mice were preloaded with $MnCl_2$ 40 minutes before LAD ligation and were scanned at 1h to 3h and 48h post-MI.

3.3.3.1 T1 relaxation analysis

T1 was generated using an in-house MATLAB code. For analysis, R1 (1/T1) values were calculated from 3 tissue types: Infarcted hearts were classified into (1) area at risk segments (AAR-MI, n=8) and (2) viable segments (Remote-MI, n=8): These were compared to (3) naïve control heart data (Healthy-Naive, n=5) acquired at the same time points after $MnCl_2$ injections. R1 values of the LV blood pool (white circle) were also measured (Figure 3.6).

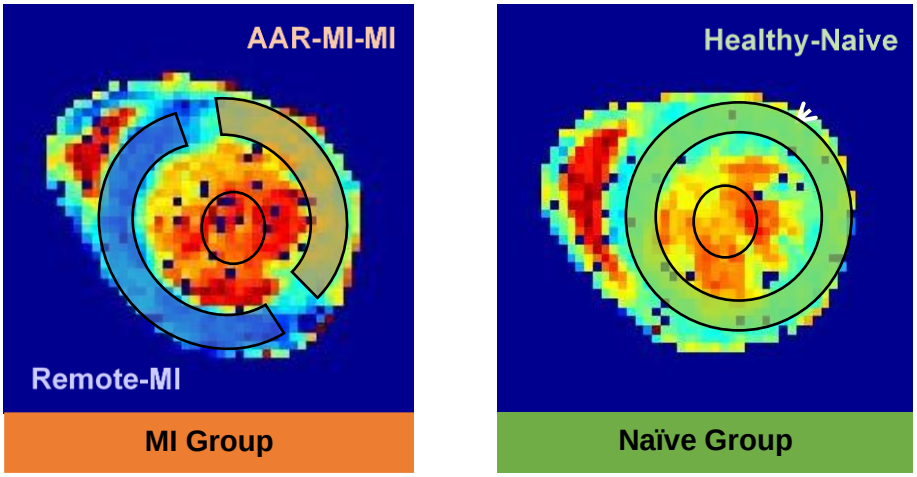

Figure 3.6: Image segmentation method for T1 mapping MEMRI.
Segmentation of myocardium and blood pool region to calculate mean T1 value. Dark pixels in myocardium indicate points where the fitting algorithm fails.

3.3.3.2 CINE MRI for assessment of cardiac function

CINE sequence, shorthand for cinematic, acquires a time series of static images of the heart that when displayed sequentially visualises the beating heart. Cine imaging relies on accurate gating for physiological motion. A gated gradient echo sequence was used to acquire cine cardiac images. Imaging parameters for mice were as follows; echo time (TE) = 1.18 ms, repetition time (TR) = 5 ms, flip angle = 15°, slice thickness = 1 mm, field of view (FOV) = 25.6 × 25.6 mm, matrix size = 128 × 128, number of signal averages = 2. The basic principles of the cine acquisition scheme and the GRE pulse sequence are described in Section 1.3.2.2.

Figure 3.7 shows an example of a segmented CINE stack. The software package applies an automatic segmentation algorithm to the images. If the automated segmentation is inaccurate, the user can correct the regions manually. Segmentation of the left ventricle endocardium in all ED slices gives end-diastolic volume (EDV). Similarly, endocardial segmentation in all ES slices gives end-systolic volume (ESV). From these two sets of measurements, stroke volume (SV) and ejection fraction (EF) can be calculated.

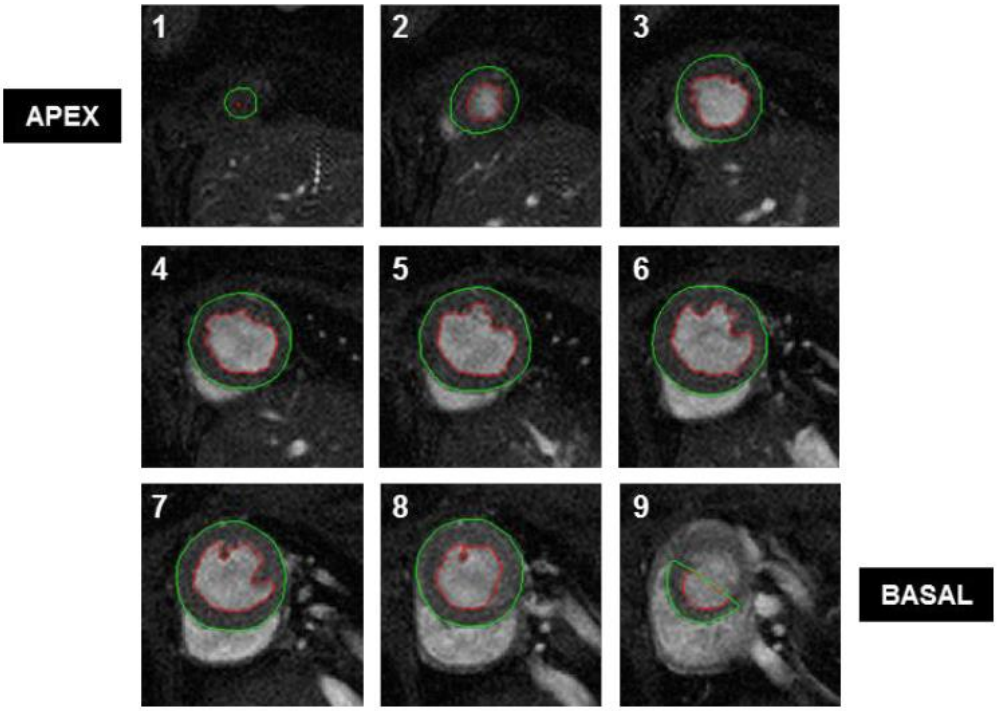

Figure 3.7: CINE MRI image analysis.

Short-axis CINE stack segmentation of the left ventricle blood pool (red) and left ventricle epicardium (green) at end-diastole for calculating systolic functional parameters. In the most basal slice (9), the segmentation intersects the ventricular and atrial tissue and blood. For analysis of functional parameters, the CINE stack is also segmented at end-systole.

3.3.4 Statistical tests

All results are presented as mean value ± standard error mean (SEM) otherwise stated. A linear regression analysis was performed between time post coronary occlusion (1-hour to 3 hours post-MI) and R1 value in the Remote-MI, AAR-MI, Healthy-Naive, Blood-MI, and Blood-Naïve groups. One-way repeated measures ANOVA Tukey's multiple comparison test were used to test the significance between 4-time points post coronary occlusion (1-hour, 2 hours, 3 hours and 48 hours) for each group (Remote-MI, AAR-MI, Healthy-Naive, Blood-MI and Blood-Naïve). One-way ANOVA was also used to test the significance between groups at each time point post coronary occlusion. In all cases, a p-value of less than 0.05 was considered significant.

3.4 Results

3.4.1 A pilot study of manganese retention in the myocardium

Representative T1 maps acquired at baseline and every 10min up to 4h after $MnCl_2$ injection and the dynamics of R1 changes are shown in Figure 3.8A-B. T1 maps show rapid T1 reduction is observed in the myocardium during the first 20 minutes as compared with the at baseline and further reduced steadily before it reaches a steady-state at 100min up to 4h post-manganese injection. Correspondingly, there is a significant increase in R1 (reflecting increased Mn^{2+} uptake) at 20min ($1.79 \pm 0.08 s^{-1}$) ($p < 0.05$) as compared to baseline ($1.06 \pm 0.08 s^{-1}$) and further increased steadily up to 100min ($2.25 \pm 0.08 s^{-1}$) and reached a steady-state ($2.44 s^{-1}$, 95% CI 2.34, 2.58) at ~200min post $MnCl_2$ injection. A one-phase decay nonlinear regression line was fitted, and the half-life was estimated. The exponential fit showed an exponential decay rate of 0.020/min, resulting in an estimated half-life of 34.2 minutes.

In blood pool regions, I observed a reduction in T1, reflecting the uptake of Mn^{2+} in blood, within the first few minutes of injection and remained constant throughout the experiment. The R1 values in the LV blood pool region were significantly increased at 20min ($1.14 \pm 0.03 s^{-1}$) ($p < 0.05$) as compared to baseline ($0.83 \pm 0.33 s^{-1}$) and remain constant up to 4h after reaching a plateau ($1.14 s^{-1}$, 95% CI 1.121, 1.164) at ~80min post $MnCl_2$ injection. The exponential fit showed an exponential decay rate of 0.25/min, resulting in an estimated half-life of 2.8 minutes. There were no obvious alterations in cardiac function, or heart rate and all mice recovered fully.

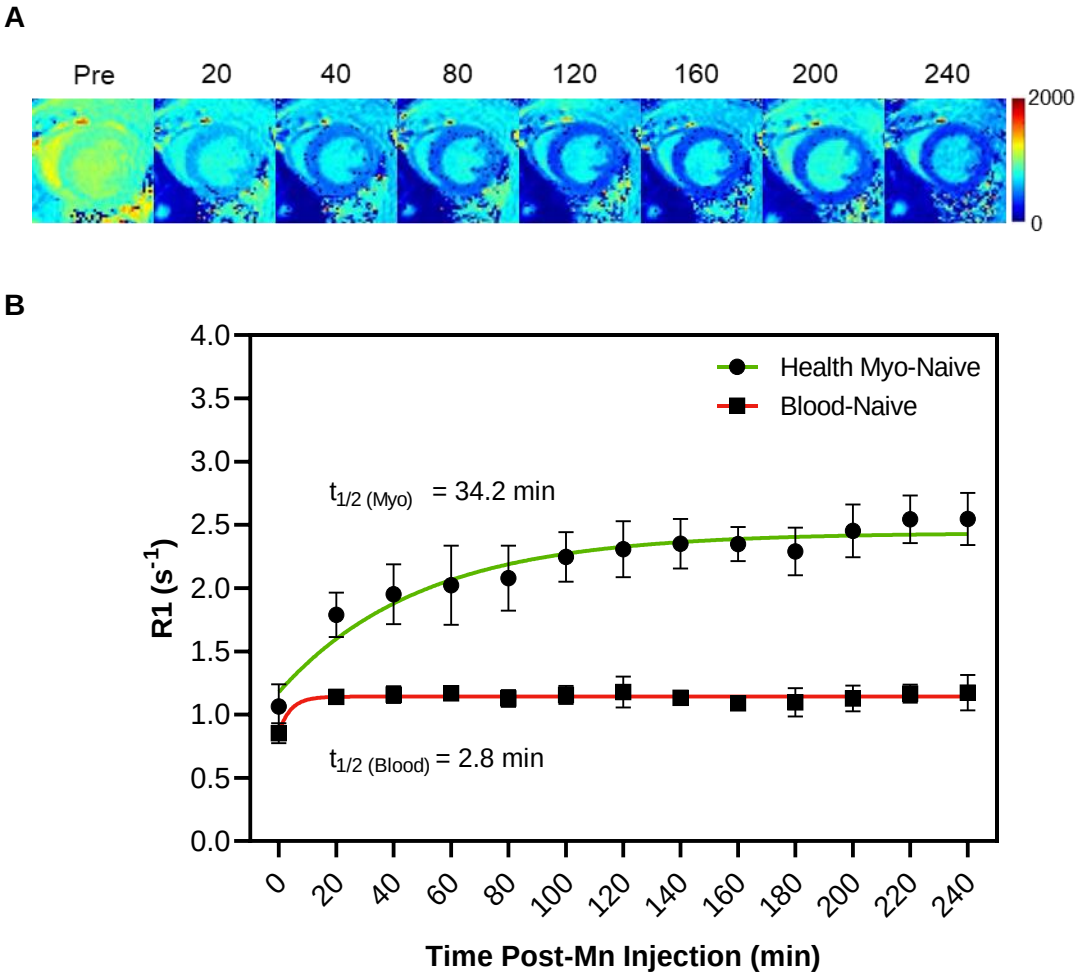

Figure 3.8: Manganese retention in the myocardium.

(A) Representative T1 maps of a heart pre- and post-$McCl_2$ injection, respectively. (B) R1 changes in dynamic MEMRI study. Time course of R1 changes in myocardium and blood pool region at baseline and every 20 minutes up to 4 hours (n=6) post $MnCl_2$ injections.

3.4.2 T1 mapping MEMRI for assessment of calcium homeostasis

Figure 3.9 shows a representative T_1 Map following *i.p.* injection of 0.1mM Mn^{2+} in a mouse model of myocardial infarction at 1h, 2h, and 3h after LAD occlusion and in a naïve mouse heart. Imaging was performed at the same time point after Mn^{2+} injection for both groups. In the naïve group, the myocardial T1 value was similar from 1h to 3h, indicating Mn^{2+} uptake was constant over this period. In the MI group at 1h post-MI, T1 in AAR-MI was similar to values for the naïve group, while the T1 in the Remote-MI tissue was dramatically reduced. The large T1 reduction and hence increase in Mn^{2+} in the Remote-MI tissue led to contrast difference between viable tissue and area at risk within one hour of coronary occlusion. This difference was also observed in the limited number of animals in which it was possible to acquire T1 maps earlier than 1 hour.

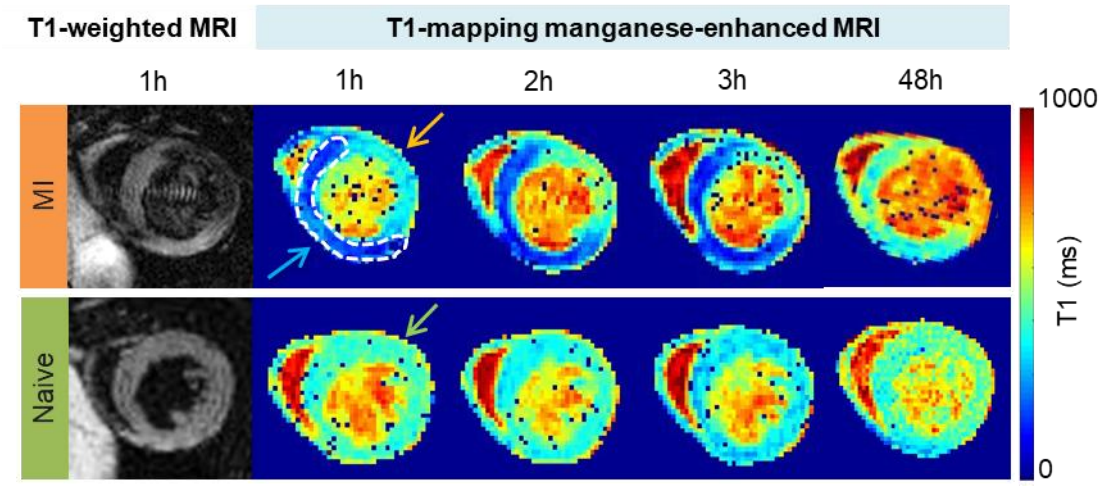

Figure 3.9: T1 mapping of manganese uptake acutely after myocardial infarction.
T1-weighted MRI (left panel) and T_1 Maps following Mn^{2+} in a mouse model of myocardial infarction. (Top row) at 1h, 2h, 3h and 48h after LAD occlusion and naïve mouse heart (bottom row). Imaging was performed at the same time point after Mn^{2+} injection for both groups. Dark pixels in myocardium indicate the point where the fitting algorithm fails. Blue arrow = Remote-MI, Yellow arrow = AAR-MI, Green arrow = Viable-Naïve.

For more convenient interpretation of the data, I will now also interpret changes expressed as relaxivity (R1) rather than T1, as R1 increases with increasing manganese concentration. As soon as 1 hour after LAD occlusion, R1 values were significantly higher in the Remote-MI tissue compared with AAR-MI tissue (5.06 ± 0.6s^{-1} and 2.90 ± 02s^{-1} respectively) (p=0.0025), allowing early delineation of the infarct region (Figure 3.9, Figure 3.10 and Table 3-1). When compared to naïve control animals, R1 values in the Remote-MI were significantly higher at 1h, 2h and 3h post-MI (p=0.0008, p=0.002, and p=0.002 respectively). In contrast, the AAR-MI tissue was not significantly different as compared to Viable-Naïve. Interestingly, R1 in the Remote-MI tissue continued to rise at 2h and 3h post-MI (p=0.051 and p=0.048 respectively and R^2 = 0.94) (Figure 3.10 and Figure 3.11), but remained constant in the AAR-MI and Healthy-Naive. The R1 values of the LV blood pool in MI and Naïve groups were similar and did not change over the 3 hours (Figure 3.11 and Table 3-1). These data show that acutely after ischemic injury, R1 increased (reflecting increased Mn^{2+} uptake) in viable myocytes remote from the AAR, likely due to elevated catecholamine levels acutely post-MI increasing cardiac work and thus increased Ca^{2+}/Mn^{2+} uptake.

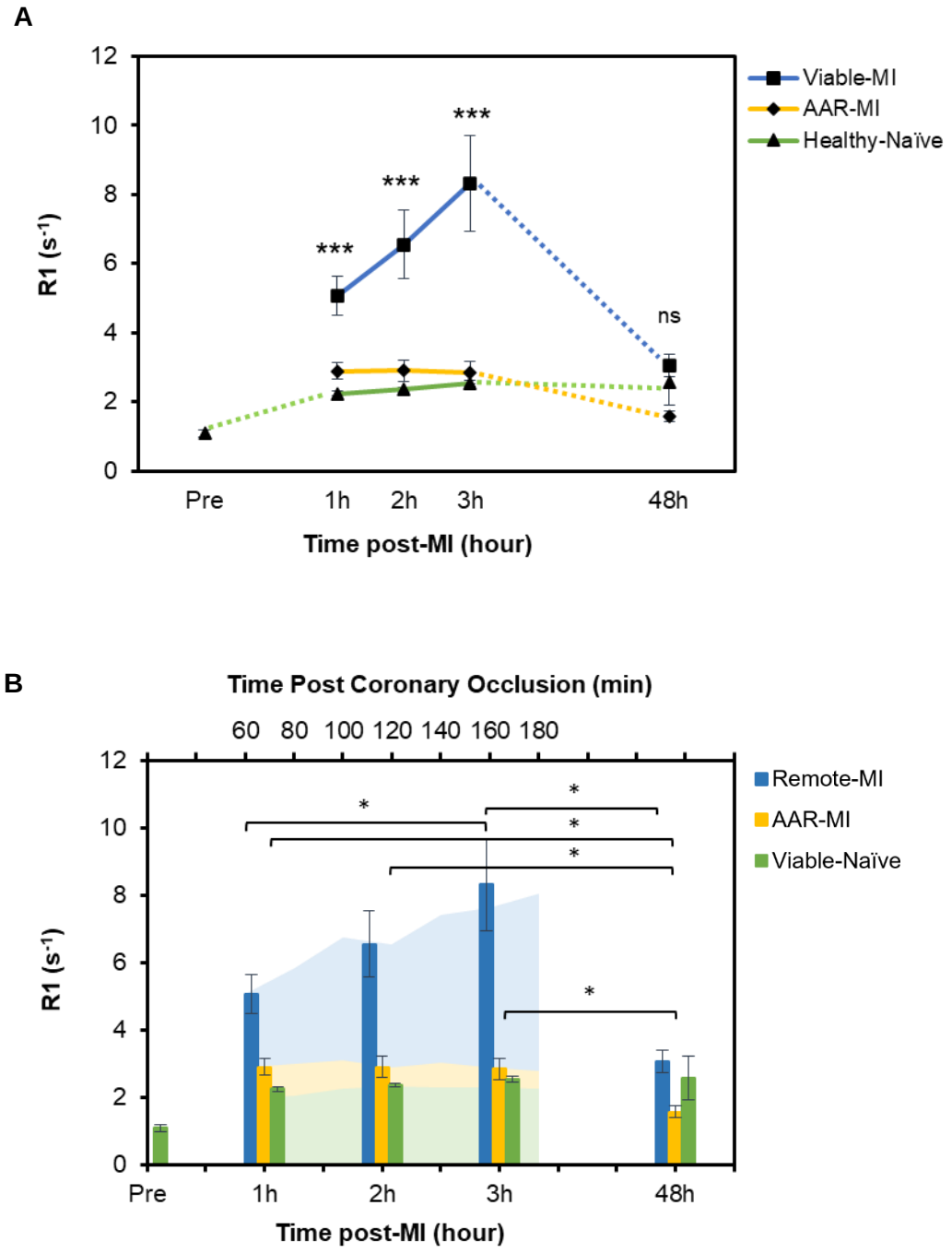

Figure 3.10: R1 reflecting manganese uptake acutely after myocardial infarction.

*R1 values in an infarcted heart at 1h, 2h, 3h and 48h after coronary occlusion (n=8) and naïve mouse heart (n=5) at the same time points after $MnCl_2$ injection. (A) Data were analysed using a one-way ANOVA (***P<0.001) with Tukey's multiple comparisons test between groups (see Table 3-1). (B) Data were analysed using a one-way ANOVA with Tukey's multiple comparisons test between time post coronary occlusion in each group (*P<0.05). Remote-MI = Remote myocardium at 1h to 3h and 48h after coronary occlusion, AAR-MI = Area at risk at 1h to 3h and 48h after coronary occlusion, Healthy-Naive = Healthy myocardium in naïve control group.*

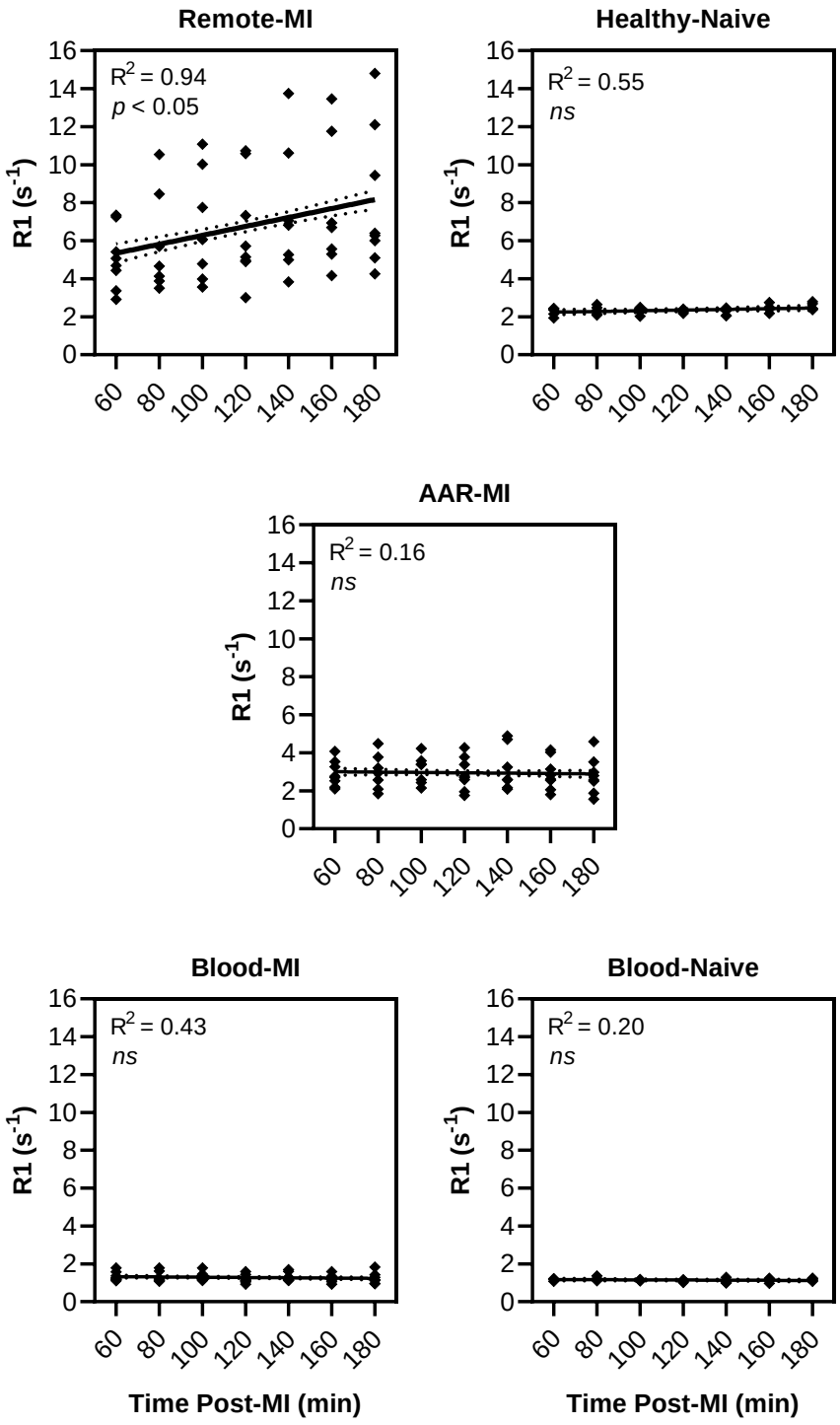

Figure 3.11: R1 reflecting manganese uptake acutely after myocardial infarction in the remote myocardium, AAR, infarct and blood pool.

Linear regressions between time post-MI (1h to 3h post-MI) and R1 value in the Remote-MI, AAR-MI, Healthy-Naive, Blood-MI, and Blood-Naïve groups. Remote-MI = Remote myocardium at 1h to 3h after coronary occlusion, AAR-MI = Area at risk at 1h to 3h after coronary occlusion, Healthy-Naive = Remote myocardium in naïve control group, Blood-MI = Blood pool area at 1h to 3h after coronary occlusion, Blood-Naïve = Blood pool area in the naïve control group.

T1 mapping was then repeated 60 minutes after Mn^{2+} re-administration at two days post-MI in 5 surviving mice (3 mice were euthanised due to severe symptoms of heart disease). By two days, the catecholamine storm had passed [206], and R1 levels in the surviving myocardium were normalised. Mn^{2+} uptake in the Remote-MI ($3.05 \pm 0.3s^{-1}$) was significantly lower compared to the measurement made at 3-hour post-MI (day 0) ($8.05 \pm 1.3s^{-1}$) ($p=0.013$) and had similar Mn^{2+} uptake to the Healthy-Naïve myocardium ($2.56 \pm 0.6s^{-1}$). When compared to the AAR-MI tissue, R1 values were still higher in the Remote-MI tissue ($3.05 \pm 0.3s^{-1}$) with borderline significant different ($p=0.06$). Also, R1 in the infarcted AAR-MI was lower than controls (not significant, $p=0.28$) (Figure 3.9, Figure 3.10, Figure 3.12 & Table 3-1) as at this time point, Mn^{2+} uptake in the AAR was reduced due to irreversible cell death and loss of functional myocytes.

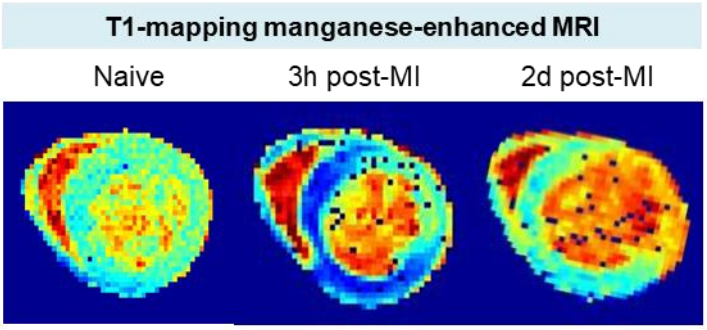

Figure 3.12: Representative T1 mapping at 2d post-MI.
Data were compared to day 0 post-MI and healthy naïve heart.

Table 3-1: R1 of the myocardium and blood pool region.

R1 was measured at 1h, 2h, 3h and 48h after LAD occlusion, naïve mouse heart at the same time points after $MnCl_2$ injection.

Time Post-MI	Remote-MI (n=8)	AAR-MI (n=8)	Healthy-Naive (n=5)	Blood-MI (n=8)	Blood-Naïve (n=5)
60	5.06 ± 0.6 ***##	2.90 ± 0.2	2.25 ± 0.1	1.34 ± 0.1	1.16 ± 0.03
80	5.84 ± 1.0	2.99 ± 0.4	2.31 ± 0.1	1.30 ± 0.1	1.18 ± 0.05
100	6.75 ± 1.1	3.12 ± 0.3	2.35 ± 0.1	1.32 ± 0.1	1.13 ± 0.01
120	6.55 ± 1.0 **##	2.90 ± 0.3	2.35 ± 0.1	1.20 ± 0.1	1.09 ± 0.02
140	7.42 ± 1.1	3.04 ± 0.4	2.27 ± 0.1	1.31 ± 0.1	1.10 ± 0.05
160	7.61 ± 1.2	2.90 ± 0.3	2.45 ± 0.1	1.24 ± 0.1	1.13 ± 0.05
180	8.05 ± 1.3 **##	2.80 ± 0.3	2.62 ± 0.1	1.24 ± 0.1	1.15 ± 0.03
48H	3.05 ± 0.3	1.57 ± 0.2	2.56 ± 0.6	1.14 ± 0.1	1.22 ± 0.04

Data were analysed using ANOVAs repeated measures paired and unpaired Student t-tests.

***P-value < 0.01 Remote-MI vs Healthy-Naive.*

****P-value < 0.001 Remote-MI compared to Healthy-Naive.*

##P-value < 0.01 Remote-MI compared to AAR-MI.

3.4.3 Cardiac function

Cardiac function was measured at ~3h and 48h after surgery using cine-MRI (Table 3.2 and Figure 3.13). As expected, LV end-diastolic volumes and end-systolic volumes were increased after coronary occlusion, and ejection fractions were reduced. No obvious changes in LV end-diastolic volumes, end-systolic volumes and ejection fraction were seen at ~3h and 48h after surgery.

Table 3-2: Cardiac morphology and function.

	Group	3 hours (n=4)	48 hours (n=4)
LV function			
EDV, µl	MI	45.50 ± 3	69.77 ± 6
	Control	65.51 ± 12	70.80 ± 5
ESV, µl	MI	14.86 ± 1	22.51 ± 2
	Control	43.90 ± 10	42.56 ± 9
SV, µl	MI	30.64 ± 2	47.25 ± 4
	Control	21.61 ± 2	28.24 ± 4
EF, %	MI	34.11 ± 3	42.09 ± 10
	Control	67.34 ± 1	67.82 ± 2
Heart rate, bpm	MI (n=8)	409 ± 17	418 ± 25
	Control (n=5)	478 ± 12	478 ± 25
LV mass, mg	MI	92.47 ± 10	102.91 ± 7
	Control	90.09 ± 9	111.28 ± 6

Values represent mean ± SEM measured at 3h and 48h post-MI. EDV indicates end-diastolic volume; ESV, end-systolic volume; SV, systolic volume; EF, ejection fraction; LV, left ventricle, and bpm; beats per minute.

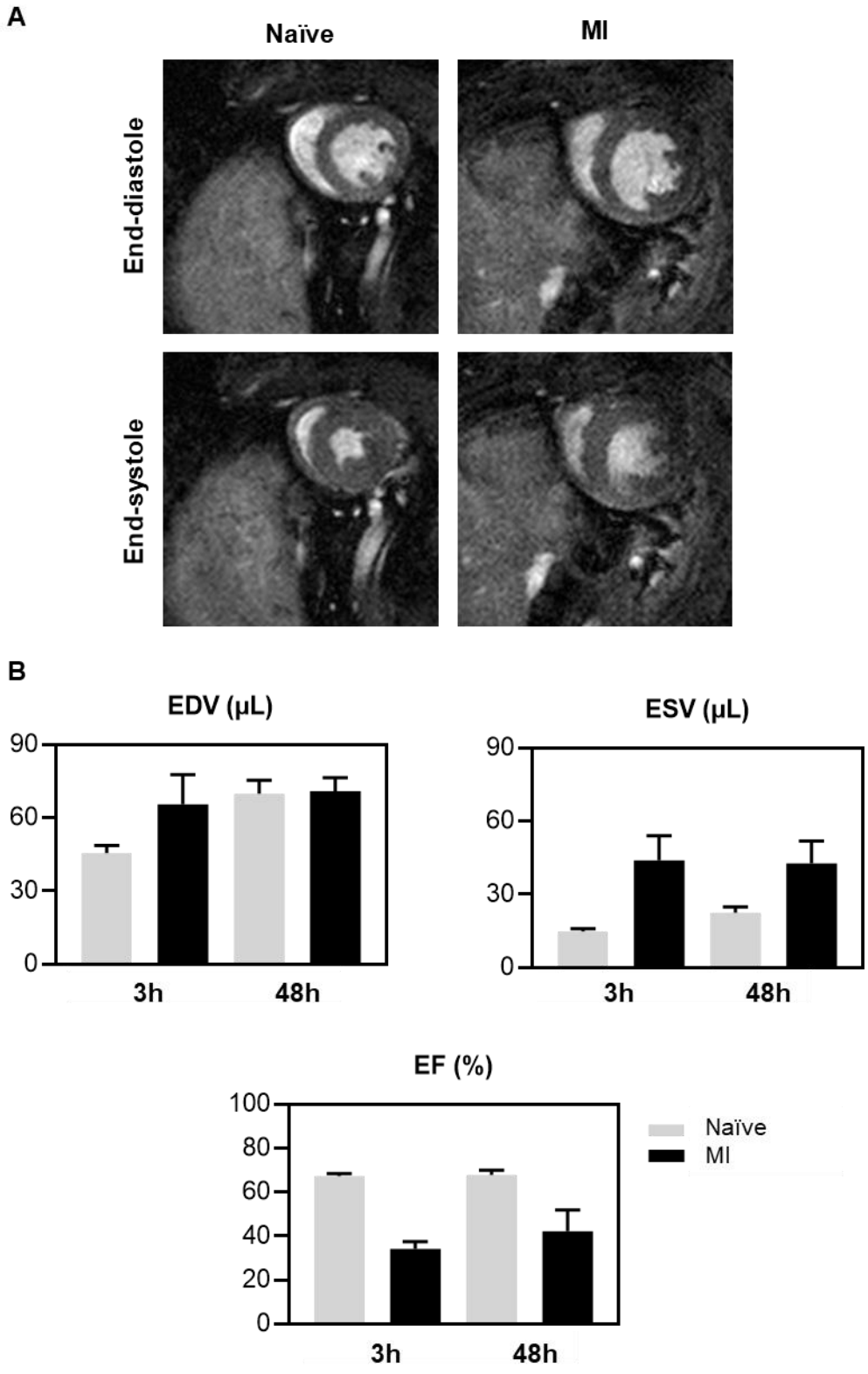

Figure 3.13: Cardiac function at 3h and 48h post-MI.

A, End-diastolic and end-systolic cine-MR images from naïve control group and MI group at 3 hours after surgery. Scale bar, 1 mm. B, Cine-MRI measurements of cardiac morphology and function made at 3 and 48 hours after coronary occlusion.

3.5 Discussion

3.5.1 Manganese retention in healthy myocardium

Cardiac T1 mapping allows quantitative assessment of subtle changes in Mn^{2+} uptake, providing a sensitive approach to measure the manganese accumulation in myocardium and blood. The retention of Mn^{2+} in the myocardium, as assessed by R1 after $MnCl_2$ injection, was studied using the optimal dose observed from our earlier experiment (0.10mmol/kg). R1 enhancement from Mn^{2+} reached a plateau at 100 minutes post-injection and maintained at a steady-state up to 4 hours with a half maximum R1 reached at 34.2 minutes after injection. This is similar to previous studies which observed a plateau effect at 30 to 40 minutes post-injection [115], [166]. A possible explanation for the slow R1 enhancement observed in this study might be the slow release of Mn^{2+} via IP injection of lower $MnCl_2$ dose [172]. A half-maximum R1 reached earlier in blood at approximately 2.8 minutes post-injection. The previous study reported a shorter half-life, less than one minutes in dogs post intravenous injection [181]. Mn^{2+} also maintained a steady-state in blood for up to four hours. This result may be explained by the fact that Mn^{2+} also binds to the plasma albumin.

T1 mapping MEMRI showed that Mn^{2+} accumulates in the myocardium at a steady state for a few hours. Mn^{2+} enters myocytes through L-type Ca^{2+} channels in the sarcolemma. Ca^{2+} fluxes across the sarcolemma are bidirectional in a beat wise manner, whereas Mn^{2+} accumulates intracellularly with each heart beat in an additive fashion and is retained for many hours [146]. The prolonged Mn^{2+} retention is most likely due to tight intracellular protein binding. After cell entry, Mn^{2+} accumulates in mitochondria, where the influx is stronger than the efflux, contributing to the retention of Mn^{2+} for hours in normal cells [95], [96]. Another possible explanation for the observed long retention time of Mn^{2+} in myocardium could be different Ca^{2+}, and Mn^{2+} extrusion rates due to their different binding constants and efflux pathway [96], [216]. This would suggest a longer imaging window for image acquisition in MEMRI, which would be useful for assessing changes in Mn^{2+} uptake in healthy and pathologic heart. This study was, however, limited to four hours after $MnCl_2$ injection. Thus, I are unable to determine the efflux rate of manganese from the myocardium. The uptake and retention of Mn^{2+} in myocardium depended on the dose and injection protocols. There is, therefore, a definite need for standardisation in the Mn^{2+} dose and injection protocols to establish reference data regarding the rate of influx, retention time and efflux on Mn^{2+} in myocardium under normal and pathologic conditions.

3.5.2 T1 Mapping MEMRI for assessment of intracellular calcium in acute myocardial infarction

Previous studies have demonstrated the sensitivity of T1 mapping-MEMRI to monitor alterations in intracellular Ca^{2+} in α-Dystrobrevin knockout mice [128], muscular dystrophy in mice [129], hypertrophic cardiomyopathy in mice [217] and myocardial infarction in murine models [99], [216], [218]. Hence, the purpose of this work was to use T1 mapping MEMRI to examine the alterations in calcium handling in the early hours after coronary occlusion. The present study is the first quantitative in vivo MRI assessment of intracellular Ca^{2+} in the early phase of myocardial ischemic injury. By pre-loading the myocardium with Mn^{2+} prior to coronary occlusion, MEMRI T1-mapping can quantitatively measure subtle changes of Mn^{2+} uptake reflecting a change in intracellular Ca^{2+} in viable myocytes in the early phase of myocardial ischemic injury.

The major findings of this work are: (1) Acutely post-ischemic injury (1-hour post coronary occlusion), R1 values were increased suggesting increase Mn^{2+} uptake in the Remote-MI (viable myocardium in MI group) allowing early delineation of the AAR-MI (area-at-risk in MI group). (2) R1 values in the remote myocardium continued to increase up to 3 hours post coronary occlusion and were higher compared to the healthy myocardium in the naïve control group. By two days post-MI, R1 levels in the surviving myocardium were normalised and now have similar Mn^{2+} uptake with the healthy myocardium in the naïve control group but were still higher in the AAR-MI tissue. (3) A small increase in R1 values at, 2h and 3h post-ischemic injury in the AAR-MI tissue which remains constant over the 3 hours but lower than controls at two days post-MI.

The increase in Mn^{2+} uptake (reflecting increased Ca^{2+} uptake) in viable myocytes remote from the AAR is likely to be due to elevated catecholamine levels acutely post-MI, which increase cardiac work and thus increase Ca^{2+}/Mn^{2+} uptake. An Increase in Mn uptake has previously been seen when the calcium and catecholamine level was increased [96], [115]. Mn^{2+} uptake was affected by catecholamines in the same way as calcium. The increase in calcium level following increases in catecholamines has been well studied [96], [196]. Elevated catecholamine levels in the remote myocardium were also reported by Richardson et al. (1960) [219], in experimental coronary occlusion in dogs. The current finding is also in agreement with previous studies that investigated the level of plasma catecholamines in patients with acute myocardial ischemia [204]–[206]. Plasma catecholamines were measured during the first 24 hours to 54 hours after admission

to hospital. Nadeau & Champlain (1979) reported a gradual elevation of plasma catecholamine during the first 4 hours and remained elevated up to 24 hours and gradually decreased in the next 24 hours. Similarly, a decrease in R1 values in the remote myocardium was seen, suggesting that the sympathetic activation has been normalised at two days post-MI. An additional analysis that would be worth doing for future work to support the finding of increased sympathetic stimulation of remote region in the present study is to measure strain in remote myocardium in the left ventricle or ejection fraction in right ventricle.

Previous studies have used T1 weighted imaging to investigate Mn^{2+} uptake [120], [122], [123], [133], [220]. However, these methods do not provide a direct R1 quantification, as only relative contrast changes are available, rather than direct Mn^{2+} uptake measurements. The initial hypothesis of this study was that the Mn^{2+} pre-loaded myocardium would lose contrast agent in the AAR over the time-course of cell death. If only T1 weighted data were used, this theory might have seemed true because of the relative difference in the contrast between AAR and the viable remote myocardium. Quantitative T1 mapping reveals that Mn^{2+} is not being lost from the ischemic zone but an increase in Mn^{2+} uptake in viable myocardium during the first 3 hours post-MI. There are two likely explanations. The first is that a loss in Ca^{2+} channel activity prevented further Mn^{2+} uptake, in contrast to what was seen in Remote-MI segments. Secondly, it may be due to the retention of pre-loaded Mn^{2+} in the AAR-MI similar to the healthy myocardium where Mn^{2+} uptake maintains at a steady-state during the first 3 hours post-MI.

Interestingly, R1 acutely post-MI in the AAR-MI segments following ischemic injury was higher compared to naïve control group. This may be a result of calcium overload in the ischemic tissue, which reduces over time as cell integrity is lost. A striking rise in cytosolic Ca^{2+} during acute ischemia has been well documented previously [188]–[191]. During myocardial ischemia, intracellular Ca^{2+} concentrations increased because of increased Ca^{2+} influx and reduced efflux [221]. Another possible explanation could be early inflammatory processes occurring after surgery as inflammatory cells such as macrophages are known to uptake Mn^{2+} [216], although this response is maximal only after 1-2 days. However, given that by two days, R1 in AAR-MI segment was lower than remote myocardium, it is unlikely that any immune cell manganese uptake is high enough to mask the reduction in manganese uptake which occurs in the infarcted region owing to loss of cell membrane integrity and impaired function of calcium channel [222].

Additional controls experiments using native T1 mapping might be helpful as ischemia results in an increase in myocardial water content manifesting as myocardial oedema, causing local changes in T1 relaxation times. In addition, there is increasing evidence indicating that remote myocardium is also subjected to pathophysiological changes after MI, although the significance of it is still largely unknown. Findings from one study [223], native T1 of remote myocardium decreased from baseline to 5 months after AMI, while in another study remote native T1 values remained constant [224]. A future study could incorporate native T1 value in remote myocardium with T1 mapping MEMRI will add additional information on the tissue changes in remote myocardium and may help to better understand the pathophysiological mechanisms. However, due to the challenging method of producing MI model, I limit the experiment to only contrast-enhanced imaging.

3.6 Summary

The present study shows that cardiac-manganese-enhanced T1 mapping provides sensitive in vivo detection of subtle changes and accumulation of Mn^{2+} in viable myocytes in the early phase after myocardial injury. The chapter presents the first quantitative in vivo MRI assessment of calcium homeostasis in the early phase of myocardial injury. The results presented should serve as an example of one approach to tracking changes in intracellular calcium levels at the early stage and the involvement of the nervous system in acute myocardial infarction model. The work is not only limited to acute myocardial infarction, but also could be applied to other cardiovascular diseases, or other diseases that involve changes in calcium levels.

Chapter 4 : Functional assessment of the myocardium for early infarct size quantification using manganese-enhanced MRI in acute myocardial infarction

Infarct size is widely assessed in the clinic using Late gadolinium-enhanced MRI (LGE-MRI). However, LGE-MRI does not specifically identify non-viable myocardium, but reflects the increased membrane rupture and extracellular space that develops after myocardial infarction. Functional assessment using MEMRI may offer a more sensitive early quantification of infarct size than LGE-MRI, which is currently preferred method. This chapter aims to compare the efficacy of MEMRI for in vivo quantification of infarct size after acute MI against LGE.

Abstract:

Functional assessment of the myocardium for early infarct size quantification using manganese-enhanced MRI in acute myocardial infarction

Introduction: Cardiomyocytes in the area of perfusion defect will die if blood flow is not restored after myocardial infarction (MI) [225]. An in vivo tool that is able to measure final infarct size at an early point after coronary occlusion would be beneficial. Late gadolinium-enhanced MRI (LGE-MRI) can accurately delineate infarct size after myocardial infarction owing to non-specific accumulation of gadolinium contrast agent within the increased extracellular volume (ECV) on the damaged tissue [226]. However, in the first hours after injury, these changes in ECV may not have occurred, and quantification of the final infarct size could be inaccurate. Manganese-enhanced MRI (MEMRI) can enhance viable myocardium as contracting myocytes accumulate manganese ions via L-type calcium channels [216]. This active process ceases under ischemia. Hence, I hypothesised that MEMRI would be able to quantify the final infarct size earlier than LGE-MRI and tested this by applying both methods to mice at 1h, 24 hours, and 14d after myocardial infarction.

Materials and Methods: All procedures complied with The UK Home Office and local animal care and welfare committees. 14 adults male C57BL/6 mice were included after left coronary artery (LAD) ligation. MEMRI was performed in 7 mice, and LGE-MRI was performed in 7 mice at 1h after LAD ligation. All animals then underwent both MEMRI and LGE-MRI at ~24 hours and 14d post-MI with a contrast washout period of at least 5 hours between scans [See pilot study on the washout of manganese (II) chloride ($MnCl_2$) and gadolinium-diethylenetriamine penta acetic acid-bismethylamide (Gd-DTPA) in Section 4.3.1]. MEMRI was acquired at 40 to 60 minutes after intraperitoneal (*i.p.*) injections of 0.1mmol/kg $MnCl_2$ while LGE-MRI images were acquired at 20min to 40min after *i.p.* injections of 0.5mmol/kg Gd-DTPA. Imaging was performed using a 9.4T Agilent MRI system and a multi-slice inversion recovery sequence as described [69] in the short-axis orientation to cover the whole left ventricle (LV) (TE/TR = 3.04/1.11ms, TI = ~600ms for MEMRI and ~350mis for LGE-MRI, 90º excitation pulse, slice thickness = 1.0mm, FOV = 25.6mm^2, and matrix size = 128^2). CINE movies were also acquired for cardiac function measurement using a gated gradient echo sequence.

Results: At 1h post-MI, viable myocardium remote from the area at risk (AAR) was enhanced in MEMRI, allowing early delineation of the infarct zone as 39.22 ± 6% of the myocardium, whereas only subtle enhancement within the AAR was observed on LGE-MRI, leading to a significantly lower measure of infarct zone (13.70 ± 1%, P=0.002) (Figure 4.10). At 1d post-MI, the MEMRI measure of infarct size remained constant (34.93 ± 4%) whilst the LGE-MRI measurement significantly increased to a level comparable with MEMRI (34.85 ± 6%) (Figure 4.10) (r = 0.97, P<0.001). The percentage of infarct sizes had reduced when measured by either technique (MEMRI 25.41 ± 6%, LGE-MRI 30.82 ± 6%) owing to the expected hypertrophy of viable myocardium and thinning of the scar at 14d (n=10). Both MEMRI and LGE-MRI indicated similar 14d infarct sizes to ex vivo infarct quantification using TTC staining (20.88 ± 4%) (r = 0.93, P < 0.001) (Figure 4.13 and Figure 4.14). End-diastolic volume, end-systolic volume, ejection fraction and LV mass were similar between the groups that initially underwent MEMRI or LGE-MRI (Figure 4.15 and Table 4-2).

Discussion: MEMRI provides accurate earlier quantification of the final infarct size, as compared to LGE-MRI. Acutely after ischemic injury Mn^{2+} uptake in viable myocytes occurs while no uptake is seen in the infarct region where myocyte function has ceased. This allows the estimated final infarct area to be distinguished early after myocardial infarction. Further, the present study suggests that LGE-MRI underestimates the final infarct size during the first hours after MI, as at this point, only minimal membrane rupture will have occurred, and gadolinium will not have accumulated.

Conclusion: The present study shows that manganese-enhanced MRI can quantify the final infarct size earlier than LGE-MRI. This provides a sensitive approach which could be used as an early measure of cell death and myocardial viability when assessing the efficacy of new drugs which target acute MI.

4.1 Introduction

Myocardial infarction rapidly leads to myocyte death in the part of the heart that suffers from reduced or obstructed coronary blood supply. Cell death rapidly occurs through uncontrolled necrosis as soon as after 30 minutes of ischemia in rats, with 13% of cardiomyocytes reported as necrotic within the area at risk [227]. Controlled cell death through apoptosis occurs at a slower rate, but without intervention can still result in substantial cell loss [228]. Apoptosis and necrosis can occur independently, subsequently, or simultaneously. The type of stimuli and the degree of stimuli determine if cells die by apoptosis or necrosis [26], [228] . In the absence of reperfusion, the necrotic tissue will be converted to an irreversible fibrotic scar. With reperfusion, depending on the degree and duration of reduction in blood flow, some effected myocardium will remain viable, in a state of stunning or hibernating, potentially reversible and regain its function. Pathophysiologically, myocardial viability refers to the alive cardiomyocyte with normal cellular, metabolic, and contractile function. On the other hand, myocardial viability in the clinical setting refers to dysfunctional cardiomyocytes, which can potentially recover its functionality when blood flow is restored.

In the previous chapter, we have shown the potential of manganese-enhanced MRI as a sensitive marker to changes in intracellular Ca in the early phase of ischemic injury. As an intracellular contrast agent, manganese acts as an analogue of Calcium (Ca^{2+}), that enters intact myocardial cells and provides direct information of a functional cell. This allows for discriminating remote myocardium, viable myocardium (alive but dysfunctional) in the area at risk, and the infarct zone early, potentially even before necrotic tissue fully developed following ischemic injury. The ability to distinguish the three zones during the early phase of ischemic injury has significant implications on the treatment and management of a patient with acute myocardial infarction.

In this chapter, a permanent occlusion mouse model of myocardial infarction is used to investigate the efficacy of manganese for quantifying infarct size as compared to the current gold standard, late-gadolinium enhancement in MRI. An understanding of the evolution of infarct, which is discussed section 4.1.1 would be helpful to aid interpret the experiments in this chapter. An overview of functional imaging after acute myocardial infarction is discussed in section 4.1.2. Next, Section 4.2 discusses the aims and objectives of the experiments in this chapter, followed by section 4.3, which describes the experimental method. Finally, the results are presented in section 4.4 and discussed in section 4.5. Work contained in this chapter

was presented at the International Society Magnetic Resonance for Medicine conference 2019 and European Molecular Imaging Meeting 2019, where it won Magna cum laude award and best poster award.

4.1.1 The evolution of myocardial infarction

Myocardial infarction is a consequence of prolonged myocardial ischemia. Myocardial ischemia is a consequence of an imbalance in supply and demand for oxygen, usually due to an extreme deficiency of the supply of coronary blood. Restriction of blood flow may be due to thrombosis, coronary atherosclerotic atherosclerotic disease or lack of atherosclerotic disease such as coronary embolism due to endocarditis. The three primary responses following myocardial ischemia are metabolic changes, ionic perturbations, and functional depression, as discussed in detail in Chapter 1, Section 1.2.2. The area in perfusion defect following myocardial ischemia is still viable during the first few minutes and salvageable upon restoration of blood flow. In the absence of coronary reperfusion, the viable myocardium within the area at risk passes from the phase of reversible to irreversible injury or also known as an infarct. The following section will give an overview of the functional depression after ischemic injury, the evolution of cell death, and the cardiac repair process after myocardial infarction.

4.1.1.1 Functional depression after ischemic injury

Functional depression is one of the early responses to reduce coronary perfusion. Ischemia causes an immediate loss of contractility in the affected myocardium develops in association with alterations in metabolic processes and ions transport system in the sarcolemma and organellar membrane, a condition termed hypokinesis. In contrast, contractility in the remaining viable myocardium increases, a process termed hyperkinesis. Cardiomyocytes contain high energy reserves of phosphate that are adequate to maintain the contractility for a few minutes of total ischemia. However, the onset of systolic dysfunction in experimental models is much quicker, as contractile force is immediately suppressed and ceases after 60 seconds of ischemia [15], despite the availability of energy reserves. There are two main mechanisms that cause immediate functional depression. Firstly, it is due to the production of inorganic phosphates from the breakdown of the creatine phosphate reserves, inhibiting the function of contractile proteins [16]. Secondly, it is due to the intracellular acidosis causing a decrease in calcium binding to contractile proteins, inhibiting cardiac contractility [17]. Rapid cessation of function can prolong the

survival of ischemic cardiomyocytes, as the limited stores of high-energy phosphates are used slowly and allow cardiomyocytes to survive longer despite lack of perfusion.

Functional depression in the ischemic region is fully recovered when blood flow is rapidly restored within ~5 minutes after coronary occlusion [229]. A longer duration of ischemia within ~5 to 20 minutes causes prolonged dysfunction despite full restoration of blood flow [229]–[231]. The failure to recover function despite complete reperfusion of coronary occlusion is termed “myocardial stunning”. Usually, it lasts for 24 to 48 hours following the restoration of blood flow [229] with subsequent complete recovery. In the pre-clinical setting, myocardial stunning is induced by subjecting the heart with 10 to 12 minutes of coronary artery occlusion [93]. In the clinical setting, myocardial stunning can also occur during exercise in the presence of coronary artery stenosis and angina [232]. Myocardial stunning involves two mechanisms: (1) generation of reactive oxygen species (ROS) during the early stages of reperfusion and (2) perturbation in cardiomyocyte calcium homeostasis. Oxidative stress and calcium overload cause contractile protein modifications, resulting in transient systolic dysfunction. The mechanism of myocardial stunning during and post-ischemic injury is summarised in Figure 4.1. Another condition that suffers from functional impairment with the potential to recover its functionality is hibernating myocardium. Myocardial hibernation occurs in response to repeated ischemia or worsening chronic coronary stenosis. Functional recovery can take several days to months after the coronary flow is restored.

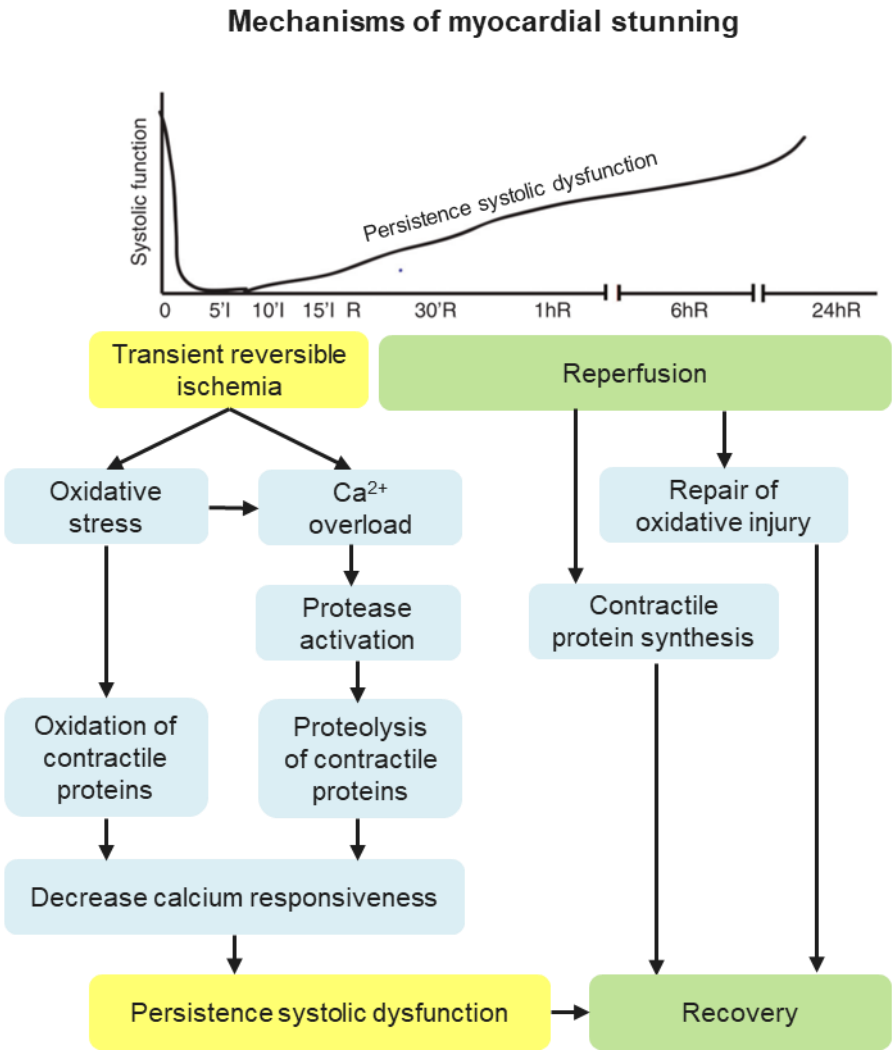

Figure 4.1: Mechanisms of myocardial stunning.

A brief (<15-21 minutes) ischemic interval is followed by a systolic dysfunction that persists for as long as 24h, despite restoration of blood flow; this pathologic condition is termed "myocardial stunning". Oxidative stress and calcium overload induce modifications of contractile proteins, resulting in transient systolic dysfunction. Adopted from Frangogiannis (2015).

4.1.1.2 Evolution of cell death in the infarcted heart

If blood flow is not restored, necrosis will start to develop. In large animals, 20-30 minutes interval of severe ischemia is sufficient to induce irreversible changes in some cardiomyocytes of the subendocardial area [231], [233]. The irreversible injury or infarct region develops as soon as 40 minutes after coronary occlusion through the 'wavefront' phenomenon, beginning with the central subendocardial tissue and spreading epicardially and toward the periphery of the AAR-MI as illustrated in Figure 5.2 [233], [234]. It remains unclear to the observed increased in vulnerability of subendocardial regions. It has been suggested that when coronary blood flow is suppressed, the subendocardial blood supply is compromised more as compared to the subepicardial blood supply [235] due to the increased resistance of subendocardial vessels [236]. It is important to note that the 'wavefront' concept is based on an experimental study in canine hearts. In a mouse model of reperfused infarction, the mid-myocardium was suggested to be the most vulnerable area to ischemic [237].

After the onset of myocardial ischaemia, ultrastructural changes developed within the first few minutes of ischemia; cellular and mitochondria swelling, progressive loss of sarcoplasmic glycogen particles, and mild margination of nuclear chromatin [238]. In the experimental models, these early changes have been shown to be reversible following restoration of blood flow within 15 to 20 minutes of coronary occlusion. Longer duration of ischemia and absence of reperfusion causes these ultrastructural features to persist and eventually manifest at the microscopic level, indicating most of the cells is death. It takes hours before tissue death can be identified by macroscopic or microscopic post-mortem examination [231]. Complete necrosis of myocardial cells at risk requires at least 2–4 hours, or longer, depending on the presence of collateral circulation to the ischaemic zone, persistent or intermittent coronary arterial occlusion, the sensitivity of the myocytes to ischaemia, and individual demand for oxygen and nutrients. Most of the cardiomyocytes in the infarcted region die within the first 24 hours after coronary occlusion [18].

The leading factor in the initiation of cardiomyocyte cell death following prolonged ischaemia is severe ATP depletion and calcium overload. Cell death, either progressive or acute is a hallmark characteristic of various cardiac diseases including myocardial infarction. Cell death occurs through two mechanisms: apoptosis and necrosis. Apoptosis is a programmed cell death associated with cell shrinkage, fragmentation, and removal by phagocytosis [228]. In contrast, necrosis is mainly

caused by physical or chemical trauma to the cell and characterises by cell swelling and loss of membrane integrity [26]. Ischaemic cell death is thought to occur predominantly by necrosis since apoptosis requires ATP; although it has been suggested that myocardial ischaemia may initiate apoptotic cell death pathways which are then executed in the presence of ATP upon reperfusion [239]. Further details of this topic, although interesting for further discussion, are beyond the scope of this thesis. The detail mechanisms of cell death are well explained in several reviews [228], [240]–[242].

4.1.1.3 Cardiac repair following myocardial infarction

Ischemic heart failure is one of the adverse endpoints after myocardial infarction. The fundamental determinants of the progression of ischemic heart failure depend on the extent of the initial and sufficiency of the cardiac repair process after myocardial function ceases. The mammalian heart has a limited regenerative capacity, hence death of large numbers of cardiomyocytes results in the replacement with a non-contractile collagen-based scar which helps maintain the structural integrity of the ventricle, preventing more detrimental events such as cardiac rupture. The first animal model of myocardial infarction close to the human to study cardiac repair was published in 1916 by Karsher and Dwyer [243]. The left anterior descending (LAD) artery in dogs was ligated and killed at various time points after surgery to study the different level of severity of infarct and the mechanism of the healing process after myocardial infarction.

The cardiac repair process has three different but overlapping phases (Figure 4.2): (1) the inflammatory phase, (2) the proliferative phase, and (3) the maturation phase. Cell death that occurs through necrosis release alarmins as a signals danger and activates immune cells to express receptors, triggering the inflammatory response to clear the infarct zone from dead cells and matrix debris [244]. An excessive inflammatory response, however, might have a detrimental effect causing left ventricular dilatation and systolic dysfunction [245]. The pro-inflammatory signalling is suppressed once dead cell and matrix debris is cleared from the infarct zone. In brief, the inflammatory phase serves to clean the injury site and prepare for the next phase to rebuild the tissue. Inflammatory phase took place approximately within the first few hours after acute myocardial infarction [244], [246], [247]. As the inflammation phase begins to end, the proliferative phase begins.

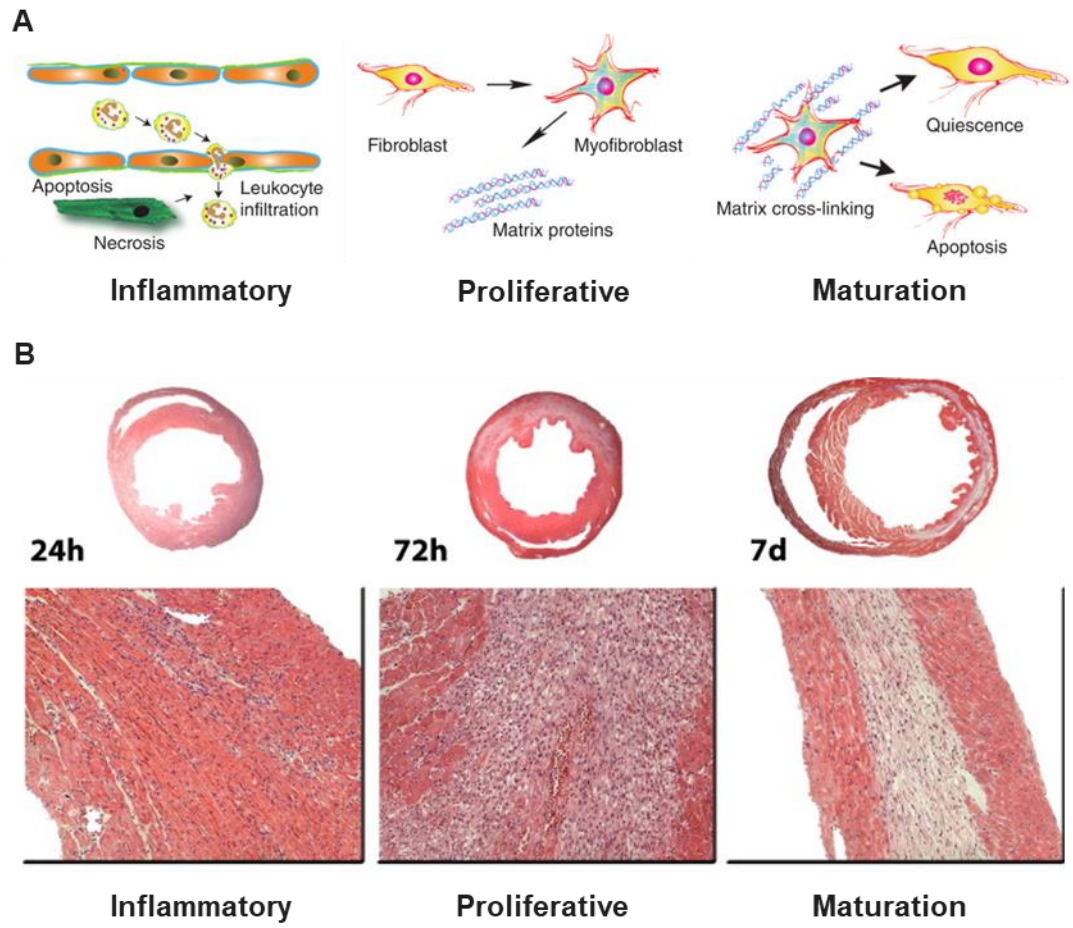

Figure 4.2: Cardiac repair after acute myocardial infarction.

(A) The phases of repair following myocardial infarction begins with an inflammatory phase, followed by proliferative and maturation phase. (B) Time course of the infarct healing process in a mouse reperfused model of myocardial infarction. Dilatation remodelling is seen in the infarcted myocardium as the infarct heals. Large animals and humans would be expected to have a longer healing process. [248], [249].

The proliferative phase is characterised by increasing numbers of fibroblasts. Under stress conditions fibroblasts become activated into myofibroblast with secret growth factors and extracellular matrix proteins to form scar tissue and a microvascular network. The initial matrix formation helps rebuild the wounded area physically and provides structural integrity. The synthesised extracellular gradually undergo extensive remodelling over several weeks, depending on the severity of the injury. The formation of this structural matrix proteins indicates the end of the proliferative phase. The proliferative phase take place within the first few days up to few weeks post infraction. In a mouse reperfused model of myocardial infarction, proliferative phase occur within 72 hours after infarction [249]. Large animals and humans would be expected to have a longer healing process.

In the third phase, the extracellular matrix is cross-linked and infarct fibroblasts become quiescent and may undergo apoptosis. Defects in the suppression of the maturation phase may result in overactive fibrotic responses and adverse cardiac remodelling. Left ventricular remodelling referred to the collective changes in cardiac geometry, function and structure. The chamber dilates and becomes more spherical, infarcted regions become thinning, and the remote myocardium undergoes hypertrophy [250], [251]. Maturation phase occur at day 7 in mouse model, but this phase could extend up to few months and years in patients [246].

During cardiac repair, both the infracted and remote myocardium undergoes remodelling such as ventricular dilatation in the infarcted area to maintain cardiac output and wall thickening in remote myocardium due to pressure and volume overload. This is an exciting topic for further investigation but is beyond the scope of this thesis. Sumanth and Frangogiannis (2016) published an excellent review discussing the biological basis for cardiac repair after myocardial infarction [252]. A better understanding of the multiples factors that influence cardiac repair after myocardial infarction is critical in reducing the adverse remodeling and development of ischemic heart failure and would path the ways for novel therapeutic strategies [253]. Imaging at different time points post-infarction would aid in the understanding of the pathogenesis of cardiac healing. It would be helpful to inform decisions on the best and successful intervention.

4.1.2 Functional imaging of acute myocardial infarction

Treatment of acute myocardial infarction comprises the restoration of coronary artery perfusion by removal of the occluding lesion. However, this depends on the presence of collaterals, time to reperfusion, and treatment. Without intervention or collateral flow from other arteries, viable myocardium will become irreversible injury, so-called an infarct, an area of complete cell death. The clinician considering coronary revascularisation will wish to have information on which patient would be benefited from the procedure. It has been suggested that recovery of function is closely related to the ratio of viable myocardium to the infarct region [254]. Hence, quantifying the viable myocardium soon after the onset of myocardial infarction is of great importance. Viable myocardium can be calculated by subtracting the area at risk with the infarct zone (Figure 5.1) or by direct assessment of the viable myocardium.

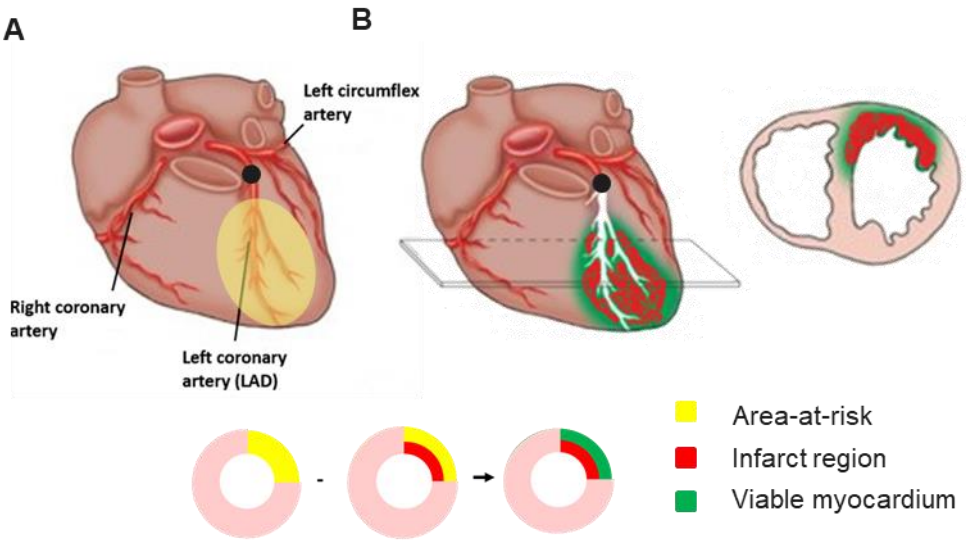

Figure 4.3: Schematic illustrating the concept of the area at risk (AAR-MI), infarct size, and viable myocardium following myocardial infarction.

(A) Coronary artery blockage (•) leads to myocardial hypoxia. The region of myocardium previously perfused by the occluded artery is defined as AAR-MI (yellow). (B) Gradually, the AAR-MI turns into infarcted tissue (red); however, if the occluded coronary artery is restored, some of the epicardial areas is still viable and potentially recover its function (green).

However, quantifying the area at risk, infarct size and viable myocardium at the early stage after ischemic remains a major challenge. Late gadolinium-enhanced MRI (LGE-MRI) sets the gold-standard for infarct size quantification in myocardial infarction. However, the accumulation of gadolinium is non-specific and reflects the increased membrane rupture and extracellular volume (ECV) that occurs several hours after myocardial infarction. Functional imaging marker may offer advantages

over LGE in quantifying early infarct size. Functional changes (metabolic change, ionic changes in cell, and reduction in contractile function) occurred before any structural changes could be detected at an early stage of the disease. Thus, imaging at this stage could serve as an early imaging marker of cardiac disease. However, to be able to detect these early changes, imaging approaches need to be highly sensitive and are able to detect changes at cellular and molecular levels. This section highlighted several imaging approaches that are capable of detecting functional changes after acute myocardial infarction.

One of the earliest imaging approaches is using single photon emission computed tomography (SPECT) by targeting the potassium using potassium analogue, thallium-201 (^{201}TI). Potassium is actively transported across the myocardial cell via Na^+/K^+ ATPase-dependent channels. ^{201}TI uptake is high in viable myocytes where cell membrane and transport mechanism remain intact. When ^{201}TI is injected at rest, it is distributed to the myocardium in proportion to the coronary arterial blood flow. Radiotracer washes out and redistributes after a 3- to 5-hour interval delay. The pattern of redistribution is dependent upon an intact Na-K ATPase pump and thus myocardial cell viability. No uptake is seen in the infarct region during the immediate and delayed images indicating a nonreversible defect. Whereas in the regions of viable myocardium, no ^{201}TI uptake is seen during immediate, but uptake is seen on delayed images suggesting reversibility [255]. Another tracer used in SPECT is ^{99m}Tc-sestamibi. Unlike ^{201}TI, ^{99m} Tc-based agents diffuse across the cell membrane via the passive mechanism. The uptake and retention of ^{99m}Tc-sestamibi depend on the maintenance of an electrochemical gradient across mitochondrial and sarcolemma membranes [256]. In clinical, ^{99m}Tc-sestamibi is more favourable imaging because of its higher photon energy and less radiation exposure to the patients.

Positron emission tomography (PET) has been used for imaging of myocardial metabolism after acute myocardial infarction and serves as the gold standard for viability imaging. PET can detect the metabolic change, glucose utilisation during ischemic injury. Higher tracers uptake is seen in the dysfunctional but viable cardiomyocytes and is currently the gold standard for viability imaging. Another tracers that could be used to assess myocardial metabolism its relation to viability are ^{11}C-palmitate, which assess fatty acid metabolism and ^{11}C-acetate, which have been used to quantify myocardial oxygen consumption [254], [257]. However, the use of ^{11}C tracers have several disadvantages, such as complex analysis, and the need for an onsite cyclotron to make the tracers.

Metabolic imaging is now possible in the heart using MRI spectroscopy leading to significant advancement in the understanding of real-time myocardial metabolism in the normal and diseased heart in vivo. Preliminary evidence suggested that MRI spectroscopy could be used in diagnosing ischemic myocardium directly by detecting the metabolic consequences of myocardial ischemia and myocardial viability. MRI spectroscopy enables detection of nuclei compound such as phosphorus (^{31}P) an carbon (^{13}C). Cardiac ^{31}P MR can identify adenosine triphosphate (ATP) and phosphor creatine in vivo in the human heart [258]. ATP content is reduced in the infarct tissue but remains constant in the viable myocardium. The second metabolic tracers, ^{13}C can be used to detect pyruvate metabolism in the heart during ischemic injury. Pyruvate plays a central role in the energy production of the heart muscle, glycolysis and oxidative phosphorylation, in which [1-13C] Pyr is converted via enzyme-mediated reactions to [1-^{13}C] lactate, [1-^{13}C] alanine, and ^{13}C-bicarbonate.

However, the natural abundance and NMR sensitivity of ^{13}C spectroscopy mean it takes several hours to acquire spectra with sufficient signal to noise. However, dynamic nuclear polerisation, or hyperpolarized MR can dramatically increase the NMR signal generated by ^{13}C compounds and and permits hyperpolarized MR imaging for the investigation of substrate metabolism in in-vivo heart after myocardial ischemia [259], [260]. The complexity of the experimental design (short half-live of the nuclei) for hyperpolarised MRI has been the major challenge for the technique to be translatable into clinical application. Imaging using hyperpolarised is logistically challenging, but it could provide important information regarding metabolic changes that occur at an early stage following myocardial ischemia. A detailed overview of this technique and its application in cardiovascular disease is review in these papers [261], [262].

The above techniques have delivered important scientific findings and essential prognostic and diagnostic information. However, their requirement for radiotracers, expensive hyperpolerization systems an dinherent low spatial resolution mean that new methods for imaging myocardial viability are required. Manganese is a potent positive MR contrast agent that reduces T1 relaxation. Manganese is cheap, can easily be supplied to GMP standards and can be images on existing MR systems with standard pulse sequences. Manganese has been used to measure Ca^{2+} uptake during ischemia in a mouse model of myocardial infarction. Several investigations using T1-weighted manganese-enhanced MRI showed reduced Mn^{2+} uptake (hypoenhanced zone) in the area-at-risk [122], [133], stunned myocardium [93] and infarct zone [120], [123], [263]. Compared to hyperpolarised MRI and nuclear imaging, manganese-enhanced MRI offers a simpler approach and capable of providing functional changes in the ischemic myocardium.

4.2 Chapter outline and aims

In this study, a permanent occlusion mouse model of myocardial infarction was used to investigate the efficacy of manganese for quantifying the area-at-risk hence the estimated infarct size during ischemic injury and quantifying the final infarct size in the acute and chronic stage of myocardial infarction as compared to the current gold standard, late-gadolinium enhancement in MRI. LGE-MRI serves as the gold-standard for infarct size quantification in myocardial infarction. However, accumulation of Gd-DTPA in the infarct tissue is non-specific, and a contrast agent that actively targets functional myocardium may offer advantages over LGE. Manganese enters intact myocardial cells via voltage-gated calcium channels [95] and shortened T1 relaxation times whenever manganese accumulates. Manganese-enhanced MRI enhances viable myocardium as contracting myocytes accumulate Mn ions. This active process ceases under ischemia. I hypothesised that MEMRI would be able to quantify the final infarct size earlier than LGE-MRI and tested this by applying both methods to mice at 1h, 1d and 14d after myocardial infarction.

4.3 Methods

This chapter consisted of two parts. In the first part, a pilot study was conducted to determine the clearance of gadolinium and manganese contrast agents using T1 mapping. In the second part, late gadolinium-enhanced MRI (LGE-MRI) and manganese-enhanced MRI (MEMRI) were performed to quantify early infarct size in acute myocardial infarction model using both gadolinium and manganese contrast agents.

4.3.1 Pilot study of manganese and gadolinium washout

So that MEMRI and LGE could be performed in the same animal, a pilot study was first performed to assess clearance of manganese and gadolinium contrast agents. Eight mice were subjected to permanent infarction at 12 weeks of age, as described in previously in Section 3.3.2. T1 mapping was performed at least 7 days after infarction at baseline and following 1mmol/kg and 0.1mmol/kg intraperitoneal injection of manganese chloride and gadolinium-diethylenetriamine penta acetic acid-bismethylamide (Gd-DTPA-DMA) respectively. Imaging parameters were as described in the Section 2.3.2.4. Imaging of a single slice was repeated at 6-time points (30 minutes, 1h, 2 hours, 4 hours, 5 hours and 24 hours) to assess the changes in R1 values (1/T1) reflecting the amount of contrast in the infarcted zone, remote myocardium and blood pool region.

4.3.2 Experimental design and animal preparation

Fourteen mice were included after surgically induced myocardial infarction. MRI with CINE and contrast enhancement was performed in the same animal group (Figure 4.4). MEMRI was performed in 7 mice, and LGE was performed in 7 mice at 1h after coronary ligation. All animals then underwent both LGE and MEMRI at ~24 hours (n=14) and day 14 (n=10) post-MI. Six animals were euthanised for histological comparison after imaging at day 14 post-MI. A washout period of at least 5 hours was given before performing MEMRI. No naïve control group group is included in this study as the main aim of the study was to see differences in contrast-enhanced pattern using different contrast agents for early infarct size quantification. Naïve control group seems does not add essential information.

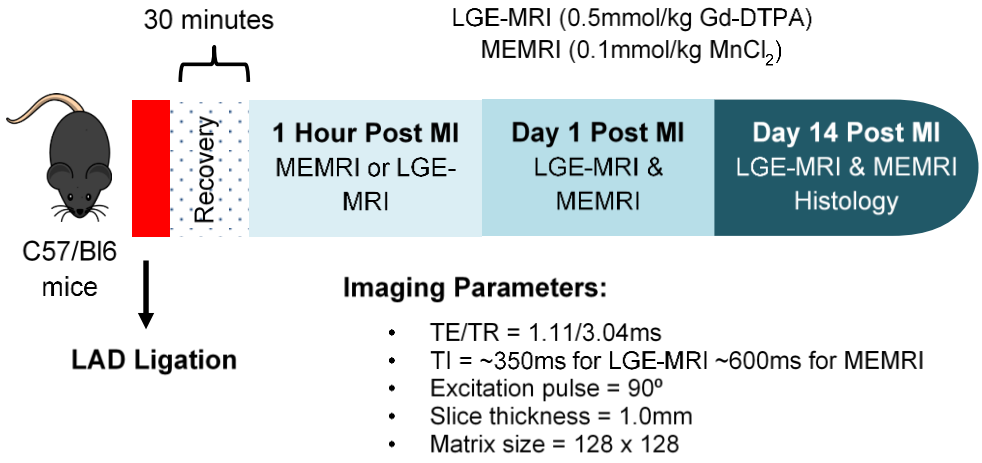

Figure 4.4: Schematic of MEMRI and LGE-MRI post-MI.

Myocardial infarction was induced by ligating the left anterior descending artery (LAD). Imaging was performed as soon as 1h post-MI using either LGE-MRI or MEMRI. The same animal was scan again at day 1 and 14 using both LGE-MRI and MEMRI.

4.3.3 MRI acquisition and analysis

4.3.3.1 CINE sequence

CINE sequence, shorthand for cinematic, acquires a time series of static images of the heart that when displayed sequentially visualises the beating heart. Cine imaging relies on accurate gating for physiological motion. A gated gradient echo sequence was used to acquire cine cardiac images. Imaging parameters for mice were as follows; echo time (TE) = 1.18 ms, repetition time (TR) = 5 ms, flip angle = 15°, slice thickness = 1 mm, field of view (FOV) = 25.6 × 25.6 mm, matrix size = 128 × 128, number of signal averages = 2. The basic principles of the cine acquisition scheme and the GRE pulse sequence are described in Section 1.3.2.2.

4.3.3.2 CINE image analysis

Figure 4.5 shows an example of a segmented CINE stack. The software package applies an automatic segmentation algorithm to the images. If the automated segmentation is inaccurate, the user can correct the regions manually. Segmentation of the left ventricle endocardium in all ED slices gives end-diastolic volume (EDV). Similarly, endocardial segmentation in all ES slices gives end-systolic volume (ESV). From these two sets of measurements, stroke volume (SV) and ejection fraction (EF) can be calculated.

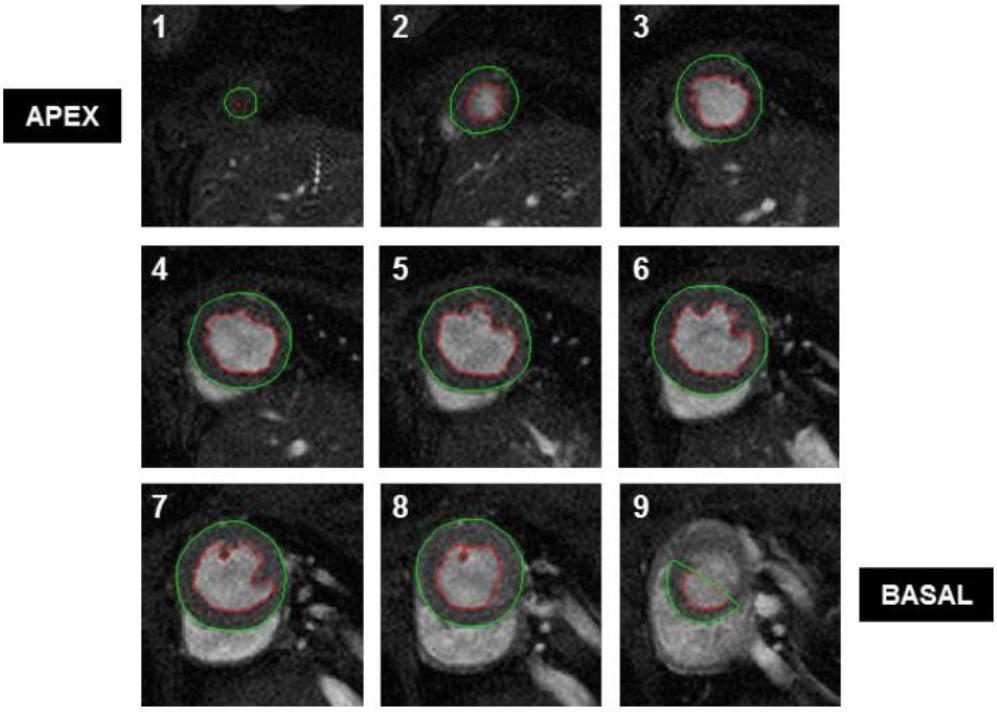

Figure 4.5: CINE MRI image analysis.

Short-axis CINE stack segmentation of the left ventricle blood pool (red) and left ventricle epicardium (green) at end-diastole for calculating systolic functional parameters. In the most basal slice (9), the segmentation intersects the ventricular and atrial tissue and blood. For analysis of functional parameters, the CINE stack is also segmented at end-systole.

4.3.3.3 T1-weighted MEMRI and LGE-MRI

Manganese (II) chloride, 1.00 ± 0.01 M solution (Sigma Chemical Co., St. Louis, Mo.) is used for manganese-enhanced MRI (MEMRI) experiments. $MnCl_2$ was diluted in NaCl 0.9% solution to achieve the desired concentrations. Another contrast agent used in this study is gadolinium-diethylenetriamine penta acetic acid-bismethylamide (Gd-DTPA-BMA) (Omniscan. GE Healthcare, Hatfield, United Kingdom). In brief, $MnCl_2$ and Gd-DTPA were administered via intraperitoneal injection as a single bolus of 0.1mmol/kg or 1mmol/kg, respectively. Mice were randomly assigned to receive either $MnCl_2$ or Gd-DTPA soon after infarction for the 1h scans. For later time points, late gadolinium enhancement MRI (LGE-MRI) was performed first with a wait of at least 6 half-lives, calculated in pilot study (Figure 4.9) to be 4 hours, before injecting manganese to performed manganese-enhanced MRI (MEMRI) to ensure the independence of contrast-enhancement patterns. The longer washout time for $MnCl_2$ prevented it being administered first. Data also shows that, LGE is best performed within 20 minutes post-Gd injection and 60 minutes post-Mn injection for MEMRI

Imaging was acquired using a multi-slice IR-GRE (IRmSL) sequence with a single inversion time (TI) point and flip angle of 90° [69]. The imaging sequence used is described in Section 1.3.2.4. The optimum TI was selected from the multiple frames of the LL inversion recovery sequence performed prior to the IRmSL sequence. TI (~600ms) was selected to to null the healthy myocardium, for manganese-enhanced MRI (MEMRI), while for late gadolinium enhancement (LGE-MRI) T1 (~350ms) was selected to null the healthy myocardium. This provides the best contrast between healthy and infarcted myocardium. The repetition time between each slice pulse (TRs) was 3ms, with a sequential acquisition order typically, 9 to 10 short-axis slices to cover the entire heart with the following parameters: TE = 3.04, TR = 1.11ms, 90º gradient echo readout pulse, slice thickness = 1.0 mm FOV = 25.6 x 25.6 mm, and matrix size = 128 x 128.

4.3.3.4 MEMRI and LGE-MRI image analysis

MEMRI and LGE-MRI images were analysed using ImageJ software (National Institutes of Health) with semi-automated left ventricular (LV) mass and infarct mass. LV mass was measured by semi-automated segmentation of the myocardial area in all slices of the inversion recovery acquisition. MEMRI defect areas (hypointense region) and LGE-MRI enhance areas (hyperintense region) were designated as infarct areas. The extent of defect areas or enhanced areas is defined as any tissue with image magnitude (signal intensity, SI) below (MEMRI) and above (LGE-MRI) a pre-defined threshold as compared to the SI of remote myocardium. Infarct mass measurement was performed in every slice by visual assessment and manual tracing of the enhanced area in MEMRI and LGE-MRI. The LV and infarcted mass are calculated as segmented LV and infracted area multiplied by the slice thickness (1 mm) and the specific gravity of the myocardium (1.05). Percent of infarct mass was calculated as (infarct mass x 100) / total LV mass.

4.3.4 Histological analysis

Triphenyltetrazolium chloride (TTC) staining method was performed to measure the infarct size in a mouse model of myocardial infarction. Mice were briefly anaesthetised with 4% isoflurane and injected intraperitoneally with the overdose of pentobarbital. After ~2.5 minutes, the chest was rapidly opened to have access to the heart. Once left ventricle region of the heart is identified, the femoral vessel was cut to allow blood to perfuse out. A 1 to 2 ml saline mixed with potassium was injected into the left ventricular chamber, very gently perfused to remove blood from the coronary system and arrest the heart at diastole. Great care must be taken to avoid any air bubbles within the syringe and needle. The beating heart is then rapidly excised and wrapped in cling film and freeze for at least an hour.

The frozen heart was then sliced in 6–8 parallel short-axis sections by hand using a razor blade on a cold surface. The heart sections were immersed in freshly prepared TTC (1% TTC in phosphate-buffered saline [PBS], pre-warmed to 37°C) for 15 minutes. The sections are then removed from the vial, and excess moisture is blotted; a possible distortion can be mended by gently flattening the sections between the index finger and the thumb. The samples are next placed in formalin for a maximum of 90 min. This step enhances the red/pale contrast between viable and necrotic tissue. In viable myocardium, TTC is converted by mitochondrial dehydrogenase enzymes to a red formazan pigment that stains the myocardium red, leaving necrotic myocardium white. Infarct sizes were manually measured using ImageJ software and compared with the corresponding MR images.

4.3.5 Statistical analysis

All statistical analyses were performed using the GraphPad Prism software Version 8.0. Results are presented as mean value ± standard error mean (SEM). Data were also tested using linear regression analysis and one-way ANOVA. In all cases, a p-value of less than 0.05 was considered significant.

4.4 Results

4.4.1 Preliminary washout study of manganese and gadolinium contrast agents

Representative T1 maps at baseline, 30min, 1h, 2h, 4h, 5h, and 24h post manganese ($MnCl_2$) and gadolinium (Gd-DTPA) injection are shown in Figure 4.6. T1 maps show rapid T1 reduction is in the remote myocardium at 30min as compared with the at baseline with peak reduction was observed at 1h to 4h post-$MnCl_2$ injection. T1 reduction began to recover at 5h and returned to baseline at 24h post-injection. Only a slight reduction in T1 was seen in the infarct region post-manganese injection. Whereas in the gadolinium group, a dramatic T1 reduction was observed in the remote myocardium, infarct region, and blood pool at 30min post-Gd-DTPA with the highest T1 reduction is seen in the infarct zone. T1 reduction began to recover at 1h and returned to baseline at 24h post-injection.

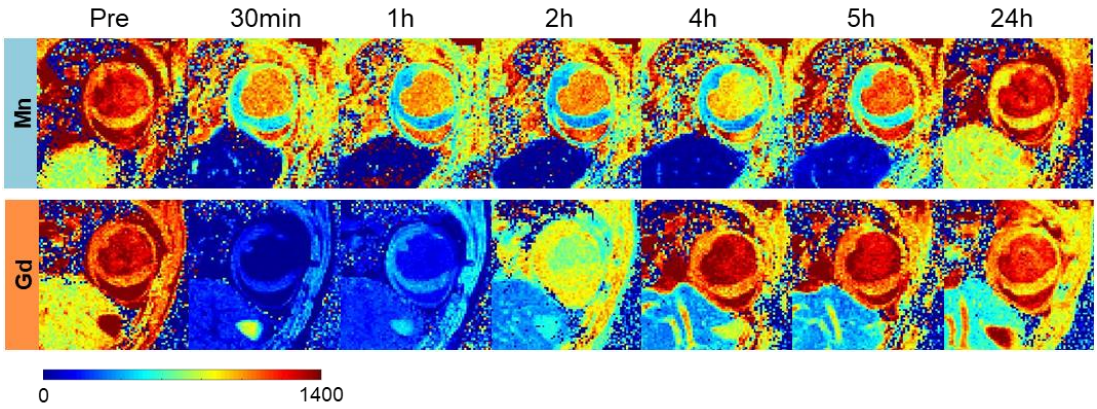

Figure 4.6: Representative T1 maps showing manganese and gadolinium washout rate.
T1 maps show a reduction in T1 relaxation time in the remote myocardium post-manganese injection and sustained for 4 hours. A rapid T1 reduction was seen in both remote myocardium and infarct region post-gadolinium injection. T1 recover more quickly, suggesting approximately 81%, and 98% Gd has washed out from the remote myocardium and infarct region respectively at 4h post-Gd injection. Mn = Manganese; Gd = Gadolinium.

Figure 4.7 and Figure 4.8 shows the R1 accumulation of manganese and gadolinium in the three regions of interest: remote myocardium, infarct region, and blood pool. The peak manganese uptake occurred at 2-hours post-Mn injection in the remote myocardium (2.71 ± 0.42 s^{-1}) and 30 minutes post-Mn in the infarct (1.46 ± 0.10 s^{-1}) and blood pool regions (1.00 ± 0.07 s^{-1}). In contrast, the peak accumulation of gadolinium in occurred at 30min post-Gd injection in all three regions (remote myocardium, 5.08 ± 0.29 s^{-1}; infarct region, 93.16 ± 27.96 s^{-1} and blood pool, 103.84 ± 16.74 s^{-1}). At 4h post-Gd injection 81%, 98% and 99% Gd is washed out from the remote myocardium (1.08 ± 0.06 s^{-1}), infarct region (1.37 ± 0.11 s^{-1}) and blood pool (0.89 ± 0.08 s^{-1}) respectively. Note that the first time points for image acquisition is 30 minutes post-injection of manganese or gadolinium. Therefore, the curve shown in Figure 4.7 in the remote myocardium post-manganese injection and in the infarct region post-gadolinium injection does not represent the first-pass perfusion. First past perfusion occurred at an earlier time points (1-3 minutes) and performed by administering the contrast agents via intravenous injection. R1 value in the remote myocardium, infarct region, and blood pool region at 30min, 1h, 2h, 4h, 5h, and 24h post intraperitoneal injection of gadolinium and manganese in a mouse model of myocardial infarction is summarised in Table 4-1.

A one-phase decay nonlinear regression line was fitted during the washout period post-contrast injection, and the half-life was estimated. The exponential fit showed an exponential decay rate of 0.02/min and 0.08/min, resulting in an estimated half-life of 33.83 minutes and 8.24 hours in the infarct region post-Gd injection and Remote myocardium post-Mn injection and respectively. I concluded that gadolinium-enhanced imaging should be done first with a wait of at least six half-lives (~4 hours) should be allowed before conduction manganese-enhanced imaging to ensure the independence of contrast enhancement patterns (Figure 4.9).

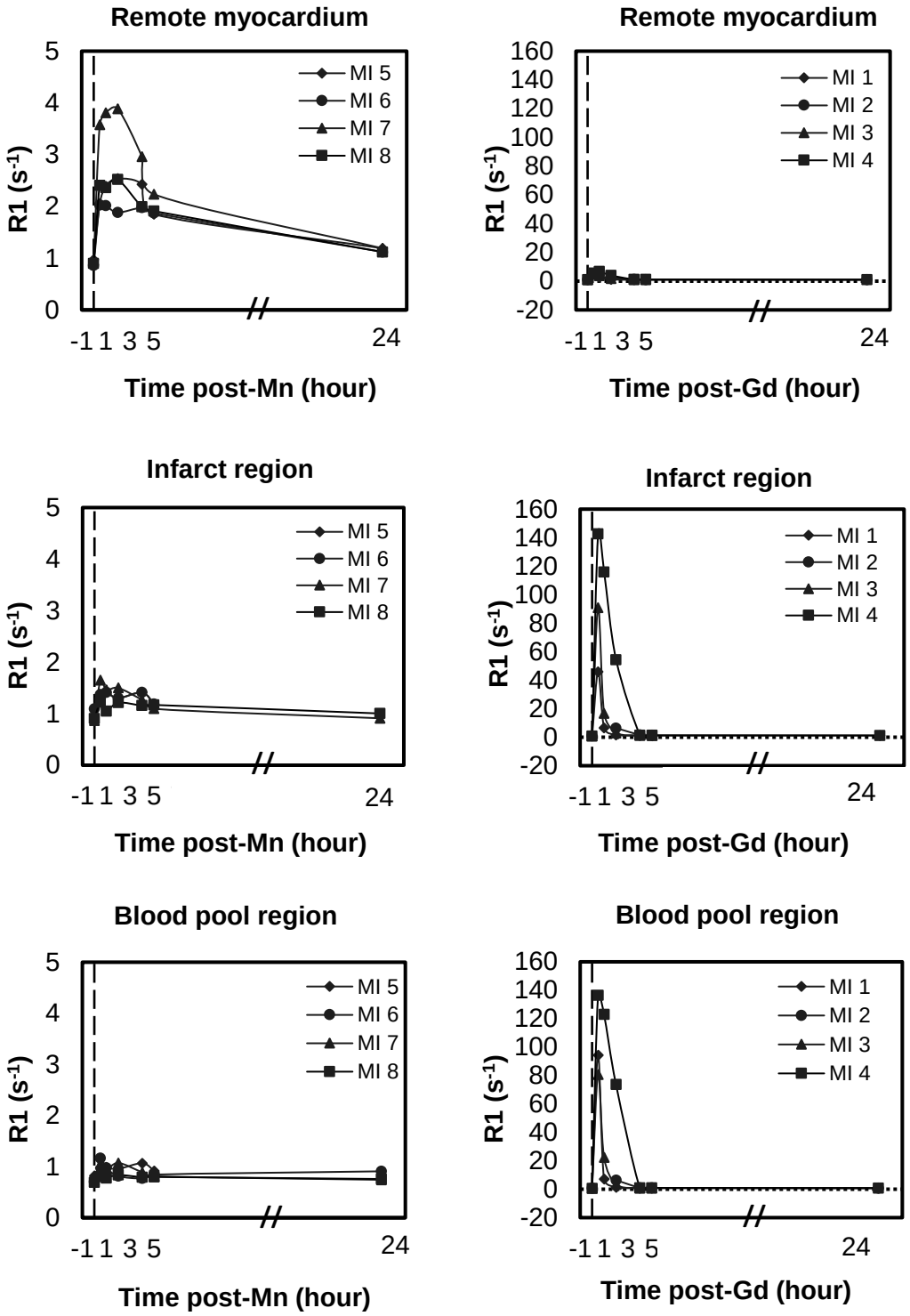

Figure 4.7: Manganese and gadolinium washout rate in each mice.

R1 value (mean ± SEM) reflecting the amount of manganese and gadolinium in the remote myocardium, infarct region, and blood pool region calculated from the mouse model of myocardial infarction (Mn, n=4 and Gd, n=4). Mn=Manganese; Gadolinium Gd=Gadolinium.

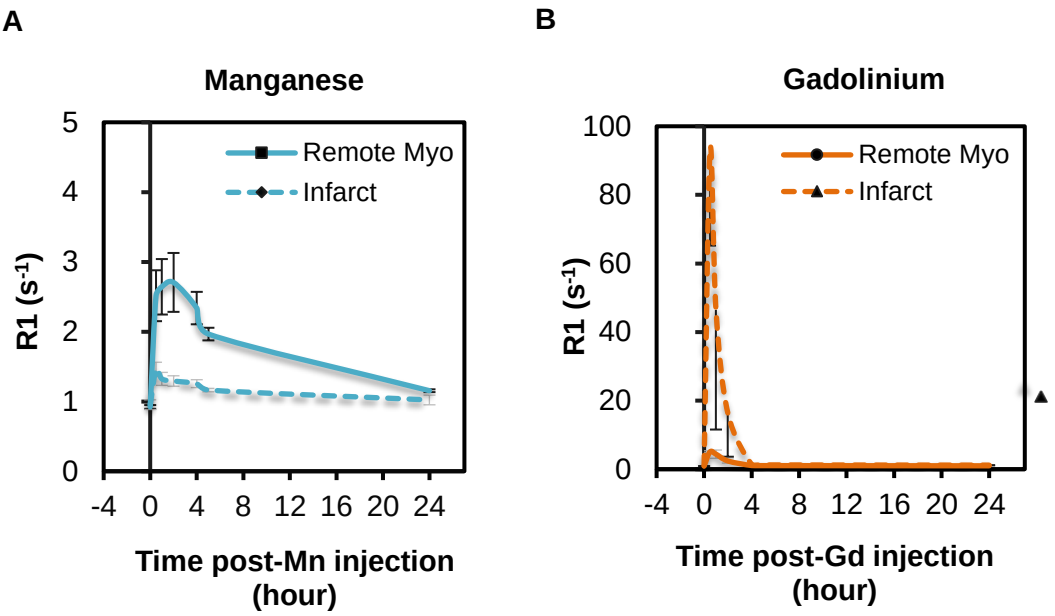

Figure 4.8: Manganese and gadolinium washout rate.

(A) R1 value reflecting the amount of manganese in the remote myocardium, infarct region, and blood pool region. The peak manganese uptake occurred at 2-hours post-Mn injection in the Remote myocardium and 30 minutes post-Mn in the infarct and blood pool regions. (B) R1 value (mean ± SEM) reflecting the amount of gadolinium in the remote myocardium, infarct region, and blood pool region. The peak accumulation of gadolinium in occurred at 30 minutes post-Gd injection in all three regions. At 4 hours post-Gd injection 81%, 98% and 99% Gd is washed out from the remote myocardium, infarct region and blood pool respectively.

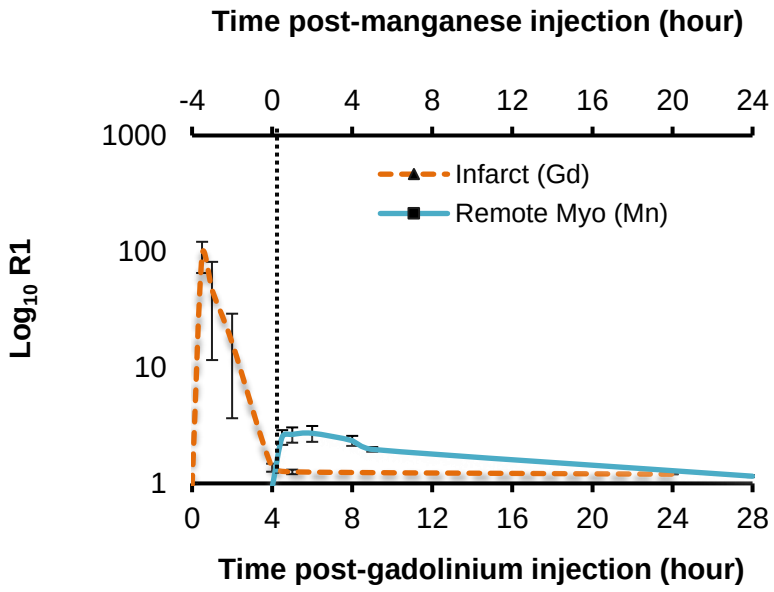

Figure 4.9: Graph shows gadolinium washout rate is faster than the washout rate of manganese.

Late gadolinium enhancement (LGE) should be performed first with a wait of at least 6 half-lives that is 4 hours before injecting manganese to performed manganese-enhanced MRI (MEMRI) to ensure the independence of contrast-enhancement patterns. It also shows that LGE is best performed within 30 minutes post-Gd injection and 60 minutes post-Mn injection for MEMRI.

Table 4-1: R1 value post manganese and gadolinium injection.

R1 value in the remote myocardium, infarct region, and blood pool region at 30min, 1h*, 2h, 4h, 5h, and 24h post intraperitoneal injection of gadolinium and manganese in mouse model of myocardial infarction.*

Manganese			
Time (hour)	Remote-MI	Infarct	Blood
Pre	0.92 ± 0.03	0.96 ± 0.07	0.74 ± 0.03
0.5	2.52 ± 0.37	1.46 ± 0.10	1.00 ± 0.07
1	2.65 ± 0.40	1.32 ± 0.09	0.92 ± 0.05
2	2.71 ± 0.42	1.29 ± 0.07	0.92 ± 0.06
4	2.34 ± 0.23	1.26 ± 0.06	0.88 ± 0.07
5	1.97 ± 0.09	1.16 ± 0.02	0.84 ± 0.03
24	1.16 ± 0.02	1.02 ± 0.07	0.80 ± 0.05
Gadolinium			
Time (hour)	Remote-MI	Infarct	Blood
Pre	0.96 ± 0.04	0.95 ± 0.05	0.74 ± 0.03
0.5	5.08 ± 0.29	93.16 ± 27.96	103.84 ± 16.74
1	4.39 ± 1.20	46.46 ± 34.88	50.88 ± 36.31
2	2.41 ± 0.62	16.36 ± 12.71	21.27 ± 17.55
4	1.08 ± 0.06	1.37 ± 0.11	0.89 ± 0.08
5	1.05 ± 0.04	1.26 ± 0.06	0.86 ± 0.05
24	1.00 ± 0.01	1.20 ± 0.00	0.77 ± 0.02

4.4.2 Quantification of infarct size using MEMRI and LGEMRI

Fourteen mice underwent successful coronary artery occlusion before CMR imaging. Seven mice underwent MEMRI at 1h post coronary occlusion, and another seven mice underwent LGE at 1h post coronary occlusion. All mice underwent both MEMRI and LGE at 1d and 14d post-MI. Two mice died in both groups due to heart complication during the first few days post-MI, leaving 10 mice at 14d post-MI.

At 1h post-MI, viable myocardium remote from the AAR was enhanced in MEMRI, allowing early delineation of the infarct zone, whereas only subtle enhancement within the AAR was observed on LGE-MRI (Figure 4.10A). Figure 4.10B shows a significant difference in the estimated final infarct size from MEMRI (39.22 ± 7%) and LGE-MRI (13.70 ± 2%) ($p = 0.002$) at 1h post-MI. The region of no Mn uptake in MEMRI and subtle enhancement in LGE were corresponding to the akinetic myocardium region in cine MRI. Cardiac function measured at ~1h post coronary occlusion using cine MRI shows an increase in LV end-systolic and a decreased in ejection fractions in both MEMRI and LGE groups. Changes in other cardiac function parameters will be described further in Section 4.4.3.

At 1d post-MI, theoretically, viable myocardium in the area-at-risk region has now shifted from the state of reversibly viable myocardium and into irreversibly infarct region. Figure 4.10A shows a direct comparison of MEMRI and LGE-MRI acquired in the same animal at 22 and 27 hours after MI, respectively. MEMRI showed a very similar pattern to 1h post-MI reflecting the sensitivity and the ability of MEMRI to quantify area-at-risk and hence early estimation of the infarct size. Infarct size measured at 1d post-MI has no significant difference to the size of area-at-risk quantify at 1h post-MI using MEMRI. Whereas in LGE MRI (34.85 ± 6%), the infarct size is significantly increased compared to 1h post-MI but has a similar size to the MEMRI group (34.93 ± 4%) (Figure 4.10) . When compared to the infarct size at 1h post-MI, there is a significant difference in the LGE-MRI ($p = 0.008$) but not in the MEMRI group. Figure 4.11 shiws an excellent correlation between infarct size at 1h versus 24h post-MI measured from MEMRI ($r = 0.97$, $p = 0.0003$). In contrast, poor correlation between infarct size at 1h versus 1d post-MI measured from LGE-MRI ($r = -0.22$., ns).

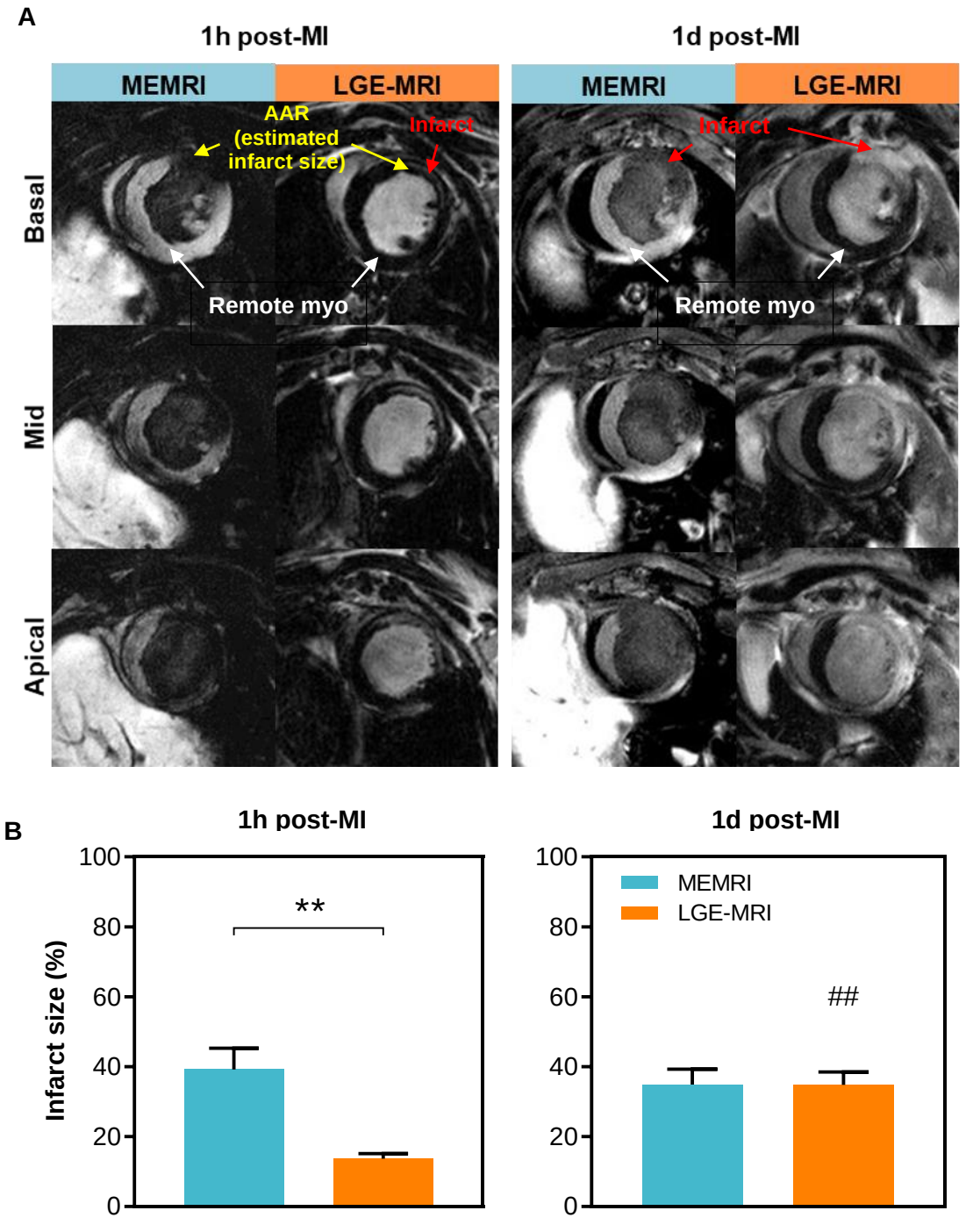

Figure 4.10: Direct comparison of MEMRI and LGE-MRI in acute myocardial infarction.

(A) Representative MEMRI and LGE-MRI images acquired in mice at 1h and 1d after myocardial infarction. (B) Mean of infarct size measured by MEMRI and LGE-MRI at 1h (n = 7) and 1d (n = 14) after myocardial infarction. Data were analysed using an MEMRI vs. LGE-MRI unpaired (1h) and paired (1d) t-tests, one-way ANOVA with Tukey's multiple comparisons test (1h vs. 1d vs. 14d). Tukey's 1h vs. 1d (##p<0.01).

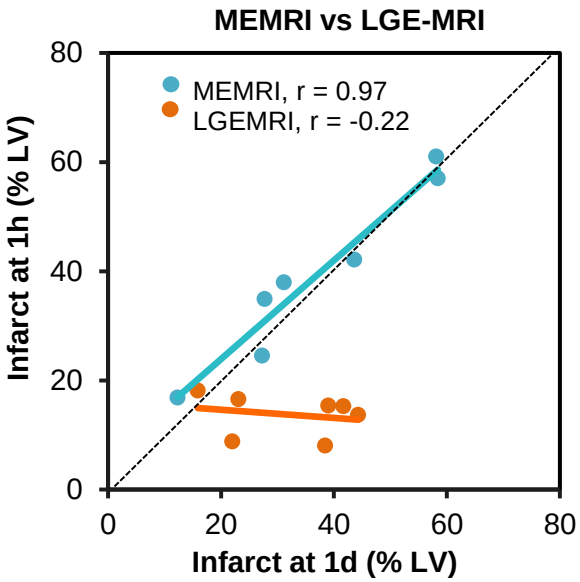

Figure 4.11: MEMRI and LGE-MRI measurements of infarct size at 1h and 1d post-MI.
*Correlation between MEMRI and LGE-MRI measurements of infarct size at 1h versus 1d. Data was analysed using linear regression analysis. MEMRI vs. LGE-MRI (**p<0.01)*

Between 1d and 14d, 4 mice (2 from each group) were euthanised owing to severe symptoms of heart disease. The 10 surviving mice were imaged with both MEMRI and LGE-MRI at 14d. Similarly, at 14d, both techniques are able to identify the infarct size during the chronic stage of myocardial infarction. Infarct size measured from MEMRI groups shows similar size to the LGE-MRI group. Figure 4.12A shows a direct comparison of MEMRI and LGE-MRI acquired in the same animal at 14d post-MI, respectively. Hypoenhancement of the infarct in the MEMRI image corresponded with hyperenhancement of the infarct in LGE MRI and corresponded with the pale region in triphenyltetrazolium chloride (TTC) staining, indicating infarcted tissue. There is no significant difference in the final infarct size quantified from MEMRI (25.41 ± 6%) as compared to LGE-MRI (30.82 ± 6%) and TTC (20.88 ± 3%). There is a significant difference in the LGE-MRI ($p = 0.02$) when compared to the infarct size at 1h post-MI but not at 1d post-MI. No significant changes were seen in the MEMRI group at all time points post-MI (Figure 4.12B).

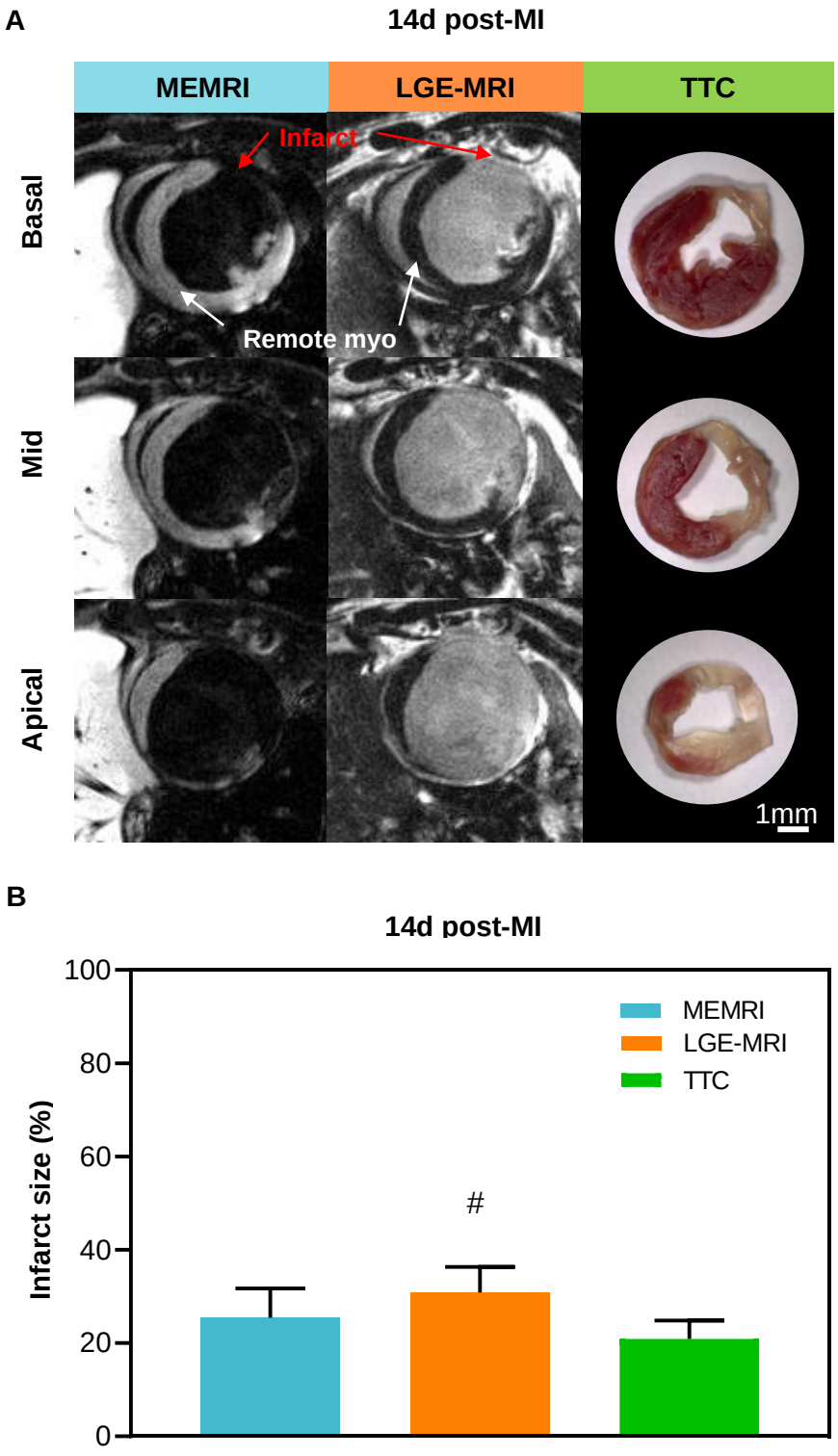

Figure 4.12: Direct comparison of MEMRI and LGE-MRI at* 14d *post-MI.

(A) Representative MEMRI and LGE-MRI images acquired 14d after myocardial infarction and compared with matching histological TTC staining for delineation of infarct area. (B) Mean of infarct size measured by MEMRI and LGE-MRI at 14d (n = 10) after myocardial infarction and compared with histological TTC staining. Data were analysed using MEMRI versus. LGE-MRI paired t-tests and one-way ANOVA with Tukey's multiple comparisons 1h versus 14d (#p<0.05).

There was a strong positive correlation between infarct size measured from MEMRI and LGE-MRI at 1d post-MI ($r = 0.90$, $p < 0.0001$) with a mean bias of 0.1 ± 7.1%. Similarly, there was excellent correlation between infarct size measured MEMRI and LGE-MRI both at 14d post-MI ($r = 0.93$, $p < 0.0001$) with a slight underestimation by Bland-Altman analysis (-5.4 ± 7.4%). The comparison of the infarct size measured from MEMRI and LGE-MRI at 1d and 14d post-MI is presented in Figure 4.13.

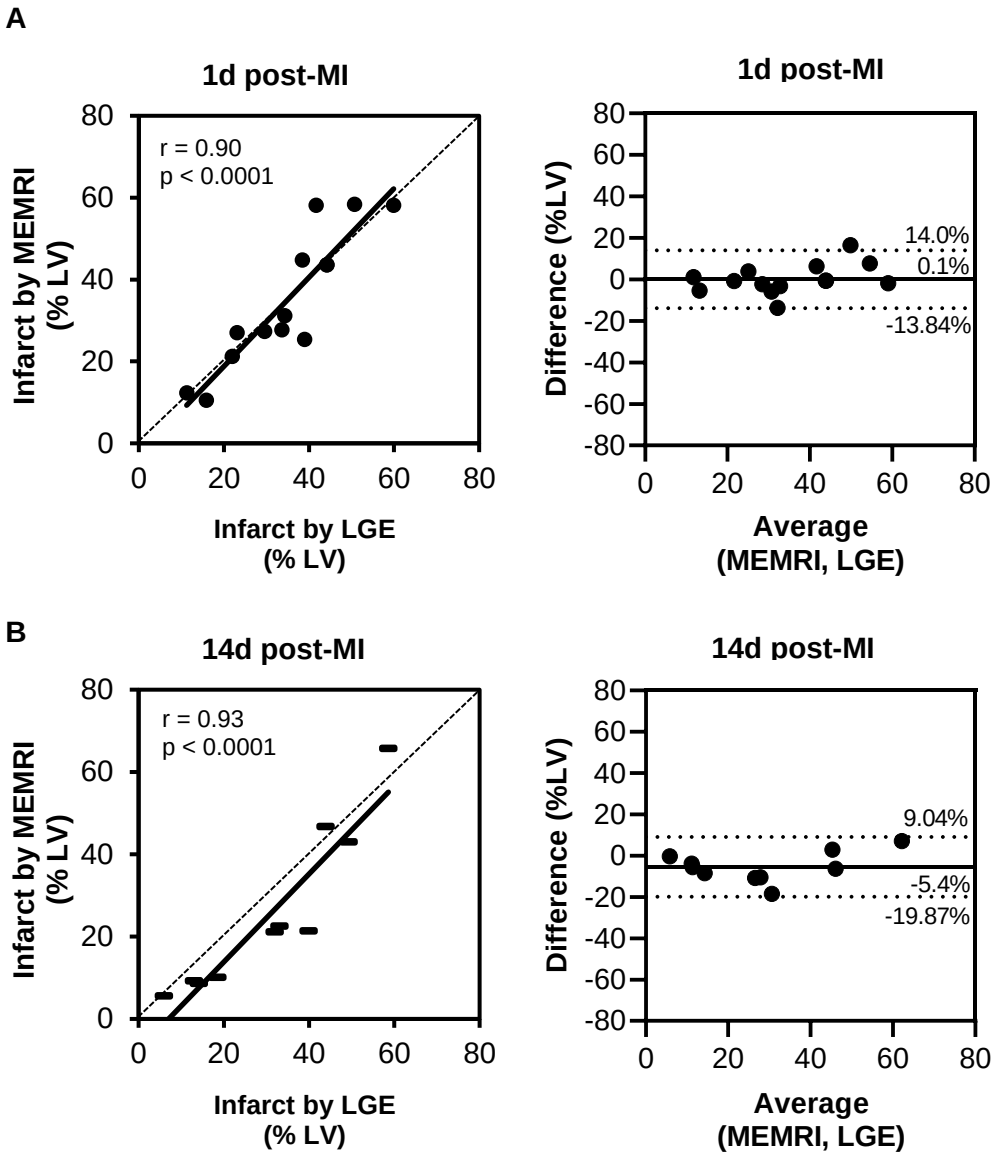

Figure 4.13: Correlation between MEMRI versus LGE-MRI measurements of infarct size at 1d and 14d post-MI.

The size of infarction by MEMRI showed excellent correlation to infarct size by LGE and minimal bias in Bland-Altman plot (right) at 1d, n=14 and 14d, n=10 post-MI. Dotted lines represent a line of identity in the scatterplot (left) and mean ± 2SD in Bland Altman plot.

Figure 4.14A shows a series of MEMRI and LGE-MRI 40min, 60min, 90min, 1d, and 14d post-MI in one of the mice in each group. Data at 40min and 90min post-MI were acquired only in few of the mice as it was experimentally challenging to image at the earlier time point (40min) and to avoid keeping the mice inside the scanner for too long (90min) which may affect their recovery post-surgery. The enhanced region in MEMRI reflects the alive and functional myocytes (remote myocardium) allowing for delineation of AAR as soon as 40min post-MI in MEMRI. A subtle small infarct region (hyperenhancement) was also seen as soon as 40min in LGE-MRI and continue to expand from the mid-myocardium transmurally at 90min post-MI. At 1d post-MI, all tissue in the area at risk was covered with infarct, and at 14d post-MI, the heart was undergoing cardiac healing, and remodelling Schematic represents the evolution of cell death in the infarcted heart. (Figure 4.14B).

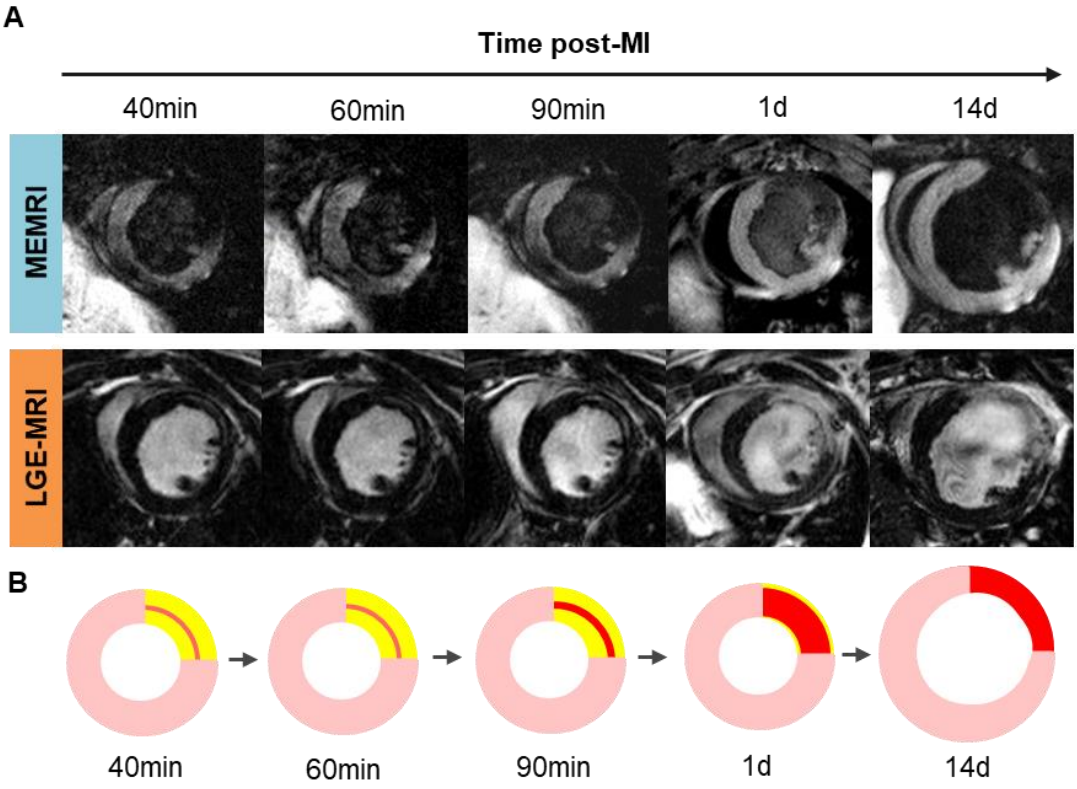

Figure 4.14: Evolution of cell death in the infarcted heart.

(A) MEMRI (n=1) and LGE-MRI (n=1) were performed at 40min, 60min, 90min,1d and 14d post-MI. AAR can be delineated as soon as 40min post-MI in MEMRI. A subtle small infarct region (hyperenhancement) was also seen as soon as 40min and continue to expand transmurally from the middle part at 90min and 24h post-MI in LGE-MRI. (B) Schematic represents the evolution of cell death in the infarcted heart. At 1d post-MI, myocardium in the area at risk has now been converted to infarcted tissue (necrosis), and at 14d post-MI, the heart was undergoing cardiac healing and remodelling.

4.4.3 Cardiac function

Figure 4.15 shows a representative end-diastolic and end-systolic cine MRI images from both the MEMRI and LGE groups at 1h (n=7), 1d (n=14) and 14d (n=10) post-MI. Physiological results show a reduction in cardiac function as soon as 1h following permanent coronary artery ligation. As soon as 1h post coronary occlusion, ejection fraction (EF) dropped to 38.21 ± 4% and 35.97 ± 5% in MEMRI and LGE group respectively. Only a slight change in EF between 1h, 1d and 14d post-MI. Bigger changes but not significantly different in EDV and ESV were seen in the three-time points post-MI (Figure 4.15 and Table 4-2). An increased in LV end-systolic volume was also seen at this early time point (43.22 ± 4% and 44.29 ± 7%) in both MEMRI and LGE group, respectively. A bigger increased in LV end-diastolic volume is seen at a later time point post coronary ligation (78.45 ± 4% and 79.51 ± 3%) at 1d in MEMRI and LGE group respectively and (108.43 ± 16% and 112.79 ± 16%) at 14d in MEMRI and LGE groups respectively.

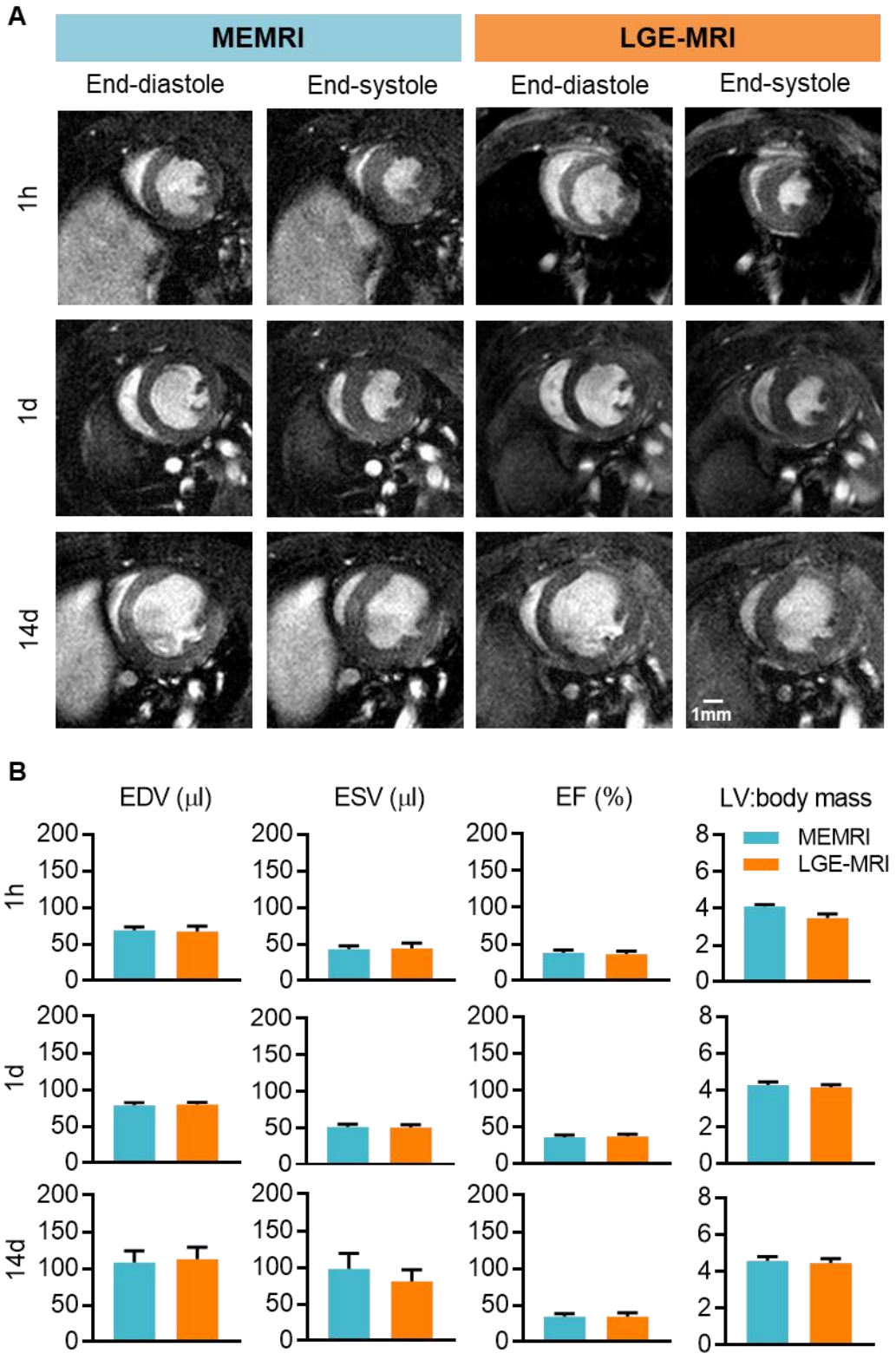

Figure 4.15: Cardiac function.

(A) End-diastolic and end-systolic cine-MRI images from both MEMRI and LGE-MRI group at 1h *(n=7),* 1d *(n=14), and* 14d *(n=10) post-MI. Scale bar, 1mm. (B) Corresponding Cine-MRI measurements of cardiac morphology and function. *P<0.05 MEMRI vs LGE-MRI. EDV indicates end-diastolic volume; EF, ejection fraction; ESV, end-systolic volume; and LV, left ventricle. No significant difference was found at different time point post-MI in both groups.*

Table 4-2: Cardiac function and morphology.

Data measured 1h, 1d and 14d post-MI in both MEMRI and LGE-MRI group.

	Contrast Agents	1h (n=7)	1d (n=14)	14d (n=10)
LV function				
EDV, µl	Mn	68.82 ± 5	78.45 ± 4	108.43 ± 16
	Gd	67.39 ± 7	79.51 ± 3	112.79 ± 16
ESV, µl	Mn	43.22 ± 4	50.90 ± 4	80.81 ± 17
	Gd	44.29 ± 7	50.23 ± 4	80.68 ± 16
SV, µl	Mn	25.61 ± 2	27.56 ± 2	32.66 ± 2
	Gd	23.10 ± 2	29.27 ± 2	31.73 ± 2
EF, %	Mn	38.21 ± 4	38.21 ± 4	34.35 ± 4
	Gd	35.97 ± 5	37.62 ± 3	34.50 ± 5
Infarct size, %	Mn	39.22 ± 6**	34.93 ± 4	25.41 ± 6
	Gd	13.7 ± 1	34.85 ± 6##	30.82 ± 6#
TTC, % (n=6)				20.88 ± 4
Heart rate, bpm	Mn	510 ± 17	518 ± 11	529 ± 11
	Gd	499 ± 20	516 ± 14	563 ± 7
LV mass, mg	Mn	113.92 ± 1	116.13 ± 4	132.09 ± 7
	Gd	100.99 ± 6	113.20 ± 3	128.78 ± 7
Body weight, g	Mn	27.83 ± 1	27.16 ± 0.4	28.82 ± 0.3
	Gd	29.20 ± 1	27.23 ± 0.4	28.82 ± 0.3
LV mass:body weight ratio	Mn	4.10 ± 0.1	4.29 ± 0.2	4.57 ± 0.2
	Gd	3.47 ± 0.2	4.17 ± 0.1	4.46 ± 0.2

Values represent mean ± SEM, EDV indicates end-diastolic volume; ESV, end-systolic volume; SV, systolic volume; EF, ejection fraction; LV, left ventricle; TTC, triphenyltetrazolium chloride, and bpm; beats per minute. Note that at 1h post-MI in MEMRI group, the % of infarct size is referring to the % of AAR (estimated final infarct size).

**P<0.05 Mn vs Gd*

***P<0.01 Mn vs Gd*

#P<0.05 ## P<0.01 1h vs 1d and 1h vs 14d

†P<0.05 1d vs 14d

4.5 Discussion

4.5.1 Preliminary washout study of manganese and gadolinium contrast agents

The present studies measure the washout rate of manganese and gadolinium contrast agents up to 24 hours post i.p. injection. The experiment aimed to assess the washout rate to ensure the independence of contrast enhancement and to get the optimal imaging window for MEMRI and LGE-MRI. This study shows that manganese accumulated and was retained in the remote myocardium for longer than the rate of gadolinium accumulation in the infarct region. A similar finding reported by Schaefer et al. (1989) [132] where they found gadolinium left the normal rat myocardium faster that manganese. This likely due to the short half-life of Gd-DTPA and tight Mn^{2+} binding with the intracellular proteins. Late gadolinium enhancement MRI (LGE-MRI) should be performed first with a wait of at least six half-lives, that is 4 hours, before injecting manganese to performed manganese-enhanced MRI (MEMRI) to ensure the independence of contrast-enhancement patterns. At 4 hours post-injection of gadolinium, 98% of gadolinium has been washed out from the infarct. It is not possible to combine Gd-DTPA and Mn^{2+} enhanced MRI at the same time as both acts through the same NMR process of increasing R1 relaxivity. This made it impossible to perform a direct comparison in the same mice at 1h after infarction. However, similar to previous reports [220], the present study showed that >4 hours of Gd-DTPA washout was sufficient to permit subsequent MEMRI, meaning all mice could be scanned at 1d post-infarction using both methods.

It is well documented that manganese and gadolinium has a different distribution pattern in the three regions; remote myocardium, infarct and blood pool region. As an intracellular contrast agent and a marker of cell viability, manganese induced a marked effect on the remote myocardium T1 relaxation time with a short half-life in the blood pool. Only a small effect on T1 relaxation was observed in the infarct region. This could be due to the transient accumulation of Mn^{2+} in the blood pool region and in the extracellular space. In contrast, both remote and infarct tissue showed accumulation of Gd-DTPA. As an extracellular contrast agent, gadolinium do not enter intact myocardial cells but distributed in the extracellular space. The rate of accumulation and wash out depends on multiple factors such as type of heart disease, myocardial blood supply. Higher accumulation and thus higher effect on T1 relaxation were seen in the infarct region as compared to the remote myocardium at 30min post-injection, as at this time point, gadolinium has been washed out from the remote myocardium that has an adequate blood supply. Gadolinium is retained longer

in the infarct region due to the poor or absence in blood supply and expansion of the extracellular space. The distribution of gadolinium also depends on the time after injection in which imaging is performed. At an early stage, gadolinium resides primarily in healthy myocardium and blood pool. At a later time point, gadolinium washed out of normal myocardium and retained in the infarcted tissue. Thus, it is important to performed LGE-MRI in the desired time window to achieved higher image contrast. Peak T1 contrast was achieved at a minimum of approximately 30 minutes of post-Gd IP injection. This finding was also reported in a previous study [137]. Compared to LGE-MRI, the imaging window in MEMRI is more prolonged, making it a desirable contrast agent to monitor dynamic T1 change in the heart. The $MnCl_2$ dosage used in this study shows that MEMRI is best performed from 60 minutes up to 4 hours post intraperitoneal injection for MEMRI.

4.5.2 Quantification of infarct size and cardiac function

This study compared the ability of Gd-DTPA and Mn^{2+} enhanced T1-weighted MRI to delineate the area at risk (AAR), reflecting the estimated final infarct size at 1h after coronary occlusion, then followed up the same mice at 1d and 14d. At 1h, infarct sizes as assessed by LGE-MRI were significantly smaller than MEMRI, and whilst the MEMRI measurements remained stable over 24 hours, the LGE-MRI measurements increased to a similar level to that reported by MEMRI. An increase in Mn^{2+} uptake is seen in alive-functional myocardium but not in an AAR. In pathologic conditions, particularly during ischemia, the L-type Ca^{2+} channel activity is greatly inhibited, thus impairing Mn^{2+} uptake [93]. These data suggest that myocytes within the AAR rapidly stop internalising Mn^{2+} under ischemic conditions, whilst T1 mapping results show increased Mn^{2+} uptake in the remote myocardium from the activation of sympathetic response at the early phase of ischemic injury. These processes combine to rapidly produce high contrast between viable and ischemic myocardium, allowing early delineation of the region of occlusion. To date, several experimental MI studies using manganese-based contrast agents have been performed in mice [101], [123], [124] to delineate infarct size and its usefulness in interrogating pathophysiology [100], [264], [265], but none have investigated such early changes after coronary occlusion in comparison to LGE-MRI. These results, along with standard measures of cardiac structure, ejection fraction and infarct size, revealed that the different groups of mice sustained equivalent myocardial injuries which resulted in similar cardiac impairment at later time points, confirming for the first time that MEMRI provides an early indicator on final infarct size after permanent coronary occlusion.

The membrane rupture and oedema that underlie Gd-DTPA accumulation in LGE-MRI occur later in the pathological process, suggesting LGE-MRI underestimates the estimated final infarct size during the first hours post-MI when cell death is still incomplete at this time point. However, the subtle enhancement seen in LGE at 1h post-MI, indicated that a subset of AAR in MEMRI is already infarcted at 1h post-MI. Several studies have shown that LGE-MRI measurements of infarct size evolve with time after MI [266]–[269], but none have made measurements as early as 1h after coronary occlusion. It is of interest that this study showed patchy mid-wall Gd-DTPA enhancement in all mice at 1h. Data presented here indicate that small regions of LGE in the mid-myocardium could represent irreversible cell death in the most severe region of myocardial ischemia. An experimental study in a mouse model of reperfused infarction reported infarction primarily involved the mid-myocardium at 3d post-MI indicated that the mid-myocardium as the most vulnerable area to ischemia [237]. Low levels of oxygen can passively diffuse up to 400 micrometers through mouse cardiac muscle tissue [270]. Hence I postulated that oxygen from the circulating blood in the left ventricles could still diffuse across the endocardium within the area of restricted blood supply. The subendocardial oxygen levels would not be sufficient to sustain function, but may delay cell death. This explains the viability of this region for longer time than the mid-myocardium post-ischemia. The present finding, however, contraindicated to the ischemic wavefront of necrosis hypothesise, stating necrosis started from the subendocardial myocardium [233], [234]. This is probably because their study was done in a large animal model where imaging was performed at a lower resolution, meaning the ~400 micrometres of viable endocardium would not be visible.

However, it is important to note that the reduced enhancement in LGE at 1h post-MI could also be due to reduced coronary blood perfusion in the setting of permanent occlusion model as at this time point, cell membrane rupture would not have occurred, and collateral vessels might not have been formed. The wash-in of gadolinium into the infarct region occur either via passive diffusion from the extracellular space in the normal myocardium into the area of perfusion defect or via collateral delivery [271]–[273]. The increased volume of gadolinium distribution is the primary mechanism for the enhancement in LGE due to two factors. First, it is due to the ruptured cell membrane causing the gadolinium to diffuse passively into the intracellular space of irreversibly injured cells. Secondly, the increased volume of gadolinium in the infarcted region is due to slow wash-out rate in the infarcted region

where functional capillary density is reduced, accumulation of intravascular neutrophil and increase in extracellular space when the collagen matrix is formed [273].

The ability to image the evolution of cell death in after ischemic injury could yield additional pathophysiological data on cellular function in acute cardiac injury. It may be possible to exploit the different mechanisms of MEMRI and LGE-MRI to image the transition from viable myocardium (alive but dysfunctional) to irreversibly infarct tissue. Data presented here showed that 14% enhancement in LGE-MRI reflecting the infarct region at 1h and 35% at 1d post-MI. This finding is in line with previous study, which has also reported 13% of necrotic cardiomyocytes in AAR as soon as 30 minutes post-MI in rat s heart [227]. In contrast, MEMRI showed a similar size of AAR (estimated infarct size) at 1h and infarct region at 1d post-MI (35%). From these data, I could hypothesise that the AAR could be defined as either the hypointensity on 1h MEMRI or hyperintensity on 1d LGE-MRI, both of which measure 35% as expected. This is because, in this study, a permanent myocardial infarction model was used. By 1d post-ligation, tissues in the perfusion bed of the occluded coronary artery have completely lost its function and infarcted. Hence, both method should give equal measurement despite having different mechanisms. Hyoerenhancement on 1h LGE-MRI may represent the irreversibly damaged infarct which compromised 14% on the LV and 40% of the AAR at 1h. This would mean that at 1h post permanent coronary occlusion 21% of the LV (60% of the AAR) was still viable. Further interrogation of this approach is required, but the combination of MEMRI and LGE-MRI could provide highly valuable information of AAR and infarct evolution. Previous studies have proposed that the hypintensity area in MEMRI depict the AAR [122], [133] and stunned myocardium [93]. However, the present study is the first MEMRI study done at an early point post coronary occlusion and validated against LGE-MRI. This shows the feasibility of MEMRI for functional assessment of the myocardium for quantification of viable myocardium and estimated final infarct size during early phase of ischemic injury. The first-hour post-ischemic injury is a crucial time in which viable myocardium could recover its function upon restoration of blood flow. Quantification of viable myocardium at this time window would greatly help improve patients outcome following therapy and help reduce final infarct size. It has been suggested that the mismatched region between unenhanced-MEMRI and enhanced-LGE-MRI reflect the area of peri-infarct zone in a large animal model [98], [170], [220]. This is an exciting phenomenon to investigate further. However, as the present study used a permanent coronary occlusion model, this border zone would be minimal and was not identified when images were coregistered. At the time

experiments were conducted, our lab was in the process of developing a reperfused model of myocardial infarction. Future studies will investigate the approach for quantification of the peri-infarct region a small animal model of reperfused MI.

There are other limitations of the present study. In the present study, by administering manganese after coronary occlusion, as mentioned previously, the area of hypo-enhancement in MEMRI reflect the AAR in the perfusion bed of occluded coronary artery. Infarcted region is a subset of the AAR in which the proportion is depending on the duration of ischemia, the presence of collaterals vessels, time to reperfusion and other related factors [18]. Without intervention or restoration of blood flow, all tissue in the AAR will be converted to infracted tissue. The data presented here indicated that the hypo-enhanced region in MEMRI at 1h gave a precise estimation of the final infarct size. However, additional experiments need to be done characterize the myocardial injury in the AAR region at 1h post-occlusion, whether it is still viable but reversibly injured or irreversibly injured. Early gadolinium enhancement (EGE), at three minutes post-intravenous bolus injection has been shown to correlate well with AAR, enhances both reversibly and irreversibly injured myocardium [274]. With this technique, we could potentially be able to co-registered early gadolinium enhancement with hypo-enhancement on MEMRI, giving additional information on the level of myocardial injury (reversible or irreversible). This should give more confidence that the hypo-enhanced region seen in MEMRI was not only due to lack of coronary blood perfusion, but also due to the loss of myocyte function, and hence loss of calcium channel function that reflected as reduced manganese uptake in MEMRI. This is also in line with the observed reduced contractility in CINE MRI image, suggesting functional depression in the corresponded hypointense region in MEMRI. However, EGE was not performed in the present study due to the complexity of the study with the need of an intravenous injection in MRI setting. Another possible approach to confirm this is to do a histological study at 1h post coronary occlusion such as TTC staining or using other biomarkers of cell viability to support the findings.

Another limitation of the present study is the absence of a sham group which would be helpful to exclude the possible effects of complication from surgery (suncs as haemorrhage) that might have affect the T1 and T2 relaxation time Secondly, additional imaging sequences such as native T1 mapping or T2-based MRI, especially during the first-hour post-MI would give additional information in characterizing different myocardial zones (remote myocardium, viable myocardium and infarct) following ischemic injury. However, these would only be possible using imaging sequences that offer a shorter scan time which is still under development in our lab.

The ability to non-invasively quantify myocardial viability could have important diagnostic and prognostic applications across a range of cardiac diseases. Firstly, accurate identification of viable myocardium could be used to identify which patients would benefit from percutaneous intervention or coronary artery bypass grafting [256]. Recent clinical trials have cast doubt on the value of PET- and SPECT-based myocardial viability imaging [275], [276], thus increasing the need for more accurate methods. Additionally, MEMRI could have a role to play in phenotyping hypertrophic and dilated cardiomyopathies. There is also great potential for evaluation of routine and experimental therapies including; optimisation of pharmacological doses to regulate cardiac inotropy [195]; monitoring the success of regenerative therapies [277] and interrogating viability of engineered heart tissues [278].

4.6 Summary

In this chapter, a manganese-enhanced MRI method for evaluating myocardial viability has been developed and tested in a permanent coronary occlusion mouse model. This method showed that MEMRI could quantify the final infarct size earlier than LGE-MRI. When combined with LGE-MRI, this approach could also be used to quantify the viable myocardium at an early phase after ischemic injury. MEMRI provides a sensitive approach which could be used as an early measure of cell death and myocardial viability and could be used to study the efficacy of cell therapy or new drugs which target acute MI.

Chapter 5: Final discussion

This thesis has described my work in developing cardiovascular imaging of myocardial viability in acute myocardial infarction.

Ischemic heart disease affects >100 million individuals worldwide and increased by 73.3% from 1990 to 2015 [279]. Despite modern therapies, up to one-third of patients with acute myocardial infarction will develop heart failure [280], which remains a common and a major healthcare burden worldwide. The early and reliable diagnosis of acute myocardial infarction has a substantial impact on clinical outcomes. Current clinical routine is mostly based on medical history, physical status, the electrocardiogram (ECG), cardiac biomarkers, and imaging to assess myocardial viability. Viability has significant clinical implications. Identifying dysfunctional myocardium that has a potential for restoration of contractile function could be helpful in therapeutic decision-making. Cardiac imaging has revolutionised our ability to diagnose heart disease and quantify mechanisms of pathology and therapy [72]. Current techniques could give information on the structure, contractility, metabolism and fibrosis [73]–[75] but struggle to directly quantify one of the most important determinants of patient morbidity, myocardial viability [76], [77]. Pre-clinical imaging using animal models plays an extremely valuable role in medical research. Imaging experimental animal models allow observation of biological processes at the cellular level allowing for the development of sensitive and specific imaging biomarkers which can be translated into the clinic, as new methods for the diagnosis and prognosis of disease.

In acute myocardial infarction, one of the earliest manifestations of functional impairment is the reduction in cardiac contractility. Cardiac contractility is highly dependent on the calcium homeostasis in the myocardium. Any changes in the influx and efflux of the calcium ion affect cardiac contractility. In acute myocardial infarction, one of the earliest mechanism following obstruction in blood flow is intracellular calcium overload in the viable myocardium, with reduce calcium uptake in the perfusion defect region likely due to disruption of calcium channels and cell membrane integrity within the area at risk or infarcted myocardium. Calcium is integral to cardiomyocyte contraction, and alterations to calcium uptake and handling are present in many cardiomyopathies such as hypertrophic cardiomyopathy [281], dilated cardiomyopathy [282], [283], and heart failure [284]. Hence, a method to quantify calcium uptake within live cells, animals and patients would give valuable information on cardiac viability and insights into pathological and therapeutic

mechanisms [76], [92], [93]. One potential approach is by using an intracellular contrast agent, manganese. Manganese is an analogue to the calcium ion, thus, changes in Mn^{2+} uptake would reflect changes in Ca^{2+}, and could potentially offer an early marker of cell viability. The overall aim of the research in this thesis was the development and validation of manganese-enhanced MRI for pre-clinical imaging of myocardial viability after acute myocardial infarction. This chapter summarises the studies carried out throughout the thesis, discusses some of the successes and limitations of each study and outlines potential avenues for future development and clinical need.

Manganese is a potent paramagnetic contrast agent that could give essential information on cellular viability. However, concern over the cardiotoxicity of manganese has limited its usage in the heart. In Chapter 2, real-time high-resolution ultrasound imaging was applied to investigate the effect of manganese on cardiac contractility and implemented three different approaches to overcome toxicity; calcium supplementation; reduced $MnCl_2$ concentration; and altered route of injection (intraperitoneal injection as opposed to intravenous). To our knowledge, this is the first study to investigate the effects of manganese on real-time cardiac contractility. Using this method, I was able to quantify the transient changes in cardiac inotropy, which resolved within seconds and would have been missed when using other imaging methods such as MRI which takes longer to acquire images. The work from this chapter shows that calcium supplement and intraperitoneal injection improve the safety of manganese. Calcium supplement helps in reducing the competition of manganese with calcium during cell entry by administering additional calcium ions together with manganese ions in the extracellular space, thereby overcoming the cardiac depression effect seen from high manganese dose. Manganese toxicity could also be negated through slow release of manganese which is seen when using intraperitoneal injection or a slow infusion. Calcium supplementation approach could easily be translatable to clinical application, and CaG based contrast agents are already approved. Intraperitoneal injection is widely used in pre-clinical study but would not be used clinically. However, a slow infusion of manganese is feasible in patients by controlling the rate of injection via intravenous line. Previous pre-clinical studies safely administered a couple of small amount of over a period of time to ensure slow release of manganese by means of intravenous infusion via a catheter placed into a tail vein [101], [151].

Also investigated was how these different manganese formulations affect MRI image contrast in vivo, and how these relate to the actual manganese concentration within tissue based upon in vitro MRI studies in phantoms. Although these experiments were not designed to inform on the safe clinical use of Mn^{2+} directly, they do provide valuable information on the mechanism through which manganese affects cardiac function and suggest Mn^{2+} based MRI contrast can be effectively utilised in pre-clinical studies. Calcium supplementation showed superior image quality over other approaches (reduced $MnCl_2$ concentration and intraperitoneal injection). In short, $MnCl_2$ appears safe either by using calcium supplementation or through slow release of manganese. It effectively decreases myocardium T1, maintaining this effect for a relatively long period of time and allowing for the development of new imaging strategies in CMR, especially in ischemia research. My data suggests that $MnCl_2$ (0.1mmol/kg) has a good cardiac safety profile in pre-clinical imaging in mise, promoting a significant decrease in myocardium T1 for a relatively long time. From this data, I believe that new strategies to study coronary heart disease with CMR can be designed with a special focus on ischemia with higher resolution sequences and out of the magnet protocols, taking advantage of the longer-lasting changes in relaxation times produced by the agent.

In Chapter 3, quantitative T1 mapping was applied to monitor calcium homeostasis during ischemic injury in a mouse model of acute myocardial infarction. This is the first quantitative imaging study to track the dynamic features of intracellular calcium response to ischemic injury. Mice were preloaded with manganese contrast agents to label the cardiomyocytes prior to the coronary artery ligation. By using T1 mapping MEMRI, I was able to quantify Mn^{2+}-mediated changes in T1 reflecting the changes in intracellular Ca^{2+} in the myocardium during ischemic injury.

Two main finding arouse from the study in Chapter 3. Firstly, I have shown that manganese can be used to detect the increased in intracellular calcium in the viable myocardium within the first 3 hours post coronary occlusion. This demonstrate the potential of T1 mapping MEMRI as a useful marker of calcium handling imbalance during ischemic injury and indicates promise for use in clinical imaging. This has important implications for how T1 mapping MEMRI could be used for evaluating the efficacy and dosing of inotropic drugs in AMI as Mn^{2+} levels may directly reflect the impact of pharmacological intervention on cardiac inotropy. For example, the effects of the positive inotropic drug dobutamine and the calcium channel blocker diltiazem can be detected using T1 weighted MEMRI [115]. In addition, recent study showed the ability of MEMRI to detect altered calcium-handling in pathological myocardium

of non-ischaemic cardiomyopathy [285]. In addition, the ability to detect changes in intracellular calcium levels give us an indirect measure of the involvement of sympathetic innervation in regulating cardiac contractility during ischemic injury. Sympathetic activation during acute myocardial infarction is an important arrhythmogenic mechanism [286]. Ischemia-induced arrhythmia could be attributed to several factors, including intracellular calcium overloaded [287]. Imaging tools could enhance our understanding on the mechanisms of ischemia-induced arrhythmia aiding in clinical management in patients with acute MI.

The other main interesting finding from this study was more surprising; T1 mapping MEMRI allow early delineation of the area-at-risk (AAR) acutely post-ischemic injury (1-hour post coronary occlusion). Quantitative T1 mapping reveals that Mn^{2+} is not being lost from the ischemic zone but an increase in Mn^{2+} uptake in viable tissue occurs early post-MI. This shows the ability of the techniques used to detect subtle changes of Mn^{2+} and hence Ca^{2+} during early ischemic injury. However, the T1 mapping protocols used in this study was not without limitations. The sequence was relatively slow, taking approximately 6 minutes to acquire a single slice for generating the T1 maps. A faster imaging sequence could allow us to acquire imaging at and earlier and multiple time points to track the dynamic changes in intracellular calcium. Improvement in the scanning time would also allow us to a multiple slices in a reasonably fast scan time covering the entire heart. This would allow us to quantitatively measure the percentage of the AAR and potentially the viable myocardium within the AAR.

Finally, in Chapter 4, the efficacy of manganese-enhanced MRI (MEMRI) was validated against the current gold standard, late gadolinium enhancement (LGE) for quantifying infarct size after acute myocardial infarction. The main finding is MEMRI could quantify infarct size early than LGE-MRI. An increase in manganese uptake in the alive-functional myocardium and reduced uptake in the AAR produces high contrast different during early phase of ischemic injury. This is possible in MEMRI as manganese is an analogue to calcium, allowing for functional assessment of myocardium post-ischemia. This method proposes new way for functional imaging of the myocardium at an early stage. Positive contrast measurement of viable tissue in MEMRI may provide a better approach for viability imaging compared to the negative contrast of viable tissue in LGE-MRI. MEMRI also offers a more accurate measure for quantifying infarct region as opposed to LGE-MRI where overestimations of infarct size are often observed in acute MI [125], [220], [263]. The first 1h post coronary ligation is the golden hour where not all myocytes in the AAR-MI has been converted to infarct region. Some

were still reversible; thus, treatment at this time point is important to increase outcome. If no treatments were given within the early time point post occlusion, all AAR-MI region will become irreversible injury and become necrotic. The current challenge now is to assess the myocardial viability and quantify the salvageable tissue. The present study shows that manganese can be used as an early biomarker of cell viability. It has a higher sensitivity as compared to gadolinium at early time points post-MI. However, the current limitation of this study was I only tested in a permanent occlusion model of myocardial infarction in which salvageable tissue is very small and potentially only present during the first few hours post-MI. Further studies could be done using a reperfused model of myocardial infarction, allowing for further investigation of the efficacy of manganese as an imaging marker of viable myocardium.

Future application of the work presented in this thesis would help in the assessment of viable myocardium that is salvageable at an acute stage intending to stratify patients into optimal treatment pathways. The ability to non-invasively quantify myocardial viability could have important diagnostic and prognostic applications across a range of cardiac diseases. Firstly, accurate identification of viable myocardium could be used to identify which patients would benefit from percutaneous intervention or coronary artery bypass grafting [256]. Recent clinical trials use SPECT and dobutamine-stress echocardiography for assessment of myocardial viability to identify patients that would benefit from coronary artery bypass grafting (CABG). However, these studies found no significant association between myocardial viability and patients selected for CABG. They have cast doubt on the value of SPECT-based myocardial viability imaging that relies on the membrane integrity and redistribution of the tracers making analysis more challenging [276], [287]. Another clinical trial using PET imaging for myocardial viability assessment highlighted the needs for expertise and timely access to imaging to have a significant outcome benefit of viability imaging in selecting patients for revascularization [275], [288]. In addition, SPECT- and PET-based imaging, are logistically challenging, which, may have limited imaging to patients who would benefit from viability imaging at the time of admission. This calls for more accurate and feasible methods [289].

Additionally, MEMRI could have a role to play in phenotyping hypertrophic and dilated cardiomyopathies. There is also great potential for evaluation of routine and experimental therapies including; optimisation of pharmacological doses to regulate cardiac inotropy [195]; interrogating viability of engineered heart tissues [278] and monitoring the success of regenerative therapies [98], [139], [277]. Previous studies

have shown that MEMRI is able to detect functional restoration following stem cell therapy in myocardial infarction model [98], [139].

To conclude, the re-emergence of safe, clinical grade Mn^{2+}-based contrast agents opens the possibility of direct evaluation of myocardial viability early after ischemic onset in patients with acute myocardial infarction and my research adds valuable information on how MEMRI can be utilised as a new diagnostic and prognostic imaging tool.

References

[1] N. Townsend, L. Wilson, P. Bhatnagar, K. Wickramasinghe, M. Rayner, and M. Nichols, “Cardiovascular disease in Europe: epidemiological update 2016,” *Eur. Heart J.*, vol. 37, no. 42, pp. 3232–3245, 2016.

[2] G. Ikonnikov, D. Yelle, E. Wong, and S. Chaudry, “Physiology of cardiac conduction and contractility,” *McMaster Pathophysiology Review*, 2018. .

[3] K. Thygesen, J. S. Alpert, A. S. Jaffe, M. L. Simoons, B. R. Chaitman, and H. D. White, “Third universal definition of myocardial infarction,” *Eur. Heart J.*, 2012.

[4] N. G. Frangogiannis, “Pathophysiology of myocardial infarction,” *Compr. Physiol.*, vol. 5, no. 4, pp. 1841–1875, 2015.

[5] M. F. M. Fathil *et al.*, “Diagnostics on acute myocardial infarction: cardiac troponin biomarkers,” *Biosens. Bioelectron.*, vol. 70, pp. 209–220, Aug. 2015.

[6] A. Mayr *et al.*, “Predictive value of NT-pro BNP after acute myocardial infarction: Relation with acute and chronic infarct size and myocardial function,” 2011.

[7] S. G. Goodman, G. Steg, K. A. Eagle, and K. A. A. Fox, “The diagnostic and prognostic impact of the redefinition of acute myocardial infarction : Lessons from the Global Registry of Acute Coronary Events (GRACE),” *Am. Heart J.*, vol. 151, pp. 654–660, 2006.

[8] K. Thygesen *et al.*, “Fourth universal definition of myocardial infarction (2018),” *Eur. Heart J.*, vol. 40, no. 3, pp. 237–269, 2019.

[9] R. B. Jennings and K. a Reimer, “Lethal myocardial ischemic injury,” *Am. J. Pathol.*, vol. 102, no. 2, pp. 241–255, 1981.

[10] W. Kübler and P. G. Spieckermann, “Regulation of glycolysis in the ischemic and the anoxic myocardium,” *J. Mol. Cell. Cardiol.*, vol. 1, no. 4, pp. 351–377, 1970.

[11] A. Katz, *Physiology of The Heart*. USA: Lippincott Williams & WIlkins, 2001.

[12] L. M. Buja, H. K. Hagler, and J. T. Willerson, “Altered calcium homeostasis in the pathogenesis of myocardial ischemic and hypoxic injury,” *Cell Calcium*, vol. 9, no. 5–6, pp. 205–217, 1988.

[13] N. Herring and D. J. Paterson, “ECG diagnosis of acute ischaemia and

infarction: past, present and future," *QJM - Mon. J. Assoc. Physicians*, vol. 99, no. 4, pp. 219–230, 2006.

[14] S. Sclarovsky, "Physiological and pathological remodeling in acute inferior wall myocardial infarction," *Isr. Med. Assoc. J.*, vol. 15, no. 4, pp. 143–146, 2013.

[15] R. B. Jennings, "Historical perspective on the pathology of myocardial ischemia/reperfusion injury," *Circ. Res.*, vol. 113, no. 4, pp. 428–438, 2013.

[16] A. C. Elliott, G. L. Smith, D. A. Eisner, and D. G. Allen, "Metabolic changes during ischaemia and their role in contractile failure in isolated ferret hearts.," *J. Physiol.*, vol. 454, no. 1, pp. 467–490, 1992.

[17] R. J. Solaro, J. A. Lee, J. C. Kentish, and D. G. Allen, "Effects of acidosis on ventricular muscle from adult and neonatal rats," *Circ. Res.*, vol. 63, no. 4, pp. 779–787, 1988.

[18] K. A. Reimer, R. B. Jennings, and A. H. Tatum, "Pathobiology of acute myocardial ischemia: metabolic, functional and ultrastructural studies," *Am. J. Cardiol.*, vol. 52, pp. 72A-81A, 1983.

[19] E. A. Amsterdam *et al.*, *2014 AHA/ACC guideline for the management of patients with non-ST-elevation acute coronary syndromes: a report of the American college of cardiology/American heart association task force on practice guidelines*, vol. 130, no. 25. 2014.

[20] T. L. Switaj, S. R. Christensen, and D. M. Brewer, "Acute coronary syndrome: Current treatment," *Am. Fam. Physician*, vol. 95, no. 4, pp. 232–240, 2017.

[21] B. Ibanez *et al.*, "2017 ESC Guidelines for the management of acute myocardial infarction in patients presenting with ST-segment elevation," *Eur. Heart J.*, no. January, pp. 119–177, 2017.

[22] F. Van De Werf, "The history of coronary reperfusion," *Eur. Heart J.*, vol. 35, no. 37, pp. 2510–2515, 2014.

[23] D. M. Yellon and D. J. Hausenloy, "Myocardial reperfusion injury," *N. Engl. J. Med.*, vol. 357, no. 11, pp. 1121–1135, Sep. 2007.

[24] D. J. Hausenloy, H. E. Botker, T. Engstrom, D. Erlinge, D. M. Yellon, and D. Garcia-Dorado, "Targeting reperfusion injury in patients with ST-segment elevation myocardial infarction: trials and tribulations," *Eur. Soc. Cardiol.*, vol. 38, pp. 935–941, 2017.

[25] S. A. Fisher, C. Dorée, S. J. Brunskill, A. Mathur, and E. Martin-Rendon, "Bone

marrow stem cell treatment for ischemic heart disease in patients with no option of revascularization: a systematic review and meta-analysis," *PLoS One*, vol. 8, no. 6, p. e64669, 2013.

[26] N. G. Frangogiannis, "Pathophysiology of myocardial infarction," *Compr. Physiol.*, vol. 5, no. 4, pp. 1841–1875, 2015.

[27] L. Carpenter, C. Carr, C. T. Yang, D. J. Stuckey, K. Clarke, and S. M. Watt, "Efficient differentiation of human induced pluripotent stem cells generates cardiac cells that provide protection following myocardial infarction in the rat.," *Stem Cells Dev.*, vol. 21, no. 6, pp. 977–986, 2012.

[28] C. A. Carr *et al.*, "Cardiosphere-derived cells improve function in the infarcted rat heart for at least 16 weeks-an MRI study.," *PLoS One*, vol. 6, no. 10, p. e25669, 2011.

[29] C. Zaragoza *et al.*, "Animal models of cardiovascular diseases," *J. Biomed. Biotechnol.*, vol. 2011, 2011.

[30] P. Chirac and R. Vieussens, "De motu cordis adversaria analytica," *Apud Joannem Martel*, 1678.

[31] M. M. Arthur, "Acute coronary artery disease," *Am. J. Med.*, vol. 2, no. 5, pp. 501–516, 1947.

[32] J. E. Erichsen, "On the influence of the coronary circulation on the action of the heart," *London Med. Gaz.*, vol. 2, pp. 561–564, 1842.

[33] R. Kolster, "Experiimentelle beitrage zur kenntniss der myomalacia cordis," *Arch. f. Physiol.*, vol. 4, pp. 1–45, 1893.

[34] W. Baumgarten, "Infraction of the heart," *Am. J. Physiol.*, vol. II, pp. 243–265, 1899.

[35] T. N. P. Johns and B. J. Olson, "Experimental myocardial infarction. I. A method of coronary occlusion in small animals," *Ann. Surg.*, vol. 140, no. 5, pp. 675–682, 1954.

[36] M. C. Fishbein, D. Maclean, and P. R. Maroko, "Experimental myocardial infarction in the rat: qualitative and quantitative changes during pathologic evolution," *Am. J. Pathol.*, vol. 90, no. 1, pp. 57–70, 1978.

[37] R. A. Kloner, M. C. Fishbein, C. M. Hare, and P. R. Maroko, "Early ischemic ultrastructural and histochemical alterations in the myocardium of the rat following coronary artery occlusion," *Exp. Mol. Pathol.*, vol. 30, no. 2, pp. 129–

143, 1979.

[38] J. S. Hochman and B. H. Bulkley, “Pathogenesis of left ventricular aneurysms: An experimental study in the rat model,” *Am. J. Cardiol.*, vol. 50, no. 1, pp. 83–88, 1982.

[39] H. Selye, E. Bajusz, S. Grasso, and P. Mendell, “Simple technique for the surgical occlusion of coronary vessels in the rat,” *Angiology*, vol. 11, pp. 398–407, 1960.

[40] X.-P. Yang *et al.*, “Ventriculographic evaluation of cardiac dysfunction,” *Am. J. Physiol.*, vol. 265, pp. H1946–H1952, 1993.

[41] G. Srikanth, P. Prakash, N. Tripathy, M. Dikshit, and S. Nityanand, “Establishment of a rat model of myocardial infarction with a high survival rate: A suitable model for evaluation of efficacy of stem cell therapy.,” *J. Stem Cells Regen. Med.*, vol. 5, no. 1, pp. 30–6, 2009.

[42] J. Wang, H. Bo, X. Meng, Y. Wu, Y. Bao, and Y. Li, “A simple and fast experimental model of myocardial infarction in the mouse.,” *Texas Hear. Inst. J.*, vol. 33, no. 3, pp. 290–3, 2006.

[43] D. Ahn, L. Cheng, C. Moon, H. Spurgeon, E. G. Lakatta, and M. I. Talan, “Induction of myocardial infarcts of a predictable size and location by branch pattern probability-assisted coronary ligation in C57BL/6 mice,” *Am. J. Physiol. - Hear. Circ. Physiol.*, vol. 286, no. 3 55-3, pp. 1201–1207, 2004.

[44] E. Gao *et al.*, “A novel and efficient model of coronary artery ligation and myocardial infarction in the mouse,” *Circ. Res.*, vol. 107, no. 12, pp. 1445–1453, 2010.

[45] M. C. Kontos, D. B. Diercks, and J. D. Kirk, “Emergency department and office-based evaluation of patients with chest pain,” *Mayo Clin Proc*, vol. 85, no. 3, pp. 284–299, 2010.

[46] B. M. Scirica, “Acute coronary syndrome: emerging tools for diagnosis and risk assessment,” *JACC*, vol. 55, no. 14, pp. 1403–1415, 2010.

[47] S. Kaul *et al.*, “A suggested roadmap for cardiovascular ultrasound research for the future,” *Am. Soc. Echocardiogr.*, pp. 455–464, 2011.

[48] F. A. Flachskampf, M. Schmid, C. Rost, S. Achenbach, A. N. Demaria, and W. G. Daniel, “Cardiac imaging after myocardial infarction,” pp. 272–283, 2011.

[49] J. Zamorano, D. R. Wallbridge, J. Ge, J. Drozd, J. Nesser, and R. Erbel, “Non-

invasive assessment of cardiac physiology by tissue Doppler echocardiography A comparison with invasive haemodynamics," pp. 330–339, 1997.

[50] A. F. L. Schinkel, J. J. Bax, D. Poldermans, A. Elhendy, and R. Ferrari, "Hibernating myocardium: diagnosis and patient outcomes," *Curr. Probl. Cardiol.*, vol. 32, pp. 375–410, 2007.

[51] A. Bhat, G. C. H. Gan, T. C. Tan, C. Hsu, and A. R. Denniss, "Myocardial Viability: From Proof of Concept to Clinical Practice.," *Cardiol. Res. Pract.*, vol. 2016, p. 1020818, 2016.

[52] H. H. Guo, "FDG Cardiac PET: The yin and yang of myocardial imaging," 2014.

[53] A. Kidambi *et al.*, "Susceptibility-weighted cardiovascular magnetic resonance in comparison to T2 and T2 star imaging for detection of intramyocardial hemorrhage following acute myocardial infarction at 3 Tesla.," *J. Cardiovasc. Magn. Reson.*, vol. 16, p. 86, 2014.

[54] I. Eitel *et al.*, "Comprehensive prognosis assessment by CMR imaging after ST-segment elevation myocardial infarction," *J. Am. Coll. Cardiol.*, vol. 64, no. 12, pp. 1217–1226, 2014.

[55] D. Locca *et al.*, "New universal definition of myocardial infarction," *JACC Cardiovasc. Interv.*, vol. 3, no. 9, pp. 950–958, 2010.

[56] D. W. McRobbie, E. A. Mooer, M. J. Graves, and M. R. Prince, *MRI From Picture to Proton*. 2015.

[57] T. A. Roberts, "Development of MRI techniques for experimental models of cardiovascular disease," 2014.

[58] J. Larmor, "The relation of the earth's free precessional nutation to its resistance against tidal deformation," *Proc. R. Soc. London*, vol. 2, pp. 89–96, 1909.

[59] E. M. Purcell, H. C. Torrey, and R. V. Pound, "Resonance absorption by nuclear magnetic moemnt in a solid," *Phys. Rev. Lett.*, vol. 69, pp. 37–38, 1946.

[60] F. Bloch, W. W. Hansen, and M. Packard, "Nuclear induction," *Phys. Rev. Lett.*, vol. 69, p. 127, 1946.

[61] J. Lux and A. D. Sherry, "Advances in gadolinium-based MRI contrast agent designs for monitoring biological processes in vivo," *Curr. Opin. Chem. Biol.*, vol. 45, pp. 1–19, 2018.

[62] P. Caravan, C. T. Farrar, L. Frullano, and R. Uppal, “Influence of molecular parameters and increasing magnetic field strength on relaxivity of gadolinium- and manganese-based T1 contrast agents,” *Contrast Media Mol. Imaging*, vol. 4, no. 2, pp. 89–100, 2009.

[63] R. M. Lang *et al.*, “Recommendations for chamber quantification,” *Eur. J. Echocardiogr.*, vol. 7, no. 2, pp. 79–108, 2006.

[64] L. H. Jackson, “Cardiac imaging for regenerative therapy and tissue engineering,” 2016.

[65] D. C. Look and D. R. Locker, “Time saving in measurement of NMR and EPR relaxation times,” *Rev. Sci. Instrum.*, vol. 41, no. 2, pp. 250–251, 1970.

[66] R. Deichmann, A. Haase, and A. Hubland, “Quantification of T1 values by SNAPSHOT-FLASH NMR imaging,” *J. Magn. Reson. Imaging*, vol. 612, pp. 1–5, 2004.

[67] N. Deichmann and M. Garcia-Fernandez, “Rupture geometry from high-precision relative hypocentre locations of microearthquake clusters,” *Geophys. J. Int.*, vol. 110, no. 3, pp. 501–517, 1992.

[68] A. L. H. Jackson, E. Vlachodimitropoulou, P. Shangaris, A. Thomas, F. Lythgoe, and D. J. Stuckey, “Non-invasive MRI biomarkers for the early assessment of iron overload in a humanized mouse model of β -thalassemia Contact author details,” *Nat. Publ. Gr.*, no. February, 2017.

[69] A. N. Price, K. K. Cheung, S. Y. Lim, D. M. Yellon, D. J. Hausenloy, and M. F. Lythgoe, “Rapid assessment of myocardial infarct size in rodents using multi-slice inversion recovery late gadolinium enhancement CMR at 9.4T,” *J. Cardiovasc. Magn. Reson.*, vol. 13, no. 1, p. 44, 2011.

[70] S. Kaul, “Assessing the myocardium after attempted reperfusion: should we bother?,” *Circulation*, vol. 98, no. 7, pp. 625–627, 1998.

[71] A. Jamiel, M. Ebid, A. M. Ahmed, and D. Ahmed, “The role of myocardial viability in contemporary cardiac practice,” pp. 401–413, 2017.

[72] F. J. Neumann *et al.*, “2018 ESC/EACTS Guidelines on myocardial revascularization,” *Eur. Heart J.*, vol. 40, no. 2, pp. 87–165, 2019.

[73] H. Bulluck, R. Dharmakumar, A. E. Arai, C. Berry, and D. J. Hausenloy, “Cardiovascular magnetic resonance in acute ST-segment-elevation myocardial infarction: recent advances, controversies, and future directions,”

Circulation, vol. 137, no. 18, pp. 1949–1964, 2018.

[74] D. J. Stuckey *et al.*, “T1 mapping detects pharmacological retardation of diffuse cardiac fibrosis in mouse pressure-overload hypertrophy,” *Circ. Cardiovasc. Imaging*, vol. 7, pp. 240–249, 2014.

[75] O. J. Rider *et al.*, “Noninvasive in vivo assessment of cardiac metabolism in the healthy and diabetic human heart using hyperpolarized 13C MRI,” *Circ. Res.*, pp. 725–736, 2020.

[76] N. Spath, A. Baker, D. Newby, and S. Semple, “Manganese-enhanced T1 mapping for the assessment of myocardial viability : clinical translation of a novel contrast agent in cardiac MRI,” in *European Heart Journal - Cardiovascular Imaging*, 2019, no. 2.

[77] M. F. Wendland, “Applications of manganese-enhanced magnetic resonance imaging (MEMRI) to imaging of the heart,” *NMR Biomed.*, vol. 17, no. 8, pp. 581–594, 2004.

[78] K. M. Choi, R. J. Kim, G. Gubernikoff, J. D. Vargas, M. Parker, and R. M. Judd, “Transmural extent of acute myocardial infarction predicts long-term improvement in contractile function,” *Circulation*, vol. 104, no. 10, pp. 1101–1107, 2001.

[79] B. L. Gerber *et al.*, “Prognostic value of myocardial viability by delayed-enhanced magnetic resonance in patients with coronary artery disease and low ejection fraction: Impact of revascularization therapy,” *J. Am. Coll. Cardiol.*, vol. 59, no. 9, pp. 825–835, 2012.

[80] M. Saeed, G. Lund, M. F. Wendland, J. Bremerich, H. J. Weinmann, and C. B. Higgins, “Magnetic resonance characterization of the peri-infarction zone of reperfused myocardial infarction with necrosis-specific and extracellular nonspecific contrast media,” *Circulation*, vol. 103, no. 6, pp. 871–876, 2001.

[81] M. P. Marra, J. A. C. Lima, and S. Iliceto, “MRI in acute myocardial infarction,” *Eur. Heart J.*, vol. 32, pp. 284–293, 2011.

[82] T. Kanda *et al.*, “Gadolinium-based contrast agent accumulates in the brain even in subjects without severe renal dysfunction: evaluation of autopsy brain specimens with inductively coupled plasma mass spectroscopy,” *Radiology*, vol. 276, no. 1, pp. 228–232, 2015.

[83] M. G. Friedrich, H. W. Kim, and R. J. Kim, “T2-weighted imaging to assess

post-infarct myocardium at risk," *JACC Cardiovasc. Imaging*, vol. 4, no. 9, pp. 1014–1021, 2011.

[84] J. Schwitter and A. E. Arai, "Assessment of cardiac ischaemia and viability: role of cardiovascular magnetic resonance," *Eur. Heart J.*, vol. 32, 2011.

[85] C. K. Katikireddy *et al.*, "Evaluation of myocardial ischemia and viability by noninvasive cardiac imaging," *Expert Rev. Cardiovasc. Ther.*, vol. 10, no. 1, pp. 55–73, 2012.

[86] G. La Canna, O. Alfieri, R. Giubbini, M. Gargano, R. Ferrari, and O. Visioli, "Echocardiography during infusion of dobutamine for identification of reversible dyfunction in patients with chronic coronary artery disease," *J. Am. Coll. Cardiol.*, vol. 23, no. 3, pp. 617–626, 1994.

[87] F. Kober, T. Jao, T. Troalen, and K. S. Nayak, "Myocardial arterial spin labeling.," *J. Cardiovasc. Magn. Reson.*, vol. 18, no. 1, p. 22, 2016.

[88] R. K. Dongworth *et al.*, "Quantifying the area-at-risk of myocardial infarction in-vivo using arterial spin labeling cardiac magnetic resonance," *Sci. Rep.*, vol. 7, no. 2271, pp. 1–12, 2017.

[89] R. Manka, I. Paetsch, B. Schnackenburg, R. Gebker, E. Fleck, and C. Jahnke, "BOLD cardiovascular magnetic resonance at 3.0 tesla in myocardial ischemia.," *J. Cardiovasc. Magn. Reson.*, vol. 12, p. 54, 2010.

[90] S. A. Tsaftaris, X. Zhou, R. Tang, and R. Dhamakumar, "Detecting Myocardial Ischemia at Rest with Cardiac Phase-Resolved BOLD CMR," *Circ. Cardiovasc. Imaging*, vol. 6, no. 2, pp. 311–319, 2013.

[91] R. A. Kloner and R. B. Jennings, "Consequences of brief ischemia: stunning, preconditioning, and their clinical implications," *Circulation*, vol. 104, pp. 3158–3167, 2001.

[92] A. P. Koretsky and A. C. Silva, "Manganese-enhanced magnetic resonance imaging (MEMRI)," *NMR Biomed.*, vol. 17, pp. 527–531, 2004.

[93] G. A. Krombach, M. Saeed, C. B. Higgins, V. Novikov, and M. F. Wendland, "Contrast-enhanced MR Delineation of Stunned Myocardium with Administration of MnCl2 in Rats1," *Radiology*, vol. 230, no. 1, pp. 183–190, 2004.

[94] Haruko Masumiya, H. Tsujika, N. Hino, and R. Ochi, "Modulation of manganese currents by 1 , 4-dihydropyridines , isoproterenol and forskolin in

rabbit ventricular cells," pp. 695–701, 2003.

[95] W. Nordhøy, H. W. Anthonsen, M. Bruvold, P. Jynge, J. Krane, and H. Brurok, "Manganese ions as intracellular contrast agents: proton relaxation and calcium interactions in rat myocardium," *NMR Biomed.*, vol. 16, no. 2, pp. 82–95, Apr. 2003.

[96] D. R. Hunter, R. A. Haworth, and H. A. Berkoff, "Cellular manganese uptake by the isolated perfused rat heart: a probe for the sarcolemma calcium channel," *J. Mol. Cell. Cardiol.*, 1981.

[97] N. B. Spath *et al.*, "Manganese-enhanced T1 mapping in the myocardium of normal and infarcted hearts," *Contrast Media Mol. Imaging*, pp. 1–13, 2018.

[98] R. Dash *et al.*, "Manganese-enhanced magnetic resonance imaging enables in vivo confirmation of peri-tnfarct restoration following stem cell therapy in a porcine ischemia-reperfusion model.," *J. Am. Heart Assoc.*, vol. 4, no. 7, pp. 1–16, 2015.

[99] B. Waghorn, T. Edwards, Y. Yang, K.-H. Chuang, N. Yanasak, and T. C.-C. Hu, "Monitoring dynamic alterations in calcium homeostasis by T1-weighted and T1-mapping cardiac manganese-enhanced MRI in a murine myocardial infarction model," *NMR Biomed.*, pp. 1102–1111, 2008.

[100] W. J. Chung *et al.*, "Apelin-13 infusion salvages the peri-infarct region to preserve cardiac function after severe myocardial injury," *Int. J. Cardiol.*, vol. 222, no. August, pp. 361–367, 2016.

[101] J. Bremerich, M. Saeed, H. Arheden, C. B. Higgins, and M. F. Wendland, "Normal and infarcted myocardium: differentiation with cellular uptake of manganese at MR imaging in a rat model," *Radiology*, vol. 216, pp. 524–530, 2000.

[102] A. Skjold *et al.*, "Manganese dipyridoxyl-diphosphate (MnDPDP) as a viability marker in patients with myocardial infarction," *J. Magn. Reson. Imaging*, vol. 26, no. 3, pp. 720–727, 2007.

[103] A. Skjold, T. R. Vangberg, A. Kristoffersen, O. Haraldseth, P. Jynge, and H. B. W. Larsson, "Relaxation enhancing properties of MnDPDP in human myocardium," *J. Magn. Reson. Imaging*, vol. 20, no. 6, pp. 948–952, 2004.

[104] J. L. Fernandes, P. Storey, A. A. da Silva, G. S. de Figueiredo, J. M. Kalaf, and O. R. Coelho, "Preliminary assessment of cardiac short term safety and

efficacy of manganese chloride for cardiovascular magnetic resonance in humans," *J. Cardiovasc. Magn. Reson.*, vol. 13, no. 6, pp. 1–9, 2011.

[105] A. Sigel, E. Freisinger, and R. K. O. Sigel, *Essential metals in medicine: therapeutic use and toxicity of metal ions in the clinic*, Volume 19. Berlin/Boston: Walter de Gruyter GmbH, 2019.

[106] P. R. Gentry *et al.*, "A tissue dose-based comparative exposure assessment of manganese using physiologically based pharmacokinetic modeling — The importance of homeostatic control for an essential metal," vol. 322, pp. 27–40, 2017.

[107] A. C. Silva, "Using manganese-enhanced MRI to understand BOLD," *Neuroimage*, vol. 62, no. 2, pp. 1009–1013, 2012.

[108] P. Lauterbur, M. Dias, and A. Rudin, "Augmentation of tissue water proton spin-lattice relaxation rates by in vivo addition of paramagnetic ions," *Electron to tissue*, 1978.

[109] Y. Huijuan, H. Ramamoorthy, P. Abraham, and B. Isaac, "Decreasing expression of α1C calcium L-type channel subunit mRNA in rat ventricular myocytes upon manganese exposure," *J. Biochem. Mol. Toxicol.*, vol. 20, no. 4, pp. 159–166, 2006.

[110] H. Masumiya, H. Tsujikawa, N. Hino, and R. Ochi, "Modulation of manganese currents by 1, 4-dihydropyridines, isoproterenol and forskolin in rabbit ventricular cells," *Pflugers Arch. Eur. J. Physiol.*, vol. 446, no. 6, pp. 695–701, 2003.

[111] G. L. Wolf and L. Baum, "Cardiovascular toxicity and tissue proton T1 response to manganese injection in the dog and rabbit," *Am. J. Roentgenol.*, vol. 141, no. 1, pp. 193–197, 1983.

[112] P. Jynge, H. Brurok, A. Asplund, R. Towart, H. Refsum, and J. O. Karlsson, "Cardiovascular safety of MnDPDP and MnCl2," *Acta Radiol*, vol. 38, no. 4 Pt 2, pp. 740–749, 1997.

[113] L. S. Maynard and G. C. Cotzias, "The partition of manganese among organs and intracellular organelles of the rat.," *J. Biol. Chem.*, 1955.

[114] R. Eriksson, L. Johansson, T. Bjerner, and H. Ahlström, "Dobutamine-induced stress affects intracellular uptake of manganese: A quantitative magnetic resonance imaging study in pigs," *J. Magn. Reson. Imaging*, vol. 21, no. 4, pp.

360–364, 2005.

[115] T. C. C. Hu, R. G. Pautler, G. A. MacGowan, and A. P. Koretsky, “Manganese-enhanced MRI of mouse heart during changes in inotropy,” *Magn. Reson. Med.*, vol. 46, 2001.

[116] K. Jiang *et al.*, “Rapid multislice T1 mapping of mouse myocardium: Application to quantification of manganese uptake in a-Dystrobrevin knockout mice,” *Magn. Reson. Med.*, vol. 74, no. 5, pp. 1370–1379, 2015.

[117] Y. Matsuura *et al.*, “Dual contrast enhanced cardiac MRI using manganese and gadolinium in patients with severe ischemic cardiomyopathy detects the peri-infarct region (PIR),” *J. Cardiovasc. Magn. Reson.*, vol. 16, no. Suppl 1, p. O96, 2014.

[118] H. Brurok, J. Schjøtt, K. Berg, J. O. Karlsson, and P. Jynge, “Manganese and the heart: acute cardiodepression and myocardial accumulation of manganese.,” *Acta Physiol. Scand.*, vol. 159, no. 1, pp. 33–40, 1997.

[119] D. Pan, A. H. Schmieder, S. A. Wickline, and G. M. Lanza, “Manganese-based MRI contrast agents: past, present and future.,” *Tetrahedron*, vol. 67, no. 44, pp. 8431–8444, Nov. 2011.

[120] T. C. C. Hu *et al.*, “Simultaneous assessment of left-ventricular infarction size, function and tissue viability in a murine model of myocardial infarction by cardiac manganese-enhanced magnetic resonance imaging (MEMRI),” *NMR Biomed.*, vol. 17, no. 8, pp. 620–626, 2004.

[121] M. Saeed, C. B. Higgins, J. F. Geschwind, and M. F. Wendland, “T1-relaxation kinetics of extracellular, intracellular and intravascular MR contrast agents in normal and acutely reperfused infarcted myocardium using echo-planar MR imaging.,” *Eur. Radiol.*, vol. 10, no. 2, pp. 310–318, 2000.

[122] A. Natanzon, A. H. Aletras, L.-Y. Hsu, and A. E. Arai, “Determining canine myocardial area at risk with manganese-enhanced MR imaging.,” *Radiology*, vol. 236, no. 3, pp. 859–66, 2005.

[123] B. M. A. Delattre, V. Braunersreuther, J. N. Hyacinthe, L. A. Crowe, F. Mach, and J. P. Vallée, “Myocardial infarction quantification with manganese-enhanced MRI (MEMRI) in mice using a 3T clinical scanner,” *NMR Biomed.*, vol. 23, no. 5, pp. 503–513, 2010.

[124] Y. Yang, M. L. W. Gruwel, J. Sun, P. Gervai, X. Yang, and V. V. Kupriyanov,

"Manganese-enhanced MRI of acute cardiac ischemia and chronic infarction in pig hearts: Kinetic analysis of enhancement development," *NMR Biomed.*, vol. 22, no. 2, pp. 165–173, 2009.

[125] K. Skårdal, N. P. L. Rolim, O. Haraldseth, P. E. Goa, and M. Thuen, "Late gadolinium enhancement in the assessment of the infarcted mouse heart: A longitudinal comparison with manganese-enhanced MRI," *J. Magn. Reson. Imaging*, vol. 38, no. 6, pp. 1388–1394, 2013.

[126] B. M. A. Delattre *et al.*, "Manganese kinetics demonstrated double contrast in acute but not in chronic infarction in a mouse model of myocardial occlusion reperfusion," *NMR Biomed.*, vol. 25, no. 4, pp. 489–497, 2012.

[127] R. J. Gumina *et al.*, "KATP channel knockout worsens myocardial calcium stress load in vivo and impairs recovery in stunned heart.," *Am. J. Physiol. Heart Circ. Physiol.*, vol. 292, no. 4, pp. H1706-13, 2007.

[128] K. Jiang *et al.*, "Rapid multislice T1 mapping of mouse myocardium: application to quantification of manganese uptake in a-dystrobrevin knockout mice," *Magn. Reson. Med.*, vol. 74, pp. 1370–1379, 2015.

[129] E. Greally *et al.*, "Heterogeneous abnormalities of in-vivo left ventricular calcium influx and function in mouse models of muscular dystrophy cardiomyopathy," *J. Cardiovasc. Magn. Reson.*, vol. 15, no. 1, p. 1, 2013.

[130] R. Wyttenbach *et al.*, "Detection of acute myocardial ischemia using first-pass dynamics of MnDPDP on inversion recovery echoplanar imaging," *J. Magn. Reson. Imaging*, vol. 9, no. 2, pp. 209–214, 1999.

[131] S. Schaefer, R. A. Lange, and D. P. Gutekunst, "Contrast-enhanced magnetic resonance imaging of hypoperfused myocardium," *Invest. Radiol.*, vol. 26, pp. 551–556, 1991.

[132] S. Schaefer *et al.*, "In vivo nuclear magnetic resonance imaging of myocardial perfusion using the paramagnetic contrast agent manganese gluconate," *From Nucl. Magn. Reson. Imaging Cent.*, vol. 14, no. 2, pp. 472–480, 1989.

[133] J. L. Daire *et al.*, "In vivo myocardial infarct area at risk assessment in the rat using manganese enhanced magnetic resonance imaging (MEMRI) at 1.5T," *Magn. Reson. Med.*, vol. 59, no. 6, pp. 1422–1430, 2008.

[134] W. Hanns-Joachim and B. Robert C, "Characteristics of gadolinium-DTPA complex: a potential NMR contrast agent," *Am. J. Roentgenol.*, vol. 142, pp.

619–624, 1984.

[135] H. W. Eichstaedt, R. Felix, F. C. Dougherty, M. Langer, W. Rutsch, and H. Schmutzler, “Magnetic resonance imaging (MRI) in different stages of myocardial infarction using the contrast agent gadolinium-DTPA,” *Clin. Cardiol.*, vol. 9, no. 11, pp. 527–535, 1986.

[136] T. Geelen, L. E. M. Paulis, B. F. Coolen, K. Nicolay, and G. J. Strijkers, “Contrast-enhanced MRI of murine myocardial infarction - Part I,” *NMR Biomed.*, vol. 25, no. 8, pp. 953–968, 2012.

[137] S. Bohl *et al.*, “Advanced methods for quantification of infarct size in mice using three-dimensional high-field late gadolinium enhancement MRI.,” *Am. J. Physiol. Heart Circ. Physiol.*, vol. 296, no. 4, pp. H1200-8, Apr. 2009.

[138] A. Faulkner and P. Madeddu, “Stem Cell Therapy: A New Approach for Treatment of Myocardial Infarction,” *J. Stem Cell Res. Ther.*, pp. 1–12, 2012.

[139] P. J. Kim *et al.*, “Direct evaluation of myocardial viability and stem cell engraftment demonstrates salvage of the injured myocardium,” *Circ. Res.*, vol. 116, no. 7, pp. e40–e50, 2015.

[140] D. R. L. Scriven, P. Dan, and E. D. W. Moore, “Distribution of proteins implicated in excitation-contraction coupling in rat ventricular myocytes,” *Biophys. J.*, vol. 79, no. 5, pp. 2682–2691, 2000.

[141] B. T. Priest and J. S. McDermott, “Cardiac ion channels,” *Channels*, vol. 9, no. 6, pp. 352–359, 2015.

[142] M. J. Berridge, M. D. Bootman, and H. L. Roderick, “Calcium signalling: Dynamics, homeostasis and remodelling,” *Nat. Rev. Mol. Cell Biol.*, vol. 4, no. 7, pp. 517–529, 2003.

[143] D. M. Bers, “Calcium fluxes involved in control of cardiac myocyte contraction,” *Circ. Res.*, vol. 87, no. 4, pp. 275–281, 2000.

[144] D. Bers, “Ca channels in cardiac myocytes: structure and function in Ca influx and intracellular Ca release,” *Cardiovasc. Res.*, vol. 42, no. 2, pp. 339–360, 1999.

[145] R. Ochi, “The slow inward current and the action of manganese ions in guinea-pig’s myocardium,” *Pflügers Arch. Eur. J. Physiol.*, vol. 316, no. 1, pp. 81–94, 1970.

[146] A. Skjold, A. Kristoffersen, T. R. Vangberg, O. Haraldseth, P. Jynge, and H. B.

W. Larsson, “An apparent unidirectional influx constant for manganese as a measure of myocardial calcium channel activity,” *J. Magn. Reson. Imaging*, vol. 24, no. 5, pp. 1047–1055, 2006.

[147] C. E. Gavin, K. K. Gunter, and T. E. Gunter, “Manganese and calcium transport in mitochondria: implications for manganese toxicity,” *Neurotoxicology*, vol. 20, no. 2–3, p. 445—453, 1999.

[148] M. Federle *et al.*, “Efficacy and safety of mangafodipir trisodium (MnDPDP) injection for hepatic MRI in adults: Results of the U.S. multicenter phase III clinical trials. Efficacy of early imaging,” *J. Magn. Reson. Imaging*, vol. 12, no. 5, pp. 689–701, 2000.

[149] P. R. Seoane, P. V Prasad, R. R. Edehnan, and P. P. Harnish, “EVP 1001-l: a new cardiac specific MR contrast agent with optimal kinetics for evaluation of the ischemic heart,” in *Proceedings of International Society of Magnetic Resonace in Medicine*, 2000, p. 63518.

[150] P. Storey, P. G. Danias, P. R. Seoane, and P. V Prasad, “Preliminary evaluation of EVP 1001-1: a new cardiac-specific magnetic resonance contrast agent with kinetic suitable for steady-state imaging of the ischemic heart,” *Invest. Radiol.*, vol. 38, no. 10, pp. 642–652, 2003.

[151] W. Lefrançois *et al.*, “A fast black-blood sequence for four-dimensional cardiac manganese-enhanced MRI in mouse,” *NMR Biomed.*, vol. 24, no. 3, pp. 291–298, Apr. 2011.

[152] M. Bruvold, W. Nordhøy, H. W. Anthonsen, H. Brurok, and P. Jynge, “Manganese-calcium interactions with contrast media for cardiac magnetic resonance imaging: a study of manganese chloride supplemented with calcium gluconate in isolated Guinea pig hearts.,” *Invest. Radiol.*, vol. 40, no. 3, pp. 117–25, 2005.

[153] H. Brurok, J. Schjott, K. Berg, J. Karlsson, and P. Jynge, “Effects of MnDPDP, DPDP--, and MnCl2 on cardiac energy metabolism and manganese accumulation: an experimental study in the isolated perfused rat heart,” *Invest. Radiol.*, vol. 32, no. 4, pp. 205–211, 1997.

[154] H. Brurok, K. Berg, L. Sneen, D. Grant, J. Karlsson, and P. Jynge, “Cardiac metal contents after infusions of manganese: an experimental evaluation in the isolated rat heart,” *Invest. Radiol.*, vol. 34, no. 7, 1999.

[155] P. Kellman and M. S. Hansen, “T1-mapping in the heart: accuracy and

precision.," *J. Cardiovasc. Magn. Reson.*, vol. 16, no. 1, p. 2, Jan. 2014.

[156] C. S. Broberg *et al.*, "Validation of the myocardial performance index by echocardiography in mice: a noninvasive measure of left ventricular function," *J. Am. Soc. Echocardiogr.*, vol. 16, no. 8, pp. 814–823, 2003.

[157] A. N. Price, K. K. Cheung, J. O. Cleary, A. E. Campbell, J. Riegler, and M. F. Lythgoe, "Cardiovascular magnetic resonance imaging in experimental models.," *Open Cardiovasc. Med. J.*, vol. 4, no. Lv, pp. 278–92, 2010.

[158] L. Jackson, V. Georgiadis, J. Habib, T. A. Roberts, D. J. Stuckey, and M. F. Lythgoe, "Regional assessment of myocardial regeneration therapies in rats using magnetic resonance tagging," *J. Cardiovasc. Magn. Reson.*, vol. 17, no. Suppl 1, p. M4, 2015.

[159] R. Ramasawmy *et al.*, "Hepatic arterial spin labelling MRI: An initial evaluation in mice," *NMR Biomed.*, vol. 28, no. 2, pp. 272–280, 2015.

[160] R. B. Lauffer, "Paramagnetic metal complexes as water proton relaxation agents for NMR imaging: theory and design," *Chem. Rev.*, vol. 87, no. 5, pp. 901–927, 1987.

[161] É. Tóth, L. Helm, and A. E. Merbach, "Relaxivity of MRI contrast agents," in *Contrast Agents I: Magnetic Resonance Imaging*, W. Krause, Ed. Berlin, Heidelberg: Springer Berlin Heidelberg, 2002, pp. 61–101.

[162] V. Jacques, S. Dumas, W.-C. Sun, J. S. Troughton, M. T. Greenfield, and P. Caravan, "High relaxivity MRI contrast agents part 2: optimisation of inner and second-sphere relaxivity," *Invest. Radiol.*, vol. 45, no. 10, pp. 613–624, 2011.

[163] W. Nordhøy *et al.*, "Intracellular manganese ions provide strong T1 relaxation in rat myocardium," *Magn. Reson. Med.*, vol. 52, no. 3, pp. 506–514, 2004.

[164] K. Thangavel and E. U. Saritas, "Aqueous paramagnetic solutions for MRI phantoms at 3 T : A detailed study on relaxivities Aqueous paramagnetic solutions for MRI phantoms at 3 T : A detailed study on relaxivities," *Turkish J. Electr. Eng. Comput. Sci.*, vol. 25, pp. 2018–2021, 2017.

[165] W. Nordhøy, H. W. Anthosen, M. Bruvold, P. Jynge, J. Krane, and H. Brurok, "Manganese ions as intracellular contrast agents: proton relaxation and calcium interactions in rat myocardium," *NMR Biomed.*, vol. 16, no. 2, pp. 82–95, 2003.

[166] W. Li, M. Griswold, and X. Yu, "Rapid T1 mapping of mouse myocardium with

saturation recovery Look-Locker method.," *Magn. Reson. Med.*, vol. 64, no. 5, pp. 1296–303, Nov. 2010.

[167] M. Bruvold, W. Nordh, H. W. Anthonsen, H. Brurok, and P. Jynge, "Manganese-Calcium Interactions With Contrast Media for Cardiac Magnetic Resonance Imaging," *Invest. Radiol.*, vol. 40, no. 3, pp. 117–125, 2005.

[168] D. M. Bers, "Excitation-contraction coupling," in *Excitation-Contraction Coupling and Cardiac Contractile Force*, 2001, pp. 203–204.

[169] H. Brurok, T. Skoglund, K. Berg, S. Skarra, J. O. G. Karlsson, and P. Jynge, "Myocardial manganese elevation and proton relaxivity enhancement with manganese dipyridoxyl diphosphate . Ex vivo assessments in normally perfused and ischemic guinea pig hearts," pp. 364–372, 1999.

[170] P. Yang, "Patent Application Publication US20160199517A1." 2016.

[171] P. P. Harnish and P. R. Seoane, "United States Patent [19] [54]," 1999.

[172] G. Lukas, S. D. Brindle, and P. Greengard, "The route of absorption of intraperitoneally administered compounds," *J. Pharmacol. Exp. Ther.*, vol. 178, no. 3, pp. 562–566, 1971.

[173] P. V. Turner, T. Brabb, C. Pekow, and M. A. Vasbinder, "Administration of substances to laboratory animals: Routes of administration and factors to consider," *J. Am. Assoc. Lab. Anim. Sci.*, vol. 50, no. 5, pp. 600–613, 2011.

[174] S. M. Rocklage, W. P. Cacheris, S. C. Quay, F. E. Hahn, and K. N. Raymond, "Manganese(II) N,N'-dipyridoxylethylenediamine-N,N'-diacetate 5,5'-bis(phosphate): synthesis and characterization of a paramagnetic chelate for magnetic resonance imaging enhancement," *Inorg. Chem.*, vol. 28, no. 3, pp. 477–485, 1989.

[175] M. Saeed, S. Wagner, M. F. Wendland, N. Derugin, W. E. Finkbeiner, and C. B. Higgins, "Occlusion and reperfused," *Radiology*, vol. 172, pp. 59–64, 1989.

[176] Pomeroy, "MRI Acute MI MnDPDP." 1989.

[177] S. L. O'Neal and W. Zheng, "Manganese toxicity upon overexposure: a decade in review.," *Curr. Environ. Heal. reports*, vol. 2, no. 3, pp. 315–28, 2015.

[178] B. Charash, E. Placek, T. A. Sos, and P. Kligfield, "Dose-related effects of manganese on the canine electrocardiogram," *J. Electrocardiol.*, vol. 15, no. 2, pp. 149–152, 1982.

[179] G. Elizondo *et al.*, "Evaluation of MnDPDP : New Paramagnetic," *Radiology*,

vol. 178, pp. 73–78, 1991.

[180] L. H. Jackson, M. F. Lythgoe, and D. J. Stuckey, “MRI tools for assessment of cardiovascular tissue engineering,” in *Magnetic Resonance Imaging in Tissue Engineering*, Hoboken, NJ, USA: John Wiley & Sons, Inc., 2017, pp. 333–365.

[181] H. L. Atkins *et al.*, “Myocardial positron tomography with manganese-52m,” *Radiology*, vol. 133, no. 3, pp. 769–774, 1979.

[182] Y. Ni *et al.*, “Comparison of manganese biodistribution and MR contrast enhancement in rats after intravenous injection of MnDPDP and MnCl,” *Acta Radiol.*, vol. 1851, 1997.

[183] J. P. Mahoney and W. J. Small, “The bilogocal half-life of radiomanganese in man and factors which affect this half-life,” *J. Clin. Invest.*, vol. 47, pp. 643–653, 1968.

[184] C. Labadie, J.-H. Lee, G. Vetek, and C. S. Springer, “Relaxographic imaging,” *J. Magn. Reson. Ser. B*, vol. 105, pp. 99–112, 1994.

[185] C. S. Landis *et al.*, “Equilibrium transcytolemmal water-exchange kinetics in skeletal muscle in vivo,” *Magn. Reson. Med.*, vol. 42, no. 3, pp. 467–478, 1999.

[186] D. M. Chauncey *et al.*, “Tissue distribution studies with radioactive manganese: a potential agent for myocardial imaging,” *J. Nucl. Med.*, vol. 18, no. 9, pp. 933–936, 1977.

[187] C. E. Anderson *et al.*, “Dual contrast - magnetic resonance fingerprinting (DC-MRF): a platform for simultaneous quantification of multiple MRI contrast agents,” *Sci. Rep.*, vol. 7, no. 1, pp. 1–10, 2017.

[188] Y. Kihara, W. Grossman, and J. P. Morgan, “Direct measurement of changes in intracellular calcium transients during hypoxia, ischemia, and reperfusion of the intact mammalian heart,” *Circ. Res.*, vol. 65, no. 4, pp. 1029–1044, 1989.

[189] H. C. Lee, R. Mohabir, N. Smith, M. R. Franz, and W. T. Clusin, “Effect of ischemia on calcium-dependent fluorescence transients in rabbit heart containing Indo 1: Correlation with monophasic action potentials and contraction,” *Circulation*, vol. 78, no. 4 I, pp. 1047–1059, 1988.

[190] H. C. Lee, N. Smith, R. Mohabir, and W. T. Clusin, “Cytosolic calcium transients from the beating mammalian heart,” *Proc. Natl. Acad. Sci. U. S. A.*, vol. 84, no. 21, pp. 7793–7797, 1987.

[191] C. Steenbergen, E. Murphy, L. Levy, and R. E. London, “Elevation in cytosolic

free calcium concentration early in myocardial ischemia in perfused rat heart," *Circ. Res.*, vol. 60, no. 5, pp. 700–707, 1987.

[192] D. A. Eisner, J. L. Caldwell, K. Kistamás, and A. W. Trafford, "Calcium and excitation-contraction coupling in the heart," *Circ. Res.*, vol. 121, no. 2, pp. 181–195, 2017.

[193] W. Catterall, "Regulation of Cardiac Calcium Channels in the Fight-or-Flight Response," *Curr. Mol. Pharmacol.*, vol. 8, no. 1, pp. 12–21, 2015.

[194] V. Rao *et al.*, "PKA phosphorylation of cardiac troponin i modulates activation and relaxation kinetics of ventricular myofibrils," *Biophys. J.*, vol. 107, no. 5, pp. 1196–1204, 2014.

[195] C. Maack *et al.*, "Treatments targeting inotropy," *Eur. Heart J.*, vol. 40, no. 44, pp. 3626-3640D, 2019.

[196] F. A. Lattanzio and B. C. Pressman, "Alterations in intracellular calcium activity and contractility of isolated perfused rabbit hearts by ionophores and adrenergic agents," *J. Chem. Inf. Model.*, vol. 139, no. 2, pp. 816–821, 1986.

[197] T. Ramanathan and H. Skinner, "Coronary blood flow," *Contin. Educ. Anaesthesia, Crit. Care Pain*, vol. 5, no. 2, pp. 61–64, 2005.

[198] F. T. Thandroyen, D. Bellotto, A. Katayama, H. K. Hagler, J. T. Willerson, and L. M. Buja, "Subcellular electrolyte alterations during progressive hypoxia and following reoxygenation in isolated neonatal rat ventricular myocytes," *Circ. Res.*, vol. 71, no. 1, pp. 106–119, 1992.

[199] E. Marban, M. Kitakaze, H. Kusuoka, J. K. Porterfield, D. T. Yue, and V. P. Chacko, "Intracellular free calcium concentration measured with 19F NMR spectroscopy in intact ferret hearts.," *Proc. Natl. Acad. Sci. U. S. A.*, vol. 84, no. 16, pp. 6005–6009, 1987.

[200] C. Stamm, I. Friehs, Y. H. Choi, D. Zurakowski, F. X. McGowan, and P. J. Del Nido, "Cytosolic calcium in the ischemic rabbit heart: assessment by pH- and temperature-adjusted rhod-2 spectrofluorometry," *Cardiovasc. Res.*, vol. 59, no. 3, pp. 695–704, 2003.

[201] K. Pittas, D. A. Vrachatis, C. Angelidis, S. Tsoucala, and S. Deftereos, "The role of calcium handling mechanisms in reperfusion injury," *Curr. Pharm. Des.*, vol. 24, pp. 4077–4089, 2018.

[202] L. M. Buja, "Myocardial ischemia and reperfusion injury," *Cardiovasc. Pathol.*,

vol. 14, no. 4, pp. 170–175, 2005.

[203] A. Schomig, “Adrenergic mechanisms in myocardial infarction: cardiac and systemic catecholamine release,” *J. Cardiovasc. Pharmacol.*, vol. 12, no. 1, pp. S1-7, 1988.

[204] O. Bertel, F. R. Buhler, G. Baitsch, R. Ritz, and F. Burkart, “Plasma adrenaline and noradrenaline in patients with acute myocardial infarction. Relationship to ventricular arrhythmias of varying severity,” *Chest*, vol. 82, no. 1, pp. 64–68, 1982.

[205] L. McDonald, “Plasma-catecholamines after cardiac infarction,” *Lancet*, no. November, pp. 1021–1023, 1969.

[206] R. A. Nadeau and J. de Champlain, “Plasma catecholamines in acute myocardial infarction,” *Clin. Commun.*, vol. 98, no. 5, pp. 548–554, 1979.

[207] A. Schomig, M. Haass, and G. Richardt, “Catecholamine release and arrhythmias in acute myocardial ischaemia,” *Eur. Heart J.*, vol. 12, no. SUPPL. F, pp. 38–47, 1991.

[208] T. M. Kolettis *et al.*, “Central sympathetic activation and arrhythmogenesis during acute myocardial infarction: modulating effects of endothelin-B receptors,” *Front. Cardiovasc. Med.*, vol. 2, no. February, pp. 1–8, 2015.

[209] A. Noble, R. Johnson, A. Thomas, and P. Bass, *The cardiovascular system*. Elseviier Churchill Livingstone, 2005.

[210] A. Fabiato, “Rapid ionic modifications during the aequorin-detected calcium transient in a skinned canine cardiac purkinje cell,” *J. Gen. Physiol.*, vol. 85, no. 2, pp. 189–246, 1985.

[211] R. Venkataraman, M. R. Holcomb, R. Harder, B. C. Knollmann, and F. Baudenbacher, “Ratiometric imaging of calcium during ischemia-reperfusion injury in isolated mouse hearts using Fura-2,” *Biomed. Eng. Online*, vol. 11, no. 39, pp. 1–16, 2012.

[212] P. J. D. E. L. Nido *et al.*, “Fluorescence measurement of calcium transients in perfused rabbit heart using rhod 2,” *Am. Physiol. Soc.*, pp. 728–741, 1998.

[213] R. Jaimes, R. D. Walton, P. Pasdois, O. Bernus, I. R. Efimov, and M. W. Kay, “A technical review of optical mapping of intracellular calcium within myocardial tissue,” *Am. J. Physiol. - Hear. Circ. Physiol.*, vol. 310, no. 11, pp. H1388–H1401, 2016.

[214] T. J. Herron, P. Lee, and J. Jalife, “Optical imaging of voltage and calcium in cardiac cells & tissues,” *Circ. Res.*, vol. 110, no. 4, pp. 609–623, 2012.

[215] Y. Chen *et al.*, “Inhibition of the sodium–calcium exchanger via SEA0400 altered manganese-induced T1 changes in isolated perfused rat hearts,” *NMR Biomed.*, vol. 25, no. 11, pp. 1280–1285, 2012.

[216] B. Waghorn *et al.*, “Indirectly probing Ca(2+) handling alterations following myocardial infarction in a murine model using T1-mapping manganese-enhanced magnetic resonance imaging.,” *Magn. Reson. Med.*, vol. 65, no. 1, pp. 239–49, 2011.

[217] M. Andrews, M. L. Giger, and B. B. Roman, “Manganese-enhanced MRI detection of impaired calcium regulation in a mouse model of cardiac hypertrophy,” *NMR Biomed.*, vol. 28, no. 2, pp. 255–263, 2015.

[218] B. Waghorn *et al.*, “Assessing manganese efflux using SEA0400 and cardiac T1-mapping manganese-enhanced MRI in a murine model,” *NMR Biomed.*, vol. 22, no. 8, pp. 874–881, 2009.

[219] J. A. Richardson, E. F. Woods, and E. E. Bagwell, “Circulating epinephrine and norepinephrine in coronary occlusion,” *Am. J. Cardiol.*, pp. 613–618, 1960.

[220] R. Dash *et al.*, “Dual manganese-enhanced and delayed gadolinium-enhanced mri detects myocardial border zone injury in a pig ischemia-reperfusion model,” *Circ. Cardiovasc. Imaging*, vol. 4, no. 5, pp. 574–582, 2011.

[221] I. B. A. Menown and A. A. J. Adgey, “Cardioprotective therapy and sodium-hydrogen exchange inhibition: Current concepts and furore goals,” *J. Am. Coll. Cardiol.*, vol. 38, no. 6, pp. 1651–1653, 2001.

[222] R. B. Jennings and C. E. Ganote, “Structural changes in myocardium during acute ischemia,” *Circ. Res.*, vol. 34, pp. 156–172, 1974.

[223] H. Bulluck *et al.*, “Quantifying the Area at Risk in Reperfused ST-Segment-Elevation Myocardial Infarction Patients Using Hybrid Cardiac Positron Emission Tomography-Magnetic Resonance Imaging,” *Circ. Cardiovasc. Imaging*, vol. 9, no. 3, pp. 1–11, 2016.

[224] J. Carberry *et al.*, “Remote Zone Extracellular Volume and Left Ventricular Remodeling in Survivors of ST-Elevation Myocardial Infarction,” *Hypertension*, vol. 68, no. 2, pp. 385–391, 2016.

[225] K. a Reimer, J. E. Lowe, M. M. Rasmussen, and R. B. Jennings, “The

wavefront phenomenon of ischemic cell death. 1. Myocardial infarct size vs duration of coronary occlusion in dogs.," *Circulation*, vol. 56, pp. 786–794, 1977.

[226] A. Doltra, B. H. Amundsen, R. Gebker, E. Fleck, and S. Kelle, "Emerging concepts for myocardial late gadolinium enhancement MRI.," *Curr. Cardiol. Rev.*, vol. 9, no. 3, pp. 185–90, Aug. 2013.

[227] E. Takashi and M. Ashraf, "Pathologic assessment of myocardial cell necrosis and apoptosis after ischemia and reperfusion with molecular and morphological markers," *J. Mol. Cell. Cardiol.*, vol. 32, no. 2, pp. 209–224, 2000.

[228] S. Elmore, "Apoptosis: A Review of Programmed Cell Death," *Toxicol. Pathol.*, vol. 35, no. 4, pp. 495–516, 2007.

[229] G. R. Heyndrickx, R. W. Millard, R. J. Mcritchie, P. R. Maroko, and S. F. Vatner, "Regional myocardial functional and electrophysiological alterations after brief coronary artery occlusion in conscious dogs," *J. Clin. Invest.*, vol. 56, no. October, pp. 978–985, 1975.

[230] P. R. Maroko *et al.*, "Factors influencing infarct size following experimental coronary artery occlusions.," *Circulation*, vol. 43, no. 1, pp. 67–82, 1971.

[231] R. B. Jennings, H. M. Sommers, P. B. Herdson, and J. P. Kaltenbach, "Ischemic Injury of Myocardium," *Ann. N. Y. Acad. Sci.*, vol. 156, pp. 61–78, 1969.

[232] M. Bayeva, K. T. Sawicki, J. Butler, M. Gheorghiade, and H. Ardehali, "Molecular and cellular basis of viable dysfunctional myocardium," *Circ. Hear. Fail.*, vol. 7, no. 4, pp. 680–691, 2014.

[233] R. B. Jennings, C. E. Murry, C. Steenbergen, and K. a Reimer, "Development of cell injury in sustained acute ischemia.," *Circulation*, vol. 82, no. 3 Suppl, pp. II2-12, 1990.

[234] K. Reimer and R. Jennings, "The 'wavefront phenomenon' of myocardial ischemic cell death. II. Transmural progression of necrosis within the framework of ischemic bed size (myocardium at risk) and collateral flow.," vol. 40, pp. 633–44, 1979.

[235] R. B. Boatwright, H. F. Downey, F. A. Bashour, and G. J. Crystal, "Transmural variation in autoregulation of coronary blood flow in hyperperfused canine

myocardium," *Circ. Res.*, vol. 47, pp. 599–609, 1980.

[236] B. G. D. Buckberg, D. E. Fixler, J. P. Archie, and J. I. E. Hoffman, "Experimental subendocardial ischemia in dogs with normal coronary arteries," *Circ. Res.*, vol. XXX, pp. 67–81, 1972.

[237] P. Christia, M. Bujak, C. Gonzalez-quesada, W. Chen, A. Reddy, and N. G. Frangogiannis, "Systematic characterization of myocardial inflammation, repair, and remodeling in a mouse model of reperfused myocardial infarction," *J. Histochem. Cytochem.*, vol. 61, no. 8, pp. 555–570, 2013.

[238] J. Schaper, J. Mulch, B. Winkler, and W. Shaper, "Ultrastructural, functional, and biochemical criteria for estimation of reversibility of ischemic injury: a study on the effects of global ischemia on the isolated dog heart.," *J. Mol. Cell. Cardiol.*, vol. 11, pp. 521–541, 1979.

[239] B. Freude *et al.*, "Apoptosis is initiated by myocardial ischemia and executed during reperfusion," *J. Mol. Cell. Cardiol.*, vol. 32, no. 2, pp. 197–208, 2000.

[240] R. S. Whelan, V. Kaplinskiy, and R. N. Kitsis, "Cell death in thepathogenesis of heart disease: mechanisms and significance," *Annu. Rev. Physiol.*, vol. 72, no. 1, pp. 19–44, 2010.

[241] R. A. Gottlieb, "Cell death pathways in acute ischemia/reperfusion injury," *J. Cardiovasc. Pharmacol. Theapeutics*, vol. 16, no. 3–4, pp. 233–238, 2011.

[242] M. Chiong *et al.*, "Cardiomyocyte death: Mechanisms and translational implications," *Cell Death Dis.*, vol. 2, no. 12, pp. 1–11, 2011.

[243] H. T. Karsner and J. E. Dwyer, "Experimental bland infarction of the myocardium, myocardial, regenerationa and cicatrization," *J. Med. Res.*, vol. 34, 1915.

[244] G. Kenneth Mallory, P. D. White, and J. Salcedo-Salgar, "The speed of healing of myocardial infarction," *Am. Heart J.*, vol. 18, no. 6, pp. 647–671, 1939.

[245] N. G. Frangogiannis, "Regulation of the inflammatory response in cardiac repair," *Circ. Res.*, vol. 110, no. 1, pp. 159–173, 2012.

[246] M. P. Czubryt, "Common threads in cardiac fibrosis, infarct scar formation, and wound healing," *Fibrogenes. Tissue Repair*, vol. 5, no. 1, pp. 1–11, 2012.

[247] G. Ertl and S. Frantz, "Healing after myocardial infarction," *Cardiovasc. Res.*, vol. 66, no. 1, pp. 22–32, 2005.

[248] N. G. Frangogiannis, "The inflammatory response in myocardial injury, repair,

and remodelling," *Nat. Rev. Cardiol.*, vol. 11, no. 5, pp. 255–265, 2014.

[249] N. G. Frangogiannis, "The immune system and cardiac repair," *Pharmacol. Res.*, vol. 58, no. 2, pp. 88–111, 2008.

[250] M. A. Pfeffer and J. M. Pfeffer, "Ventricular enlargement and reduced survival after myocardial infarction," *Circulation*, vol. 75, no. 5 II SUPPL., pp. 93–97, 1987.

[251] M. Pfeffer and E. Braunwald, "Ventricular remodeling after myocardial infarction," *Circulation*, vol. 81, no. 4, pp. 1161–1172, 1990.

[252] S. D. Prabhu and N. G. Frangogiannis, "The biological basis for cardiac repair after myocardial infarction," *Circulation Research*. 2016.

[253] D. Fraccarollo, P. Galuppo, and J. Bauersachs, "Novel therapeutic approaches to post-infarction remodelling," *Cardiovasc. Res.*, vol. 94, no. 2, pp. 293–303, 2012.

[254] H. Gewirtz and V. Dilsizian, "Myocardial viability: survival mechanisms and molecular imaging targets in acute and chronic ischemia," *Circ. Res.*, vol. 120, no. 7, pp. 1197–1212, 2017.

[255] L. A. Piérard and E. Picano, "Myocardial viability," *Stress Echocardiogr. Sixth Ed.*, pp. 327–350, 2015.

[256] M. J. Garcia *et al.*, "State of the art: imaging for myocardial viability: a scientific statement from the american heart association," *Circ. Cardiovasc. Imaging*, vol. 13, no. 7, pp. 1–18, 2020.

[257] L. R. Peterson and R. J. Gropler, "Radionuclide imaging of myocardial metabolism," *Circ. Cardiovasc. Imaging*, vol. 3, no. 2, pp. 211–222, 2010.

[258] T. Yabe, K. Mitsunami, T. Inubushi, and M. Kinoshita, "Quantitative measurements of cardiac phosphorus metabolites in coronary artery disease by [31]P magnetic resonance spectroscopy," *Circulation*, vol. 92, no. 1, pp. 15–23, 1995.

[259] K. Golman *et al.*, "Cardiac metabolism measured noninvasively by hyperpolarized 13C MRI," *Magn. Reson. Med.*, vol. 59, no. 5, pp. 1005–1013, 2008.

[260] C. M. Moon, Y. H. Kim, Y. K. Ahn, M. H. Jeong, and G. W. Jeong, "Metabolic alterations in acute myocardial ischemia-reperfusion injury and necrosis using in vivo hyperpolarized [1-13C] pyruvate MR spectroscopy," *Sci. Rep.*, vol. 9,

no. 1, pp. 1–11, 2019.

[261] M. A. Schroeder, K. Clarke, S. Neubauer, and F. Facc, “Hyperpolarized magnetic resonance: a novel technique for the in vivo assessment of cardiovascular disease,” *Circulation*, vol. 124, no. 14, pp. 1580–1594, 2011.

[262] O. J. Rider and D. J. Tyler, “Clinical Implications of Cardiac Hyperpolarized Magnetic Resonance Imaging,” pp. 1–9, 2013.

[263] S. Flacke *et al.*, “Characterization of viable and nonviable myocardium at MR imaging: comparison of gadolinium-based extracellular and blood pool contrast materials versus manganese-based contrast materials in a rat myocardial infarction model.,” *Radiology*, vol. 226, no. 3, pp. 731–8, 2003.

[264] M. H. Vandsburger, B. A. French, C. M. Kramer, X. Zhong, and F. H. Epstein, “Displacement-encoded and manganese-enhanced cardiac MRI reveal that nNOS, not eNOS, plays a dominant role in modulating contraction and calcium influx in the mammalian heart,” *Am. J. Physiol. - Hear. Circ. Physiol.*, vol. 302, no. 2, pp. 412–419, 2012.

[265] I. Toma *et al.*, “Telmisartan in the diabetic murine model of acute myocardial infarction: Dual contrast manganese-enhanced and delayed enhancement MRI evaluation of the peri-infarct region,” *Cardiovasc. Diabetol.*, vol. 15, no. 1, pp. 1–12, 2016.

[266] Y. Ichikawa *et al.*, “Late gadolinium-enhanced magnetic resonance imaging in acute and chronic myocardial infarction: Improved prediction of regional myocardial contraction in the chronic state by measuring thickness of nonenhanced myocardium,” *J. Am. Coll. Cardiol.*, vol. 45, no. 6, pp. 901–909, 2005.

[267] W. P. Ingkanisorn, K. L. Rhoads, A. H. Aletras, P. Kellman, and A. E. Arai, “Gadolinium delayed enhancement cardiovascular magnetic resonance correlates with clinical measures of myocardial infarction,” *J. Am. Coll. Cardiol.*, vol. 43, no. 12, pp. 2253–2259, 2004.

[268] E. Dall’Armellina *et al.*, “Dynamic changes of edema and late gadolinium enhancement after acute myocardial infarction and their relationship to functional recovery and salvage index,” *Circ. Cardiovasc. Imaging*, vol. 4, no. 3, pp. 228–236, 2011.

[269] J. Schulz-Menger, M. Gross, D. Messroghli, F. Uhlich, R. Dietz, and M. G. Friedrich, “Cardiovascular magnetic resonance of acute myocardial infarction

at a very early stage," *J. Am. Coll. Cardiol.*, vol. 42, no. 3, pp. 513–518, 2003.

[270] C. J. Barclay, "Modelling diffusive O2 supply to isolated preparations of mammalian skeletal and cardiac muscle," *J. Muscle Res. Cell Motil.*, vol. 26, no. 4–5, pp. 225–235, 2005.

[271] S. J. Flacke, S. E. Fischer, and C. H. Lorenz, "Measurement of the gadopentetate dimeglumine partition coefficient in human myocardium in vivo: Normal distribution and elevation in acute and chronic infarction," *Radiology*, vol. 218, no. 3, pp. 703–710, 2001.

[272] H. Arheden *et al.*, "Measurement of the distribution volume of gadopentetate dimeglumine at echo-planar MR imaging to quantify myocardial infarction: Comparison with 99mTc-DTPA autoradiography in rats," *Radiology*, vol. 211, no. 3, pp. 698–708, 1999.

[273] C. Klein, T. R. Schmal, S. G. Nekolla, B. Schnackenburg, E. Fleck, and E. Nagel, "Mechanism of late gadolinium enhancement in patients with acute myocardial infarction," *J. Cardiovasc. Magn. Reson.*, vol. 9, no. 4, pp. 653–658, 2007.

[274] S. Hammer-Hansen *et al.*, "Early Gadolinium Enhancement for Determination of Area at Risk A Preclinical Validation Study," *JACC Cardiovasc. Imaging*, vol. 10, pp. 130–139, 2017.

[275] B. Mc Ardle *et al.*, "Long-term follow-up of outcomes with F-18-fluorodeoxyglucose positron emission tomography imaging-assisted management of patients with severe left ventricular dysfunction secondary to coronary disease," *Circ. Cardiovasc. Imaging*, vol. 9, no. 9, pp. 1–8, 2016.

[276] R. O. Bonow, G. Maurer, K. L. Lee, T. A. Holly, P. F. Binkley, and J. A. Panza, "Myocardial viability in ischemic left ventricular dysfunction," *N. Engl. J. Med.*, vol. 364, no. 17, pp. 1617–1625, 2011.

[277] P. S. Patrick *et al.*, "Radio-metal cross-linking of alginate hydrogels for non-invasive in vivo imaging," *Biomaterials*, vol. 243, no. March, p. 119930, 2020.

[278] J. Bargehr *et al.*, "Epicardial cells derived from human embryonic stem cells augment cardiomyocyte-driven heart regeneration," *Nat. Biotechnol.*, vol. 37, no. 8, pp. 895–906, 2019.

[279] E. J. Benjamin *et al.*, *Heart disease and stroke statistics-2019 update: a report from the american heart association*, vol. 139, no. 10. 2019.

[280] T. J. Cahill and R. K. Kharbanda, “Heart failure after myocardial infarction in the era of primary percutaneous coronary intervention: Mechanisms, incidence and identification of patients at risk,” *World J. Cardiol.*, vol. 9, no. 5, p. 407, 2017.

[281] H. M. Viola and L. C. Hool, “Impaired calcium handling and mitochondrial metabolic dysfunction as early markers of hypertrophic cardiomyopathy,” *Arch. Biochem. Biophys.*, vol. 665, no. January, pp. 166–174, 2019.

[282] M. L. Law, H. Cohen, A. A. Martin, A. B. B. Angulski, and J. M. Metzger, “Dysregulation of calcium handling in duchenne muscular dystrophy-associated dilated cardiomyopathy: mechanisms and experimental therapeutic strategies,” *J. Clin. Med.*, vol. 9, no. 2, p. 520, 2020.

[283] M. M. G. Van Den Hoogenhof *et al.*, “RBM20 mutations induce an arrhythmogenic dilated cardiomyopathy related to disturbed calcium handling,” *Circulation*, vol. 138, no. 13, pp. 1330–1342, 2018.

[284] Q. Lou, A. Janardhan, and I. R. Efimov, “Remodeling of calcium handling in human heart failure,” *Adv Exp Med Bio*, vol. 740, p. 1267, 2012.

[285] N. Spath, M. R. Dweck, A. H. Baker, D. E. Newby, and S. I. Semple, “Functional assessment of the myocardium in non-ischaemic cardiomyopathy using manganese-enhanced T1 mapping,” in *ESC Congress 2019 together with World Congress of Cardiology*, 2019, p. 2455.

[286] M. Tawa, S. Yamamoto, M. Ohkita, and Y. Matsumura, “Endothelin-1 and norepinephrine overflow from cardiac sympathetic nerve endings in myocardial ischemia,” *Cardiol. Res. Pract.*, vol. 1, no. 1, 2012.

[287] J. G. Akar and F. G. Akar, “Regulation of ion channels and arrhythmias in the ischemic heart,” *J. Electrocardiol.*, vol. 40, no. 6 SUPPL. 1, pp. 37–41, 2007.

[288] A. Abraham *et al.*, “18F-FDG PET imaging of myocardial viability in an experienced center with access to 18F-FDG and integration with clinical management teams: The Ottawa-FIVE substudy of the PARR 2 trial,” *J. Nucl. Med.*, vol. 51, no. 4, pp. 567–574, 2010.

[289] L. M. Mielniczuk, G. G. Toth, J. X. Xie, B. De Bruyne, L. J. Shaw, and R. S. Beanlands, “Can functional testing for ischemia and viability guide revascularization?,” *JACC Cardiovasc. Imaging*, vol. 10, no. 3, pp. 354–364, 2017.